https://doi.org/10.15388/vu.thesis.56
https://orcid.org/0000-0003-1850-5157

VILNIUS UNIVERSITY
CENTER FOR PHYSICAL SCIENCES AND TECHNOLOGY

Giedrė
GAIDAMAVIČIENĖ

Synthesis and characterization of multicomponent oxide materials prepared by an aqueous sol-gel method

DOCTORAL DISSERTATION

Natural Sciences,
Chemistry N 003

VILNIUS 2020

This dissertation was written between 2016 and 2020 at Vilnius University.

Academic supervisor:

Assoc. Prof. Dr. Artūras Žalga (Vilnius University, Natural Sciences, Chemistry – N 003).

This doctoral dissertation will be defended in a public meeting of the Dissertation Defence Panel:

Chairman – **Prof. Habil. Dr. Rimantas Ramanauskas** (Center for Physical Sciences and Technology, Natural Sciences, Chemistry – N 003).

Members:

Prof. Dr. Ingrida Ancutienė (Kaunas University of Technology, Natural Sciences, Chemistry – N 003);

Assoc. Prof. Dr. Inga Grigoravičiūtė-Puronienė (Vilnius University, Natural Sciences, Chemistry – N 003);

Prof. Dr. Gerd Meyer (Royal Institute of Technology (KTH), Stockholm, Sweden, Natural Sciences, Chemistry – N 003);

Dr. Živilė Stankevičiūtė (Vilnius University, Natural Sciences, Chemistry – N 003).

The dissertation shall be defended at a public meeting of the Dissertation Defence Panel at 3 p.m. on 18 September 2020 at the Inorganic Chemistry auditorium 141 of the Institute of Chemistry, Faculty of Chemistry and Geosciences, Vilnius University.

Address: Naugarduko str. 24, LT-03225, Vilnius, Lithuania

Tel. +370 5 219 3108; e-mail: info@chgf.vu.lt

The text of this dissertation can be accessed at the Libraries of Vilnius University and Center for Physical Sciences and Technology, as well as on the website of Vilnius University: www.vu.lt/lt/naujienos/ivykiu-kalendorius

https://doi.org/10.15388/vu.thesis.56
https://orcid.org/0000-0003-1850-5157

VILNIAUS UNIVERSITETAS
FIZINIŲ IR TECHNOLOGIJOS MOKSLŲ CENTRAS

Giedrė
GAIDAMAVIČIENĖ

Daugiakomponenčių oksidinių medžiagų sintezė vandeniniu zolių-gelių metodu ir apibūdinimas

DAKTARO DISERTACIJA

Gamtos mokslai,
Chemija N 003

VILNIUS 2020

Disertacija rengta 2016 – 2020 metais Vilniaus universitete.

Mokslinis vadovas:
doc. dr. Artūras Žalga (Vilniaus universitetas, gamtos mokslai, chemija – N 003).

Gynimo taryba:
Pirmininkas – **prof**. **habil. dr. Rimantas Ramanauskas** (Fizinių ir technologijos mokslų centras, gamtos mokslai, chemija – N 003).
Nariai:
prof. dr. Ingrida Ancutienė (Kauno technologijos universitetas, gamtos mokslai, chemija – N 003);
doc. dr. Inga Grigoravičiūtė-Puronienė (Vilniaus universitetas, gamtos mokslai, chemija – N 003);
prof. dr. Gerd Meyer (Karališkasis technologijos institutas, Švedija, gamtos mokslai, chemija – N 003);
dr. Živilė Stankevičiūtė (Vilniaus universitetas, gamtos mokslai, chemija – N 003).

Disertacija bus ginama viešame Chemijos mokslų krypties gynimo tarybos posėdyje 2020 m. rugsėjo mėn. 18 d. 15 val. Vilniaus universiteto Chemijos ir geomokslų fakulteto Chemijos instituto Neorganinės chemijos auditorijoje 141. Adresas: Naugarduko g. 24, LT-03225, Vilnius, Lietuva, tel. +370 5 219 3108; el. paštas info@chgf.vu.lt.

Disertaciją galima peržiūrėti Vilniaus universiteto, Fizinių ir technologijos mokslų centro bibliotekose ir VU interneto svetainėje adresu: https://www.vu.lt/naujienos/ivykiu-kalendorius

ABSTRACT

Nowadays, a lot of attention has been attracted to the investigation of the new multicomponent oxide materials and their preparation methods. Due to their unique structural, electronic and catalytic properties, such materials can be used in various applications. Metal molybdates with scheelite-type structure could be used in scintillators, as luminescent materials and photocatalysts. Such materials, which are partially substituted by the rare earth elements, possess a high emission efficiency and used in the production of advanced lighting and display panels. Meanwhile, LAMOX-type materials and gadolinium-doped ceria oxides due to their unique electric properties show the great potential in solid oxide fuel cells as electrolytes. These compounds could also be used in oxygen pumps, gas sensors and membranes for oxygen separation.

It is well known that chemical and physical properties are strongly related to structural and morphological properties of prepared oxides; hence it is important to choose the right synthesis method and conditions. In this work, the multicomponent oxides with general formula of $Ca_{1-x}Sr_xMoO_4$, $M_{0.05}Eu_{0.05}Ca_{0.9}MoO_4$ (M=Li, Na, K, Rb, Cs), $La_2Mo_2O_9$ and $Ce_{0.9}Gd_{0.1}O_{1.95}$ were prepared using aqueous sol-gel synthesis route. The tartaric acid or the oxalic acid was used as a chelating agent. The obtained precursor gels were additionally calcined at different temperatures. In order to investigate thermal decomposition of prepared samples, thermogravimetric and differential scanning calorimetry (TGA–DSC) analysis was performed. Structural and morphological properties were investigated using X-Ray diffraction (XRD) and scanning electron microscopy (SEM) techniques. Different analysis methods such as infrared (FTIR), Raman and photoluminescence spectroscopies were performed to characterize structure and composition, and to estimate the optical properties of europium oxide in $M_{0.05}Eu_{0.05}Ca_{0.9}MoO_4$ ceramic as a dopant in samples according to the nature of alkali metals. The electrical properties of $La_2Mo_2O_9$ were investigated using two different impedance spectroscopy techniques by a newly developed impedance spectrometer.

The TGA–DSC results showed that the thermal decomposition of tartrate gel precursors for scheelite-type ceramics is very similar despite any additional ion substitutions. Additionally, it was found that the excess of tartaric acid decomposes to CO, CO_2 and lower molecular mass acids. Meanwhile, the thermal decomposition of La–Mo–O gel precursor slightly

differs, in spite of synthesis conditions being very similar. Moreover, the thermal decomposition of Ce–Gd–O oxalate precursor was investigated. It was found that the oxalate precursor decomposition mechanism is much simpler and occurs in three main steps.

The results obtained from XRD analysis showed that in all cases single-phase oxides formed. This leads to a conclusion, that aqueous sol-gel synthesis route is suitable for the preparation of multicomponent oxides. FTIR analysis showed that absorption bands related to organic compounds functional groups occur in lower temperatures before crystalline compound formation. These results are in good agreement with TGA–DSC analysis data which showed that the main organic part of the gel decomposes up to 300 °C of temperature.

It was found that surface morphology of $Ca_{1-x}Sr_xMoO_4$ samples consist of agglomerated irregular sphere-like particles. The particle size distribution indicates that samples with higher substitution of Sr^{2+} ion have larger particles than those with lower substitution amount. The lanthanum molybdate surface morphology revealed that the ceramic consists of circular-shape crystals with well-connected grains. Such a dense structure is very important for further investigation of electrical properties that allow eliminating factors such as porosity and low connectivity between the grains that usually affect physical properties of the ceramic obtained. Interesting results were obtained in the $Ce_{0.9}Gd_{0.1}O_{1.95}$ oxide surface analysis. It was found that in temperatures above 1000 °C the surface morphology completely changes from irregular plate-like shape particles to agglomerated sphere-like particles.

The Raman spectroscopy analysis confirmed the initial composition of $Ca_{1-x}Sr_xMoO_4$ ceramic. The calculated and experimental composition showed only a small deviation that could have been caused by measurement errors. This leads to a conclusion that the aqueous sol-gel method is suitable for multicomponent oxides preparation with an exact molar ratio. Moreover, a photoluminescent spectroscopy analysis showed an interesting relation between optical properties and crystallite size. Measured electrical properties of the $La_2Mo_2O_9$ ceramic showed that the activation energy is slightly higher in the phase transition of monoclinic α-phase to cubic β-phase (1.09 eV) than the opposite process measured at 1.01 eV.

Keywords: multicomponent oxides, scheelite-type, molybdates, LAMOX, gadolinium-doped ceria, sol-gel process, tartaric acid, oxalic acid, thermal properties, thermal decomposition mechanism, Rietveld refinement, spectroscopy, optical properties, electrical properties.

LIST OF PUBLICATIONS

This thesis is based on the articles included in the Web of Science database:

I. **G. Gaidamavičienė**, A. Žalga, Synthesis, a structural and thermoanalytical study of $Ca_{1-x}Sr_xMoO_4$ ceramic, *Materials Chemistry and Physics* 241 (2020) 122339. *doi: https://doi.org/10.1016/j.matchemphys.2019.122339*.

II. **G. Gaidamavičienė**, G. Janulevičius, E. Venslauskaitė, A. Žalga, Aqueous sol-gel synthesis, thermoanalytical study and luminescent properties of $M_{0.05}Eu_{0.05}Ca_{0.9}MoO_4$ (M=Li, Na, K, Rb, Cs) nanocrystallites, *Journal of Thermal Analysis and Calorimetry* 140 (2020) 2185-2201. *doi: https://doi.org/10.1007/s10973-019-08962-7*

III. A. Žalga, **G. Gaidamavičienė**, Ž. Gricius, E. Užpurvytė, J. Gadeikis, A. Diktanaitė, M. Barré, T. Šalkus, A. Kežionis, E. Kazakevičius, Aqueous sol-gel synthesis, thermoanalytical study and electrical properties of $La_2Mo_2O_9$, *Journal of Thermal Analysis and Calorimetry* 132(3) (2018) 1499-1511. *doi: https://doi.org/10.1007/s10973-018-7120-3*

IV. **G. Gaidamavičienė**, B. Abakevičienė, A. Žalga, Oxalic acid assisted synthesis of the gadolinium-doped ceria oxide-ion conductor as electrolyte for the solid oxide fuel cells, *Chemical Papers* 73(4) (2019) 891-899. *doi: https://doi.org/10.1007/s11696-018-0648-7*

AUTHOR'S CONTRIBUTION TO THE ARTICLES

I. The author designed the conditions for synthesis of Ca–Sr–Mo–O tartrate gel precursors with the initial composition of $Ca_{1-x}Sr_xMoO_4$ (x=0; 0.1; 0.2; 0.3; 0.4; 0.5; 0.6; 0.7; 0.8; 0.9; 1). Determined the thermal decomposition mechanism from thermogravimetric and differential scanning calorimetry analysis results. Performed X-Ray diffraction, scanning electron microscopy and infrared analyses for determination of crystal structure and morphology of prepared ceramics. Investigated the calculations of initial composition of $Ca_{1-x}Sr_xMoO_4$ oxides using Raman spectroscopy analysis results. In cooperation with the co-authors presented the results for publication.

II. The author carried out the synthesis of M–Eu–Ca–Mo–O (M=Li, Na, K, Rb, Cs) tartrate gel precursors for $M_{0.05}Eu_{0.05}Ca_{0.9}MoO_4$ ceramics. Performed X-Ray diffraction, scanning electron microscopy and infrared spectroscopy analyses to determine the crystal structure and morphology of prepared M–Eu–Ca–Mo–O tartrate gel precursors and ceramics heat-treated at different temperatures. The results were investigated and summarized with co-authors and presented in the article.

III. The author synthesized La–Mo–O tartrate gel precursor for $La_2Mo_2O_9$ oxide. Calculated the thermal decomposition mechanism from thermogravimetric and differential scanning calorimetry analysis data. Performed X-Ray diffraction and scanning electron microscopy analyses to determine the structure and surface morphology of prepared oxides heat-treated at different temperatures. The results were investigated with co-authors and presented in the article.

IV. The author carried out the synthesis of Ce–Gd–O oxalate precursor gel for $Ce_{0.9}Gd_{0.1}O_{1.95}$ ceramic. Calculated thermal decomposition mechanism based on thermogravimetric and differential scanning calorimetry analysis data. Performed X-Ray diffraction analysis of prepared Ce–Gd–O oxalate gel precursors annealed at different temperatures and determined the crystal structure. Investigated surface morphology changes and characteristic vibrations of functional groups. Summarized the results and in cooperation with the co-authors prepared the publication.

TABLE OF CONTENTS

LIST OF ABBREVIATIONS

CCP	Cubic closed-packed
CHP	Combined heat and power
DSC	Differential scanning calorimetry
DTA	Differential thermal analysis
DTG	Derivative thermogravimetry
EDTA	Ethylenediamine tetraacetic acid
FTIR	Fourier-transform infrared spectroscopy
GDC	Gadolinium-doped ceria
HMTA	Hexamethylene tetraamine
LAMOX	$La_2Mo_2O_9$-type compounds
PL	Photoluminescence
PT	Phase transition
PVA	Polyvinyl alcohol
SEM	Scanning electron microscopy
SGC	Sol-gel combustion
SOFC	Solid oxide fuel cell
TA	Tartaric acid
TGA	Thermogravimetric analysis
XRD	X-Ray diffraction
YSZ	Yttria-stabilized zirconia

INTRODUCTION

Nowadays, many scientists are interested in multicomponent crystalline oxides due to their various applications and unique physical and chemical properties. Due to the useful applicability, different scheelite-type oxides with a general formula of $MMoO_4$ could be used in various fields of applications such as a host of lanthanide-activated lasers [1], luminescence materials [2], microwave applications [3], catalysts [4] and scintillators [5]. The specific characteristics of the ceramic materials could be modified incorporating other ions to produce binary solid solutions with better properties than individual compounds [6, 7]. However, the preparation of mixed double oxides remains a great challenge due to the mixing stage aimed to obtain a homogenous final compound.

Scheelite-type $CaMoO_4$ materials due to their self-emitting nature of blue, green and sometimes orange colors under UV-light excitation in 250 – 320 nm region, are promising phosphors for advanced lighting and display applications when doped with rare earth elements (Eu^{3+}, Tb^{3+}) [8, 9]. Calcium molybdate doped by Eu^{3+} ion exhibits strong red luminescence [10]. It was observed that doping $CaMoO_4$ with two or more ions: a rare-earth element and a charge-compensating element, luminescent intensity is significantly improved without increasing rare-earth ion amount [11]. It is widely known that luminescent properties are strongly related to the final ceramic morphology. It was found that a spherical particle reduces the light scattering on surfaces and allows forming denser phosphor layers because of close-packing of the spheres [12].

Due to the increasing ecological requirements for power sources, the development of new efficient and environmentally friendly devices take priority. During the past decade, solid oxide fuel cells have been extensively investigated as a next generation of the green energy system which exhibits high ionic conductivity, chemical and thermal stability and has high energy efficiency, especially when combined with a gas turbine as well as low pollution emission when compared to other fuel cells [13-15]. Electrolytes such as LAMOX family materials and gadolinium-doped ceria are considered as potential materials for intermediate temperature solid oxide fuel cells [16, 17] due to their enhanced oxide ion conductivity, high density of ceramics and low electronic conductivity [18, 19]. However, the lower temperatures result in the greater loss of power density due to the decrease in the ionic conductivity. To solve this problem, an innumerable amount of work has been

carried out by different research groups such as looking for the ideal doping ratio and the appropriate ion to balance stability.

It was found that the preparation method strongly affects the structural and morphological properties of the final ceramic. There are various published methods to synthesize multicomponent oxides. Methods that require harsh reaction conditions, additional milling or precipitate separation have poor homogeneity, low crystallinity, impurities and additionally do not allow obtaining dense ceramic. In order to eliminate these drawbacks, a lot of attention has been drawn by the wet-chemical methods. The simplest, cheapest and environmentally friendly method is the aqueous sol-gel synthesis. The possibility to control reaction conditions such as temperature, concentration, time, pH and others open the way to controlling the final ceramic structure, crystallite size and morphology.

The aim of this PhD thesis was to synthesize different single-phase multicomponent oxides by an aqueous sol-gel method and to investigate detailed thermal decomposition mechanisms of prepared precursor gels. In order to achieve this aim, the following tasks were formulated:

1. To synthesize single-phase multicomponent oxides with the general formula of $Ca_{1-x}Sr_xMoO_4$, $M_{0.05}Eu_{0.05}Ca_{0.9}MoO_4$ (M=Li, Na, K, Rb, Cs), $La_2Mo_2O_9$ and $Ce_{0.9}Gd_{0.1}O_{1.95}$ by an aqueous sol-gel synthesis method.
2. To investigate the thermal decomposition mechanism of prepared gel precursors by the thermogravimetric and differential scanning calorimetric analysis.
3. To investigate the crystal structure and surface morphology changes from the temperature of the heat-treatment of prepared samples using X-Ray diffraction analysis, scanning electron microscopy and infrared spectroscopy.
4. To calculate the molar composition for $Ca_{1-x}Sr_xMoO_4$ system by Raman spectroscopy.
5. To determine the relation between crystallite size growth and optical properties for $M_{0.05}Eu_{0.05}Ca_{0.9}MoO_4$ oxides.
6. To investigate the electrical properties for $La_2Mo_2O_9$ ceramic.
7. To determine the onset and end temperatures of the phase transition from monoclinic α-phase to cubic β-phase and the opposite process for $La_2Mo_2O_9$ system by differential scanning calorimetry analysis.

Statements to be defended:

1. For the first time the aqueous tartaric acid-assisted sol-gel synthesis technique was successfully proposed for the preparation of $La_2Mo_2O_9$, $Ca_{1-x}Sr_xMoO_4$ and $M_{0.05}Eu_{0.05}Ca_{0.9}MoO_4$ (M=Li, Na, K, Rb, and Cs) ceramic materials.
2. TGA–DSC analysis is a powerful and suitable tool for both the investigation of decomposition mechanisms of La–Mo–O, Ca–Sr–Mo–O, and M–Eu–Ca–Mo–O (M=Li, Na, K, Rb, and Cs) tartrate gel precursors and the estimation of the crystallization processes of the final $La_2Mo_2O_9$, $Ca_{1-x}Sr_xMoO_4$ and $M_{0.05}Eu_{0.05}Ca_{0.9}MoO_4$ ceramic oxides.
3. The nature of the complexing agent is the critical stage in the sol-gel process, which strongly influences the morphological, structural, optical and electrical properties of obtained ceramic compounds.
4. The thermal decomposition mechanism of the as-prepared metal tartrate gel precursors is directly related to the degradation of tartaric acid and corresponding metal tartrates.
5. The heat-treatment atmosphere does not have any influence on either the thermal decomposition of synthesized gel precursors or the crystallization of the final ceramics.
6. The combination of thermal analysis and different characterization techniques is a useful tool that enables the demonstration of interesting relations between chemical and physical properties of obtained ceramics.

1. LITERATURE OVERVIEW

1.1. Scheelite-type molybdates

In the past decades, scheelite type AMO_4 ternary oxides attracted many scientists' attention due to their unique luminescent [20], catalytic [21], electronic [22] and structural properties [23]. These materials could be used in optical devices ($CaMoO_4$, $PbMoO_4$) [24-26], laser crystals ($SrMoO_4$, $PbWO_4$) [27-29], scintillators [30-33], catalysts [34-36], oxide-ion conductors [37, 38], solid oxide fuel cells [39], and magnetic materials [40]. The properties of such materials can be modified using binary solid solutions with better characteristics than individual compounds. Yue Wu et al. reported that binary perovskite-type materials might have better properties than individual compounds [6, 41]. Moreover, S. L. Porto et al. demonstrated that $CaWO_4$ doped by strontium has better photoluminescent properties than individual $CaWO_4$ ceramic [7]. Furthermore, it was observed that by doping these materials with rare earth metals or transitional oxides these systems can be easily adapted to the synthesis of luminescent materials [42]. According to the literature [43] it was indicated that Ca–Sr–Mo–O phosphors doped with Eu^{3+} in the excitation with ultraviolet (395 nm) and blue light (467 nm) exhibits bright red emission (615 nm).

1.1.1 Crystal structure

Calcium and strontium molybdates crystallize into the so-called scheelite structure [44]. This structure was first discovered by Carl Wilhelm Scheele in 1781. Alkaline earth metal molybdates $AMoO_4$ (A=Ca, Sr) have tetragonal crystal lattice ($a=b\neq c$, $\alpha=\beta=\gamma=90°$) with a space group $I4_1/a$ [45, 46] and symmetry point group S_4 having two formula units per unit cell [47, 48]. In such a structure, oxygen atoms are located by cubic closed-packed (CCP) array where tetrahedral and octahedral holes are formed [49, 50]. Each Mo^{6+} atom is surrounded by four oxygen atoms forming a tetrahedral unit. Two types of tetrahedral holes exist in such a lattice, an upwards-directed tetrahedral top (T+) and a downwards-directed tetrahedral (T-). The number of these different holes must be equal in CCP array. Calcium or strontium ions are surrounded by eight oxygen atoms forming bisdisphenoid polyhedral (AO_8). Each polyhedral cluster shares four of its edges with four other AO_8 polyhedrals resulting in zigzag chains along the c-axis [51]. Tetrahedrals are

isolated against each other, but connected with AO_8 polyhedrals by sharing their oxygen atom corners (Fig. 1) [52, 53].

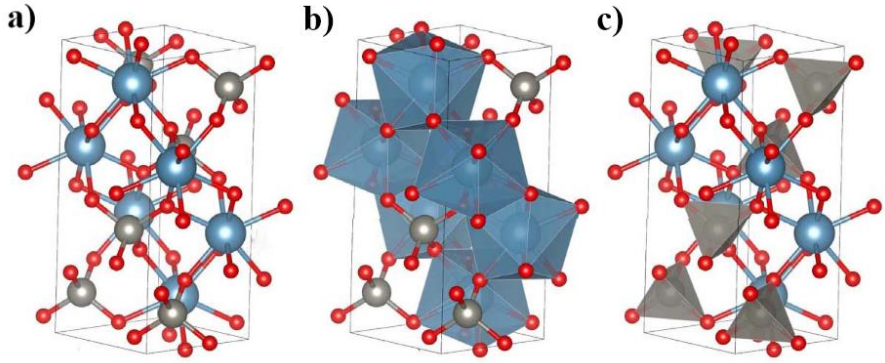

Fig. 1 (a) $AMoO_4$ (A=Ca, Sr) scheelite type structure; (b) octahedral units [AO_8]; (c) tetrahedral units [MoO_4]. Blue spheres represent alkaline earth metal atoms, grey – molybdenum atoms, and red – oxygen atoms [54]

According to the literature, calcium molybdate substitution with other alkaline earth metals affects only the parameters of the crystal lattice rather than its structure.

1.1.2 Synthesis methods

There are many synthesis methods to synthesize alkaline earth metal molybdates, such as solid-state reaction [55-58], co-precipitation [59], molten salt [60], sonochemical [61], microwave assisted synthesis [62], Czochraski [63], combustion [64] and sol-gel method. Solid-state method is the most widely used synthesis for the preparation of oxides from solid starting materials. It is one of the simplest and cheapest solvent-free methods. Ramarao with coworkers successfully synthesized mixed double $Ca_{1-x}Sr_xMoO_4$ oxides via conventional solid-state reaction method. Starting materials $CaCO_3$, $SrCO_3$ and MoO_3 were mixed in an agate mortar with distilled water. Usually, a few drops of organic [65] or inorganic solvents [66] are added to reach higher homogeneity before sintering reaction mixture. After mixing, the prepared mixture was calcined at 900 °C temperature for 3 h and additionally sintered in 1100 – 1300 °C temperature for 3 h. After X-Ray diffraction (XRD) analysis it was determined that all prepared ceramics had tetragonal scheelite structure and no impurities were found [67]. However, there are some drawbacks to this method, such as intermediate mixing to bring new surfaces in contact, poor homogeneity due to molybdenum oxide

tendency to vaporize at high temperatures, and treatment temperature which should be higher than the melting point of starting materials in order to start ion diffusion [2].

Another very often used method is co-precipitation synthesis. This method is simple and it is easy to control particle size and shape by changing various parameters such as concentration, pH, temperature, reaction time and nature of materials [68]. Also, it does not require harsh reaction conditions and is friendly to the environment [69]. The starting materials, usually metal nitrates or oxides, are dissolved in the water [23] or organic solvent [70]. Precursors are mixed together and heated. Nucleation and growth process starts and a large number of small particles forms. Post-nucleation process results in aggregation which affects particle size and shape. Aqueous solutions containing different concentrations of Sr^{2+} and MoO_4^{2-} ions were mixed under continuous stirring. Depending of molar ratio of $[MoO_4^{2-}]/[Sr^{2+}]$, pure $SrMoO_4$ powders with different morphology were synthesized. At the lower ratio the rods and flower-like spheres formed, while increasing molar ratio resulted in peanut-like and dumbbell morphologies formation [71]. In addition, this method is suitable for mixed alkaline earth metal molybdates. Starting materials were dissolved in the deionized water and the reaction was carried out at a constant pH=2 with nitric acid. Molybdate ion solution pH value to 10 – 11 was increased by addition of ammonia solution. Oxide precipitate was formed after an aqueous solution was dropped to prepared precipitator. As a result, pure calcium-strontium molybdates were formed [59]. As all methods, this technique has some drawbacks: impurities could be precipitated together contaminating the final product, precipitate separation from solvent and agglomeration.

One of the most popular, simplest and environmentally friendly synthesis for oxides is sol-gel method. By changing synthesis parameters like temperature, nature of starting materials, concentration, pH, nature of complexing agent, solvent, reaction time etc., it is possible to control the final product's particle size, morphology, purity, homogeneity and properties [72]. Sol-gel synthesis is based on the dissolution of metal salts, oxides or organic metal compounds in water, aqueous solutions or organic solvents. Aqueous sol-gel synthesis is a good candidate to avoid toxic waste as much as possible because water is used as a main solvent. After dissolution in water, metal ions start to react with water molecules combining hydroxides which usually possess low solubility. The removal of this hydrolysis process consists of replacing the hydroxy groups by other anions. Such competition effect of

ligand reduces the level of hydrolysis with solvent molecules and enhances the solubility of metal ions which are strongly coordinated by ligand molecules. Many mono- and di-carboxylic acids such as glycolic acid [73], oxalic acid [74], tartaric acid (TA) [75-77], ethylenediamine tetraacetic acid (EDTA) [78] and polyacrylic acid [79] have been reported as good chelating agents in the sol-gel synthesis. However, the most commonly used ligand in a sol-gel method is a weak triprotic citric acid which is able to dissociate in three steps depending on pH [80].

Pure single-phase $Ba_{0.5}Sr_{0.5}MoO_4$ nanopowders were synthesized using citric acid-assisted sol-gel synthesis route. Stoichiometric amount of metal nitrates and ammonium molybdate were dissolved in citric acid and ethylene glycol mixture. Prepared samples were heat-treated at 600 °C temperature. X-Ray diffraction analysis showed that a pure solid solution formed [81]. Furthermore, mixed strontium-calcium molybdates were successfully synthesized via a sol-gel method using citric acid as a chelating agent. Metal nitrates and ammonium molybdate were dissolved in deionized water and mixed with citric acid with a molar ratio of 1:1.5. After heat-treatment at 800 °C a tetragonal scheelite structure ceramics of general formula $Sr_{1-x}Ca_xMoO_4$ formed [82]. However, it is not always easy to synthesize the samples desired. In order to synthesize $Ca_{0.5}Sr_{0.5}MoO_4$ powders, metal nitrates and ammonium molybdate were dissolved in citric acid with nitric acid (v/v=5 – 10 %) solution. Obtained gel was calcined at 500 °C temperature for 60 h. According to the XRD analysis results it was clear that the produced powders consisted of the mixture of two solid solutions: $Ca_{0.8}Sr_{0.2}MoO_4$ and $Ca_{0.2}Sr_{0.8}MoO_4$ [6].

This method is also suitable for mixed double oxides substituted by rare earth elements. Aqueous solutions of metal nitrates were added into europium oxide and dilute nitric acid solution. After that, excess of citric acid and glycol mixture with a pH value of 2 – 3 was added directly into the reaction mixture. Obtained powders were calcined at 600 °C for 3 h in air. After XRD analysis it was observed that prepared sample peaks in diffractogram match $Ca_{0.5}Sr_{0.5}MoO_4:Eu^{3+}$ phase with tetragonal structure. Moreover, scanning electron microscopy (SEM) analysis showed that most of the synthesized particles have homogeneous morphology [43].

In another study, starting materials CaO, $SrCO_3$, Eu_2O_3, Li_2CO_3 were dissolved in dilute HNO_3 solution. After that, ammonium molybdate and ammonium tungstate were added directly into the beaker. Next, citric acid with molar ratio 1:6 was added into the reaction solution. Mixture pH was

increased to 8 by adding a dilute ammonia solution and a transparent sol was formed. After drying, gel was calcined at 700 – 1100 °C temperatures for 2 h. XRD results showed that single-phase solid solutions with a general formula of $Ca_{0.6}Sr_{0.4-1.5x-0.5y}Mo_{0.4}W_{0.6}O_4:Eu_xLi_y$ formed. In addition, SEM results showed that upon increasing annealing temperature the particle size grew rapidly, but the shape was not affected [83]. These results indicate that the sol-gel synthesis is appropriate for more complex samples with exact molar composition.

Other methods for the preparation of alkaline earth metal oxides have also been reported [42, 84-86]. However, these reactions usually require harsh reaction conditions, additional separation procedure, expensive or special equipment or reagents and higher energy consumption. Synthesized ceramics in most cases have poor homogeneity and impurities; it is hard to control the molar composition of the final product when small amounts of dopant should be incorporated.

1.1.3 Thermal properties

Thermal analysis is a powerful tool for the characterization of materials and processes such as decomposition mechanism, phase transition (PT), thermal stability, etc. It is well known that thermal processes strongly depend on precursor preparation method. Due to that, in this section, different synthesis techniques will be described for thermal analyses of $CaMoO_4$ and $SrMoO_4$ precursors.

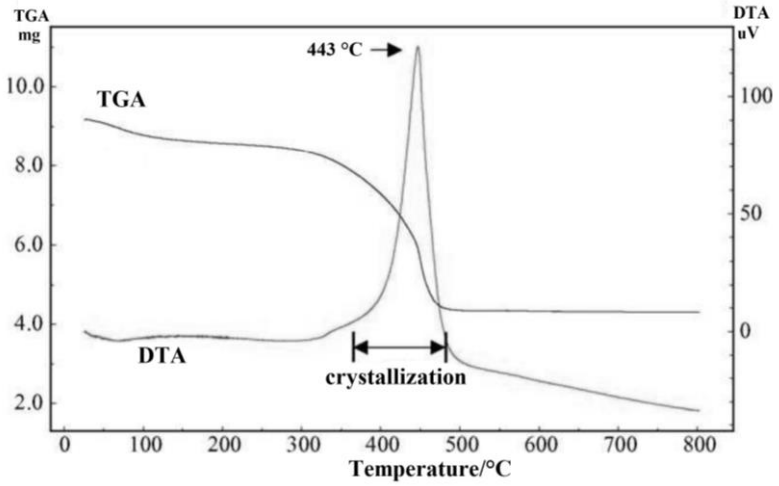

Fig. 2 TGA–DTA curves of the $CaMoO_4$ precursor prepared by microwave-assisted citrate complex method in flowing air [3]

Jeong Ho Ryu with coworkers reported thermogravimetric (TGA) and differential thermal analysis (DTA) results of $CaMoO_4$ synthesized by microwave-assisted citrate complex method using calcium nitrate and ammonium molybdate as starting materials. According to the results (Fig. 2), the biggest mass loss occurs from 300 °C up to 480 °C. This mass loss could be related to decomposition and combustion of the organic materials. From the DTA curve two different effects were observed: at 350 °C the curve corresponds to the initial decomposition of the precursor and formation of the nucleus; at 443 °C the intensive exothermic peak corresponds to the crystallization of the final ceramic [3].

Very similar results were achieved by synthesizing calcium molybdate via a polymerized complex method using calcium nitrate and ammonium molybdate as metallic cations and citric acid as a complexing agent. Fig. 3 shows TGA–DTA curves in flowing air. The mass loss occurs when increasing the temperature up to 500 °C. The single sharp intensive exothermic peak at 475 °C is related to the decomposition of organic compounds that starts at approximately 350 °C. The weight remains constant after the decomposition and crystallization processes [26].

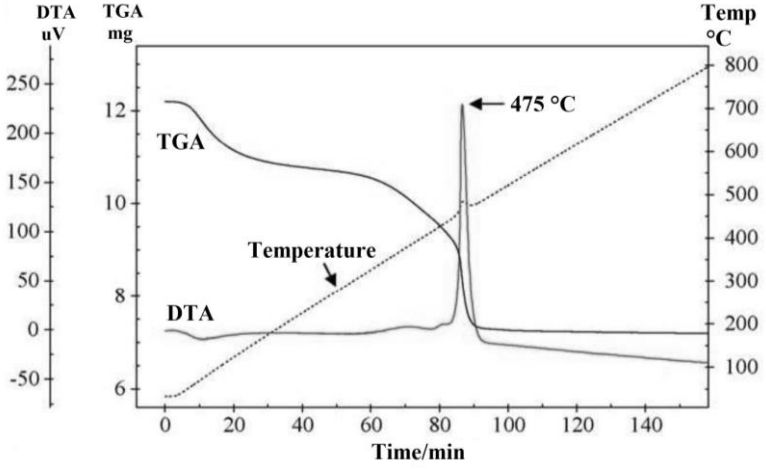

Fig. 3 TGA–DTA curves of the $CaMoO_4$ precursor prepared by a polymerized complex method in flowing air [26]

In 2001, Indian scientists reported combined TGA–DTA results of $CaMoO_4$ synthesis using polymer precursor method. From analysis results (Fig. 4) it is clear that the biggest mass loss occurs from 332 °C to 528 °C and is attributed to organic compounds' (sucrose, polyvinyl alcohol (PVA), diethanolamine and EDTA) oxidation to various gases such as CO, CO_2, water

vapor and NO_2. All these processes overlap and cause one big mass loss. Moreover, the mass remains stable when increasing temperature over 700 °C [36].

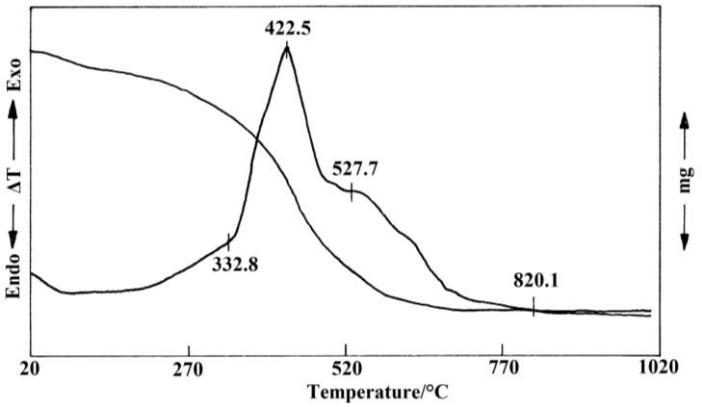

Fig. 4 TGA–DTA curves of the $CaMoO_4$ precursor prepared by polymer precursor method [36]

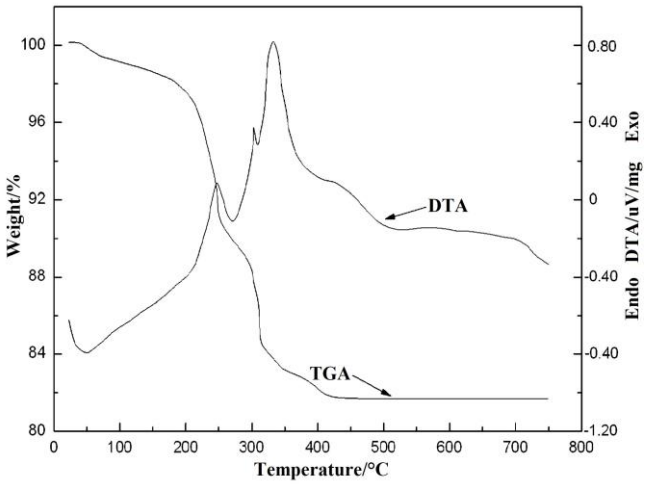

Fig. 5 TGA–DTA curves of the $CaMoO_4$ precursor prepared by HMTA-assisted rheological phase reaction method [87]

Slightly different results were obtained synthesizing rod-like calcium molybdate nanocrystals via hexamethylene tetraamine (HMTA)-assisted rheological phase reaction method using ammonium molybdate and calcium acetate as starting materials (Fig. 5). First mass loss occurs before 200 °C and is related to absorbed water and ammonia removal. The first of the two endothermic peaks in the region of 200 – 422 °C corresponds to the

decomposition of acetic and ammonia salts; the second one – to the reoxidation process of gases. Finally, the exothermic peak at 423 °C is attributed to the crystallization of $CaMoO_4$. After this stage, sample mass remains constant [87].

Brazil scientists in 2018 described TGA and differential scanning calorimetry (DSC) results of $SrMoO_4$ prepared by EDTA-citrate complex method using strontium nitrate and ammonium molybdate as starting materials (Fig. 6). The first stage of mass loss is related to absorbed water removal from gel. Increasing temperature up to 300 °C the elimination of residual ammonia from organic matrix occurs. Moreover, the exothermic peak at 342 °C is related to the decomposition of metal chelates and organic compounds which leads to 23.85 % of mass loss. The last intensive and broad exothermic peak corresponds to $SrMoO_4$ crystallization and after this stage from 650 °C the mass is stabilized. The overall mass loss of this synthesis method is about 72 % [88].

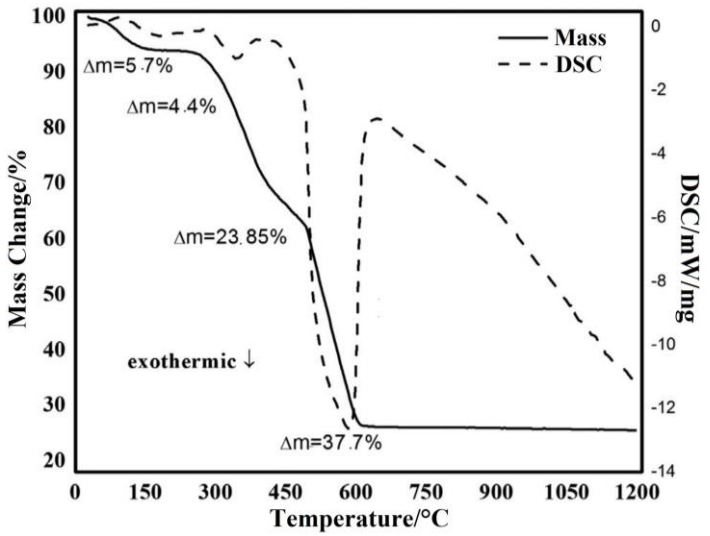

Fig. 6 TGA–DSC curves of the $SrMoO_4$ precursor prepared by EDTA-citrate complex method in flowing air [88]

In the article published in 2019, the scientists present thermogravimetric analysis of $SrMoO_4$ ceramic powders synthesized by solid-state reaction from $SrCO_3$ and MoO_3 precursors. From Fig. 7 three stages could be distinguished. In the first (up to 450 °C) and the third (650 – 900 °C) stages mass loss is insignificant. In the stage two from 450 °C to 650 °C the mass loss is about 13 % and is related to reducing carbonate and formation of sub-oxides [89].

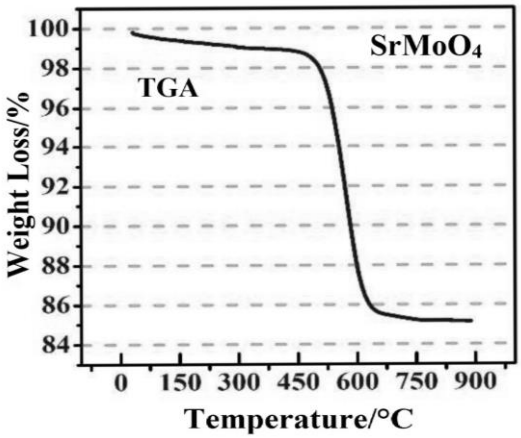

Fig. 7 TGA curve of the $SrMoO_4$ ceramic prepared by solid-state reaction method [89]

In 2017, the scientists published TGA–DSC results (Fig. 8) of $SrMoO_4$ synthesized by precipitation reaction. $NaMoO_4 \cdot 2H_2O$, $SrCl_2 \cdot 6H_2O$ and $Na_3C_6H_5O_7 \cdot 2H_2O$ were used as starting materials. From thermogravimetric results it could be seen that these powders have excellent thermal stability. Increasing the temperature up to 1200 °C the total mass loss is slightly less than 5 % [90].

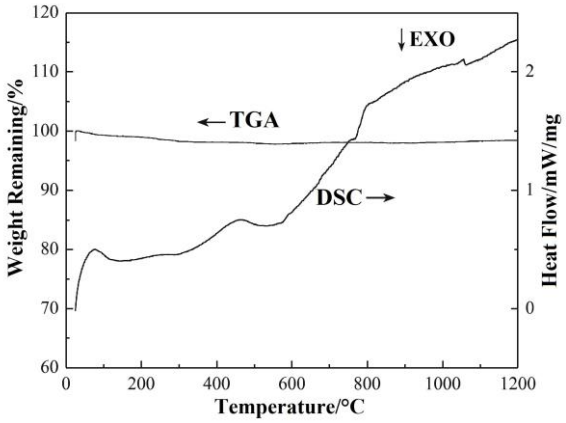

Fig. 8 TGA–DSC curves of the $SrMoO_4$ precursor prepared by precipitation method in flowing air [90]

In summary, previously reviewed results exhibited that the lowest mass loss is observed from precipitation and solid-state reaction techniques. These methods do not use complexing agents that are incorporated in precursor composition. Usually from DTA or DSC curves it is clear that there is just one

peak that is related to carbonate combustion or crystallization process. Methods such as sol-gel, citrate complex and polymer precursor methods that use organic compounds such as citric acid, PVA, EDTA and others as chelating agents have mass loss of about 60 %. Moreover, thermal decomposition is generally followed by three or more processes: the first one is absorbed water removal; the next one is related to organic compounds decomposition and combustion; the last one is related to combustion of formed carbonates and crystallization of the final ceramic.

After analyzing scientific literature, it is clear that there is no detailed information of alkaline earth metal molybdates' thermal decomposition. Although there are some articles that include thermal analysis, the results are not well described.

1.2. Solid oxide fuel cells

Fuel cells were discovered by William Grove in the early 1839. The basic operating principle of these devices is to generate electricity and heat from hydrogen and oxygen as long as fuel and oxidant are supplied [91]. The only product after electrochemical reaction is water (when only hydrogen is used as fuel), thus leading to a conclusion that these fuel cells are environmentally friendly and clean [92, 93]. Comparing these devices with other conventional and distributed generation systems it was observed that energy efficiency of fuel cells is always higher and pollution emission is much lower [94, 95].

Solid oxide fuel cells (SOFCs) were discovered by Swiss scientists Emil Baur and Hans Preis in the late 1930s. After almost a century of scientists' work, an interest in developing new materials and designs increased dramatically [96, 97]. SOFC is an energy conversion device that generates electricity and heat by electrochemical reaction [98, 99]. It is one of the most environmentally-friendly and efficient technologies to produce electric power and heat [100, 101]. These fuel cells could be used in transportation and military market sectors [102]. Furthermore, it is expected that combined heat and power (CHP) systems such as SOFC/gas-turbine could achieve efficiency approximately up to 70 %. In addition, SOFC could be applied in small CHP generation systems in personal houses. Moreover, it is possible to design portable power generators for electronic devices [103-105]. To apply SOFCs to a wide variety of applications, the system cost would have to be reduced and long-term stability would have to be improved [106]. The cost reduction

could be achieved by researching new materials for electrolytes and electrodes, synthesis methods, cell concepts, and a suitable stack design [107].

Fuels such as hydrogen, natural gas and other renewable energy sources are fed into the anode where fuel oxidation happens (Eq. 1). Oxygen from the air is oxidized in a reduction reaction (Eq. 2).

(Anode reaction) $O^{2-} + H_2 \rightarrow H_2O + 2\bar{e}$ (1)

(Cathode reaction) $O_2 + 2\bar{e} \rightarrow O^{2-}$ (2)

After hydrogen oxidation the electrons flow from the anode to the cathode where a continuous supply of oxygen ions is maintained. Oxygen ions migrate through electrolyte to the anode where O^{2-} ions react with H^+ ions producing electric power and water [108, 109]. Principal scheme of SOFC is shown in Fig. 9.

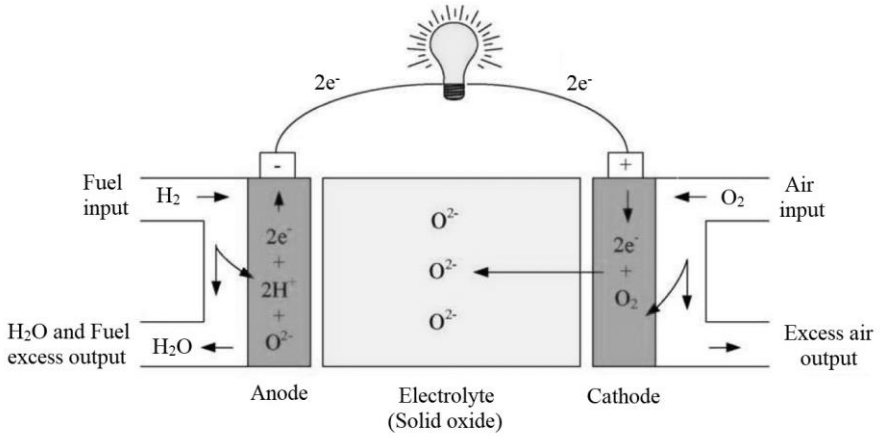

Fig. 9 Principal scheme of solid oxide fuel cell (SOFC) [110]

Despite two major drawbacks such as high operating temperature and high cost of materials [111], fuel cells provide many advantages: high efficiency [112-114], high energy density [115], reliability, modularity [116], fuel flexibility [107, 117], no need for noble metal catalyst [110] and very low levels of SO_x and NO_x emissions [118]; these devices are also quiet and vibration free [102].

SOFCs could operate at medium temperatures of 600 – 1000 °C [108]. Considering the requirements for SOFC components, the choice of materials is limited [119]. Common requirements of all cell components are: chemical and thermal stability in the fuel cell environment and compatibility between

other cell parts; minimum thermal expansion mismatch between various cell components; reasonable strength and toughness at cell working temperature; low cost; low vapour pressure to avoid loss of the material [120].

Electrolyte has the most important role during the SOFC operation. As all the other components, electrolyte also has some requirements that have to be implemented in order for it to become a possible candidate in SOFC it must have high oxide ion conductivity due to oxide ions migration via oxygen vacancies; have high density ceramics to avoid crossover of gases; be insulator of electrons [18, 19]. There is a wide variety of materials that can be used as an electrolyte in SOFCs. The most widely used electrolyte is fluorite-type yttria-stabilized zirconia (YSZ). It crystalizes in cubic crystal structure and has good properties, such as good thermal and chemical stability, low thermal conductivity and high oxygen-ion conductivity. Doping amount of yttria in ZrO_2 crystal structure must be controlled because it could affect grain size, strength and conductivity properties. According to the literature [121, 122], the best amount of yttria is 8 mol% and such ceramic shows the highest ionic conductivity 0.1 S cm^{-1} at 1000 °C.

The next great candidate for a SOFC electrolyte is also the fluorite-type ceria based ceramic. It was found that doping CeO_2 with rare earth elements with lower valence cations such as Gd^{3+}, Nd^{3+}, Pr^{3+}, Sm^{3+} and Y^{3+} dramatically increases ionic conductivity due to increasing oxygen vacancies. The best conductivity was achieved by incorporating gadolinium or samarium into crystal lattice in the 10 – 20 % dopant range (0.1 S cm^{-1} at 800 °C) [122, 123]. However, gadolinium-doped ceria (GDC) oxides showed mixed ionic and electronic conductivity under a reducing atmosphere which depends on temperature [124]. Another possible electrolyte for SOFC is a high-temperature cubic β-$La_2Mo_2O_9$ phase that has high ionic conductivity of about 0.06 S cm^{-1} at 800 °C. The main drawback of this material is the phase transition at 580 °C. Below this temperature lanthanum molybdate crystallizes to low-temperature monoclinic α-$La_2Mo_2O_9$ phase with poor conductivity.

According to research undertaken, there are many other possible electrolytes such as perovskite-structured $LaGaO_3$-based ceramics, δ-Bi_2O_3 and $Bi_4V_2O_{11}$-based oxides, and pyrochlore family materials with the general formula of $A_2B_2O_7$ [125, 126]. However, some disadvantages such as low chemical stability, high operating temperature, partial electronic conductivity and poor ionic conductivity limit their practical applications [127].

1.2.1 $La_2Mo_2O_9$ crystal structure, synthesis methods and thermal properties

In the past decades, the LAMOX family materials with parent compound of $La_2Mo_2O_9$ have attracted the scientists' attention due to their high oxide-ion conductivity in medium temperatures. It was found that ionic conductivity of this material is strongly associated with the PT from a low-temperature monoclinic α-phase to a high-temperature cubic β-phase at 580 °C. The structure of the monoclinic phase (Fig. 10b) is unnatural compared with other inorganic oxides. In the asymmetric unit cell there are 312 atoms. In this phase Mo atoms exist in three different coordination types: there are 15 tetrahedral, 15 trigonal bipyramidal and 18 octahedral Mo atoms (Fig. 10c) [128]. La atom is surrounded by nine oxygen atoms forming tetrakaidecahedron [129].

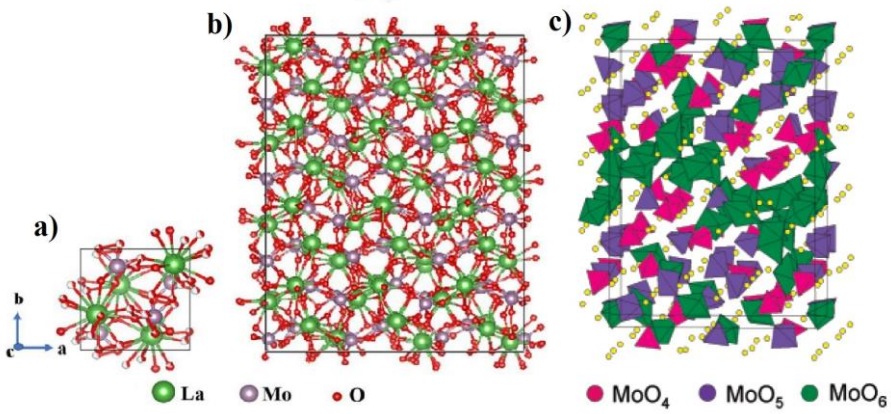

Fig. 10 (a) Cell structure of β-$La_2Mo_2O_9$; (b) cell structure of α-$La_2Mo_2O_9$; (c) polyhedrals in α-$La_2Mo_2O_9$: tetrahedral groups shown in pink, trigonal bipyramidal – blue, octahedral – green, yellow spheres represents La atoms [128, 133]

Meanwhile, the cubic β-phase (space group $P2_13$) occurs in the temperature above 580 °C and is isostructural to cubic β-$SnWO_4$ oxide. The unit cell contains 32 atoms: 4 lanthanum, 4 molybdenum, and 24 oxygen atoms (Fig. 10a). On average, Mo atom is surrounded by four oxygen atoms and molybdenum polyhedra are separated from each other whereas the La atom is surrounded by nine oxygen atoms and lanthanum polyhedra are connected to each other via oxygen atom [130, 131]. Three different types of oxygen atom sites exist in such a structure: O1 site is fully occupied, 78 % of O2 and O3 sites are partially occupied. β-$La_2Mo_2O_9$ has high oxygen vacancies concentration which means that there are enough paths for oxygen ions diffusion, leading to high anionic conductivity [132].

Nowadays it is a great challenge to stabilize high-temperature cubic β-phase at low temperatures substituting Mo or La sites with other cations. For example, the substitution of Mo by W significantly increases resistance against the reducing environment [134]. Lanthanum substitution by alkaline (Na, K, Rb) and alkaline earth (Ca, Sr, Ba) metals introduces extra oxygen vacancies due to the charge compensation mechanism, which leads to a higher anionic conductivity [135, 136]. Moreover, substitution of rare earth elements (Gd, Y) could suppress cubic β-phase at room temperature and slightly increase ionic conductivity when compared to undoped $La_2Mo_2O_9$ compound [137].

It is also well known that the preparation method has a significant effect on chemical and physical characteristics of the final compound. There are many ways to synthesize LAMOX family materials. The microstructure makes a significant contribution to the transport properties. A negative effect could be caused by low connectivity between grains and porosity, which leads to a low ionic conductivity. Moreover, it was found that materials with smaller grains are thermomechanicallly more stable than ceramics with larger grains. Using different synthesis methods and conditions it is possible to obtain better mechanical and transport properties of final ceramics [138]. One of the most common methods is a solid-state route. However, this method does not allow to obtain dense ceramic directly and requires additional milling steps and sintering. Every additional synthesis step increases the possibility of higher concentration of impurities, especially when the milling balls/jar are made of zirconia [139, 140]. Wet chemical methods such as citrate [129], EDTA complexation [141], a Pechini or modified Pechini [136, 142], sol-gel [143] and precipitation [138] are widely used to produce LAMOX family materials. These routes open up opportunities for controlling various synthesis parameters affecting the properties and morphology of the final product. Also, these methods reduce the possibility of contaminating the final product and increasing homogeneity. Some synthesis methods and their basic aspects were described in section 1.1.2.

To understand processes such as decomposition, PT and thermal stability, some thermal analysis results using different synthesis methods, dopant amount and nature will be discussed. In order to investigate the phase transition of $La_2Mo_2O_9$ oxide prepared via conventional solid-state route DSC analysis was performed. It was observed that PT of $La_2Mo_2O_9$ has a clear split in exothermic peak during the cooling period. This peak division indicates that β-phase firstly converts to metastable γ-phase and then goes to monoclinic

α-phase (Fig. 11a). Moreover, it was determined that γ-phase only occurs for samples heated in low temperatures. Figure 11b shows LAMOX family samples substituted with either V^{5+} or Sr^{2+} or both. It was indicated that doping lanthanum molybdate by strontium does not suppress PT. Meanwhile, the substitution with vanadium lowered the temperature and enthalpy of phase transition [144].

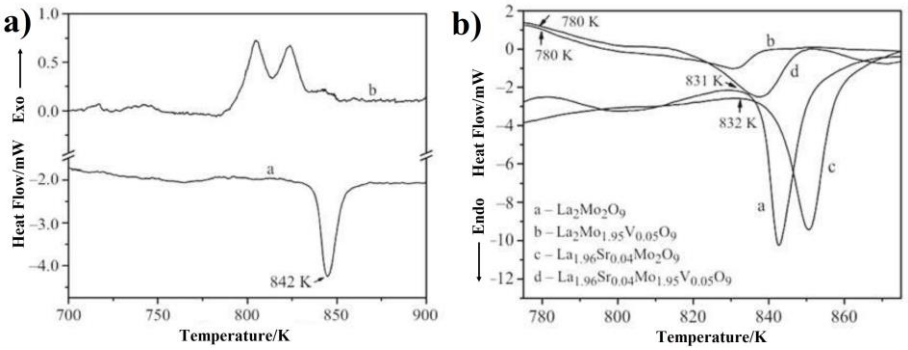

Fig. 11 DSC curves of (a) $La_2Mo_2O_9$ during a-heating and b-cooling; (b) LAMOX family samples prepared by conventional solid-state route [144]

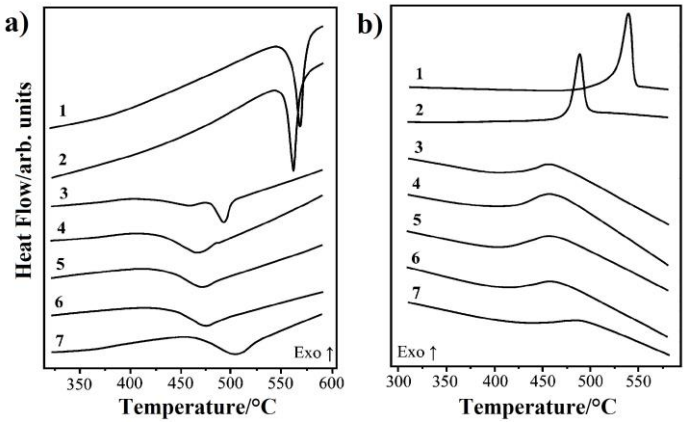

Fig. 12 DSC (a) heating and (b) cooling curves of polycrystalline $La_{2-x}Bi_xMo_2O_y$: x=(1) 0; (2) 0.02; (3) 0.04; (4) 0.05; (5) 0.06; (6) 0.08 and (7) 0.3 prepared by solid-state route [145]

In addition, it was observed that PT suppression does not always depend on dopant ion nature, but is strongly affected by its amount. From DSC analysis results it was found that samples with low Bi content (x<0.05) have a sharp and intensive endothermic PT peak. Furthermore, increasing Bi amount in the ceramic shifts the PT temperature to lower temperatures and

reduces enthalpy. The broad, weak endothermic peak in samples with x≥0.06 could be explained as a phase transformation from metastable phase to cubic β-phase (Fig. 12) [145].

As was mentioned earlier, thermal decomposition mechanism strongly depends on the preparation method. Combined results of the TGA–DTA–DSC analysis of $La_2Mo_2O_9$ amorphous precursors prepared by different methods are shown in Fig. 13. It was observed that the sample prepared by the citrate method consists of two exothermic peaks in the DTA curve and is related to pyrolysis of the organic matter (Fig. 13a). It was found that precursor synthesized by the acetylacetonate method fully decomposes at higher temperatures (550 °C) than using the citrate method (~310 °C) (Fig. 13c). The thermogravimetric analysis results of samples prepared by precipitation and freeze-dried methods are very similar. However, from DTA results it is clear that the thermal decomposition is extremely different, although they were both prepared using the same solution. Precipitation method has many exothermic and endothermic peaks throughout the whole temperature range (Fig. 13b).

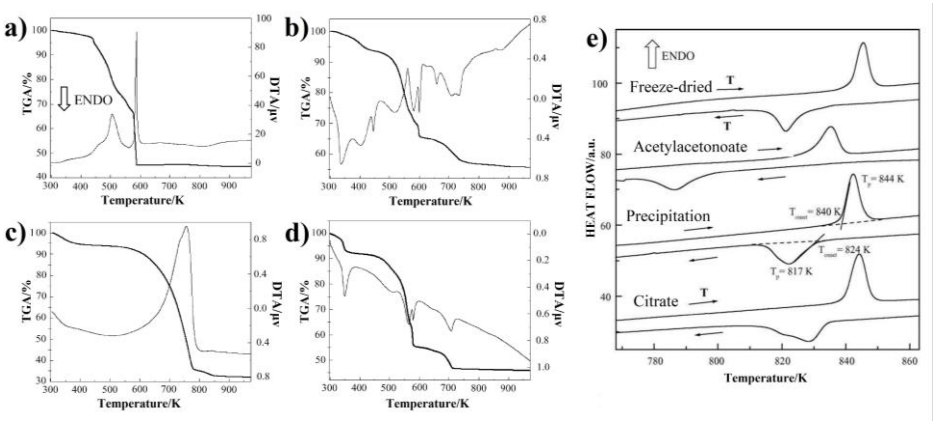

Fig. 13 TGA–DTA curves of $La_2Mo_2O_9$ precursors prepared by (a) citrate; (b) precipitation; (c) acetylacetonate; (d) freeze-dried method, (e) DSC curves of $La_2Mo_2O_9$ powders sintered at 900 °C and prepared by different synthesis techniques [138]

DSC results showed that a different preparation technique also has significant influences for the $La_2Mo_2O_9$ PT temperature. The lowest onset temperature of PT was observed in a sample prepared by the acetylacetonate method (Fig. 13e). Moreover, the PT enthalpy is lower than that obtained by the other synthesis routes [138].

Lanthanum molybdate sample, produced by sol-gel technique, thermal decomposition mechanism is usually split into three main stages (Fig. 14). The first stage is related to residual water, decomposition of organic complexing agent, nitrate and carbon precursors. This stage mass loss is the highest and consists of approximately 40 – 50 % of the total sample mass. The second stage is observed in the temperature range of 580 – 650 °C which is related to oxygenolysis of nitrates (mass loss of about 15 %). The last stage with strong exothermic peak (~600 °C) in DSC curve is related to the final ceramic crystallization process. Above 650 °C the mass remains constant and a stable β-phase of LAMOX family materials is formed [146].

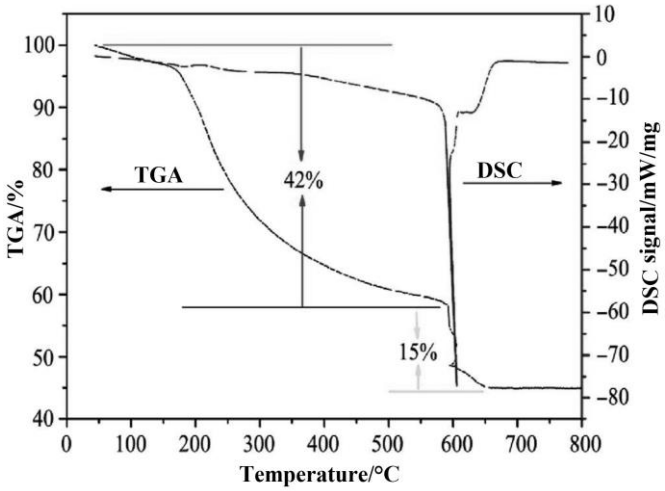

Fig. 14 TGA–DSC curves of $La_{1.9}Ba_{0.1}Mo_{1.85}W_{0.15}O_{8.95}$ powder precursor prepared by sol-gel synthesis method [146]

1.2.2 Gadolinium-doped ceria oxide crystal structure and thermal properties

Ceria-based oxides are promising materials for intermediate temperature SOFCs due to their high oxygen-ion conductivity in operating temperature. It was found that doped ceria oxides have higher ionic conductivity when compared with YSZ in an intermediate-temperature range (500 – 700 °C). Moreover, gadolinium-doped ceria showed the best results for SOFC operation [147] among reported results with different nature of dopant. GDC crystallizes to cubic fluorite-type structure with space group *Fm-3m* and remains stable to the melting point (2400 °C) [123]. In such a structure, each Ce^{4+} or Gd^{3+} ion is coordinated with eight oxygen atoms arranged in a perfect cube, while the oxygen atom is surrounded by four cerium/gadolinium atoms forming a tetrahedral (Fig. 15).

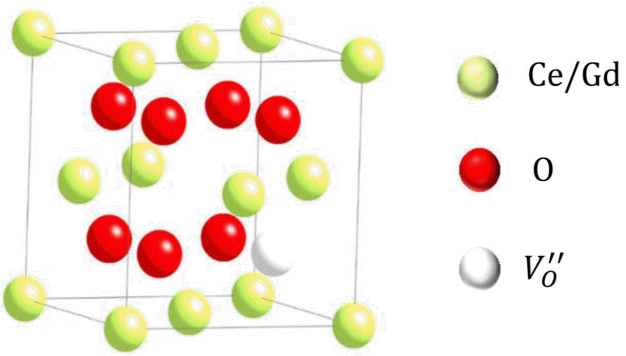

Fig. 15 Crystal structure of gadolinium-doped ceria oxide [148]

In addition, cerium-based oxides have relatively large unit cells and, as a consequence, oxygen ions can pass through large channels during the conduction. When cerium is substituted with a lower-valence cation such as Gd^{3+}, one oxygen vacancy is formed for every two trivalent ions (Eq. 3) [149]. Moreover, it was reported that solid solubility limit doping rare earth elements in fluorite CeO_2 structure is 40 at%, but the highest ionic conductivity is observed when the concentration is between 10 and 20 at% [150, 151].

$$Gd_2O_3 + 2\ CeO_2 \rightarrow 2\ Gd'_{Ce} + 3\ O^x_O + V^{\bullet\bullet}_O \quad (3)$$

The final ceramic chemical, thermal and physical properties strongly depend on the preparation method and conditions. The best results can be achieved using a so-called wet chemical method overcoming many of the limitations of the conventional solid-state reaction and other high-temperature methods. Nonetheless, using harsh reaction condition methods for GDC synthesis excellent results were achieved [152], however sometimes expensive processing cost, low energy efficiency, long time-to-product and high temperatures were required [123]. Solution-based methods usually use metal nitrates, chlorides, acetates and oxalates as starting materials. Besides, metal salts are useful, inexpensive, and very easy to handle in comparison to the metal alkoxides. They can also be dissolved in inorganic solvents with organic chelating agents forming metal complexes, which leads to the high homogeneity. These techniques have good control of starting materials and processing parameters, high purity of raw materials and low temperature of the process.

In order to understand the influence of different molar composition, synthesis method, and nature of complexing agent to decomposition mechanism, some thermal analysis results will be discussed. GDC precursors

were prepared by modified sol-gel combustion method with the same synthesis parameters. TGA–DTA curves of the samples obtained are presented in Fig. 16. From these results it is clear that decomposition occurs in two steps. The first mass loss occurs below 180 °C (<10 %) and is related to absorbed water removal. The biggest mass loss is observed slightly below 200 °C and could be mainly related to the presence of organic and nitrate ligands decomposition into CO_2, H_2O and NO gases. When Gd incorporation amount is 10 at%, we can see two exothermic peaks in the DTA curve, but when Gd incorporation is increased to 20 at% only one peak is observed. It was determined that when the calcination temperature is 600 °C, elimination of organic residuals is completed [123].

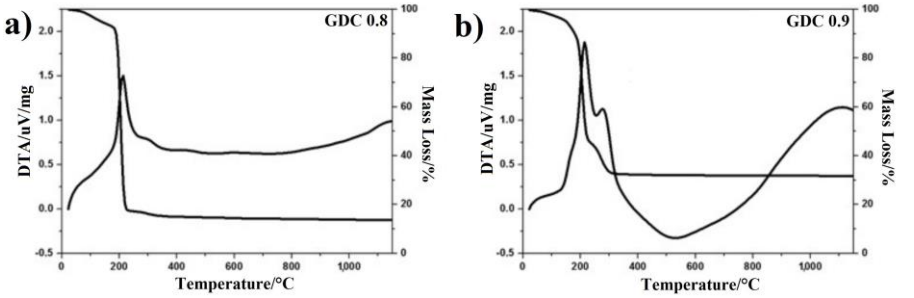

Fig. 16 TGA–DTA curves of (a) $Ce_{0.8}Gd_{0.2}O_{1.9}$ and (b) $Ce_{0.9}Gd_{0.1}O_{1.95}$ precursor powders prepared by modified combustion sol-gel method [123]

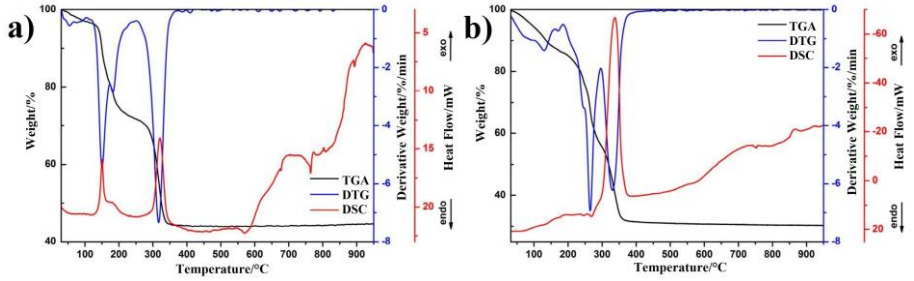

Fig. 17 TGA–DTG–DSC curves of $Ce_{0.9}Gd_{0.1}O_{1.95}$ precursor gels prepared by (a) sol-gel combustion and (b) sol-gel synthesis methods when TA was used as a complexing agent [153]

In addition, thermal decomposition strongly depends on precursor preparation method. Fig. 17 shows thermogravimetric, derivative thermogravimetric (DTG) and differential scanning calorimetric (TGA–DTG–DSC) curves of $Ce_{0.9}Gd_{0.1}O_{1.95}$ precursor gels prepared by the sol-gel combustion (SGC) (Fig. 17a) and the sol-gel (Fig. 17b) synthesis

methods. The thermal decomposition of GDC gel prepared by SGC method consists of three stages. The first stage is related to the absorbed water removal from the room temperature to 120 °C. The second stage occurs at about 150 °C and results in the exothermic peak in DSC curve that indicates decomposition of nitrates and an excess of tartaric acid. The last stage is related to the decomposition of residual metal tartrates at ~320 °C. From 350 °C the mass remains stable indicating that all organic and inorganic residuals are completely decomposed.

Slightly different results are obtained using sol-gel method (Fig. 17b). From TGA curve it is clear that decomposition occurs in three stages. The first is also related to residual water removal from gel (weight loss ~14 %). The biggest weight loss (~30 %) occurs during the second stage that is associated with decomposition of ammonium tartrate and ammonium acetate network. The last stage results in a sharp and intensive exothermic peak in the DSC curve that could be caused by the pyrolysis of coordination compounds and residual organic parts of the gel. Using the sol-gel method the residual mass remains constant in a higher temperature (400 °C) if compared with the SGC method [153].

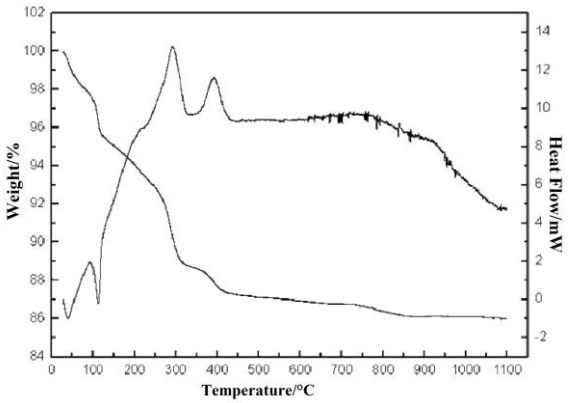

Fig. 18 TGA–DSC curves of GDC powders prepared by glycothermal method [154]

Another example of a thermal decomposition using a different synthesis technique was described by Korean scientists in 2010. GDC powders were obtained using the glycothermal process from metal nitrates in 1 M ammonia solution (Fig. 18). From the TGA curve we can see five stages of mass loss. The first two stages are related to the absorbed water and solvent removal. Sharp exothermic peaks between 300 °C and 400 °C correspond to the

crystallization of GDC nanopowders. The residual mass remains constant in much higher temperature (~950 °C) if compared with the previously described results.

Moreover, decomposition is also strongly related to the ligand nature. Fig. 17 and 19 represents $Ce_{0.9}Gd_{0.1}O_{1.95}$ thermal analysis results synthesized by sol-gel method using different chelating agents: ethylene glycol (Fig. 19a), glycerol (Fig. 19b) and tartaric acid (Fig. 17b). In all samples the first stage is associated with absorbed water and solvent evaporation. The second stage remains very similar in that all organic compounds decompose in a similar temperature. The main difference is related to the temperature of complete decomposition when the sample weight remains constant. The lowest temperature is obtained when TA is used as a ligand; in contrast, the highest temperature is observed using ethylene glycol.

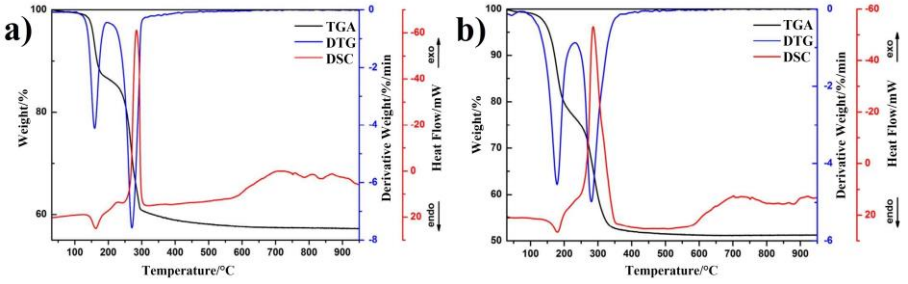

Fig. 19 TGA–DTG–DSC curves of $Ce_{0.9}Gd_{0.1}O_{1.95}$ precursor gels prepared by sol-gel methods with different chelating agent: (a) ethylene glycol; (b) glycerol [153]

According to the reviewed results, it is clear that the synthesis of the $CaMoO_4$, $SrMoO_4$, $Ca_{1-x}Sr_xMoO_4$, $La_2Mo_2O_9$ and $Ce_xGd_{1-x}O_{2-x/2}$ oxides was widely performed. However, the thermal analysis as a powerful tool that enhances the understanding of the origin of obtained properties for synthesized ceramics is still negligible.

2. EXPERIMENTAL

After discussing the published scientific literature, this chapter will describe the reagents used in the research, summarize the synthesis process, and briefly discuss the analytical instruments and apparatus used in the study of synthesized materials.

2.1 Materials

In this work, the following materials were used: calcium (II) nitrate tetrahydrate ($Ca(NO_3)_2 \cdot 4H_2O$, 99 %, Alfa Aesar); strontium (II) nitrate ($Sr(NO_3)_2$, 99.0 %, Alfa Aesar); molybdenum (VI) oxide (MoO_3, 99.95 %, Alfa Aesar); lanthanum (III) oxide (La_2O_3, 99.99 %, Alfa Aesar); gadolinium (III) acetate tetrahydrate ($Gd(CH_3COO)_3 \cdot 4H_2O$, 99.9 %, Alfa Aesar); cerium (IV) acetate hydrate ($Ce(CH_3COO)_4 \cdot H_2O$, 99.9 %, Alfa Aesar); lithium (I) nitrate ($LiNO_3$, 99 %, Alfa Aesar); sodium (I) nitrate ($NaNO_3$, 99.5 %, Alfa Aesar); potassium (I) nitrate (KNO_3, 99.5 %, Alfa Aesar); rubidium (I) nitrate ($RbNO_3$, 99.9 %, Alfa Aesar); cesium (I) nitrate ($CsNO_3$, 99.8 %, Alfa Aesar); europium (III) oxide (Eu_2O_3, 99.99 %, Alfa Aesar); tartaric acid (L-(+)-Tartaric acid ($C_4H_6O_6$), ≥99.5 %, Sigma-Aldrich); oxalic acid ($C_2H_2O_4 \cdot H_2O$, 99.5 %, Sigma-Aldrich); nitric acid (HNO_3, 66 %, Reachem); ammonia solution ($NH_3 \cdot H_2O$, 25 %, PENTA); acetic acid (CH_3COOH, 99.8 %, PENTA).

2.2 Synthesis of $CaMoO_4$, $SrMoO_4$ and mixed double $Ca_{1-x}Sr_xMoO_4$ ceramics

$Ca(NO_3)_2 \cdot 4H_2O$ and $Sr(NO_3)_2$ were weighted according to the desired stoichiometric ratio and dissolved in 40 ml of deionized water. Next to that, in another beaker, MoO_3 was dissolved in the mixture of 30 ml of deionized water and 1 ml of concentrated ammonia. Further, to reduce the possibility of precipitates of polymolybdates, an excess of tartaric acid ($^{Mo}/_{TA}$=0.25) was added into the reaction mixture. Under the continuous stirring and heating at 70 °C of temperature, the mixture of calcium and/or strontium ions was added to the solution of molybdate ions. The obtained clear solution was concentrated by evaporation in an open beaker at the same temperature for several hours. The as-formed gel precursor was additionally dried in a drying-oven at 120 °C for 3 hours until the fine-grained light brown gel powders were obtained. In the final stage, the gel precursor powders were ground in an agate

mortar and additionally heat-treated at different temperatures of 350 °C, 400 °C, 500 °C, 600 °C, 700 °C for 5 hours in the air (heating rate 1 °C/min).

2.3 Synthesis of $M_{0.05}Eu_{0.05}Ca_{0.9}MoO_4$ (M=Li, Na, K, Rb, Cs) ceramics

At first, the stoichiometric amount of MoO_3 was dissolved in 25 ml of deionized water with the addition of 1 ml concentrated ammonia. Under the continuous stirring at about 90 °C of temperature, an excess of TA ($^{Mo}/_{TA}$=0.25) was added directly into the reaction mixture. Then stoichiometric amount of $Ca(NO_3)_2 \cdot 4H_2O$ was added. After that, the required amount of alkali metal nitrate was weighed and poured into the reaction mixture. Then, a stoichiometric amount of Eu_2O_3 and 6 ml of concentrated nitric acid were added directly into the beaker. The obtained clear solution was concentrated by evaporation in an open beaker at the same temperature. The synthesized gel precursor was dried in a drying-oven at 120 °C of temperature for 2 hours in an air atmosphere. After that, the gel precursor powders were additionally heat-treated at different temperatures of 350 °C, 400 °C, 500 °C, 600 °C, 700 °C, 800 °C, 900 °C and 1000 °C for 5 h in the air (heating rate 1 °C/min).

2.4 Synthesis of $La_2Mo_2O_9$ ceramic

In the first synthesis stage, the powders of MoO_3 were dissolved in a mixture of 25 ml of deionized water and 0.5 ml of concentrated ammonia under continuous stirring at the temperature of 80 °C. Then, the tartaric acid ($^{Mo}/_{TA}$=0.25) was added into the reaction mixture under continuous stirring. Next to that, the powders of La_2O_3 and 6 ml of concentrated nitric acid were poured into the beaker. An obtained clear solution was concentrated by slow evaporation in an open beaker under continuous stirring at the same temperature for several hours. Finally, a yellow transparent sol was dried in the drying-oven at 120 °C of temperature for 2 hours. The obtained dark blue gel powders were heat-treated at 500 °C, 550 °C, 600 °C, 800 °C and 1000 °C of temperature for 5 hours in the air (heating rate 1 °C/min). The powders annealed at 1000 °C of temperature were pelletized and additionally heat-treated at 1200 °C for 5 hours in air atmosphere (heating rate 5 °C/min).

2.5 Synthesis of $Ce_{0.9}Gd_{0.1}O_{1.95}$ ceramic

In the first stage, the powders of $Gd(CH_3COO)_3 \cdot 4H_2O$ and $Ce(CH_3COO)_4 \cdot H_2O$ were weighted according to the desired stoichiometric

ratios, dissolved in a mixture of acetic acid and distilled water at 50 °C of temperature under continuous stirring. Next to that, the oxalic acid was dissolved in 20 ml of deionized water and added to the reaction mixture under continuous stirring of the same temperature. After that, the solution of the reaction mixture was additionally mixed in a closed beaker for 2 hours. The pH of the aqueous solution was increased to 9.0 by adding concentrated ammonia solution. The obtained white precipitates were separated from the solution by the filtration procedure and dried in an oven at 100 °C of temperature for 24 hours in the air. After that, the double metal oxide was obtained by heat-treating the precipitates at 900 °C, 950 °C, 1000 °C, 1100 °C and 1200 °C of temperature for 5 hours in air atmosphere (heating rate 1 °C/min).

2.6 Sample characterization techniques

The thermogravimetric and differential scanning calorimetric (TGA–DSC) analysis was performed by the simultaneous thermal analyzer (STA) 6000 PerkinElmer using a sample mass of 10 mg in either air or nitrogen atmosphere with a heating rate of 20 °C/min in the range of temperature from 30 °C to 950 °C. X-Ray diffraction (XRD) analysis of the synthesized powders and pellets was recorded in the air at room temperature with Rigaku MiniFlex II diffractometer using Cu K_α radiation (λ=1.5418 Å). $\theta/2\theta$ diffractograms were recorded at the rate of 1.5 °/min in a range from 5 to 80 °. The Rietveld refinement of the obtained XRD patterns was performed using X'Pert HighScore Plus software. The refined parameters included background, unit-cell and peak shape parameters. To study the surface morphology and microstructure of the obtained powders and compressed tablets, the scanning electron microscopes (SEM) Hitachi TM3000 and Hitachi SU-70 were used. The characteristic vibrations of the functional groups using the PerkinElmer FTIR Frontier infrared spectrometer (FTIR) were estimated. The measurements of photoluminescence (PL) and photoluminescence excitation spectra were recorded using the PerkinElmer LS-55 fluorescence spectrometer. The Raman spectra were recorded with a combined Raman and scanning near-field optical microscope (SNOM) WiTec Alpha 300 R using a green excitation laser (λ=532 nm). Finally, the measurements of the electrical properties were performed using two different impedance spectroscopy techniques by newly developed impedance spectrometer [155, 156].

3. RESULTS AND DISCUSSION

3.1 Characterization of $CaMoO_4$, $SrMoO_4$ and $Ca_{1-x}Sr_xMoO_4$ ceramics

3.1.1 Thermal analysis of Ca–Mo–O, Sr–Mo–O and Ca–Sr–Mo–O tartrate gel precursors and decomposition mechanism

In order to determine the thermal decomposition mechanism of prepared Ca–Sr–Mo–O tartrate gel precursors, the partial removal of tartaric acid during the evaporation process was analyzed and described in Eqs. 4 and 5. The value of r slightly depends on the nature of the alkaline earth metal, when the decomposition of tartaric acid generates the carbon monoxide, carbon dioxide and two molecules of acetic acid (Eq. 5). The mass loss during the evaporation process varies from 4 to 6 % in the individual oxides. It was also found that mass loss is much higher (varies from 7 to 11 %) in the samples for $Ca_{1-x}Sr_xMoO_4$ ceramics and could be explained by the common ion effect when two different cations create weaker coordination power than in $CaMoO_4$ or $SrMoO_4$ compounds.

$$q\ C_4H_6O_6\ (aq) \rightarrow (q - r)\ C_4H_6O_6\ (s) + r\ C_8H_8O_{10}\ (s) + 2r\ H_2O\ (g) \quad (4)$$

$$r\ C_8H_8O_{10}\ (s) \rightarrow 2r\ CO\ (g) + 2r\ CO_2\ (g) + 2r\ CH_3COOH\ (g) \quad (5)$$

The combined TGA–DTG–DSC curves of the Ca–Sr–Mo–O tartrate gel precursor for $Ca_{0.5}Sr_{0.5}MoO_4$ ceramic are presented in Fig. 20. The first mass loss is related to the evaporation of absorbed water molecules and occurs in the range of temperatures from 30 °C to 143 °C (Eq. 4). In all cases, the mass loss between 2.4 and 3.8 % is observed. The second mass loss could be attributed to the decomposition of the tartaric acid dimer, which starts at a temperature of 144 °C. This decomposition is described by Eqs. 5 and 6, respectively. The first exothermic peak, which identified from the DSC curve at about 185 °C of temperature is attributed to the release of carbon dioxide. Straight after that, the second endothermic band in the DSC curve does occur. This effect ends at a temperature of 220 °C and could be attributed to the evaporation of pyruvic acid.

$$(r - k)\ C_8H_8O_{10}\ (s) \rightarrow k\ CO_2\ (g) + k\ C_7H_8O_8\ (s) \rightarrow 2k\ CH_3COCOOH\ (g) \quad (6)$$

By increasing the temperature from 220 °C to 295 °C the broad exothermic peak was identified, which could be attributed to the release of CO_2 gases.

This process slightly overlaps with the evaporation of pyruvic acid, which indicates the ability of tartaric acid act as complexing agent and as a self-oxidizing fuel, as shown in Eqs. 7 and 8.

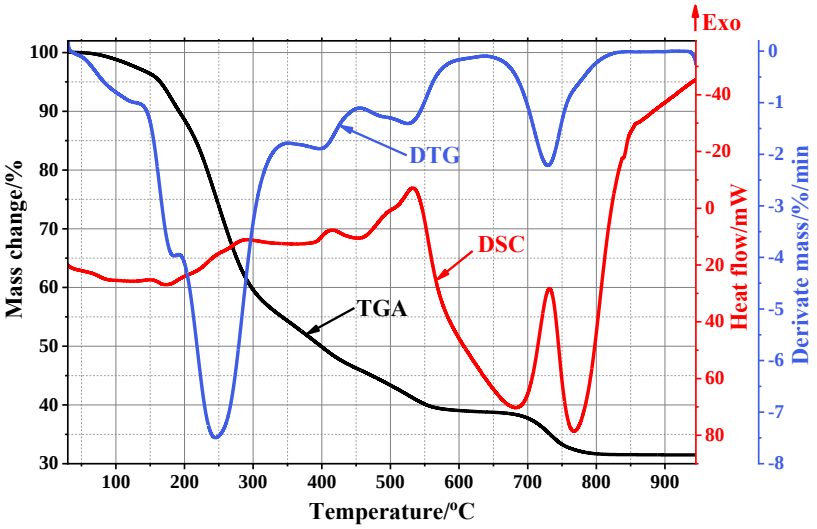

Fig. 20 Combined TGA–DTG–DSC curves of the Ca–Sr–Mo–O tartrate gel precursor for $Ca_{0.5}Sr_{0.5}MoO_4$ ceramic

$$(k - s)\ C_7H_8O_8\ (s) + O_2\ (g) \rightarrow 3s\ CO_2\ (g) + 4s\ H_2O\ (g) \quad (7)$$

$$(k - s)\ C_7H_8O_8\ (s) + s\ CO_2\ (g) \rightarrow 2s\ CO\ (g) + 4s\ H_2O\ (g) \quad (8)$$

Finally, the crystallization of the final ceramic compounds has started with the broad endothermic band in the range of temperatures from 295 °C to 395 °C. By further increase of the temperature up to 520 °C the partial decomposition of metal tartrates occurred as indicated in Eq. 9.

$$Ca_{1-x}Sr_x[MoO_4(C_4H_6O_6)_{4-q}]\ (s) \rightarrow Ca_{1-x}Sr_x[MoO_4(C_2H_2)_{4-q}]\ (s) + (8 - 2q)\ CO_2\ (g) + (8 - 2q)\ H_2O\ (g) \quad (9)$$

The decomposition of the residue of the gel precursors in the range of temperature from 520 °C to 820 °C is observed. These chemical processes that occurred in this stage are shown in Eqs. 10 and 11, respectively, which slightly differs according to the heat-treatment atmosphere.

$$Ca_{1-x}Sr_x[MoO_4(C_2H_2)_{4-q}]\ (s) + (10 - 2.5q)\ O_2\ (g) \rightarrow Ca_{1-x}Sr_xMoO_4\ (s) + (8 - 2q)\ CO_2\ (g) + (4 - q)\ H_2O\ (g) \quad (10)$$

$$Ca_{1-x}Sr_x[MoO_4(C_2H_2)_{4-q}]\ (s) \rightarrow Ca_{1-x}Sr_xMoO_4\ (s) + (4 - q)\ C_2H_2\ (g) \quad (11)$$

Identical conclusions were made from the results obtained from other Ca–Sr–Mo–O tartrate gel precursors (see ***Article I***). A relatively small mass change of the residue (from 29.3 to 32.1 %) confirms the previous statement.

3.1.2 Structural properties and morphology analysis of $Ca_{1-x}Sr_xMoO_4$ ceramics

The XRD patterns of $CaMoO_4$ and $SrMoO_4$ tartrate gel precursors heat-treated at different temperatures are shown in Fig. 21. The corresponding patterns well match with standard XRD data of $CaMoO_4$ (ICSD 62219) and $SrMoO_4$ (ICSD 173120), which are presented in the bottom panels. According to obtained results, pure tetragonal calcium and strontium molybdates with perovskite-type crystal structures have formed in the range of temperatures from 350 °C to 700 °C. In all cases, no side phases were identified. In addition, it is clear that dried gel precursors showed fully amorphous characters and no characteristic peaks were found after drying at 120 °C of temperature for several hours. The start of crystallization for final compounds at about 350 °C of temperature is in a good agreement with the results obtained from the TGA–DSC analysis.

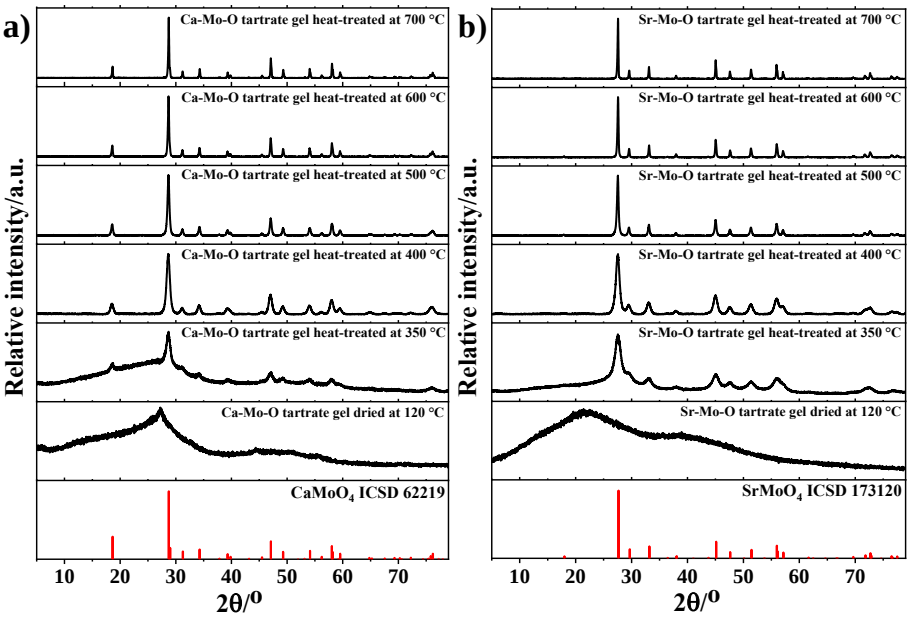

Fig. 21 XRD patterns of (a) Ca–Mo–O and (b) Sr–Mo–O precursors dried at 120 °C and heat-treated at 350, 400, 500, 600 and 700 °C temperatures for 5 hours in the air

Similar results were obtained by heat-treating the $Ca_{1-x}Sr_xMoO_4$ ceramics in a whole range of temperatures from 350 °C to 700 °C (see ***Article I***, *Appendix B*). From these results, it is clear that the crystallization process starts at the same temperature as the decomposition of corresponding metal tartrates. Depending on the final ceramic composition, the onset temperature slightly varies. The XRD patterns of the mixed $Ca_{1-x}Sr_xMoO_4$ oxides heat-treated at 700 °C are shown in ***Article I***, *Fig. 7*. As can be seen, in all cases pure tetragonal crystal structure of mixed ceramics were obtained. It was also observed that upon replacing Ca^{2+} (1.14 Å) with higher ionic radius Sr^{2+} (1.32 Å) ion diffraction reflections shifted to a lower angle side due to the increase in lattice parameters and its volume.

The Rietveld refinement of the XRD data (see ***Article I***, *Table 2*) clearly revealed that the dependence of lattice parameter values versus molar composition, as presented in Fig. 22, depend linearly on the calcium molar ratio in $Ca_{1-x}Sr_xMoO_4$ ceramics. Moreover, it is clear that by the increase of heat-treatment temperature, the size of crystallites tends also to increase.

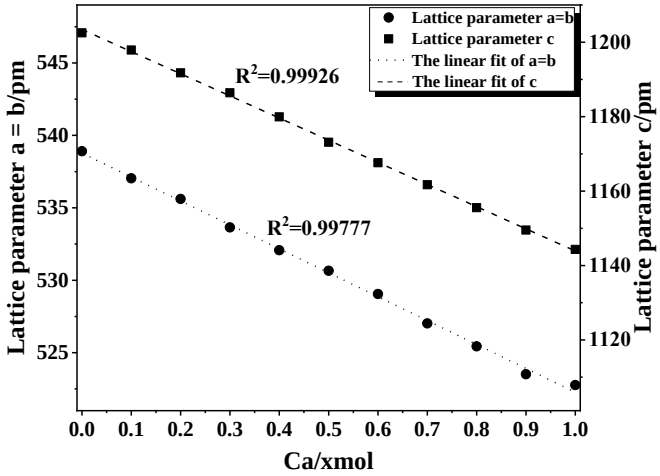

Fig. 22 Dependence of lattice parameters versus calcium molar ratio in $Ca_{1-x}Sr_xMoO_4$ ceramics

In order to investigate the surface morphology of synthesized samples scanning electron microscopy (SEM) was used. SEM micrographs of $Ca_{0.2}Sr_{0.8}MoO_4$ ceramics heat-treated at 400 °C, 500 °C, 600 °C and 700 °C of temperatures are presented in Fig. 23. From the corresponding pictures, it can be clearly seen that the surface of the samples heat-treated at 400 °C, 500 °C and 600 °C of temperatures is composed of agglomerated small particles.

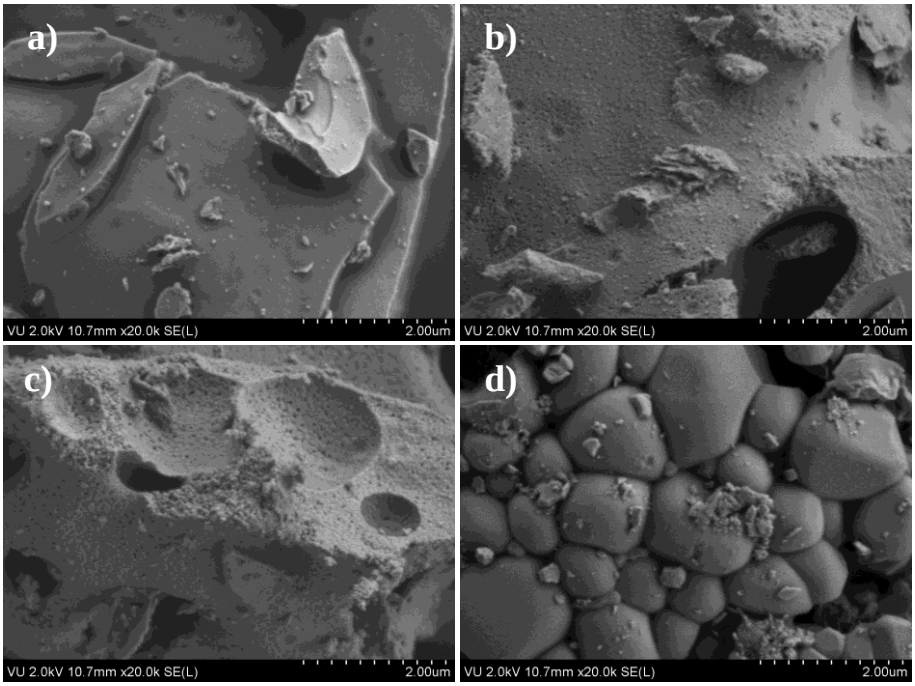

Fig. 23 SEM micrographs of Ca–Sr–Mo–O tartrate gel precursor for $Ca_{0.2}Sr_{0.8}MoO_4$ ceramic heat-treated at the temperatures of (a) 400 °C, (b) 500 °C, (c) 600 °C, and (d) 700 °C in the air for 5 hours at ambient pressure

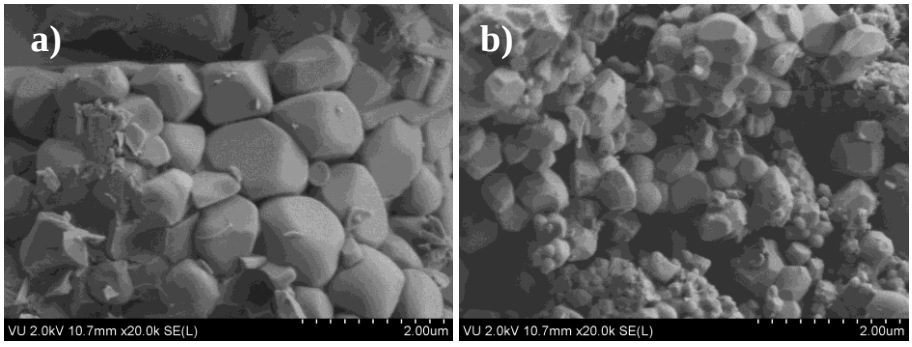

Fig. 24 SEM micrographs of Ca–Sr–Mo–O tartrate gel precursor for (a) $Ca_{0.5}Sr_{0.5}MoO_4$, (b) $Ca_{0.8}Sr_{0.2}MoO_4$ ceramics heat-treated at 700 °C temperature in the air for 5 hours at ambient pressure

The Rietveld refinement analysis determined that the size of crystallites have increased from 11 nm to 47 nm. Such tendencies of growth could be related to the emission of carbon oxides, which slightly slows down the crystallization process. By increasing the temperature to 700 °C the burning

and decomposition effects lose their energy and the growth of both the crystallites and particles start. According to the Rietveld analysis results the size of the crystallites increases almost twice to 80 nm and the dimensions of particles change from nano- to micro-sizes. Very similar results were obtained for all synthesized samples. From the SEM results, it was found that by increasing the strontium amount in the multicomponent oxide the size of particles also increase (Fig. 23 (d) and Fig. 24). The graphical representation of the particle size distribution is shown in Fig. 25.

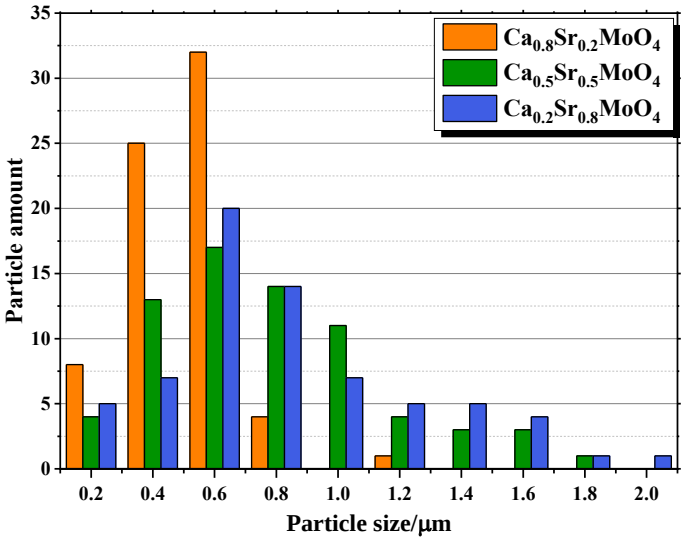

Fig. 25 Particle size distribution of $Ca_{0.8}Sr_{0.2}MoO_4$, $Ca_{0.5}Sr_{0.5}MoO_4$ and $Ca_{0.2}Sr_{0.8}MoO_4$ ceramics heat-treated at 700 °C of temperature

It was estimated that the samples with higher substitution degree of Sr^{2+} ion have broader particle size distribution and larger size of particles. Such a conclusion indicates a slightly different crystallization temperature for $Ca_{1-x}Sr_xMoO_4$, which affects the surface morphology of the synthesized ceramics.

3.1.3 Vibrational spectroscopy analysis of $Ca_{1-x}Sr_xMoO_4$ ceramics

In order to show the characteristic vibrations of the functional groups in the gel precursors, the infrared spectroscopy (FTIR) was performed. FTIR spectra of the Ca–Mo–O, Ca–Sr–Mo–O and Sr–Mo–O tartrate gel precursors for $CaMoO_4$, $Ca_{0.5}Sr_{0.5}MoO_4$ and $SrMoO_4$ ceramics are shown in Fig. 26. It is well-known that the carboxylic acids usually exist as dimers due to the strong intermolecular hydrogen-bonding. This is the case of a strong broad O–H

stretching band that is characterized as chelates in the range from 3300 cm^{-1} to 2500 cm^{-1}. Two sharp peaks at 2920 cm^{-1} and 2850 cm^{-1} could be attributed to C–H stretching vibrations of carboxylic acid groups, which was identified only for the Sr–Mo–O tartrate gel precursor. The C=O stretching vibration that could be attributed to the carboxylic acids dimers are observed at 1705 cm^{-1} [157, 158]. Moreover, the –COO asymmetric and symmetric stretching combined with O–H in-plane bending vibrations are observed at ~1599 cm^{-1} and ~1380 cm^{-1}, respectively [159].

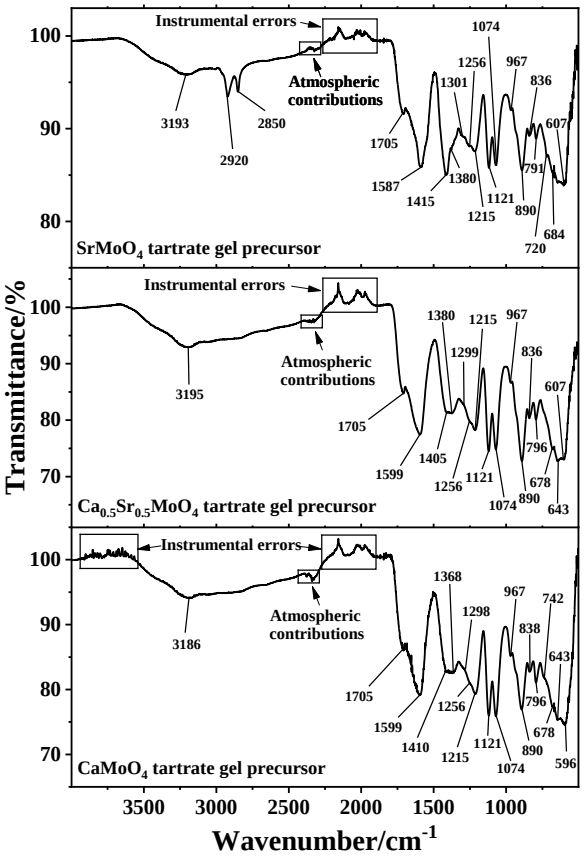

Fig. 26 FTIR spectra of Ca–Mo–O, Ca–Sr–Mo–O and Sr–Mo–O tartrate gel precursors for $CaMoO_4$, $Ca_{0.5}Sr_{0.5}MoO_4$ and $SrMoO_4$ ceramics dried at 120 °C of temperature

The characteristic vibration of carboxylic acids C–O stretching combined with O–H in-plane bending is also observed at 1405 cm^{-1}. The peak observed at about 1300 cm^{-1} is attributed to O–H deformational vibration. Meanwhile, the medium intensity bands of C–H in-plane stretching vibrations at

1256 cm^{-1} and 1215 cm^{-1} are also observed [160]. In addition, two sharp and intensive peaks are observed at 1121 cm^{-1} and 1074 cm^{-1} and relate to C–OH and CH–OH stretching vibrations, respectively [161]. The band at 967 cm^{-1} is observed and could be attributed to the C–C symmetric stretching vibration.

The vibrational frequencies of tetrahedral MoO_4^{2-}-type compound for their Mo–O vibrations are observed at 890 cm^{-1} (ν_3) and 838 cm^{-1} (ν_1) [162]. The weak peak observed at 796 cm^{-1} is attributed to O–H...H out-of-plane bending vibration. The overlapped band in the range from 750 cm^{-1} to 720 cm^{-1} is associated with crystal water vibrations. –COO scissoring, wagging, bending and metal-oxygen characteristic vibrations similar to those observed in the crystalline Powellite structure of $CaMoO_4$ are observed in the range from 680 cm^{-1} to 590 cm^{-1}. Similar vibrations were observed in all cases of Ca–Sr–Mo–O tartrate gel precursors.

The Ca–Sr–Mo–O gel precursors heat-treated at 400 °C, 500 °C, 600 °C and 700 °C of temperature for $Ca_{0.5}Sr_{0.5}MoO_4$ ceramic is presented in ***Article I*** *Fig. 11*. The FTIR spectra of the samples heat-treated at 400 °C can be divided into two parts. The first one, in the range from 1750 cm^{-1} to 1000 cm^{-1} is attributed to the organic part, which confirms organic residue of metal tartrates. The increase of temperature these characteristic vibrations tend to disappear, which proofs the complete decomposition of the organic part. The intensity, width and shape of the metal-oxygen band, which appears at 1000 – 500 cm^{-1} depends on several factors, such as degree of crystallinity, surface area and crystal structure of the ceramic. By increasing the temperature, the crystallinity of crystalline compounds also increases. Meanwhile, the opposite effect is observed when the crystallites and particles grow and the surface area to volume ratio decreases. From the results of this analysis, it is clear that the highest peak area value is observed at the annealing temperature of 500 °C in all cases (see ***Article I***, *Fig. 12, 13, 14*). The further increase of the temperature to 700 °C decreases the value of the peak area. This effect is directly related to the surface morphology of the sample. Moreover, it was also observed that $SrMoO_4$ and the samples with a lower amount of calcium have a higher crystallinity and surface area at the temperature of 400 °C than those with a higher amount of calcium. Such behavior confirms the difference in the crystallization point of calcium and strontium molybdates at higher temperatures. In conclusion, comparing this case with the peak area changes of the strontium molybdate curve it is clear that despite similar tendencies of crystallite growth the crystallization mechanism of both systems slightly differ. The difference could be explained

by means of the different radius of alkaline earth metals, which creates an almost identical crystal structure of corresponding metal molybdates with well-pronounced different distances in all directions inside the crystal lattice.

In order to expand the results obtained from the FTIR analysis and XRD diffraction, and to determine the molar composition of prepared samples of $Ca_{1-x}Sr_xMoO_4$ ceramics the Raman spectroscopy analysis was used. Raman spectra of all prepared Ca–Sr–Mo–O tartrate gel precursors for $Ca_{1-x}Sr_xMoO_4$ ceramics heat-treated at 700 °C temperature are presented in ***Article I*** *Fig. 15*. The corresponding modes that were identified from the Raman spectra of $SrMoO_4$ oxide and which are common for all the rest of ceramic samples are presented in Fig. 27. In addition, Table 1 shows the values of Raman active modes for the $CaMoO_4$ and $SrMoO_4$ powders obtained in this work in comparison with those reported in the literature [163-166].

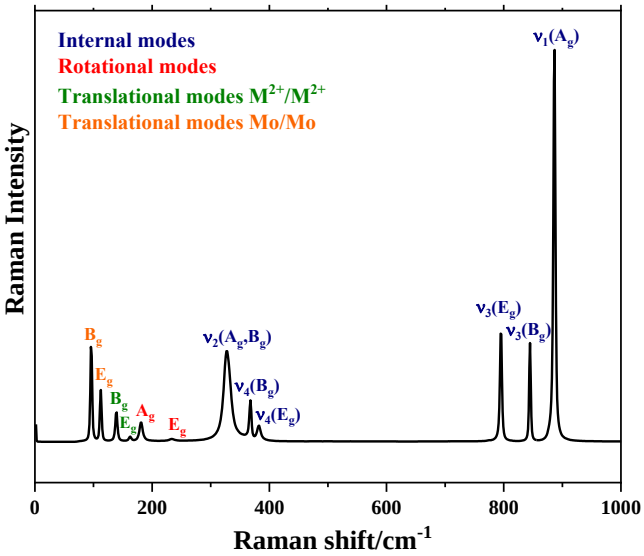

Fig. 27 Indexes of the vibrational modes for the Raman spectrum of Sr–Mo–O tartrate gel precursor for $SrMoO_4$ ceramic heat-treated at 700 °C of temperature

It was found that A_g mode in Raman spectra shifts when calcium is substituted with strontium ions in multicomponent oxides. This shift was observed in the range of wavenumber from 250 cm^{-1} to 180 cm^{-1}. The shift into the lower wavenumber side occurs due to replacing lower ionic radius Ca^{2+} ion by higher ionic radius Sr^{2+} ion. The volume of crystal lattice increases causing the decrease of the covalent bonding between the MoO_4^{2-} tetrahedra and M^{2+} ions [67].

Table 1 Comparative results of active Raman modes for the $CaMoO_4$ and $SrMoO_4$ powders obtained in this work with those reported in the literature

Active Raman modes		Wave-number (cm^{-1}) of $CaMoO_4$	References			Wave-number (cm^{-1}) of $SrMoO_4$	References	
			[163]	[164]	[165]		[165]	[166]
ν_1 (A_g)		877	878	878	879	887	887	886
ν_3 (B_g)		847	844	847	848	845	845	845
ν_3 (E_g)		793	797	793	794	795	796	795
ν_4 (E_g)		402	401	402	403	383	382	381
ν_4 (B_g)		392	393	391	392	368	367	367
ν_2 (A_g, B_g)		323	333	323	323	327	327	327
E_g		267	263	267	269	234	234	234
A_g		204	205	205	205	180	182	180
M^{2+}/M^{2+}	B_g	-	219	-	219	163	163	163
	E_g	190	189	189	191	139	139	138
Mo/Mo	E_g	143	145	145	145	112	112	112
	B_g	112	110	111	112	96	96	95

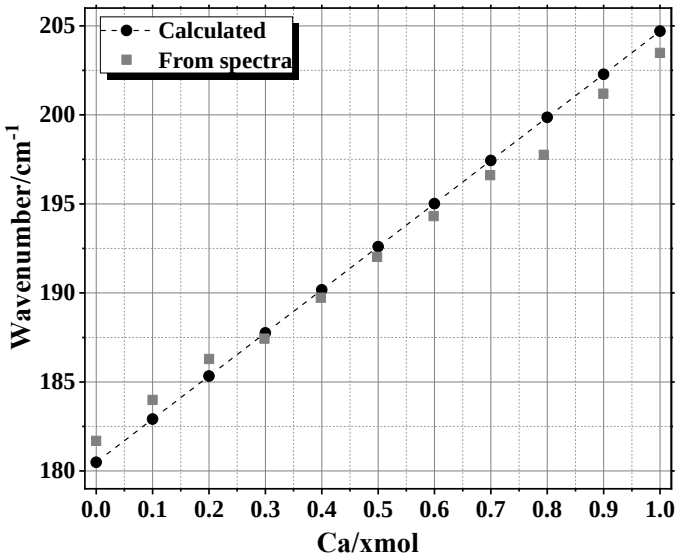

Fig. 28 Calculated and experimental dependencies of A_g mode vs. molar part of calcium in the $Ca_{1-x}Sr_xMoO_4$ samples

These findings allow the calculation of molar composition. A comprehensive study of molar composition calculation is presented in ***Article I*** (*Eqs. 15, 16, 17 and 18*). A graphical view of the experimental and

calculated data is presented in Fig. 28. It is clear that deviation of the ideal case is small (0.32 %) and could be mainly caused by unexpected measurement errors.

3.2 Characterization of $M_{0.05}Eu_{0.05}Ca_{0.9}MoO_4$ (M=Li, Na, K, Rb, and Cs) ceramics

3.2.1 Thermal analysis of M–Eu–Ca–Mo–O tartrate gel precursors

The main aspects of thermal decomposition mechanism of M–Eu–Ca–Mo–O tartrate gel precursors remain very similar to those described in the section 3.1.1. Combined TGA–DTG–DSC curves in air atmosphere of K–Eu–Ca–Mo–O tartrate gel precursor are presented in Fig. 29.

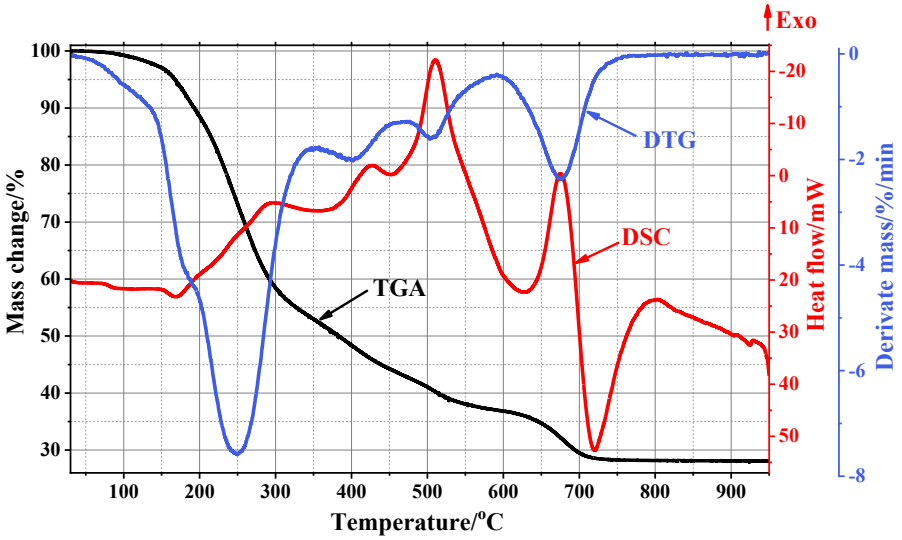

Fig. 29 Combined TGA–DTG–DSC curves of the K–Eu–Ca–Mo–O tartrate gel precursor for $K_{0.05}Eu_{0.05}Ca_{0.9}MoO_4$ ceramic in air atmosphere

The thermal decomposition can be divided into at least six stages. The first stage, endothermic behavior, occurs in the range of temperature from 30 °C to 142 °C and is related to the removal of water molecules. The next stage is related to an excess of tartaric acid decomposition to CO, CO_2 and lower molecular mass acids [167]. However, the nature of alkali metal plays an important role. Although the synthesis parameters of prepared gels were identical, from Fig. 30 DTG curves we can see small differences. It is clear that the exothermic process from 143 °C to 177 °C temperature also depends on the nature of alkali metals. This leads to a conclusion that this step is not

only related to the release of carbon dioxide, but also to the removal of volatile components from the metal tartrate gel. The following steps of TA decomposition remain the same. The mass loss of all prepared tartrate gel precursors varies between 36 – 43 %.

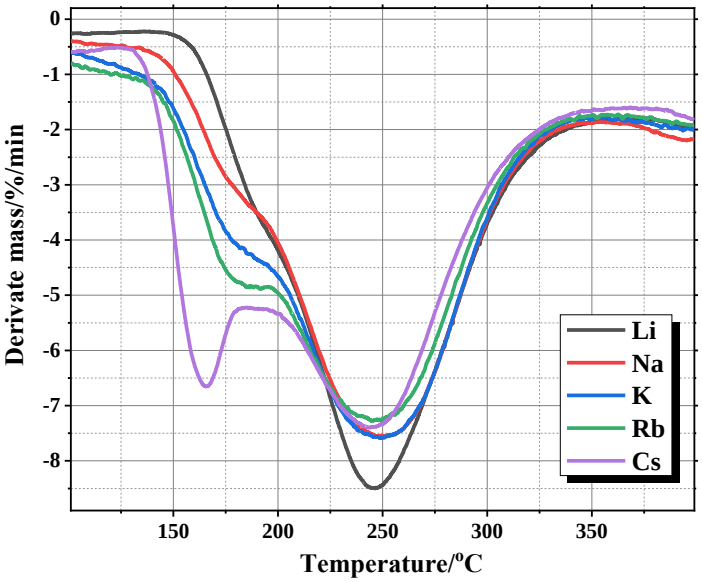

Fig. 30 DTG curves of the M–Eu–Ca–Mo–O (M=Li, Na, K, Rb, Cs) tartrate gel precursors for $M_{0.05}Eu_{0.05}Ca_{0.9}MoO_4$ ceramics in air atmosphere

The third stage occurs in the temperature range from 295 °C to 510 °C and is related to the decomposition of metal tartrates. The biggest mass loss was observed in Li–Eu–Ca–Mo–O (20.24 %) and the lowest in Cs–Eu–Ca–Mo–O (18.83 %) sample. It is important to mention, that from the temperature of 300 °C the endothermic process of crystallization of the final ceramic occurs. The next mass loss stage is attributed to the burning of carbon-based residue, which was formed from the TA and metal tartrates at lower temperatures. A broad endothermic band with the peak at 627 °C of temperature is related to the evaporation of water molecules. Meanwhile, a strong exothermic peak at 676 °C corresponds to the removal of CO_2 molecules. In other words, two different kinds of processes occur at the same time. It was also observed that the mass loss slightly depends on alkali metal nature. It means that by the increase of the molecular weight of corresponding alkali metal in the M–Eu–Ca–Mo–O tartrate gel precursor the coordination ability of organometallic complex decreases. As a result, the molecular mass increase of the final ceramics leads to a larger mass change for the gel precursors. The

final mass loss in the range of temperature from 785 °C to 950 °C did not exceed 0.15 %. However, the endothermic behavior in the DSC curve was observed due to a further growth of the crystalline phase.

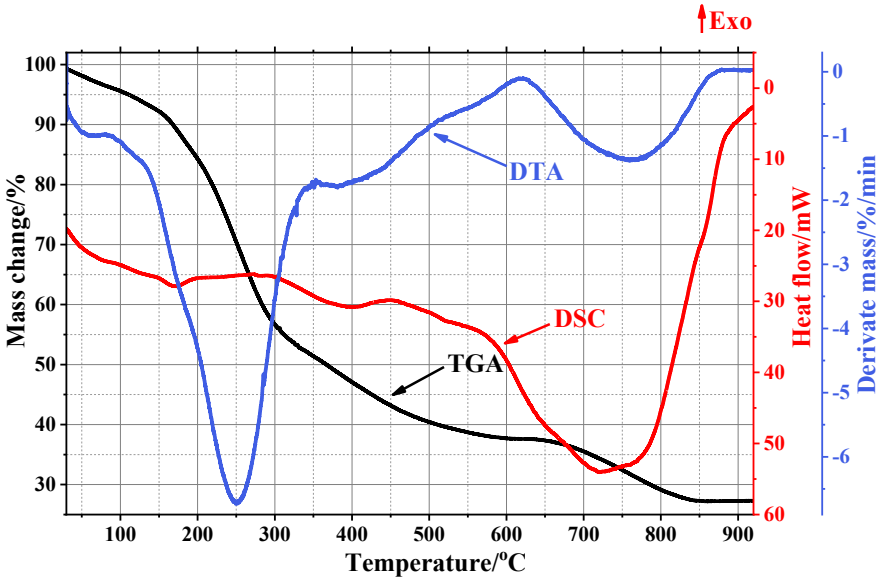

Fig. 31 Combined TGA–DTG–DSC curves of the K–Eu–Ca–Mo–O tartrate gel precursor for $K_{0.05}Eu_{0.05}Ca_{0.9}MoO_4$ ceramic in inert nitrogen atmosphere

In order to investigate both the decomposition process and the mass change peculiarities of volatile components, a thermal analysis of prepared samples was recorded under inert nitrogen flow (Fig. 31). After having investigated the results, it is clear that the decomposition of TA only slightly depends on the heating atmosphere. From combined TGA–DTG–DSC curves it is clear that the main principles of K–Eu–Ca–Mo–O decomposition remain very similar of temperatures up to 600 °C. The endothermic behavior of the last mass change in the range of temperatures from 600 °C to 850 °C is attributed to the decomposition of carbon-based residue from the gel. The main difference between the results obtained under both air (Fig. 29) and inert (Fig. 31) atmospheres is a different temperature of stable mass at 785 °C and 850 °C, respectively.

In conclusion, it has been found that thermal decomposition mechanism of prepared M–Eu–Ca–Mo–O (M=Li, Na, K, Rb, and Cs) tartrate gel precursors for $M_{0.05}Eu_{0.05}Ca_{0.9}MoO_4$ ceramics remains very similar in all cases. The detailed decomposition data of each sample are presented in ***Article II***, *Tables 2-6*.

3.2.2 Structural properties and morphology analysis of $M_{0.05}Eu_{0.05}Ca_{0.9}MoO_4$ ceramics

The XRD patterns of K–Eu–Ca–Mo–O tartrate gel precursor and powders heat-treated at different temperatures in the range from 350 °C to 1000 °C for 5 hours are presented in Fig. 32. The dried K–Eu–Ca–Mo–O tartrate gel precursor at 120 °C showed an amorphous character. Each peak of heat-treated samples matches with the tetragonal phase $CaMoO_4$ reference pattern (ICSD 62219) that is presented in the bottom panel. No characteristic peaks attributed to impurities were identified throughout the entire temperature range. From XRD analysis results it is clear that the crystallization of the final tetragonal ceramic occurs from 350 °C. These results are in good agreement with thermal analysis data that the crystallization process starts below 350 °C. The characteristic peaks at the lower temperatures are broad. Increasing the temperature resulted in the narrowing of the peaks indicating the growth of crystallites.

In order to establish the same tendencies in all prepared samples, the XRD analysis was performed. XRD patterns of $M_{0.05}Eu_{0.05}Ca_{0.9}MoO_4$ (M=Li, Na, K, Rb, Cs) powders annealed at temperatures of 350 °C and 1000 °C are presented in Fig. 33. In all cases, single tetragonal crystal structure $M_{0.05}Eu_{0.05}Ca_{0.9}MoO_4$ ceramics were obtained. Additionally, it is important to mention that these results are in good agreement with the thermal analysis data. From Fig. 33a it is clear that in all cases the crystallization starts from 350 °C of temperature.

In order to show crystal lattice parameters and the dependency of crystallite size growth from the temperature, the Rietvield refinement analysis was performed. The detailed results are shown in ***Article II***, *Table 7*. The Rietveld analysis revealed two types of crystallites in the synthesized ceramic samples, which have a tendency to increase by increasing the heat-treatment in the range of temperature from 350 °C to 700 °C. Such a tendency of crystallite growth is well-pronounced for the $Na_{0.05}Eu_{0.05}Ca_{0.9}MoO_4$ ceramic sample (Fig. 34). In this case, the size of crystallites increases by increasing the heat-treatment in the whole range of temperatures. It is also interesting to note that other examples have shown different trends of crystallites growths, which were particularly pronounced above the temperature of 700 °C. For example, in the $Li_{0.05}Eu_{0.05}Ca_{0.9}MoO_4$ and $Cs_{0.05}Eu_{0.05}Ca_{0.9}MoO_4$ ceramic samples, the decrease of the crystallite size starts just above the temperature of 800 °C.

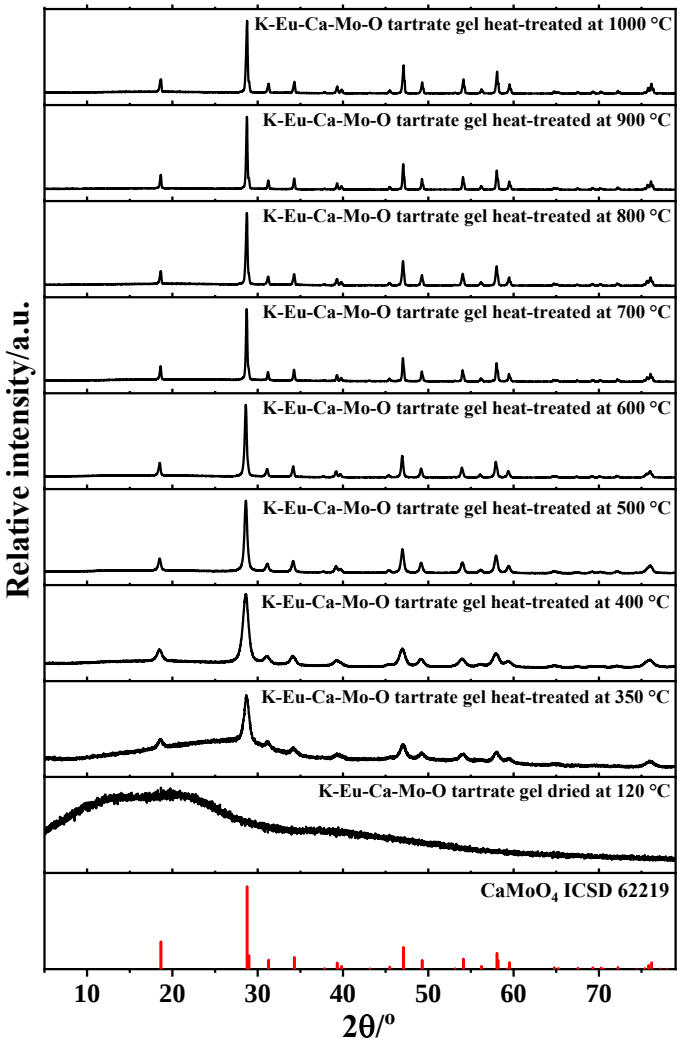

Fig. 32 XRD patterns of the K–Eu–Ca–Mo–O tartrate gel precursor dried at 120 °C and heat-treated at 350, 400, 500, 600, 700, 800, 900 and 1000 °C of temperatures for 5 hours in the air

Meanwhile, the decrease of crystallites for $K_{0.05}Eu_{0.05}Ca_{0.9}MoO_4$ and $Rb_{0.05}Eu_{0.05}Ca_{0.9}MoO_4$ ceramics starts just above the temperature of 700 °C. Probably this anomalous effect of crystallites growth by increasing the heat-treatment temperature is directly related to the crystallization of europium oxide [168]. Thus, depending on the nature of alkali metal in the $M_{0.05}Eu_{0.05}Ca_{0.9}MoO_4$ ceramic, the growth of crystallites takes place at slightly different heat-treatment conditions.

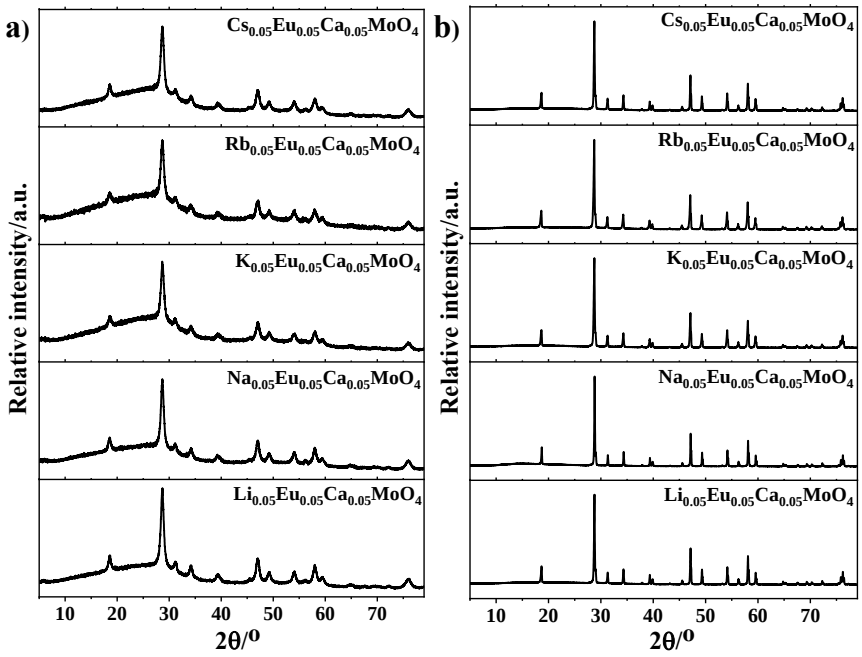

Fig. 33 XRD patterns of the M–Eu–Ca–Mo–O (M=Li, Na, K, Rb, Cs) tartrate gel precursors for $M_{0.05}Eu_{0.05}Ca_{0.9}MoO_4$ ceramics heat-treated at the temperatures of (a) 350 °C and (b) 1000 °C for 5 hours in the air

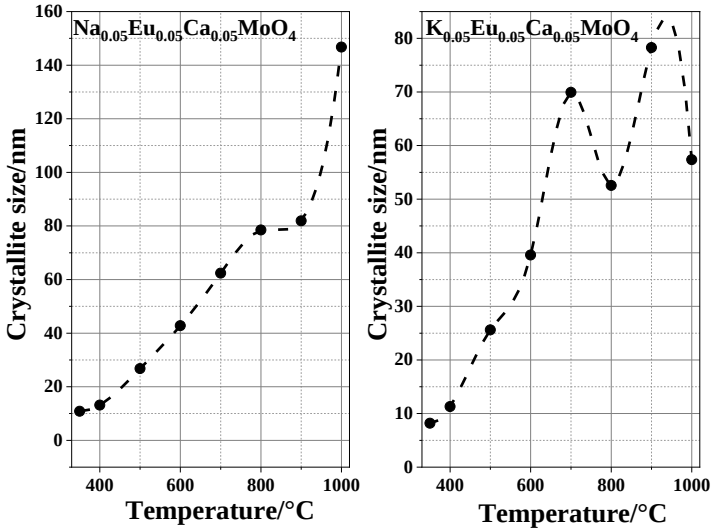

Fig. 34 Plot of crystallite size versus heat-treatment temperature

As seen from Fig 35, the dependency of lattice parameters versus heat-treatment temperature shows almost identical character for all cases. This

result confirms the statement that the size of crystallites is much more affected by the heat-treatment temperature than the crystal structure of the corresponding phase.

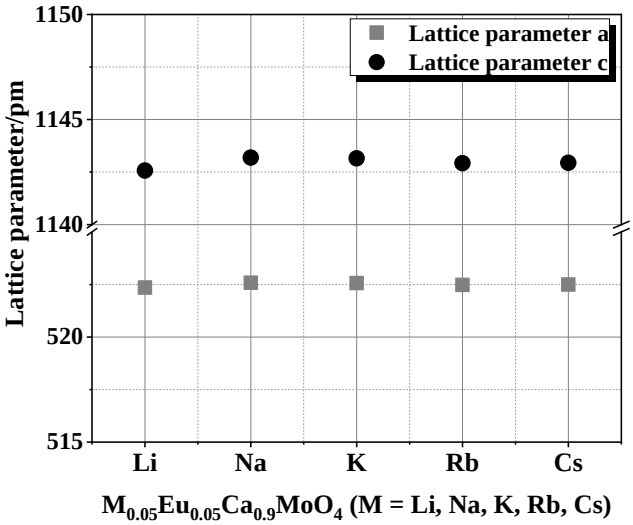

Fig. 35 Lattice parameters versus alkali metal nature in the $M_{0.05}Eu_{0.05}Ca_{0.9}MoO_4$ system heat-treated at 1000 °C

In order to show the possible changes in surface morphology according to the heat-treatment temperature, the scanning electron microscopy was used. The corresponding SEM images of $K_{0.05}Eu_{0.05}Ca_{0.9}MoO_4$ and $Rb_{0.05}Eu_{0.05}Ca_{0.9}MoO_4$ ceramics heat-treated at the temperature of 800 °C are shown in Fig. 36, respectively.

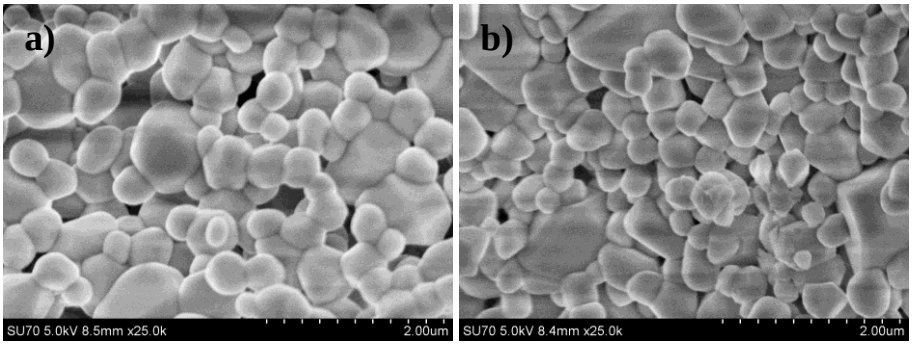

Fig. 36 SEM micrographs of (a) $K_{0.05}Eu_{0.05}Ca_{0.9}MoO_4$ and (b) $Rb_{0.05}Eu_{0.05}Ca_{0.9}MoO_4$ ceramics heat-treated at 800 °C of temperature

In both cases, irregular sphere-like aggregated particles have formed, which sizes varies from 200 nm to 1.2 μm and from 200 nm to 1.8 μm. It is

seen that the morphology of both ceramic samples is almost identical and the difference in crystallite growth tendencies is only related to the degree of either agglomeration or aggregation of individual particles.

3.2.3 FTIR and PL analyses of $M_{0.05}Eu_{0.05}Ca_{0.9}MoO_4$ ceramics

The FTIR spectrum of K–Eu–Ca–Mo–O tartrate gel precursor sample dried at 120 °C temperature is presented in Fig. 37. It is obvious that most of the characteristic vibrations of functional groups could be attributed to tartaric acid. An almost identical result was obtained from FTIR analysis of Ca–Sr–Mo–O tartrate gel precursors of which a detailed description is presented in section 3.1.3.

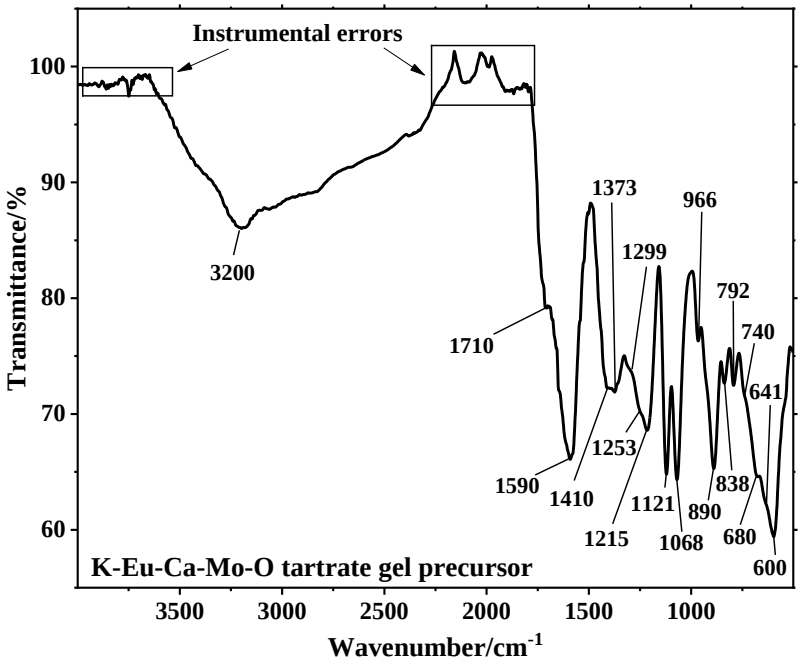

Fig. 37 FTIR spectra of K–Eu–Ca–Mo–O tartrate gel precursor dried at 120 °C of temperature

The FTIR spectra of K–Eu–Ca–Mo–O tartrate gel precursor for $K_{0.05}Eu_{0.05}Ca_{0.9}MoO_4$ ceramic heat-treated at temperatures of 350 °C, 400 °C, 500 °C, 600 °C, 700 °C and 800 °C are presented in Fig. 38. The ceramic heat-treated at the temperature of 350 °C possesses two broad bands in the FTIR spectrum. The first one in the range from 3600 cm^{-1} to 2500 cm^{-1} is attributed to an O–H stretching band characteristic to chelates. As the temperature reaches 600 °C and above, this band disappears. The second band in the range

of 1700 cm^{-1} to 1350 cm^{-1} is related to the organic residue of metal tartrates. This band disappears gradually as the temperature increases up to 800 °C. Absorption bands in the range of wavenumbers from 1000 cm^{-1} to 500 cm^{-1} are attributed to the vibrations characteristic of metal-oxygen and remain very similar throughout the range of heat-treating temperatures from 350 °C to 800 °C.

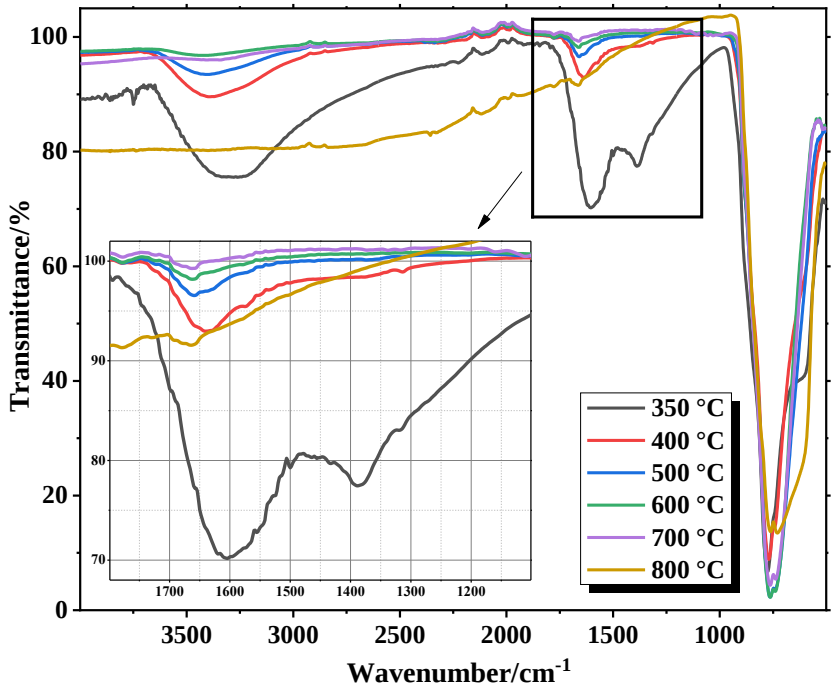

Fig. 38 FTIR spectra of $K_{0.05}Eu_{0.05}Ca_{0.9}MoO_4$ ceramic heat-treated at 350, 400, 500, 600, 700 and 800 °C of temperatures

In order to investigate the relation between the crystallite growth mechanism and luminescent properties of prepared ceramic samples heat-treated at the temperature of 600 °C, a photoluminescence analysis was performed. The PL properties of prepared $M_{0.05}Eu_{0.05}Ca_{0.9}MoO_4$ oxides are described in ***Article II***, *PL analysis section* in detail. These PL properties showed interesting results – they are related to both the size of crystallites that have grown at 600 °C and the formation mechanism of crystallites that have been obtained at higher heat-treating temperatures. In other words, the photoluminescence properties predict different crystallite growth tendencies (Fig. 34) that have not yet been evident in the XRD analysis.

3.3 Characterization of $La_2Mo_2O_9$ ceramic

3.3.1 Formation mechanism and thermal decomposition of La–Mo–O tartrate gel precursor

In this work, the synthesis of La–Mo–O tartrate gel precursor for $La_2Mo_2O_9$ ceramic was prepared by an aqueous sol-gel synthesis using tartaric acid as a chelating agent that interacts as a ligand at the molecular level with the reaction mixture during both dissolution in water and sol-gel formation. The preparation of sol and gel could be divided into several steps as follows. At first, the dissolution of MoO_3 in a dilute ammonia solution (~0.263 M) was performed as shown in Eq. 12. Next to that, the tartaric acid is added to the reaction mixture according to the Eq. 13 [169]. In the third step, lanthanum oxide and nitric acid are mixed and added to the reaction mixture as shown in Eq. 14. The final formation of La–Mo–O tartrate gel precursor is presented in Eqs. 15 and 16, respectively.

$$MoO_3\ (s) + 2\ NH_3 \cdot 2\ H_2O\ (aq) \rightarrow (NH_4)_2MoO_4 \cdot 2\ H_2O\ (aq) \quad (12)$$

$$p\ (NH_4)_2MoO_4\ (aq) + q\ C_4H_6O_6\ (aq) \rightarrow [(MoO_4)_p(C_4H_4O_6)_qH_r]^{(2p+2q-r)-}\ (aq) + 2p\ NH_4^+\ (aq) \quad (13)$$

$$La_2O_3\ (s) + 6\ HNO_3\ (aq) \rightarrow 2\ La(NO_3)_3\ (aq) + 3\ H_2O\ (l) \quad (14)$$

$$[(MoO_4)_p(C_4H_4O_6)_qH_r]^{(2p+2q-r)-}\ (aq) + p\ La^{3+}\ (aq) \rightarrow La_p[(MoO_4)_p(C_4H_4O_6)_qH_r]^{3p-(2p+2q-r)}\ (aq) \quad (15)$$

$$La_p[(MoO_4)_p(C_4H_4O_6)_qH_r]^{3p-(2p+2q-r)}\ (aq) + 3p\ C_4H_4O_6\ (aq) \rightarrow \xrightarrow{\text{Drying at 120 °C}} \text{Dark blue gel} \quad (16)$$

In order to study the thermal decomposition mechanism a combined TGA–DTG–DSC analysis was performed and the results are presented in Fig. 39. The thermal decomposition process could be divided into at least six parts. The first mass loss (4.3 %) occurs in the range of temperatures from 30 °C to 147 °C. This stage is related to the removal of absorbed water molecules and loss of water molecules from tartaric acid (Eq. 4). The second mass change is related to the decomposition of excess of TA and occurs in the range of temperature from 147 °C to 300 °C (Fig. 40). This stage can be divided into two smaller steps: the first occurs in the range from 148 °C to

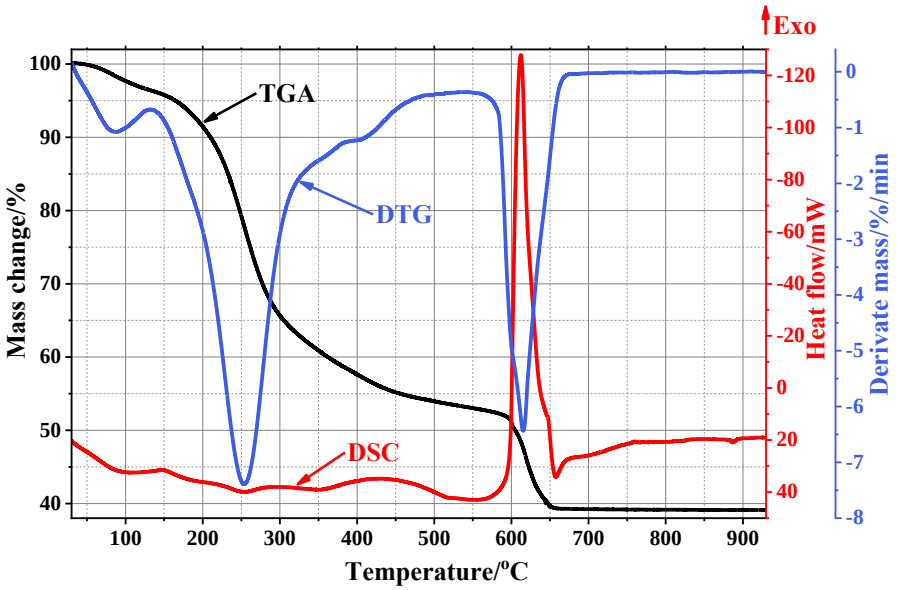

Fig. 39 Combined TGA–DTG–DSC curves of the La–Mo–O tartrate gel precursor for $La_2Mo_2O_9$ ceramic

220 °C and is related to the decomposition of TA dimer into CO, CO_2 and acetic acid (Eq. 5).The exothermic peak at 150 °C in DSC curve is attributed to the removal of CO and CO_2 molecules. Meanwhile, the broad endothermic peak throughout this region is related to the evaporation of the acetic acid. The second step starts from the temperature of 220 °C and ends at 300 °C. This process of the dimer decomposition to pyruvic acid and CO_2 molecules is characterized by an endothermic band and an exothermic peak, respectively (Eq. 17). The total mass loss at this stage is 30.2 %.

$$C_8H_8O_{10}\ (s) \longrightarrow 2\ CH_3COCOOH\ (g) + 2\ CO_2\ (g) \qquad (17)$$

$$16\ La_{10}[(MoO_4)_{10}(C_4H_4O_6)_{14}H_{18}] \longrightarrow 160\ La^{3+} + 160\ MoO_4^{2-} + C_{747}O_{454} + 149\ CO_2 + 592\ H_2O \qquad (18)$$

After the decomposition of the excess of TA the third stage starts and is related to the decomposition of metal tartrates in the range of temperature from 301 °C to 520 °C. As can be seen from Eq. 18, this stage consists of two processes. The endothermic band in the range of temperatures from 301 °C to 385 °C is attributed to the evaporation process of water molecules. The second one with the exothermic behavior in the range of temperatures from 386 °C to

520 °C is related to the removal of CO_2 molecules. The mass loss during this stage is 12 %.

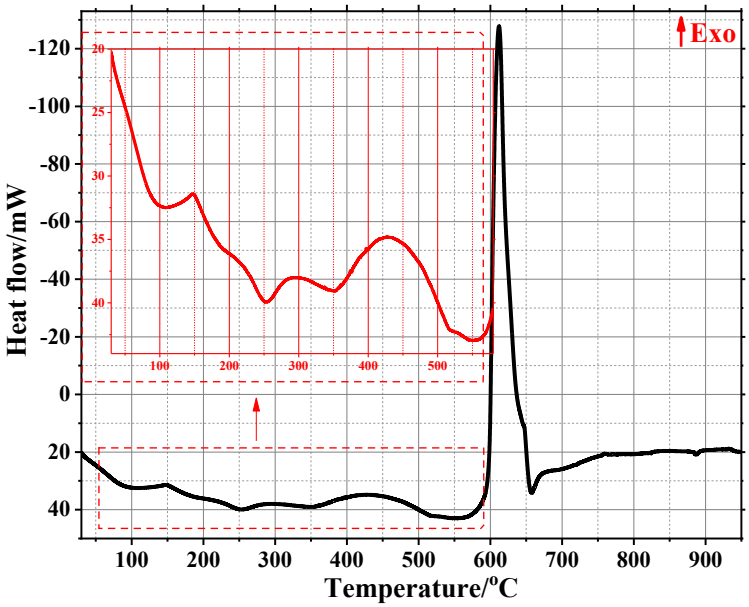

Fig. 40 DSC curve of the La–Mo–O tartrate gel precursor for $La_2Mo_2O_9$ ceramic

In the next stage, the change of mass loss has almost stopped and is at about 0.8 %. This part is directly related to the endothermic crystallization process that occurs in the range of temperatures from 521 °C to 570 °C and is described in Eq. 19. The crystallization of $La_2Mo_2O_9$ to a cubic β-phase occurs directly from the residue of the metal tartrate gel precursor.

$$160\ La^{3+} + 160\ MoO_4^{2-} + C_{747}O_{454} \rightarrow 80\ La_2Mo_2O_9 + C_{747}O_{374} \qquad (19)$$

The last mass change (13.3 %) occurs in the range of temperature from 571 °C to 680 °C and is attributed to the burning of inorganic carbon, which is formed from the tartrates. This exothermic process is presented in Eq. 20. By the further increasing the temperature to 950 °C only 0.1 % of the mass and no heat changes were detected in the DSC curve. This means that the crystalline phase of lanthanum molybdate forms at the temperature below 680 °C.

$$80\ La_2Mo_2O_9 + C_{747}O_{374} + 560\ O_2 \rightarrow 80\ La_2Mo_2O_9 + 747\ CO_2 \qquad (20)$$

A differential scanning calorimetry can also be used to analyze physical transformations such as a phase transition. In order to investigate the phase

transition of $La_2Mo_2O_9$ ceramic, the DSC analysis was performed and the results are presented in Fig. 41. The phase transition to a cubic β-phase occurs in the range of temperatures from 555 °C to 570 °C (Fig. 41 heating stage). The phase transition from β-phase to a monoclinic α-phase occurs in the range of temperatures from 538 °C to 514 °C (Fig. 41 cooling stage). This leads to the conclusion that the phase transition from α-phase to β-phase occurs in higher temperatures than the opposite process.

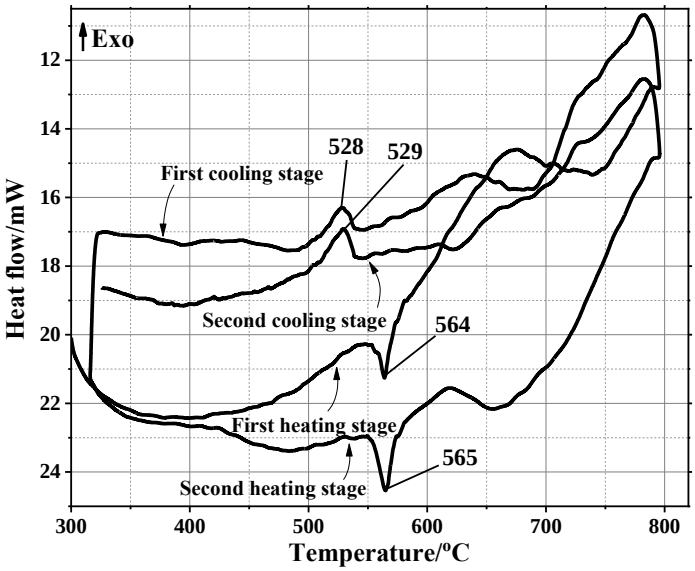

Fig. 41 DSC curve of the $La_2Mo_2O_9$ ceramic heat-treated at 1200 °C of temperature

A detailed investigation of phase transition dependence on sample mass and initial annealing temperature is presented in ***Article III***.

3.3.2 Structural properties and morphology analysis of $La_2Mo_2O_9$ ceramic

XRD patterns of the La–Mo–O tartrate gel precursor dried at 120 °C and heat-treated at different temperatures are shown in Fig. 42. All characteristic reflections from the XRD patters can be attributed to the monoclinic α-$La_2Mo_2O_9$ crystal phase and match well with the reference data of lanthanum molybdate (ICSD 172479) that is presented in the bottom panel. The gel dried at the temperature of 120 °C showed a fully amorphous character. In addition, La–Mo–O tartrate gel precursor heat-treated at 500 °C of temperature also showed an amorphous character. However, a small peak characteristic of monoclinic $La_2Mo_2O_9$ phase at 2θ angle of 27.7 ° (404) reflection was observed. These results slightly differ from the thermal analysis

data where the crystallization process started in the range of temperatures from 521 °C to 570 °C. This deviation might have been observed due to the differences in heating ratio, heating time, sample mass and other conditions. The pure monoclinic phase of lanthanum molybdate formed when the heat-treatment was increased from 550 °C to 1200 °C of temperatures.

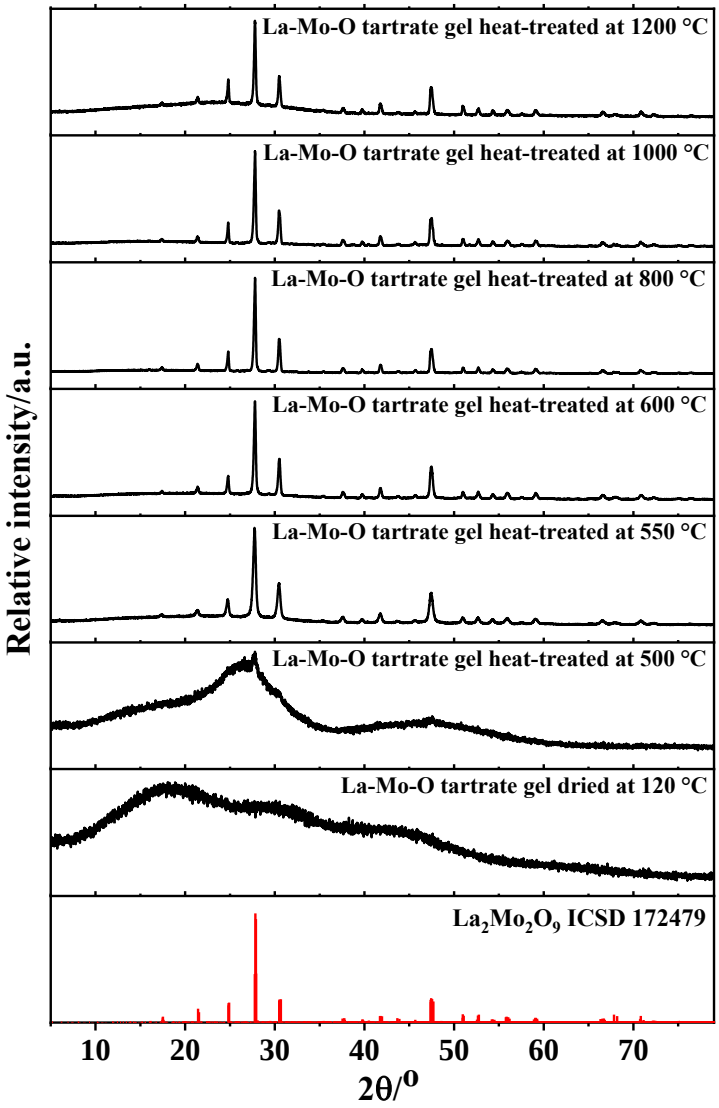

Fig. 42 XRD patterns of the La–Mo–O tartrate gel precursor for $La_2Mo_2O_9$ ceramic dried at 120 °C and heat-treated at 500, 550, 600, 800, 1000 and 1200 °C temperatures for 5 hours in the air

In order to investigate the crystallite size growth tendencies, the Rietveld refinement analysis was performed. Detailed results are presented in ***Article III***, *Table. 4*. A graphical representation of obtained results is shown in Fig. 43. It was found that the growth of crystallite size tends to increase in the range of temperatures from 550 °C to 800 °C. These results have a significant influence on the phase transition. In other words, the investigation of phase transition should be done with samples heat-treated at the temperatures above 800 °C. Otherwise, the crystallite growth process could affect the onset temperature of the corresponding phase transition.

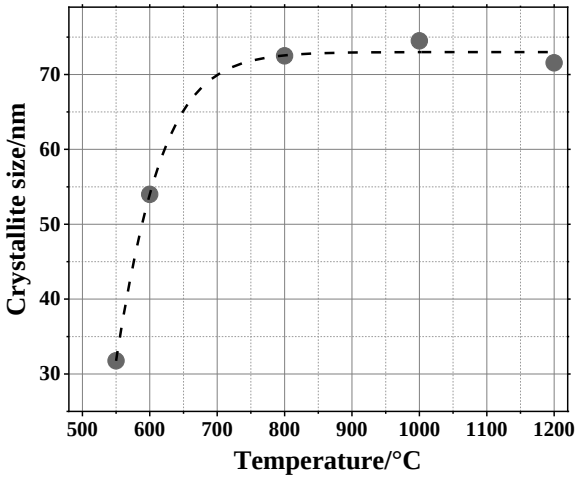

Fig. 43 Plot of crystallite size versus heat-treatment temperature for $La_2Mo_2O_9$ ceramic

SEM micrographs of the La–Mo–O sample for $La_2Mo_2O_9$ ceramics annealed at 500, 550, 600 and 1200 °C are shown in Fig. 44. The obtained results clearly show that the samples heat-treated at the temperatures of 500 °C and 550 °C consist of irregularly shaped agglomerates with smaller sphere-like particles (200 – 500 nm) on the surface. Moreover, the agglomerates are composed of well-connected sphere-like particles in size of about 82 – 85 nm in the sample heat-treated at the temperature of 550 °C (see ***Article III***, *Fig. 14*). By increasing the temperature up to 600 °C the sample morphology changes completely. The tendency of growth of both the particles and pores was identified. This result is in a good agreement with Rietveld analysis data when the growth of the crystallites by increasing the heat-treatment temperature was also observed. As shown in Fig. 44c, the surface

morphology of the heat-treated sample is composed of the sphere-like or elliptical particles, which size varies from 100 nm to 200 nm.

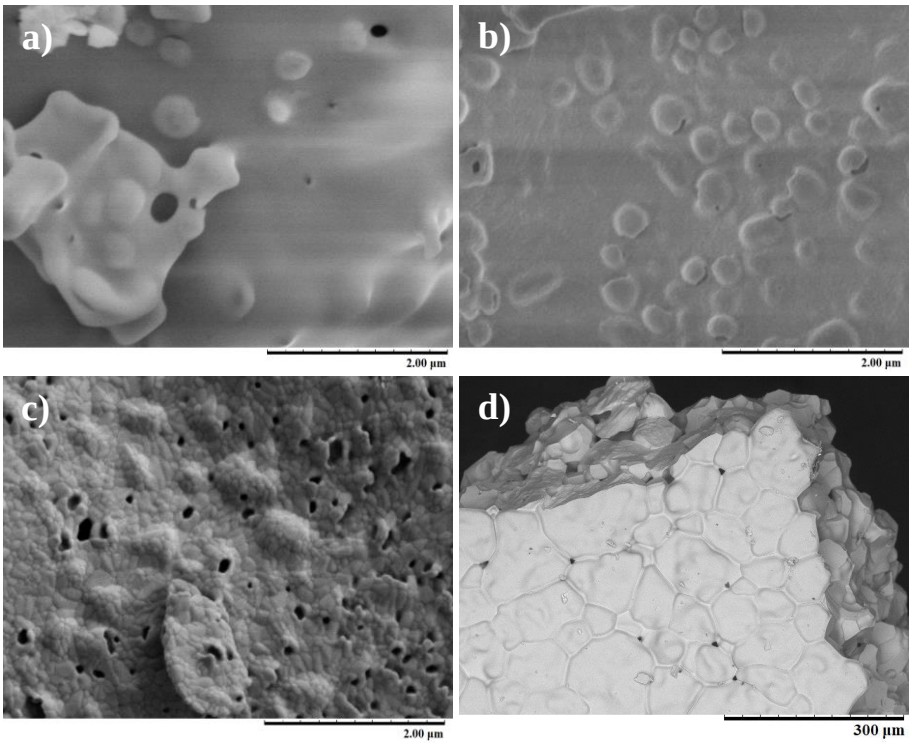

Fig. 44 SEM micrographs of La–Mo–O tartrate gel precursor for $La_2Mo_2O_9$ ceramic heat-treated at the temperatures of (a) 500 °C. (b) 550 °C, (c) 600 °C and (d) 1200 °C in air for 5 hours at ambient pressure

It is well known that physical properties are strongly related to surface morphology. Unfavorable effects could be caused by the enhanced porosity of the sample and low connectivity between the grains. In order to eliminate such kind of negative factors, the powders were additionally grounded, pressed into pellet and additionally heat-treated at the temperature of 1200 °C. The obtained results are presented in Fig. 44 (d), which show that the dense ceramic surface composed from the irregularly-shaped 100 – 200 μm well-connected grains has formed. Besides, on the surface of the sample small amount of pores, which diameter varies from about 2.8 μm to 11 μm were identified. Though the density of the as-prepared ceramic remains relatively high. It also should be noted that above the temperature of 800 °C the size of crystallites stops growing, which is directly related to the specific phase transition properties in the final ceramic.

3.3.3 Impedance spectroscopy analysis of $La_2Mo_2O_9$ ceramic

Typical Arrhenius plots of temperature dependencies of standard deviation for α- and β-phase transition processes in $La_2Mo_2O_9$ ceramic are shown in Fig. 45.

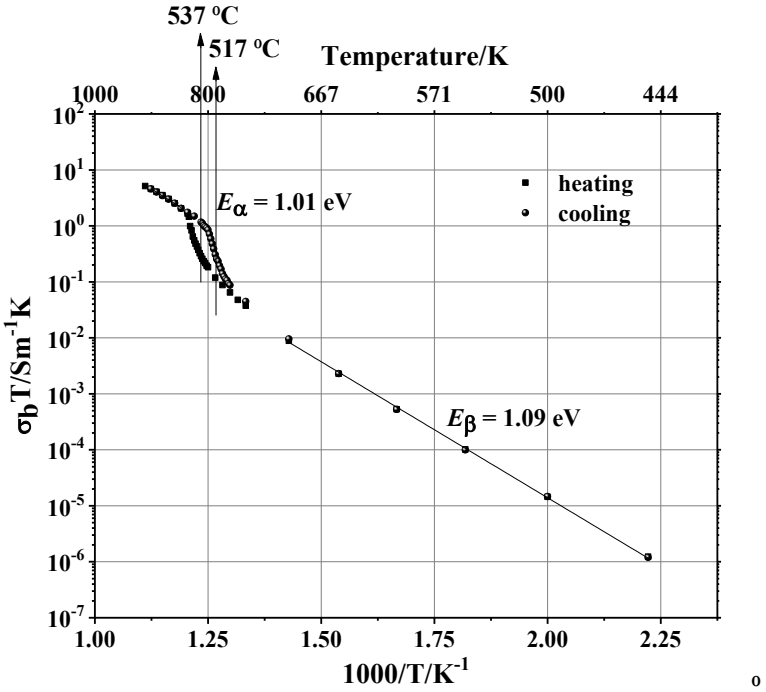

Fig. 45 Arrhenius plots of temperature dependencies of standard deviation for α- and β-phase transition processes in $La_2Mo_2O_9$ ceramic

These results indicate that ionic conductivity increases by two orders of magnitude in temperatures ranging from 517 °C to 537 °C. The activation energy of the cubic β-phase (1.09 eV) is slightly higher than that of the monoclinic α–phase (1.01 eV) and leads to a conclusion that the low-temperature monoclinic phase is more stable.

According to the literature [16] available, the phase activation energies of low- and high-temperature phases of $La_2Mo_2O_9$ are at about 0.9 eV and 1.2 eV, respectively. The obtained results are in good agreement with those found in the literature.

3.4 Characterization of $Ce_{0.9}Gd_{0.1}O_{1.95}$ ceramic

3.4.1 Thermal analysis of Ce–Gd–O oxalate gel precursor and decomposition mechanism

Combined TGA–DTG–DSC curves in air atmosphere of Ce–Gd–O oxalate gel precursor are presented in Fig. 46. The thermal decomposition of Ce–Gd–O oxalate gel precursor could be divided into four stages. The first mass loss occurs in the range of temperatures from 30 °C to 140 °C. The endothermic effect is related to the removal of absorbed water molecules and the mass loss consist of about 2.6 % of the total mass. The second mass loss occurs in the range of temperatures from 141 °C to 320 °C and could be divided into two parts: the first stage with the mass loss of 4.1 % is related to a broad exothermic band and attributed to the decomposition of ammonium oxalate into CO_2, CO and NH_3 (Eq. 21) [170]. The second part is attributed to the evaporation of water molecules from the ammonium oxalate decomposition and water molecules from coordination sphere. The peak at 234 °C shows an endothermic process behavior with the mass loss of about 2.9 %. The total mass loss in this stage is about 7.0 %.

$$(NH_4)_2C_2O_4\ (s) \rightarrow CO\ (g) + CO_2\ (g) + 2\ NH_3\ (g) + H_2O\ (g) \qquad (21)$$

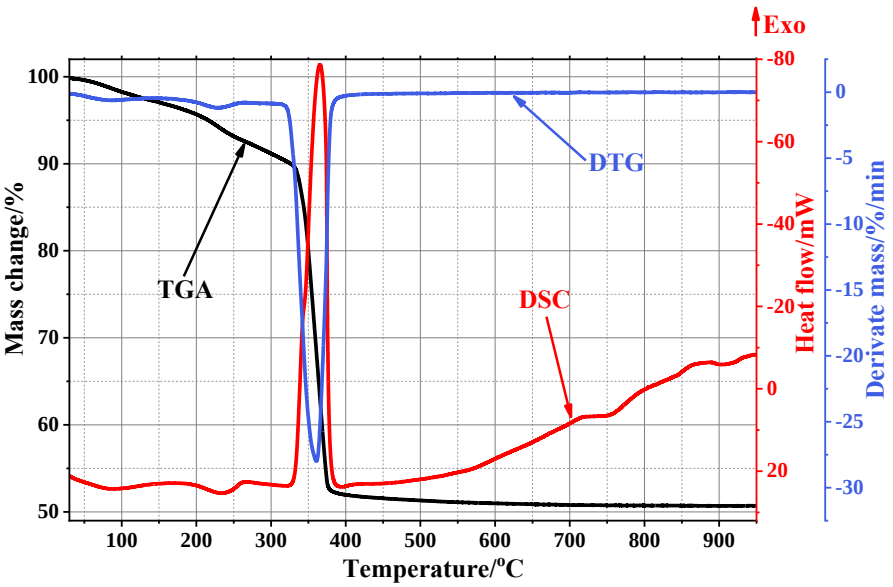

Fig. 46 Combined TGA–DTG–DSC curves of the Ce–Gd–O oxalate gel precursor for $Ce_{0.9}Gd_{0.1}O_{1.95}$ ceramic

The third mass change (38.0 %) is directly related to the thermal decomposition of cerium and gadolinium oxalates (Eqs. 22 and 23) [171]. This exothermic effect creates a sharp and intensive peak at about 365 °C that corresponds to the conversion of corresponding salts into carbon dioxide and the final ceramics. By further increasing the temperature the mass of the sample remains almost constant, which indicates full decomposition of all volatile residue in the final mixture.

$$4\ Ce_{1-x}Gd_x(C_2O_4)_r\ (s) \rightarrow 4\ Ce_{1-x}Gd_xO_{2-0.5x}\cdot C_pO_q\ (s) + 6r\ CO_2\ (g) + \\ + r\ CO\ (g) \quad (22)$$

$$2r\ CO\ (g) + O_2\ (g) \rightarrow 2r\ CO_2\ (g) \quad (23)$$

Finally, further minor mass change of about 1.2 % in the range of temperature from 396 °C to 650 °C corresponds to the burning of residual inorganic carbon in the mixture of oxides, which formed during the partial decomposition of oxalates at lower temperatures. The exothermic character of the DSC curve confirms this conclusion. The corresponding chemical changes are illustrated in Eq. 24, respectively.

$$2\ Ce_{1-x}Gd_xO_{2-0.5x}\cdot C_pO_q\ (s) + (2p - q)\ O_2\ (g) \rightarrow 2\ Ce_{1-x}Gd_xO_{2-0.5x}\ (s) + \\ + 2p\ CO_2\ (g) \quad (24)$$

The small exothermic bands in the DSC curve at the temperatures of 750 °C, 825 °C and 900 °C could be attributed to the growth of crystallites for the final ceramic. It is interesting to note, that the same synthesis performed in the sol-gel process using tartaric acid [153] showed the final decomposition of volatile residue at a slightly lower temperature than previous one obtained from the oxalate precursor.

3.4.2 Structural properties and morphology analysis of $Ce_{0.9}Gd_{0.1}O_{1.95}$ ceramic

The XRD patterns of Ce–Gd–O oxalate gel precursor dried at 100 °C and heat-treated at the temperatures of 900 °C, 950 °C, 1000 °C, 1100 °C and 1200 °C are presented in Fig. 47. From the XRD pattern, it can be seen that the Ce–Gd–O oxalate gel precursor dried at the temperature of 100 °C has an amorphous character. No characteristic peaks for any crystalline compounds were found. This means that the precipitates formed during the synthesis procedure are insignificant because of the prepared precursor that acts like a non-crystalline solid. Besides, XRD patterns of the metal oxalate precursor heat-treated at 900 °C, 950 °C, 1000 °C, 1100 °C and 1200 °C of temperatures

are well-matched with the cubic fluorite-type structure of $Ce_{0.9}Gd_{0.1}O_{1.95}$ (ICSD 28795) oxide. In all cases, a single crystalline phase of $Ce_{0.9}Gd_{0.1}O_{1.95}$ ceramic was obtained and no characteristic peaks attributed to the impurities were identified. It is also evident that the 900 °C temperature is high enough to obtain a single-phase cubic $Ce_{0.9}Gd_{0.1}O_{1.95}$ oxide with the space group *Fm-3m*.

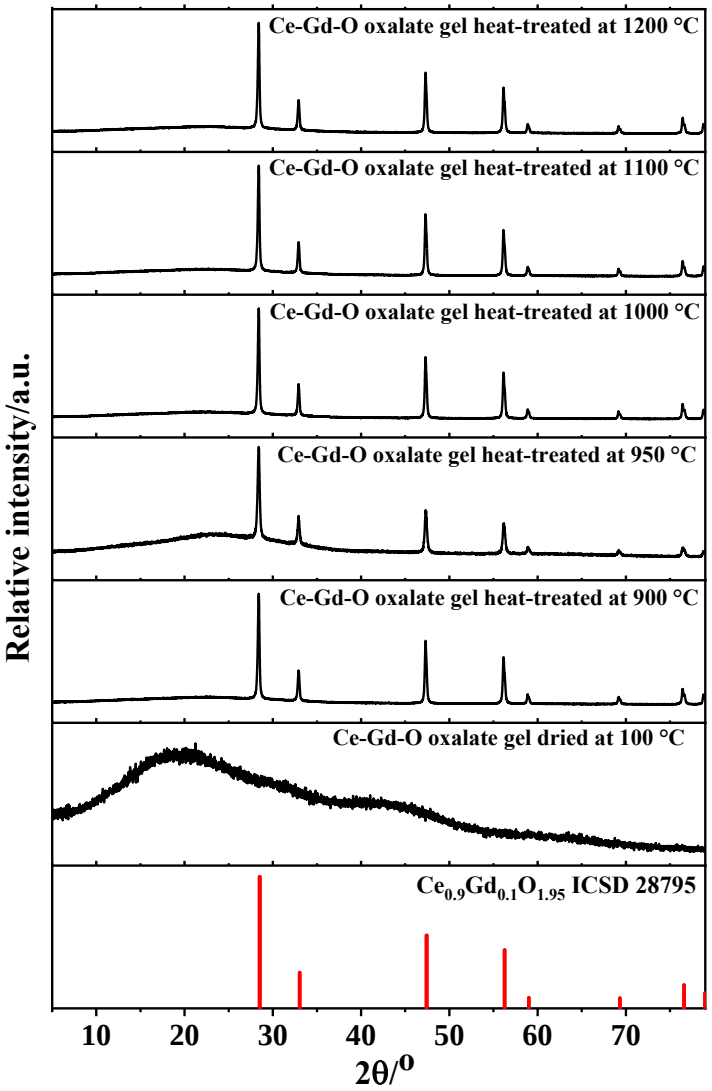

Fig. 47 XRD patterns of the Ce–Gd–O oxalate gel precursor for $Ce_{0.9}Gd_{0.1}O_{1.95}$ ceramic dried at 100 °C and heat-treated at 900, 950, 1000, 1100 and 1200 °C of temperatures for 5 hours in the air

In order to investigate the phase formation of the gadolinium-doped ceria oxide in different atmospheric conditions, the measurements in air and nitrogen atmosphere were performed and the results are presented in ***Article IV***, *Fig. 3*. It was found that in both cases single-phase $Ce_{0.9}Gd_{0.1}O_{1.95}$ oxides were formed. In addition, it became apparent that the sample prepared in an air atmosphere had a higher crystallinity due to the intensity of the peaks than the one prepared in inert conditions. The amorphous character of prepared samples could be caused by the sample preparation method on an amorphous glass surface. Additionally, the peak width of the sample heat-treated in an inert atmosphere was broader than that of the sample in an air atmosphere. Besides, these results imply that in both cases a nano-crystalline ceramic was formed. These results are in good agreement with the Rietveld refinement results that are presented in ***Article IV***, *Table 2 and 3*.

The Rietveld refinement results of crystallite size dependence on heat-treating temperature are presented in Fig. 48. These results showed that neither the size nor the lattice parameter had any significant changes throughout all the prepared samples. This leads to the conclusion that a prepared oxide has a high thermal stability. According to the Rietveld refinement results it is clear that the synthesis conditions slightly affect the lattice parameter and the size of crystallites. These results let us conclude that oxidation atmosphere is a more favorable condition for the crystallization of the final oxide.

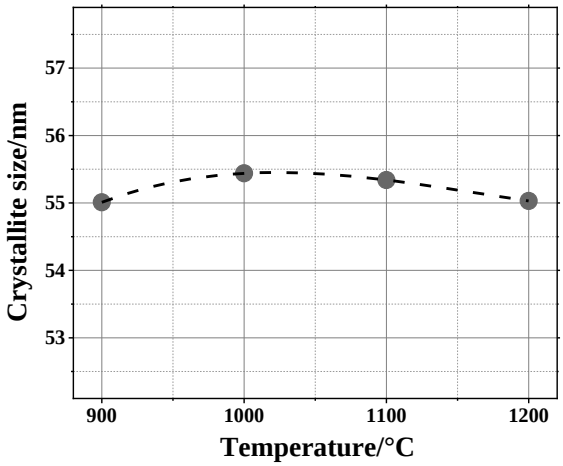

Fig. 48 Plot of crystallite size versus heat-treating temperature for $Ce_{0.9}Gd_{0.1}O_{1.95}$ ceramic

SEM micrographs of the $Ce_{0.9}Gd_{0.1}O_{1.95}$ oxide heat-treated in the range of temperature from 900 °C to 1200 °C are shown in Fig. 49. The surface of GDC

oxalate precursor heat-treated at 900 °C is composed of irregular agglomerated plate-like particles, the size of which varies from 100 nm to 1 μm (Fig. 49a). Slightly different morphology appears in a sample heat-treated at the temperature of 1000 °C. Agglomerates are composed of sphere-like particles with a size of about 50 – 100 nm. Increasing the heat-treating temperature to 1100 °C the surface morphology changes completely (Fig. 49c). The ceramic surface consists of agglomerated irregular sharp-edged particles with a size from 200 nm to 400 nm. The sample surface, heat-treated at the highest temperature, contains agglomerated irregular shape particles with a size varying from 100 nm to 600 nm. This leads to a conclusion that particle size increases as the heat-treating temperature is increased. Moreover, it has been observed that upon increasing the temperature the particle shape changes from plate-like to sphere-like sharp-edged particles.

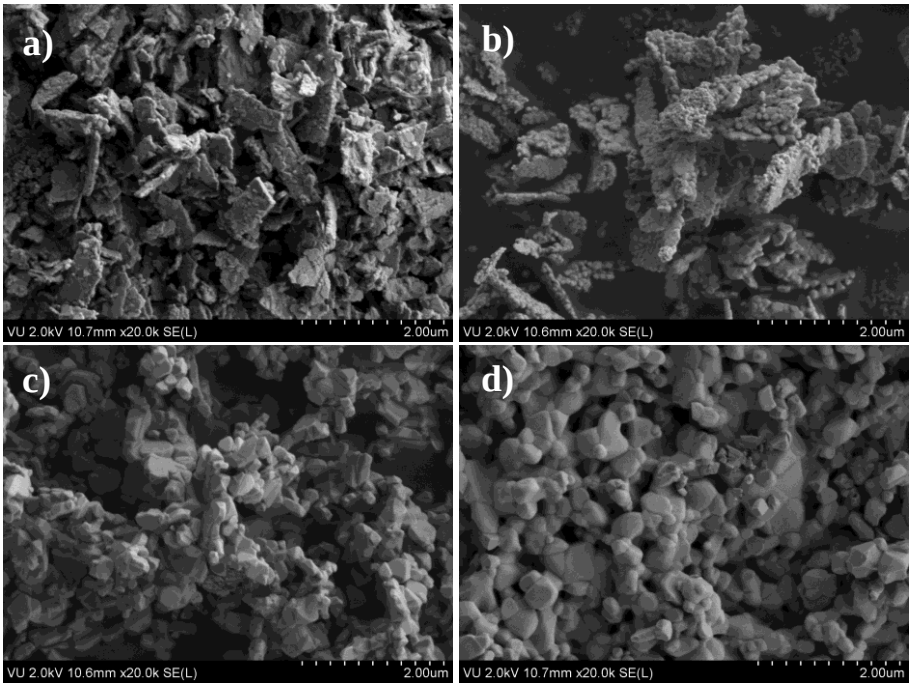

Fig. 49 SEM micrographs of Ce–Gd–O oxalate gel precursor for $Ce_{0.9}Gd_{0.1}O_{1.95}$ ceramic heat-treated at the temperatures of (a) 900 °C. (b) 1000 °C, (c) 1100 °C and (d) 1200 °C in air for 5 hours at ambient pressure

In addition, the influence of synthesis atmospheric conditions has been investigated and the results are presented in ***Article IV***, *Fig. 5*. In this case, no significant changes in either the particle size or the shape were observed.

The FTIR spectra of Ce–Gd–O oxalate precursor heat-treated in the range of temperatures from 900 °C to 1200 °C are shown in Fig. 50. The obtained results showed that in the range of the wavenumber from 4000 cm^{-1} to 1000 cm^{-1} no characteristic vibrations of organic compounds were found (Fig. 50a). The samples heat-treated at temperatures of 900 °C, 1100 °C and 1200 °C showed intensive absorption bands at 580 cm^{-1} and 458 cm^{-1}. These bands could be assigned to Ce–O and/or Gd–O stretching vibrations [153, 172-174].

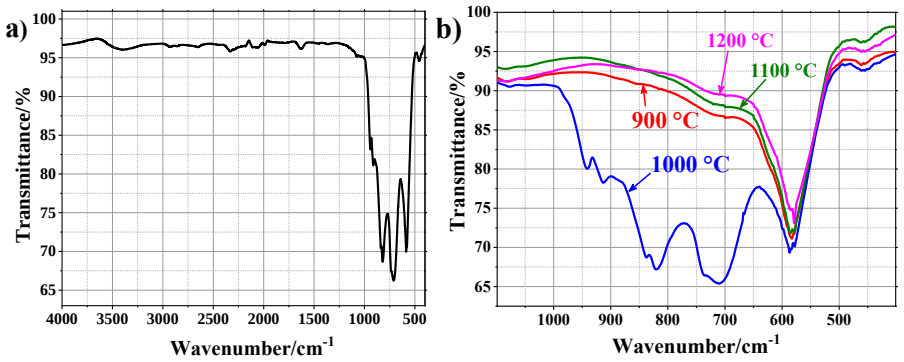

Fig. 50 FTIR spectra of $Ce_{0.9}Gd_{0.1}O_{1.95}$ oxide heat-treated (a) at 1000 °C of temperature in the range from 4000 cm^{-1} to 450 cm^{-1} and (b) at 900 °C, 1000 °C, 1100 °C and 1200 °C of temperatures in the range from 1100 cm^{-1} to 400 cm^{-1}

Meanwhile, the sample heat-treated at the temperature of 1000 °C showed more absorption bands. Characteristic vibrations of tetrahedral groups were identified at 838 cm^{-1}. The band at 820 cm^{-1} is related to O–Ce–O and/or O–Gd–O bonding nature of gadolinium-doped ceria nanoparticles [175].The remaining bands in the range of 1000 cm^{-1} to 400 cm^{-1} could be attributed to Ce–O and/or Gd–O stretching vibrations [176]. These differences in FTIR spectra could be caused by the increase of the surface area of sphere-like particles that result in a higher concentration of oxygen-metal-oxygen and metal-oxygen vibrations.

The results of TGA–DTG–DSC, XRD, SEM and FTIR analyses prove the formation of single-phase GDC ceramic. These results revealed that the heat-treatment at the temperatures above 1000 °C creates a great thermal and chemical stability of the final ceramic. Such kind of investigations is useful for further research due to their possible applications in SOFC as a solid electrolyte.

CONCLUSIONS

1. For the first time, the aqueous tartaric acid-assisted sol-gel synthesis technique was successfully proposed for the preparation of La–Mo–O, Ca–Sr–Mo–O and M–Eu–Ca–Mo–O (M=Li, Na, K, Rb, Cs) tartrate gel precursors for the $La_2Mo_2O_9$, $Ca_{1-x}Sr_xMoO_4$ and $M_{0.05}Eu_{0.05}Ca_{0.9}MoO_4$ multicomponent systems.
2. It was demonstrated that thermal analysis is a powerful technique, which allowed the estimation of the decomposition process course that enabled the creation of a possible reaction mechanism on the formation of final multicomponent crystalline compounds.
3. By the comparison of different complexing agents during the sol-gel process it was concluded that an oxalic acid assisted synthesis of gadolinium-doped ceria produced a relatively pure amorphous powder, initially enriched by the oxalate salts as impurities formed of both the salts of metal precursors and the precipitating agent. Almost identical thermal decomposition behavior was observed in the samples prepared from the tartaric gel precursors, which mechanism mainly depends on the coordination ability of the molybdate (MoO_4^{2-}) anion.
4. Moreover, the DSC measurements clearly showed that the thermal degradation of tartaric acid differs from corresponding metal tartrates and takes place below 300 ^oC of temperature. According to the enhanced thermal stability of metal molybdates, their decomposition into the ceramic and volatile carbon-hydrogen-oxygen based materials takes place at much higher temperatures than the fission of corresponding tartaric acid residues.
5. The total mass loss of all gel precursors heat-treated in the nitrogen flow well matches the results obtained in an air atmosphere, while a prior mass change for M–Eu–Ca–Mo–O samples above 600 ^oC of temperature has no sufficient influence on the results, which were obtained through other heating conditions. Therefore, such an action is important only in the inert atmosphere and it is determined by the stability of final ceramics in a reducing environment. In this case, the combustion process in the air at temperatures above 600 ^oC eliminates any specific conditions created by elemental carbon present in the sample.
6. The results of the PL studies revealed that the crystallite size and the mechanism of their growing tendencies for the $M_{0.05}Eu_{0.05}Ca_{0.9}MoO_4$

compounds are closely related to the ratio R of intensities for $^5D_0 \rightarrow {}^7F_2$ and $^5D_0 \rightarrow {}^7F_1$ characteristic emissions.

7. Besides, the nature of alkali metal strongly affects the distribution of Eu_2O_3 in the $CaMoO_4$ host and the reasons of such behavior is basically determined by the different chemical activity of alkali metals in the range of temperature from 350 °C to 800 °C.
8. DSC investigation of $La_2Mo_2O_9$ ceramic revealed that phase transition from the α-phase to the β-phase occurs in the higher temperatures (from 555 °C to 570 °C) than the opposite process (from 514 °C to 538 °C). Besides, slightly lower activation energy of monoclinic phase (1.01 eV) formation than of cubic phase (1.09 eV) shows that low-temperature phase is more stable.
9. The heat-treatment of the Ce–Gd–O oxalate precursor in nitrogen atmosphere slightly more affects both the lattice parameter and crystallite size of the final cubic $Ce_{0.9}Gd_{0.1}O_{1.95}$ crystal structure comparing with the sample, which was prepared in air. This result leads to the conclusion that an air atmosphere is a more favorable condition for the crystallization of the final GDC ceramic.
10. Moreover, Raman analysis results showed that this technique is suitable for the calculation of the exact molar composition of the multicomponent Ca–Sr–Mo–O oxides from the A_g mode position. The shift towards the lower wavenumber side occurs while increasing the bigger ionic radius Sr^{2+} ion concentration that indicates the decrease of covalent bonding between MoO_4^{2-} tetrahedra and M^{2+} ion. The calculated deviation from the theoretical composition did not exceed 0.32 %. According to the infrared spectroscopy results, it is clear that the sol-gel processing and heat-treatment temperature much more affects on the morphological features than the initial composition of final ceramics. Such a conclusion only enhances the uniqueness and suitability of this preparation technique for the synthesis of the multicomponent system for the metal molybdate based compounds.

REFERENCES

[1] J. H. Ryu, J.-W. Yoon, C. S. Lim, K. B. Shim, Materials Research Bulletin, 40 (2005) 1468-1476.
[2] Y. Wang, J. Ma, J. Tao, X. Zhu, J. Zhou, Z. Zhao, L. Xie, H. Tian, Ceramics International, 33 (2007) 693-695.
[3] J. H. Ryu, J.-W. Yoon, C. S. Lim, W.-C. Oh, K. B. Shim, Journal of Alloys and Compounds, 390 (2005) 245-249.
[4] Y. Zhang, F. Yang, J. Yang, Y. Tang, P. Yuan, Solid State Communications, 133 (2005) 759-763.
[5] Y. Jin, J. Zhang, S. Lü, H. Zhao, X. Zhang, X.-J. Wang, The Journal of Physical Chemistry C, 112 (2008) 5860-5864.
[6] V. Zhuravlev, O. Reznitskikh, Y. A. Velikodnyi, T. Patrusheva, O. Sivtsova, Journal of Solid State Chemistry, 184 (2011) 2785-2789.
[7] S. Pôrto, E. Longo, P. Pizani, T. Boschi, L. Simoes, S. Lima, J. Ferreira, L. Soledade, J. Espinoza, M. Cássia-Santos, Journal of Solid State Chemistry, 181 (2008) 1876-1881.
[8] X. Li, Z. Yang, L. Guan, J. Guo, Y. Wang, Q. Guo, Journal of Alloys and Compounds, 478 (2009) 684-686.
[9] G. S. R. Raju, E. Pavitra, Y. H. Ko, J. S. Yu, Journal of Materials Chemistry, 22 (2012) 15562-15569.
[10] M. M. Haque, D.-K. Kim, Materials Letters, 63 (2009) 793-796.
[11] X. Liu, L. Li, H. M. Noh, J. H. Jeong, K. Jang, D. S. Shin, Rsc Advances, 5 (2015) 9441-9454.
[12] J.-G. Li, X. Li, X. Sun, T. Ishigaki, The Journal of Physical Chemistry C, 112 (2008) 11707-11716.
[13] L. Carrette, K. A. Friedrich, U. Stimming, ChemPhysChem, 1 (2000) 162-193.
[14] X. Zhou, J. Ma, F. Deng, G. Meng, X. Liu, Journal of Power Sources, 162 (2006) 279-285.
[15] S. Giddey, S. Badwal, A. Kulkarni, C. Munnings, Progress in Energy and Combustion Science, 38 (2012) 360-399.
[16] P. Lacorre, F. Goutenoire, O. Bohnke, R. Retoux, Y. Laligant, Nature, 404 (2000) 856-858.
[17] R. M. Batista, E. Muccillo, Journal of Thermal Analysis and Calorimetry, 132 (2018) 851-857.
[18] K. Tanwar, N. Jaiswal, D. Kumar, O. Parkash, Journal of Alloys and Compounds, 684 (2016) 683-690.
[19] F. S. Da Silva, T. M. de Souza, International Journal of Hydrogen Energy, 42 (2017) 26020-26036.
[20] Y. Zhang, N. Holzwarth, R. Williams, Physical Review B, 57 (1998) 12738.

[21] A. M. Huerta-Flores, I. Juárez-Ramírez, L. M. Torres-Martínez, J. E. Carrera-Crespo, T. Gómez-Bustamante, O. Sarabia-Ramos, Journal of Photochemistry and Photobiology A: Chemistry, 356 (2018) 29-37.
[22] Z. Yang, C. Hou, G. Duan, F. Yang, P. Liu, C. Wang, L. Liu, G. Dong, Journal of Alloys and Compounds, 604 (2014) 346-351.
[23] A. Bayat, A. R. Mahjoub, M. M. Amini, Materials Chemistry and Physics, 223 (2019) 583-590.
[24] D. Spassky, S. Ivanov, I. Kitaeva, V. Kolobanov, V. Mikhailin, L. Ivleva, I. Voronina, Physica Status Solidi (c), 2 (2005) 65-68.
[25] C.-J. Mao, J. Geng, X.-C. Wu, J.-J. Zhu, The Journal of Physical Chemistry C, 114 (2010) 1982-1988.
[26] J.-W. Yoon, J. H. Ryu, K. B. Shim, Materials Science and Engineering: B, 127 (2006) 154-158.
[27] W. Chen, Y. Inagawa, T. Omatsu, M. Tateda, N. Takeuchi, Y. Usuki, Optics Communications, 194 (2001) 401-407.
[28] S. Kwan, F. Kim, J. Akana, P. Yang, Chemical Communications, (2001) 447-448.
[29] H. Yu, Z. Li, A. J. Lee, J. Li, H. Zhang, J. Wang, H. M. Pask, J. A. Piper, M. Jiang, Optics Letters, 36 (2011) 579-581.
[30] J. Bi, L. Wu, Y. Zhang, Z. Li, J. Li, X. Fu, Applied Catalysis B: Environmental, 91 (2009) 135-143.
[31] D. Gao, Y. Li, X. Lai, Y. Wei, J. Bi, Y. Li, M. Liu, Materials Chemistry and Physics, 126 (2011) 391-397.
[32] V. M. Longo, L. S. Cavalcante, E. C. Paris, J. C. Sczancoski, P. S. Pizani, M. S. Li, J. Andrés, E. Longo, J. A. Varela, The Journal of Physical Chemistry C, 115 (2011) 5207-5219.
[33] M. Minowa, K. Itakura, S. Moriyama, W. Ootani, Nuclear Instruments and Methods in Physics Research section A: Accelerators, Spectrometers, Detectors and Associated Equipment, 320 (1992) 500-503.
[34] K. K. Aruna, R. Manoharan, International Journal of Hydrogen Energy, 38 (2013) 12695-12703.
[35] J. Zhang, L. Li, W. Zi, N. Guo, L. Zou, S. Gan, G. Ji, Journal of Physics and Chemistry of Solids, 75 (2014) 878-887.
[36] A. Sen, P. Pramanik, Materials Letters, 50 (2001) 287-294.
[37] J. López-Solano, P. Rodríguez-Hernández, S. Radescu, A. Mujica, A. Muñoz, D. Errandonea, F. Manjón, J. Pellicer-Porres, N. Garro, A. Segura, Physica Status Solidi (b), 244 (2007) 325-330.
[38] S. Takai, S. Touda, K. Oikawa, K. Mori, S. Torii, T. Kamiyama, T. Esaka, Solid State Ionics, 148 (2002) 123-133.
[39] J. Cheng, J. He, Materials Letters, 209 (2017) 525-527.
[40] J. Liu, J. Ma, B. Lin, Y. Ren, X. Jiang, J. Tao, X. Zhu, Ceramics International, 34 (2008) 1557-1560.

[41] Y. Wu, T. Yu, B.-S. Dou, C.-X. Wang, X.-F. Xie, Z.-L. Yu, S.-R. Fan, Z.-R. Fan, L.-C. Wang, Journal of Catalysis, 120 (1989) 88-107.
[42] Y. C. X. Geng, L. Xiao, Y. Yang, Y. Xie, Journal of the Chinese Ceramic Society, 43 (2015) 4.
[43] W. Shi, J. Chen S. Gao, Journal of the Chinese Ceramic Society, 39 (2011) 219-222.
[44] G. Wandahl, A. N. Christensen, Acta Chemica Scandinavica, 41 (1987) 358-360.
[45] V. Marques, L. Cavalcante, J. Sczancoski, A. Alcântara, M. O. Orlandi, E. Moraes, E. Longo, J. A. Varela, M. Siu Li, M. Santos, Crystal Growth & Design, 10 (2010) 4752-4768.
[46] L. Barbosa, D. R. Ardila, C. Cusatis, J. Andreeta, Journal of Crystal Growth, 235 (2002) 327-332.
[47] S. K. Gupta, M. Sahu, P. Ghosh, D. Tyagi, M. Saxena, R. Kadam, Dalton Transactions, 44 (2015) 18957-18969.
[48] A. Barker Jr, Physical Review, 135 (1964) A742.
[49] A. Sleight, Acta Crystallographica Section B: Structural Crystallography and Crystal Chemistry, 28 (1972) 2899-2902.
[50] S. Achary, S. Patwe, M. Mathews, A. Tyagi, Journal of Physics and Chemistry of Solids, 67 (2006) 774-781.
[51] F. A. Rabuffetti, S. P. Culver, L. Suescun, R. L. Brutchey, Inorganic Chemistry, 53 (2014) 1056-1061.
[52] H.-N. Im, M.-B. Choi, S.-Y. Jeon, S.-J. Song, Ceramics International, 37 (2011) 49-53.
[53] D. Errandonea, F. J. Manjon, Progress in Materials Science, 53 (2008) 711-773.
[54] C. Tablero, Chemical Physics Letters, 635 (2015) 190-195.
[55] Y. Hu, W. Zhuang, H. Ye, D. Wang, S. Zhang, X. Huang, Journal of Alloys and Compounds, 390 (2005) 226-229.
[56] P. Dutta, A. Khanna, ECS Journal of Solid State Science and Technology, 2 (2012) R3153.
[57] C. Bouzidi, K. Horchani-Naifer, Z. Khadraoui, H. Elhouichet, M. Ferid, Physica B: Condensed Matter, 497 (2016) 34-38.
[58] S. Rama Rao, S. Roopas Kiran, V. Murthy, Journal of the American Ceramic Society, 95 (2012) 3532-3537.
[59] L. Wan, S. Lü, L. Sun, X. Qu, Optical Materials, 36 (2014) 628-632.
[60] L. Wei, Y. Liu, Y. Lu, T. Wu, Journal of Nanomaterials, 2012 (2012).
[61] Y. Wang, L. Yang, Y. Wang, X. Wang, G. Han, Journal of the Ceramic Society of Japan, 120 (2012) 378-381.
[62] C. Hazra, T. Samanta, A. V. Asaithambi, V. Mahalingam, Dalton Transactions, 43 (2014) 6623-6630.
[63] R. Oeder, A. Scharmann, D. Schwabe, Journal of Crystal Growth, 49 (1980) 349-356.

[64] S. Vidya, J. Thomas, Bulletin of Pure & Applied Sciences-Chemistry, 37 (2018) 26-34.
[65] X. Li, Z. Yang, L. Guan, Q. Guo, Materials Letters, 63 (2009) 1096-1098.
[66] K. Toda, S. W. Kim, T. Hasegawa, M. Watanabe, T. Kaneko, A. Toda, R. Yamanashi, S. Kumagai, M. Muto, A. Itadani, Key Engineering Materials, 741 (2017) 353-357.
[67] S. Ramarao, S. R. Kiran, V. Murthy, Materials Research Bulletin, 56 (2014) 71-79.
[68] Y. Xiang, J. Song, G. Hu, Y. Liu, Applied Surface Science, 349 (2015) 374-379.
[69] M. Ghaed-Amini, M. Bazarganipour, M. Salavati-Niasari, Journal of Industrial and Engineering Chemistry, 21 (2015) 1089-1097.
[70] T. Thongtem, S. Kungwankunakorn, B. Kuntalue, A. Phuruangrat, S. Thongtem, Journal of Alloys and Compounds, 506 (2010) 475-481.
[71] G. Xing, Y. Li, Y. Li, Z. Wu, P. Sun, Y. Wang, C. Zhao, G. Wu, Materials Chemistry and Physics, 127 (2011) 465-470.
[72] B. Hwang, R. Santhanam, D. Liu, Journal of Power Sources, 101 (2001) 86-89.
[73] S. H. Park, Y.-K. Sun, Journal of Power Sources, 119 (2003) 161-165.
[74] R. Thirunakaran, K.-T. Kim, Y.-M. Kang, J. Young-Lee, Materials Research Bulletin, 40 (2005) 177-186.
[75] A. Kareiva, M. Karppinen, L. Niinistö, Journal of Materials Chemistry, 4 (1994) 1267-1270.
[76] A. Žalga, B. Abakevičienė, A. Žarkov, A. Beganskienė, A. Kareiva, S. Tamulevičius, Materials Science, 17 (2011) 191-196.
[77] G. Braziulis, G. Janulevičius, R. Stankevičiūtė, A. Žalga, Journal of Thermal Analysis and Calorimetry, 118 (2014) 613-621.
[78] A. Hashem, A. Abdel-Ghany, H. Abuzeid, R. El-Tawil, S. Indris, H. Ehrenberg, A. Mauger, C. Julien, Journal of Alloys and Compounds, 737 (2018) 758-766.
[79] D.-H. Chen, X.-R. He, Materials Research Bulletin, 36 (2001) 1369-1377.
[80] A. E. Danks, S. R. Hall, Z. Schnepp, Materials Horizons, 3 (2016) 91-112.
[81] M. R. Vaezi, Sensors and Materials, 20 (2008) 211-219.
[82] P. Xiao, X. Ge, Z. Liu, J.-Y. Wang, X. Wang, Journal of Alloys and Compounds, 587 (2014) 326-331.
[83] F. Li, H. Xie, H. Xi, F. Dang, X. Wang, Luminescence, 30 (2015) 600-604.
[84] H. Xie, F. Li, H. Xi, R. Tian, X. Wang, Journal of Materials Science: Materials in Electronics, 26 (2015) 23-31.
[85] V. Longo, E. Orhan, L. Cavalcante, S. Porto, J. Espinosa, J. A. Varela, E. Longo, Chemical Physics, 334 (2007) 180-188.

[86] A. Phuruangrat, T. Thongtem, S. Thongtem, Materials science-Poland, 28 (2010) 557-563.
[87] Y. Liang, X. Han, Z. Yi, W. Tang, L. Zhou, J. Sun, S. Yang, Y. Zhou, Journal of Solid State Electrochemistry, 11 (2007) 1127-1131.
[88] M. Silva, M. Sena, A. Lopes-Moriyama, C. Souza, A. Santos, Ceramics International, 44 (2018) 16606-16614.
[89] A. Shandilya, K. Sreenivas, AIP Conference Proceedings, AIP Publishing LLC, (2019) 070028.
[90] X.-b. Li, Y.-F. Li, Tribology Letters, 65 (2017) 116.
[91] G. Hoogers, Fuel Cell Technology Handbook, CRC press, 2002.
[92] A. B. Stambouli, E. Traversa, Renewable and Sustainable Energy Reviews, 6 (2002) 295-304.
[93] A. B. Stambouli, Renewable and Sustainable Energy Reviews, 15 (2011) 4507-4520.
[94] A. Kirubakaran, S. Jain, R. Nema, Renewable and Sustainable Energy Reviews, 13 (2009) 2430-2440.
[95] H. Xu, L. Kong, X. Wen, IEEE Transactions on Power Electronics, 19 (2004) 1250-1255.
[96] K. Huang, J. B. Goodenough, Solid oxide fuel cell technology: principles, performance and operations, Elsevier, 2009.
[97] A. B. Stambouli, E. Traversa, Renewable and Sustainable Energy Reviews, 6 (2002) 433-455.
[98] N. Mahato, A. Banerjee, A. Gupta, S. Omar, K. Balani, Progress in Materials Science, 72 (2015) 141-337.
[99] H. Tu, U. Stimming, Journal of Power Sources, 127 (2004) 284-293.
[100] A. Choudhury, H. Chandra, A. Arora, Renewable and Sustainable Energy Reviews, 20 (2013) 430-442.
[101] N. Laosiripojana, W. Wiyaratn, W. Kiatkittipong, A. Arpornwichanop, A. Soottitantawat, S. Assabumrungrat, Engineering Journal, 13 (2009) 65-84.
[102] S. C. Singhal, Solid State Ionics, 152 (2002) 405-410.
[103] M. Cassir, A. Ringuedé, L. Niinistö, Journal of Materials Chemistry, 20 (2010) 8987-8993.
[104] J. Molenda, K. Świerczek, W. Zając, Journal of Power Sources, 173 (2007) 657-670.
[105] T. Suzuki, Y. Funahashi, T. Yamaguchi, Y. Fujishiro, M. Awano, Journal of Fuel Cell Science and Technology, 5 (2008).
[106] D. Pla, A. Sánchez-González, I. Garbayo, M. Salleras, A. Morata, A. Tarancón, Journal of Power Sources, 293 (2015) 264-273.
[107] A. Weber, E. Ivers-Tiffée, Journal of Power Sources, 127 (2004) 273-283.
[108] S. Mekhilef, R. Saidur, A. Safari, Renewable and Sustainable Energy Reviews, 16 (2012) 981-989.
[109] R. M. Ormerod, Chemical Society Reviews, 32 (2003) 17-28.

[110] J. M. Andújar, F. Segura, Renewable and Sustainable Energy Reviews, 13 (2009) 2309-2322.
[111] B. Zhu, International Journal of Energy Research, 33 (2009) 1126-1137.
[112] N. Q. Minh, Journal of the American Ceramic Society, 76 (1993) 563-588.
[113] D.-S. Lee, W. Kim, S. Choi, J. Kim, H.-W. Lee, J.-H. Lee, Solid State Ionics, 176 (2005) 33-39.
[114] H. Jung, S.-H. Choi, H. Kim, J.-W. Son, J. Kim, H.-W. Lee, J.-H. Lee, Journal of Power Sources, 159 (2006) 478-483.
[115] T. L. Cable, S. W. Sofie, Journal of Power Sources, 174 (2007) 221-227.
[116] W. Zhu, S. Deevi, Materials Science and Engineering: A, 362 (2003) 228-239.
[117] T.-L. Wen, D. Wang, H. Tu, M. Chen, Z. Lu, Z. Zhang, H. Nie, W. Huang, Solid State Ionics, 152 (2002) 399-404.
[118] J.-H. Myung, H.-J. Ko, J.-J. Lee, J.-H. Lee, S.-H. Hyun, International Journal of Hydrogen Energy, 37 (2012) 11351-11359.
[119] S. Badwal, Solid State Ionics, 143 (2001) 39-46.
[120] S. Badwal, K. Foger, Ceramics International, 22 (1996) 257-265.
[121] N. Rahimi, S. T. Thirugnana, S. Ghoshal, Journal of Environmental Treatment Techniques, 8 (2020) 604-609.
[122] F. Figueiredo, F. Marques, Wiley Interdisciplinary Reviews: Energy and Environment, 2 (2013) 52-72.
[123] G. Accardo, C. Ferone, R. Cioffi, D. Frattini, L. Spiridigliozzi, G. Dell'Agli, Journal of Applied Biomaterials & Functional Materials, 14 (2016) 35-41.
[124] J. Zhang, C. Lenser, N. H. Menzler, O. Guillon, Solid State Ionics, 344 (2020) 115138.
[125] V. Kharton, F. Marques, A. Atkinson, Solid State Ionics, 174 (2004) 135-149.
[126] M. Han, X. Tang, H. Yin, S. Peng, Journal of Power Sources, 165 (2007) 757-763.
[127] L. Malavasi, C. A. Fisher, M. S. Islam, Chemical Society Reviews, 39 (2010) 4370-4387.
[128] I. R. Evans, J. A. Howard, J. S. Evans, Chemistry of Materials, 17 (2005) 4074-4077.
[129] L. Haoran, W. Chang-An, Journal of the American Ceramic Society, 98 (2015) 1385-1388.
[130] S. Abtmeyer, R. Pązik, R. J. Wiglusz, M. Małecka, G. A. Seisenbaeva, V. G. Kessler, Inorganic Chemistry, 53 (2014) 943-951.
[131] S. A. Hayward, S. A. Redfern, Journal of Physics: Condensed Matter, 16 (2004) 3571.

[132] H. Chun-Ju, Z. Xu, L. Chang-Song, W. Xian-Ping, F. Qian-Feng, Chinese Physics Letters, 25 (2008) 3342.
[133] Y. Li, R. Pu, L. Wen, X. Peng, Z. Ning, B. Wu, Y. Zhao, X. Lai, J. Bi, D. Gao, Journal of Materials Science: Materials in Electronics, 29 (2018) 12932-12943.
[134] S. Georges, O. Bohnké, F. Goutenoire, Y. Laligant, J. Fouletier, P. Lacorre, Solid State Ionics, 177 (2006) 1715-1720.
[135] C. Tealdi, G. Chiodelli, L. Malavasi, G. Flor, Journal of Materials Chemistry, 14 (2004) 3553-3557.
[136] D. Zhang, Z. Zhuang, Y. Gao, X. Wang, Q. Fang, Solid State Ionics, 181 (2010) 1510-1515.
[137] S. Georges, F. Goutenoire, F. Altorfer, D. Sheptyakov, F. Fauth, E. Suard, P. Lacorre, Solid State Ionics, 161 (2003) 231-241.
[138] D. Marrero-López, J. Pena-Martinez, D. Pérez-Coll, P. Nunez, Journal of Alloys and Compounds, 422 (2006) 249-257.
[139] S. Georges, F. Goutenoire, O. Bohnke, M. Steil, S. Skinner, H. Wiemhofer, P. Lacorre, Journal of New Materials for Electrochemical Systems, 7 (2004) 51-58.
[140] D. Kolesnikova, E. Kharitonova, V. Voronkova, Crystallography Reports, 56 (2011) 315.
[141] H. CHENG, W. Hongen, L. Liang, L. Zhouguang, Q. Dong, Rare Metals, 27 (2008) 340-344.
[142] I. Weber, P. Baracho, F. Rangel, E. Paris, E. Muccillo, Materials Science and Technology, 25 (2009) 1346-1350.
[143] Z. Yi, Q. Fang, X. Wang, G. Zhang, Solid State Ionics, 160 (2003) 117-124.
[144] M. Ali, B. Wani, S. Bharadwaj, Journal of Thermal Analysis and Calorimetry, 96 (2009) 463-468.
[145] V. Voronkova, E. Kharitonova, A. Krasilnikova, Physica Status Solidi (a), 206 (2009) 2564-2568.
[146] L. Shao, D. Ji, J. Yang, J. Xie, Q. Yin, H. Le, Journal of Rare Earths, 37 (2019) 984-988.
[147] P. P. Dholabhai, S. Anwar, J. B. Adams, P. A. Crozier, R. Sharma, Modelling and Simulation in Materials Science and Engineering, 20 (2011) 015004.
[148] H. J. Jung, S.-Y. Chung, Journal of the Korean Ceramic Society, 54 (2017) 413-421.
[149] S. Anirban, T. Paul, A. Dutta, RSC Advances, 5 (2015) 50186-50195.
[150] J. Zhang, C. Ke, H. Wu, J. Yu, J. Wang, Y. Wang, Journal of Alloys and Compounds, 718 (2017) 85-91.
[151] F. Ye, T. Mori, D. R. Ou, J. Zou, G. Auchterlonie, J. Drennan, Solid State Ionics, 179 (2008) 827-831.

[152] Y. Leng, S. Chan, S. Jiang, K. Khor, Solid State Ionics, 170 (2004) 9-15.
[153] A. Žarkov, A. Stanulis, T. Šalkus, A. Kežionis, V. Jasulaitienė, R. Ramanauskas, S. Tautkus, A. Kareiva, Ceramics International, 42 (2016) 3972-3988.
[154] H. J. Kim, H. Y. Park, M. C. Chu, D. S. Bae, Defect and Diffusion Forum, 297 (2010) 1140-1145.
[155] A. Kežionis, S. Kazlauskas, D. Petrulionis, A. F. Orliukas, IEEE Transactions on Microwave Theory and Techniques, 62 (2014) 2456-2461.
[156] S. Kazlauskas, A. Kežionis, E. Kazakevičius, A. F. Orliukas, Electrochimica Acta, 134 (2014) 176-181.
[157] S. Debrus, M. Marchewka, J. Baran, M. Drozd, R. Czopnik, A. Pietraszko, H. Ratajczak, Journal of Solid State Chemistry, 178 (2005) 2880-2896.
[158] B. H. Stuart, Infrared Spectroscopy: Fundamentals and Applications, J. Wiley & Sons, 2004.
[159] B. Fu, Q. Shen, W. Qian, Y. Zeng, X. Sun, M. Hannig, Journal of Materials Science: Materials in Medicine, 16 (2005) 827-831.
[160] V. Sasikala, D. Sajan, N. Vijayan, K. Chaitanya, M. B. Raj, B. S. Joy, Spectrochimica Acta Part A: Molecular and Biomolecular Spectroscopy, 123 (2014) 127-141.
[161] Z. Dega-Szafran, G. Dutkiewicz, Z. Kosturkiewicz, M. Szafran, Journal of Molecular Structure, 889 (2008) 286-296.
[162] K. Nakamoto, Handbook of Vibrational Spectroscopy, (2006).
[163] M. Nicol, J. F. Durana, The Journal of Chemical Physics, 54 (1971) 1436-1440.
[164] V. M. Longo, A. T. d. Figueiredo, A. B. Campos, J. W. Espinosa, A. C. Hernandes, C. Taft, J. R. Sambrano, J. A. Varela, E. Longo, The Journal of Physical Chemistry A, 112 (2008) 8920-8928.
[165] M. Liegeois-Duyckaerts, P. Tarte, Spectrochimica Acta Part A: Molecular Spectroscopy, 28 (1972) 2037-2051.
[166] A. P. A. Marques, M. T. S. Tanaka, E. Longo, E. R. Leite, I. L. V. Rosa, Journal of Fluorescence, 21 (2011) 893-899.
[167] F. D. Chattaway, F. E. Ray, Journal of the Chemical Society, Transactions, 119 (1921) 34-37.
[168] C. Curtis, A. Tharp, Journal of the American Ceramic Society, 42 (1959) 151-156.
[169] J. Bernard B áHeyns, Journal of the Chemical Society, Dalton Transactions, 6 (1990) 1951-1956.
[170] H. Papazian, P. Pizzolato, J. Patrick, Journal of the American Ceramic Society, 54 (1971) 250-254.
[171] K. Nusrath, K. Muraleedharan, Journal of Analytical and Applied Pyrolysis, 120 (2016) 379-388.

[172] R. K. Tamrakar, D. P. Bisen, N. Brahme, Journal of Radiation Research and Applied Sciences, 7 (2014) 550-559.
[173] R. K. Tamrakar, D. P. Bisen, I. P. Sahu, N. Brahme, Journal of Radiation Research and Applied Sciences, 7 (2014) 417-429.
[174] S. Pezeshkpour, A. Z. Abdullah, B. Salamatinia, B. A. Horri, Ceramics International, 43 (2017) 7123-7135.
[175] Y. S. Khadar, A. Balamurugan, V. Devarajan, R. Subramanian, Oriental Journal of Chemistry, 33 (2017) 2405-2411.
[176] A. Arabaci, Ceramics International, 41 (2015) 5836-5842.

CURRICULUM VITAE

PERSONAL INFORMATION		
Name, Surname	Giedrė Gaidamavičienė	
Date of birth	1991-02-09	
Address	Architektų str. 91-49, Vilnius	
Phone number	+37065639452	
E-mail	giedre.prievelyte@gmail.com	
ACADEMIC EDUCATION		
2010 – 2014	Bachelor of Science in Chemistry, Vilnius University	
2014 – 2016	Master of Science in Chemistry, Vilnius University	
ACADEMIC AFFILIATIONS		
2017-09 – 2019-05	Laboratory of General and Inorganic Chemistry, Vilnius University	Junior specialist
2019-06 – to date	Laboratory of General and Inorganic Chemistry, Vilnius University	Laboratory assistant
TRAINING SCHOOLS		
2016-10-17 – 2016-10-21	Training of general competencies of young researchers	
2017-08-27 – 2017-08-31	19th international school Advanced materials and technologies, Palanga, Lithuania	
2018-08-27 – 2018-08-31	20th international school Advanced materials and technologies, Palanga, Lithuania	
2019-08-19 – 2019-08-23	21st international school Advanced materials and technologies, Palanga, Lithuania	
ADDITIONAL ACTIVITIES		
2019-09 – to date	Coordinator of Vilnius University, Faculty of Chemistry and Geosciences for Lithuanian student schools laboratory practices.	

SANTRAUKA

ĮVADAS

Pastaraisiais metais, daugiakomponentės oksidinės medžiagos, pasižyminčios unikaliomis cheminėmis ir fizikinėmis savybėmis, pritraukė daugelio mokslininkų dėmesį. Šelito tipo junginiai, turintys tetragoninę kristalinę struktūrą, pasižymi įdomiomis savybėmis, kurios leidžia šiuos junginius pritaikyti įvairiose pramonės srityse: optoelektronikoje, scintiliatorių, katalizatorių, mikrobangų dažnio prietaisų ir liuminescencinių medžiagų gamyboje bei kieto kūno lazeriuose. [1-5]. Buvo pastebėta, kad derinant tokias medžiagas, gaunami mišrūs oksidai, kurie pasižymi patrauklesnėmis savybėmis nei individualūs junginiai [6, 7]. Kita vertus, tokių junginių sintezė yra sudėtinga ir kelia pagrįstus iššūkius daugeliui mokslininkų.

Tetragoninės kristalinės struktūros kalcio molibdatas, sužadintas UV spinduliuote 250 – 320 nm bangų ilgio intervale, pasižymi savybe skleisti mėlynos, žalios ir oranžinės spalvos šviesą. Tokie junginiai, legiruoti retųjų žemių elementais (Eu^{3+}, Tb^{3+}) [8, 9], gali būti pritaikyti pažangaus apšvietimo ir ekranų gamyboje. Kalcio molibdatas legiruotas europio jonais pasižymi intensyvia raudonos spalvos liuminescencija [10]. Į tokią struktūrą įvedant krūvį kompensuojančias šarminių metalų priemaišas galima sustiprinti šių junginių optines savybes [11]. Kita vertus, tokių medžiagų liuminescencinės savybės yra taip pat glaudžiai susijusios ir su dalelių morfologija. Sferinės formos dalelės sumažina šviesos išbarstymą ir dėl tankios sanglaudos, leidžia susiformuoti tankiems fosforų sluoksniams [12].

Kiekvienais metais dėl labai įvairių priežasčių energijos poreikiai ženkliai didėja. Atsižvelgiant į ekologines problemas, naujų, efektyvių bei draugiškų aplinkai energijos šaltinių kūrimas įgauna vis didesnį pagreitį. Pastaruoju metu, išskirtinis dėmesys yra skiriamas kieto oksido kuro elementams, kurie jau dabar naudojami kaip „švarios“ energijos šaltiniai. Šie kuro elementai pasižymi aukštu deguonies jonų laidumu, cheminiu bei terminiu stabilumu, maža tarša ir dideliu efektyvumu lyginant su kitų tipų kuro elementais. Siekiant padidinti jų našumą, kieto oksido kuro elementai gali būti kombinuojami su garo turbinomis [13-15]. Lantano molibdatas ir cerio oksidas legiruotas gadoliniu pasižymi aukštu joniniu laidumu, tankia keramika ir neigiamu elektroniniu laidumu [16-19]. Dėl šių savybių, jie gali būti naudojami dujų jutikliuose, deguonies siurbliuose bei kieto oksido kuro

elementuose kaip kietieji elektrolitai. Yra žinoma, kad tokių junginių struktūra ir paviršiaus morfologija stipriai priklauso nuo sintezės būdo, kuris lemia skirtingas gautojo produkto chemines bei fizikines savybes.

Norint gauti aukštos kokybės homogeniškas medžiagas, būtina atidžiai parinkti sintezės metodą, bei įvertinti jo parametrus. Mokslinėje literatūroje yra gausu sintezės metodų, kurie buvo taikomi daugiakomponenčių medžiagų gamyboje. Net pažangiausi būdai, kurie reikalauja griežtų sąlygų ar papildomų sintezės etapų dažniausiai lemia prastą medžiagų homogeniškumą, žemą kristališkumą, priemaišų atsiradimą ir neleidžia susidaryti tankiai keramikai. Dėl šių priežasčių labai svarbu pritaikyti tokių medžiagų gavimui pigų, greitą bei ekologišką sintezės metodą, kuris leistų kontroliuoti galutinių medžiagų fazinį grynumą, morfologiją bei dalelių dydį. Vandeninė zolių-gelių sintezė suteikia galimybę kontroliuoti įvairius jos parametrus tokius, kaip pH, temperatūra, koncentracija, laikas ir kt. Toks platus metodo universalumas atveria duris puikiai galutinės keramikos struktūros bei morfologijos kontrolei.

Atsižvelgiant į tai, šio disertacinio darbo tikslas buvo vandeniniu zolių-gelių metodu susintetinti daugiakomponenčius oksidus bei ištirti gautųjų gelių terminio skilimo mechanizmą. Siekiant įgyvendinti šį tikslą, buvo suformuluoti tokie uždaviniai:

1. Vandeniniu zolių-gelių sintezės metodu susintetinti vienfazius kristalinius daugiakomponenčius $Ca_{1-x}Sr_xMoO_4$, $M_{0,05}Eu_{0,05}Ca_{0,9}MoO_4$ (M=Li, Na, K, Rb, Cs), $La_2Mo_2O_9$ ir $Ce_{0,9}Gd_{0,1}O_{1,95}$ oksidus.
2. Termogravimetrinės ir diferencinės skenuojančiosios kalorimetrinės analizės pagalba nustatyti susintetintų gelių terminio skilimo mechanizmus.
3. Pasitelkiant Rentgeno spindulių difrakcinę analizę (XRD), skenuojančiąją elektroninę mikroskopiją (SEM) ir infraraudonąją spektroskopiją (FTIR) nustatyti susintetintų junginių kristalinę struktūrą bei paviršiaus morfologijos pokyčius esant skirtingoms gelio mėginių kaitinimo temperatūroms.
4. Ramano spektroskopijos metodu apskaičiuoti molinę $Ca_{1-x}Sr_xMoO_4$ sistemos sudėtį.
5. Ištirti $M_{0,05}Eu_{0,05}Ca_{0,9}MoO_4$ keramikų optinių savybių ryšį su kristalitų augimo tendencijomis.
6. Nustatyti $La_2Mo_2O_9$ keramikos elektrines savybes.

7. Diferencinės kalorimetrinės analizės metodu įvertinti $La_2Mo_2O_9$ keramikos fazinio virsmo pradžios ir pabaigos temperatūras iš monoklininės α-fazės į aukštatemperatūrinę kubinę β-fazę ir atvirkščiai.

Darbo rezultatai, leidžia ginti šiuos disertacijos ginamuosius teiginius:

1. Pirmą kartą vyno rūgštis buvo sėkmingai panaudota vandeniniu zolių-gelių metodu sintetinant $La_2Mo_2O_9$, $Ca_{1-x}Sr_xMoO_4$ ir $M_{0,05}Eu_{0,05}Ca_{0,9}MoO_4$ (M=Li, Na, K, Rb ir Cs) daugiakomponenčius oksidus.
2. Terminės analizės (TGA–DSC) metodas yra tinkamas įrankis La–Mo–O, Ca–Sr–Mo–O ir M–Eu–Ca–Mo–O tartratinių gelių terminio skilimo bei galutinių $La_2Mo_2O_9$, $Ca_{1-x}Sr_xMoO_4$ ir $M_{0,05}Eu_{0,05}Ca_{0,9}MoO_4$ (M=Li, Na, K, Rb, ir Cs) junginių kristalizacijos tyrimams.
3. Kompleksus su metalais sudarančio reagento prigimtis lemia gautųjų kristalinių junginių morfologinius, struktūrinius ypatumus bei jų optines ir elektrines savybes.
4. Gelių skilimo mechanizmas yra tiesiogiai susijęs su vyno rūgšties ir atskirų metalų tartratų termine degradacija.
5. Susintetintų gelių kaitinimo atmosfera neturi įtakos nei jų skilimo procesams, nei galutinių kristalinių fazių formavimosi ypatumams.
6. Terminės analizės derinimas su papildomais medžiagų apibūdinimo metodais yra parankus įrankis įgalinantis tirti galutinių kristalinių daugiakomponenčių oksidų cheminių ir fizikinių savybių tarpusavio ryšius.

EKSPERIMENTO METODIKA

Visi šiame darbe aprašyti junginiai buvo gauti panaudojus vandeninį zolių-gelių sintezės metodą. Šiuo atveju, pateikiamos tik optimizuotos sintezių sąlygos.

$CaMoO_4$, $SrMoO_4$ ir mišrių $Ca_{1-x}Sr_xMoO_4$ junginių sintezė

Stechiometriniai $Ca(NO_3)_2 \cdot 4H_2O$ ir/ar $Sr(NO_3)_2$ kiekiai buvo ištirpinti 40 ml dejonizuoto vandens. Tuo tarpu, kitoje stiklinėlėje pasiruošta 30 ml dejonizuoto vandens, 1 ml koncentruoto amoniako ir MoO_3 vandeninis tirpalas. Į reakcijos mišinį su ištirpusiais druskų nitratais buvo subertas keturis kartus didesnis vyno rūgšties kiekis, lyginant jį su molibdeno kiekiu. Ištirpus vyno rūgščiai, MoO_3 vandeninis tirpalas supiltas į pirmąją stiklinėlę.

Susidaręs skaidrus reakcijos mišinys toliau buvo garintas ant magnetinės maišyklės toje pačioje 70 °C temperatūroje. Gautasis gelis džiovintas 120 °C temperatūroje džiovinimo spintoje apie 3 valandas. Šviesiai rudos spalvos gelis sutrintas agatinėje grūstuvėje, o gautieji milteliai papildomai kaitinti 350 °C, 400 °C, 500 °C, 600 °C ir 700 °C temperatūrose 5 valandas. Temperatūros kėlimo greitis – 1 °C/min.

$M_{0,05}Eu_{0,05}Ca_{0,9}MoO_4$ (M=Li, Na, K, Rb ir Cs) junginių sintezė

Pradinėje sintezės stadijoje, stechiometrinis MoO_3 kiekis buvo ištirpintas mišinyje sudarytame iš 25 ml dejonizuoto vandens ir 1 ml koncentruoto amoniako. Tirpalas maišytas magnetine maišykle 90 °C temperatūroje. Keturis kartus didesnis vyno rūgšties stechiometrinis kiekis subertas tiesiai į reakcijos mišinį siekiant išvengti nuosėdų susidarymo. Ištirpus rūgščiai, į reakcijos mišinį subertas stechiometrinis kiekis $Ca(NO_3)_2{\cdot}4H_2O$. Po to, subertas reikiamas kiekis šarminio metalo nitrato ($LiNO_3$, $NaNO_3$, KNO_3, $RbNO_3$ ar $CsNO_3$). Galiausiai, įdėta Eu_2O_3 ir 6 ml koncentruotos azoto rūgšties. Susidaręs skaidrus tirpalas garintas ant magnetinės maišyklės palaikant tą pačią kaitinimo temperatūrą. Gelis džiovintas 120 °C temperatūroje apie 2 valandas. Sausas tartratinis gelis susmulkintas agatinėje grūstuvėje ir kaitintas 350 °C, 400 °C, 500 °C, 600 °C, 700 °C, 800 °C, 900 °C ir 1000 °C temperatūrose 5 valandas. Temperatūros kėlimo greitis – 1 °C/min.

$La_2Mo_2O_9$ keramikos sintezė

Pirmiausia, 80 °C temperatūroje stechiometrinis MoO_3 kiekis buvo ištirpintas mišinyje, sudarytame iš 25 ml dejonizuoto vandens ir 0,5 ml koncentruoto amoniako. Vyno rūgštis suberta tiesiai į reakcijos mišinį nekeičiant kitų sintezės sąlygų. Pilnai ištirpus vyno rūgščiai, į reakcijos mišinį supiltas La_2O_3 kartu su 6 ml koncentruotos azoto rūgšties. Gautas skaidrus tirpalas toliau garintas ant magnetinės maišyklės toje pačioje temperatūroje. Skaidrus, gelsvos spalvos zolis džiovintas 120 °C džiovinimo spintoje apie 2 valandas. Susidaręs tamsiai mėlynos spalvos gelis papildomai kaitintas 500 °C, 550 °C, 600 °C, 800 °C ir 1000 °C temperatūrose 5 valandas. Temperatūros kėlimo greitis – 1 °C/min. Išdžiovinti gelio milteliai, kaitinti 1000 °C temperatūroje, papildomai sutrinti ir suspausti į tabletę. Ji kaitinta 1200 °C temperatūroje 5 valandas. Temperatūros kėlimo greitis – 5 °C/min.

$Ce_{0,9}Gd_{0,1}O_{1,95}$ keramikos sintezė

Pradžioje, stechiometriniai kiekiai $Gd(CH_3COO)_3 \cdot 4H_2O$ ir $Ce(CH_3COO)_4 \cdot H_2O$ ištirpinti dejonizuoto vandens ir acto rūgšties mišinyje 50 °C temperatūroje. Oksalo rūgštis suberiama tiesiai į reakcijos mišinį nekeičiant sintezės sąlygų. Po to, mišinio pH padidintas iki 9,0 lėtai sulašinus koncentruotą amoniaką. Iškritusios baltos nuosėdos buvo atskirtos nuo tirpalo gravitacinio filtravimo būdu ir džiovintos 100 °C temperatūroje 24 valandas. Gautieji baltos spalvos milteliai kaitinti 900 °C, 950 °C, 1000 °C, 1100 °C ir 1200 °C temperatūrose 5 valandas. Temperatūros kėlimo greitis – 1 °C/min.

Tyrimų aparatūra ir metodai

Termogravimetrinė ir diferencinė skenuojanti kalorimetrinė analizė (TGA–DSC) buvo atlikta naudojant PerkinElmer STA 6000 prietaisą. Tyrimo metu mėginio masė atitiko 10 mg. Temperatūros intervalas – nuo 30 °C iki 950 °C; kaitinimo atmosfera – oras arba azoto dujos; temperatūros kėlimo greitis – 20 °C/min. Susintetintų junginių Rentgeno spindulių difrakcinė (XRD) analizė atlikta naudojant Rigaku MiniFlex II difraktometrą su vario anodu (Cu K_α, λ=1,5418 Å). $\theta/2\theta$ difraktogramos užrašytos matuojant 1,5 °/min greičiu intervale nuo 5 iki 80 °. Rietveld'o struktūros patikslinimo analizė vykdyta naudojant X'Pert HighScore Plus programą. Ši analizė buvo atlikta tikslinant kristalinių gardelių parametrus, fono kontūrus ir XRD smailių profilio parametrus. Siekiant įvertinti susintetintų junginių paviršiaus morfologiją buvo naudoti skenuojantys elektroniniai (SEM) – Hitachi TM3000 ir Hitachi SU-70 mikroskopai. Infraraudonosios spektroskopijos (FTIR) analizė atlikta su PerkinElmer FTIR Frontier spektrometru. Ramano spektroskopija vykdyta su WiTec Alpha 300 R prietaisu naudojant 532 nm bangos ilgio sužadinimo lazerį. Kalcio molibdato, legiruoto šarminiais metalais ir europiu, mėginių optinių savybių matavimai atlikti PerkinElmer LS-55 fluorimetru. Galiausiai, lantano molibdato elektrinės savybės išmatuotos naudojant dvi skirtingas impedanso spektroskopijos įrangas naujai sukurtu impedanso spektrometru [155, 156].

REZULTATŲ APTARIMAS

$CaMoO_4$, $SrMoO_4$ ir mišrių $Ca_{1-x}Sr_xMoO_4$ oksidų analizė

Ca–Sr–Mo–O tartratinių gelių terminės analizės rezultatai parodė, jog skilimo mechanizmas išlieka labai panašus nepriklausomai nuo stroncio molinės koncentracijos junginyje. Tartratinio gelio, kuriame kalcio molinė

dalis junginyje – 0,5 mol%, TGA–DTG–DSC kreivės pateiktos 20 pav. 40 psl. Pirmasis masės netekties etapas, kuris įvyksta 30 – 143 °C temperatūrų intervale, yra susijęs su absorbuotų vandens molekulių pasišalinimu iš mėginio. Stebimas masės sumažėjimas svyruoja tarp 2,4 – 3,8 %, priklausomai nuo molinės junginio sudėties. Didžiausias masės netekties etapas (~35 %) vyksta 144 – 295 °C temperatūrų intervale ir yra susijęs su perteklinės vyno rūgšties dimero skilimu. Šiame etape vyksta du dujų išsiskyrimo procesai: egzoterminis, stebimas CO_2 išsiskyrimo metu, bei endoterminis, vykstant piruvato rūgšties garavimui. Plati endoterminė smailė esanti ties 295 – 395 °C yra siejama su galutinio produkto kristalizacijos pradžia. Taip pat, šiame temperatūrų intervale, prasideda metalų tartratų skilimas iki CO_2 ir H_2O junginių. Nuo 520 °C iki 820 °C įvyksta baigtinis metalų tartratų skilimas. Šio proceso metu likutinis $(C_2H_2)_{4-q}$ fragmentas suskyla iki anglies dioksido ir vandens molekulių. Visas terminio skilimo mechanizmas aprašytas 4 – 11 formulėmis ir yra pateiktas 39 ir 40 psl.

$CaMoO_4$ ir $SrMoO_4$ mėginių, kaitintų skirtingose temperatūrose, XRD analizės rezultatai yra pateikti 21 pav. 41 psl. Šie duomenys parodė, kad geliai, džiovinti 120 °C temperatūroje, pasižymi amorfine struktūra. Iš gautųjų rezultatų matyti, kad vienfaziai, tetragoninę kristalinę struktūrą turintys molibdatai, susiformuoja jau 350 °C temperatūroje. Šie rezultatai puikiai sutampa su terminės analizės metu gautaisiais duomenimis, kurie įrodė, jog kristalizacijos procesas prasideda 295 °C temperatūroje. Mėginiuose, kaitintuose aukštesnėse temperatūrose, jokie faziniai pokyčiai nėra stebimi. Mišrių $Ca_{1-x}Sr_xMoO_4$ oksidų XRD analizės duomenys patvirtino, kad vienfazės, tetragoninės kristalinės fazės susidarymas vyksta tokioje pat temperatūroje, kaip ir individualių oksidų. Be to, buvo pastebėta, kad didinant Sr^{2+} kiekį okside, difrakciniai atspindžiai slenkasi link mažesnės vertės kampų. Šis poslinkis yra tiesiogiai susijęs su gardelės parametrų ir jos tūrio didėjimu. Pasitelkus Rietveld'o struktūros patikslinimo analizę buvo nustatytas tiesinę priklausomybę atitinkantis gardelės parametrų pokytis nuo Ca^{2+} molinės dalies okside (22 pav. 42 psl.).

Siekiant nustatyti gautosios keramikos paviršiaus morfologiją, buvo atlikta SEM analizė, o rezultatai yra pateikti 23 ir 24 pav. 43 psl. Iš šios analizės duomenų, buvo nustatyta, kad mėginių, kaitintų 400 °C, 500 °C ir 600 °C temperatūrose, paviršius yra sudarytas iš aglomeravusių, netaisyklingos formos, panašaus dydžio dalelių. Apskaičiuotas kristalitų dydis svyravo tarp 11 – 47 nm. Tokio mažo dydžio dalelių susidarymas gali būti siejamas su CO_2 dujų išsiskyrimu, kuris galimai sulėtina kristalizacijos procesą. Ryškus dalelių

dydžio padidėjimas stebimas mėginiuose, kaitintuose 700 °C temperatūroje. Šie rezultatai gerai sutampa su Rietveld'o analizės duomenimis, kuomet pastebėtas beveik dvigubas kristalitų dydžio padidėjimas (~80 nm). Panašios dalelių bei kristalitų augimo tendencijos stebėtos visais susintetintų mėginių atvejais. Atlikta dalelių dydžio pasiskirstymo analizė parodė, jog didinant Sr^{2+} kiekį $Ca_{1-x}Sr_xMoO_4$ okside, dalelių pasiskirstymo intervalas platėja, o dalelės didėja.

FTIR analizės metu gautieji rezultatai yra pateikti 26 pav. 45 psl. Gelių, džiovintų 120 °C temperatūroje, spektre stebimos absorbcijos juostos yra būdingos vyno rūgšties funkcinėms grupėms. Mišrių oksidų, kaitintų 400 °C temperatūroje, FTIR spektruose, srityje nuo 1750 cm^{-1} iki 1000 cm^{-1}, buvo stebimi organinės prigimties medžiagoms būdingi virpesiai, kurie įrodo metalų tartratų egzistavimą mėginyje.

Atlikus Ramano spektroskopijos analizę pastebėta, jog A_g virpesys, būdingas ryšiui tarp MoO_4^{2-} tetraedro ir M^{2+} jono, didinant Sr^{2+} kiekį mėginiuose, slenkasi link mažesnio bangos skaičiaus. Šis smailės poslinkis leido apskaičiuoti tikslią mišrių $Ca_{1-x}Sr_xMoO_4$ oksidų molinę sudėtį. Gautieji rezultatai pateikti 28 pav. 48 psl. Apskaičiuotas nuokrypis nuo teorinės sudėties nesiekė 0,32 %. Tai leidžia daryti išvadą, jog vandeninis zolių-gelių metodas yra tinkamas tikslios molinės sudėties junginių sintezei.

$M_{0,05}Eu_{0,05}Ca_{0,9}MoO_4$ (M=Li, Na, K, Rb, Cs) oksidų analizė

Junginių, atitinkančių bendrą formulę $M_{0,05}Eu_{0,05}Ca_{0,9}MoO_4$, terminės analizės rezultatai parodė, jog terminio skilimo mechanizmas yra labai panašus į prieš tai aprašytąjį Ca–Sr–Mo–O tartratinių gelių atvejį. K–Eu–Ca–Mo–O tartratinio gelio TGA–DTG–DSC kreivės yra pateiktos 29 pav. 49 psl. Pirmasis masės netekties etapas, vykstantis iki 142 °C, yra lydimas endoterminės smailės prigimties ir susijęs su absorbuotų vandens molekulių pasišalinimu iš gelio. Didžiausias masės pokyčio etapas (36 – 43 %) stebimas 143 – 295 °C temperatūrų intervale. Šio proceso metu perteklinė vyno rūgšties skyla iki CO, CO_2 ir žemesnės molekulinės masės rūgščių [167]. Pastebėta, kad egzoterminis procesas vykstantis nuo 143 °C iki 177 °C temperatūros, yra susijęs su šarminio metalo prigimtimi ir lakių metalų tartratų produktų pašalinimu. Suminis endoterminis procesas, vykstantis 295 – 510 °C temperatūrų intervale, siejamas su baigtiniu metalų tartratų skilimu iki CO_2 ir H_2O junginių. Šio proceso metu, masės netektis svyruoja tarp 18,83 – 24,24 % priklausomai nuo šarminio metalo prigimties. Svarbu paminėti, jog 300 °C temperatūroje, kartu su tartratų skilimu, prasideda

endoterminis galutinių produktų kristalizacijos procesas. Paskutinis masės netekties etapas yra susijęs su susidariusios neorganinės anglies degimu. Šis degimas yra sudarytas iš kelių procesų. Pirmasis procesas, lydimas endoterminės smailės ties 627 °C, yra siejamas su vandens molekulių pasišalinimu. Antrasis – egzoterminis, ties 676 °C – susijęs su CO_2 molekulių išsiskyrimu iš mėginio. Galiausiai, 785 – 950 °C temperatūrų intervale stebimas DSC kreivės kilimas (endoterminis procesas) įrodo tolimesnį kristalitų augimą. Aprašyti pagrindiniai skilimo aspektai buvo stebimi visuose paruoštuose mėginiuose, nepriklausomai nuo šarminio metalo prigimties.

Siekiant įvertinti skilimo procesus ir lakių komponentų masės pokyčių ypatumus, TGA–DSC analizė buvo atlikta inertinės azoto atmosferos sąlygomis. Gautieji rezultatai neparodė jokių esminių pokyčių, vykstant skilimo procesams iki 600 °C. Stabili mėginio masė buvo pasiekta aukštesnėje temperatūroje nei kaitinant oksiduojančioje oro atmosferoje.

M–Eu–Ca–Mo–O gelių, kaitintų skirtingose temperatūrose, XRD tyrimo rezultatai įrodė, kad visais atvejais, jau nuo 350 °C temperatūros susiformuoja $CaMoO_4$ būdingos tetragoninės kristalinės struktūros junginiai (32 ir 33 pav. 53 ir 54 psl.). Šie duomenys puikiai sutampa su gautaisiais terminės analizės duomenimis, kuomet kristalizacijos proceso pradžia nustatyta esant 300 °C temperatūrai. Verta paminėti, kad atlikta Rietveld'o struktūros patikslinimo analizė parodė skirtingas bei įdomias kristalitų augimo tendencijas (34 pav. 54 psl.). Kristalitų dydžio nenutrūkstamas augimas stebėtas vieninteliame $Na_{0,05}Eu_{0,05}Ca_{0,9}MoO_4$ mėginyje. Tuo tarpu, ličio ir cezio atvejais, nuo 800 °C buvo stebimas kristalitų dydžio mažėjimas, o kalio ir rubidžio atvejais – nuo 700 °C. Netikėtas kristalitų dydžio sumažėjimas gali būti siejamas su Eu_2O_3 kristalizacijos procesu [168].

Atlikta SEM analizė neparodė jokių esminių paviršiaus morfologijos pasikeitimų. Tiek kalio, tiek rubidžio atveju, miltelių paviršius buvo sudarytas iš aglomeravusių, sferinę formą primenančių dalelių, kurių dydis svyravo tarp 0,2 – 1,2 μm ir 0,2 – 1,8 μm, atitinkamai (36 pav. 55 psl.). FTIR analizės rezultatai parodė, jog nuo 800 °C temperatūros, nėra aptinkami organiniams junginiams būdingi virpesiai 4000 – 1000 cm^{-1} intervale. Tai gerai sutampa su terminės analizės rezultatais, kuomet nustatytasis tartratų skilimas vyksta iki 785 °C temperatūros (38 pav. 57 psl.).

Įdomūs rezultatai buvo gauti tiriant optinių savybių priklausomybę nuo kristalitų dydžio. Nustatyta, kad apskaičiuota $^5D_0 \rightarrow {}^7F_2$ ir $^5D_0 \rightarrow {}^7F_1$ smailių intensyvumų santykio R vertė, esant skirtingiems įterptiniams šarminiams metalams, mėginiuose kaitintuose 600 °C temperatūroje, pasižymėjo labai

panašia į kristalitų augimo tendencija. Taigi, galima teigti, kad iš optinių savybių duomenų, atliktų žemesnėje temperatūroje, apskaičiuotasis R dydis, atspindi kristalitų augimo ypatumus aukštesnėse temperatūrose.

$La_2Mo_2O_9$ keramikos analizė

Lantano molibdato terminio skilimo mechanizmą galima suskirstyti į šešis pagrindinius etapus (39 pav. 59 psl.). Pirmasis masės netekties etapas, kurio metu, mėginio masė sumažėja 4,3 %, vyksta iki 147 °C temperatūros. Užfiksuotas endoterminis procesas liudija apie absorbuotų vandens molekulių garavimą iš tiriamojo mėginio. Keliant temperatūrą iki 300 °C, įvyksta galutinis perteklinės vyno rūgšties skilimas iki CO, CO_2 ir mažesnės molekulinės masės rūgščių, kurio metu, mėginys netenka 30,2 % likutinės masės. Egzoterminė smailė, esanti ties 150 °C, yra susijusi su anglies monoksido ir dioksido pasišalinimu iš mėginio. Tuo tarpu, šiek tiek aukštesnėje temperatūroje įvyksta acto rūgšties garavimas, kuris yra lydimas endoterminio proceso. Temperatūrų intervale tarp 220 – 300 °C vyksta pilnutinis susidariusių vyno rūgšties dimerų skilimas. DSC kreivėje stebimas endoterminis procesas yra susijęs su piruvato rūgšties garavimu, o egzoterminis procesas rodo CO_2 molekulių pasišalinimą iš junginio. Tolimesnis etapas, vykstantis 301 – 520 °C temperatūrose yra susijęs su metalų tartratų skilimu. DSC kreivėje yra stebimi du procesai: endoterminis procesas susijęs su vandens molekulių garavimu, o egzoterminis – su CO_2 dujų pašalinimu iš mėginio. Šio etapo metu masė sumažėja apie 12 %. Virš 520 °C, prasideda galutinio produkto kristalizacija į aukštatemperatūrinę kubinę fazę. Paskutinis masės netekties etapas, kurio metu netenkama 13,3 % masės, yra susijęs su neorganinės anglies degimu. Nuo 680 °C temperatūros, mėginio masė nebekinta, tačiau DSC kreivėje stebimas egzoterminis procesas rodo toliau vykstančius kristalizacijos procesus ir tolimesnį dalelių augimą. Formulės, aprašančios detalų La–Mo–O tartratinio gelio terminio skilimo mechanizmą yra pateiktos 58 – 60 psl.

XRD analizės metu, gautieji rezultatai parodė, kad vienfazis, monoklininės kristalinės struktūros lantano molibdatas susidaro jau 550 °C temperatūroje. Aukštesnėse temperatūrose kaitintų mėginių difraktogramos neparodė esminių pokyčių struktūrinėje srityje ir puikiai atitiko monoklininės lantano molibdato fazės duomenis iš ICSD duomenų bazės (42 pav. 62 psl.). Mėginys, kaitintas 500 °C temperatūroje, pasižymėjo amorfinėms medžiagoms būdinga struktūra, tačiau, buvo aptiktas (404) plokštumos atspindys, kuris įrodo, jog šioje temperatūroje yra prasidėjusi galutinio produkto kristalizacija. Šis

nuokrypis nuo TGA–DSC duomenų galėjo atsirasti dėl skirtingos mėginio masės bei temperatūros kėlimo greičio. Rietveld'o struktūros patikslinimo analizė parodė, kad kristalitų dydis auga iki 800 °C temperatūros. Gautieji rezultatai yra labai svarbūs tikslaus fazinio virsmo nustatymui, nes vykstantis kristalizacijos procesas gali paveikti fazinio virsmo metu išskiriamos ar sugeriamos šilumos kiekį.

DSC analizė buvo panaudota siekiant nustatyti lantano molibdatui būdingą fazinį virsmą. Atlikus rezultatų analizę, buvo nustatyta, jog fazinis virsmas iš α-fazės į β-fazę vyksta 555 – 570 °C temperatūrų intervale. Priešingas procesas yra stebimas 538 – 514 °C temperatūrų intervale. Šie rezultatai rodo, kad fazinis virsmas į kubinę fazę vyksta aukštesnėje temperatūroje, nei grįžtamasis procesas.

Siekiant įvertinti gautosios keramikos paviršiaus morfologiją, SEM analizė buvo atlikta mėginiams kaitintiems 500 °C, 550 °C, 600 °C ir 1200 °C temperatūrose (44 pav. 64 psl.). Buvo nustatyta, kad mėginiai, kaitinti iki 600 °C, pasižymi panašia morfologija. Gautoji keramika yra sudaryta iš aglomeratų, kurių paviršiuje matomos 200 – 500 nm dydžio dalelės. Ženklus morfologijos pokytis yra stebimas 600 °C temperatūroje. Šiuo atveju, porėtas miltelių paviršius yra sudarytas iš 100 – 200 nm dydžio, sferinės ar elipsinės formos dalelių. Galiausiai, tirta keramikos, kaitintos 1200 °C temperatūroje, morfologija, kuri yra labai svarbi atliekant tolimesnius elektrinių savybių tyrimus. Gautieji duomenys parodė, kad tabletės paviršius yra sudarytas iš netaisyklingos formos, 100 – 200 μm dydžio sukepusių dalelių. Taigi, galima teigti, kad vandeninis zolių-gelių metodas yra tinkamas tankios $La_2Mo_2O_9$ keramikos sintezei.

Atlikta impedanso spektroskopijos analizė parodė, kad joninis laidumas stipriai padidėja 517 – 537 °C temperatūrų intervale. Šie rezultatai puikiai sutampa, su nustatyta fazinio virsmo temperatūra iš DSC analizės duomenų. Mažesnė fazinio virsmo aktyvacijos energija į monoklininę fazę (1,01 eV) rodo, kad šis virsmas vyksta šiek tiek palankesnėmis sąlygomis, nei priešingas procesas (1,09 eV) (45 pav. 65 psl.).

$Ce_{0,9}Gd_{0,1}O_{1,95}$ keramikos analizė

Cerio oksido legiruoto gadoliniu sintezė buvo atliekama panaudojant oksalo rūgštį, kaip kompleksus su metalais sudarantį reagentą. Gautojo gelio terminė analizė parodė, kad šio junginio skilimas yra sudarytas iš keturių pagrindinių etapų. Pirmasis masės sumažėjimas (2,6 %) įvyksta iki 140 °C temperatūros. DSC kreivėje stebimas endoterminis efektas yra susijęs su

absorbuotos drėgmės pasišalinimu. Antrasis masės netekties etapas yra susijęs su pilnu priemaišinių amonio oksalato druskų skilimu ir yra lydimas dviejų greta vykstančių procesų: egzoterminis signalas DSC kreivėje yra stebimas dėl CO, CO_2 ir NH_3 dujų garavimo [170], endoterminis – dėl vandens molekulių netekties. Šių procesų metu yra netenkama 7,0 % likutinės mėginio masės. Didžiausias masės sumažėjimas (38,0 %) yra priskiriamas cerio ir gadolinio oksalatų skilimui 234 – 395 °C temperatūrų intervale [171]. Šiame etape yra stebimi du, kartu vykstantys, egzoterminiai procesai, kurie lėmė asimetrišką smailės formą. Pirmiausiai, oksalatai skyla iki CO_2 ir CO molekulių. Iš karto susidarant anglies monoksido molekulėms, vyksta jų pilnutinis degimas iki CO_2 dujų. Egzoterminis procesas vykstantis iki 650 °C temperatūros susijęs su paskutiniu masės netekties etapu, kurio metu netenkama 1,2 % mėginio masės. Šio proceso metu įvyksta viso skilimo metu susidariusios neorganinės anglies degimas. Toliau keliant temperatūrą iki 950 °C mėginio masė išlieka stabili, nors DSC kreivėje stebimas egzoterminis efektas yra susijęs su tolimesniais kristalizaciniais procesais bei kristalitų augimu (46 pav. 66 psl.).

XRD analizės duomenys parodė, jog 100 °C temperatūroje džiovintas mėginys pasižymi amorfine struktūra. Mėginių, kaitintų 900 – 1200 °C temperatūrose, rezultatai patvirtino, jog visais atvejais buvo gauti vienfaziai, kubinę fluorito tipo struktūrą turintys oksidai (47 pav. 68 psl.). Šie gautieji rezultatai leidžia teigti, jog 900 °C temperatūra yra pakankama norint gauti gryną $Ce_{0,9}Gd_{0,1}O_{1,95}$ keramiką. Rietveld'o struktūros patikslinimo analizės skaičiavimai parodė, kad visame kaitinimo intervale kristalitų dydis išliko labai panašus. Tai įrodo, jog gautasis GDC oksidas pasižymi geru terminiu stabilumu.

Iš gautųjų SEM nuotraukų matyti (49 pav. 70 psl.), kad mėginio, kaitinto 900 °C temperatūroje, paviršius yra sudarytas iš plokštelių formos dalelių, kurių dydis svyruoja nuo 100 nm iki 1 μm dydžio. Keliant temperatūrą iki 1200 °C, stebimas aiškus paviršiaus morfologijos pokytis. Aukštesnėse temperatūrose kaitintų miltelių paviršius yra sudarytas iš sferinę formą primenančių dalelių, kurių dydis svyruoja tarp 100 – 600 nm.

Atlikus skirtingose temperatūrose kaitintų mėginių FTIR analizę, aiškiai matoma, kad 4000 – 1000 cm^{-1} intervale nėra aptinkami organinių junginių funkcinėms grupėms būdingi virpesiai. Intensyvios absorbcijos juostos ties 580 cm^{-1} ir 458 cm^{-1} yra priskiriamos Ce–O ir/ar Gd–O cheminių ryšių savitiesiems virpesiams [172-174]. Ryškus skirtumas matomas mėginio, kaitinto 1000 °C temperatūroje, FTIR spektre. Smailė, esanti ties 838 cm^{-1} yra

priskiriama tetraedrinėms grupėms būdingiems virpesiams. Absorbcijos juosta ties 820 cm^{-1} atitinka O–Ce–O ir/ar O–Gd–O ryšių vibracijoms būdingus virpesius [175], o likusieji – priklauso Ce–O ir/ar Gd–O ryšių vibracijoms (50 pav. 71 psl.) [176]. Šis skirtumas, tarp skirtingose temperatūrose kaitintų mėginių, yra susijęs su morfologiniais dalelių pokyčiais. Susidariusių sferinės formos dalelių paviršiaus ploto padidėjimas lėmė didesnę deguonis-metalas-deguonis ir metalas-deguonis virpesių koncentraciją.

Apibendrinant galima teigti, jog TGA–DTG–DSC, XRD, SEM ir FTIR analizių metu gautieji duomenys įrodė, kad vandeninis zolių-gelių sintezės metodas yra tinkamas vienfazio, kubinę kristalinę struktūrą turinčio $Ce_{0,9}Gd_{0,1}O_{1,95}$ junginio sintezei. Mėginiai, kaitinti aukštesnėje nei 1000 °C temperatūroje, pasižymėjo geru terminiu bei cheminiu stabilumu. Gautieji rezultatai yra svarbūs atliekant tolimesnius tyrimus, dėl galimo šių medžiagų platesnio pritaikymo kieto oksido kuro elementuose.

IŠVADOS

1. Pirmą kartą, panaudojant vandeninį zolių-gelių sintezės metodą ir vyno rūgštį, kaip kompleksus su metalais sudarantį reagentą, pavyko susintetinti homogeniškus La–Mo–O, Ca–Sr–Mo–O ir M–Eu–Ca–Mo–O (M=Li, Na, K, Rb, Cs) tartratinius gelius bei daugiakomponenčius $La_2Mo_2O_9$, $Ca_{1-x}Sr_xMoO_4$ ir $M_{0,05}Eu_{0,05}Ca_{0,9}MoO_4$ junginius.
2. Parodyta, jog terminės analizės metodas yra galingas įrankis leidžiantis tiksliai įvertinti susintetintų metaloorganinių junginių termino skilimo ir galutinių neorganinių fazių formavimosi mechanizmus.
3. Palyginus skirtingų kompleksus su metalais sudarančių reagentų įtaką vandeniniam zolių-gelių sintezės procesui nustatyta, jog gautųjų gelių terminis skilimas akivaizdžiai skiriasi, o tai nulemia galutinių junginių struktūrines ir paviršiaus morfologines ypatybes. Vyno rūgšties įtaka gautųjų gelių terminiam skilimui yra labai panaši nepriklausomai nuo sintetinamos metalų sistemos. Akivaizdu, jog šiuos panašumus labiausiai lemia molibdato (MoO_4^{2-}) anijono koordinavimo geba.
4. Iš DSC duomenų nustatyta, jog vyno rūgšties skilimas gelyje įvyksta iki 300 °C temperatūros. Tuo tarpu, metalų tartratai, dėl savo padidinto stabilumo, suskyla aukštesnėje temperatūroje susidarant stabilioms

neorganinių junginių kristalinėms fazėms ir lakiems organinių junginių skilimo produktams.

5. M–Eu–Ca–Mo–O tartratinių gelių terminis skilimas oro ir azoto dujų atmosferose iki 600 ^{o}C temperatūros vyksta identiškai. Galutinio junginio kristalizacijai kaitinimo atmosfera didelės įtakos neturi. Nustatyta, kad aukštesnėje nei 600 ^{o}C temperatūroje, deguonies atmosferoje, greičiau sudega neorganinės anglies likučiai nei azoto dujose.
6. Fotoliuminescenciniai $M_{0,05}Eu_{0,05}Ca_{0,9}MoO_4$ junginio matavimai parodė, jog kristalitų augimo mechanizmas nulemia gautąsias galutinio junginio optines charakteristikas ir yra susijęs su europio jonams būdingų perėjimų $^5D_0 \rightarrow {}^7F_2$ ir $^5D_0 \rightarrow {}^7F_1$ santykinio dydžio R verte.
7. Nustatyta, jog šarminio metalo prigimtis $M_{0,05}Eu_{0,05}Ca_{0,9}MoO_4$ okside nulemia skirtingą Eu_2O_3 pasiskirstymą $CaMoO_4$ sistemoje, kuris gali būti siejamas su skirtingu šarminių metalų aktyvumu 350 – 800 °C temperatūrų intervale.
8. DSC analizės pagalba nustatyta, jog $La_2Mo_2O_9$ keramikos fazinis virsmas iš α-fazės į β-fazę vyksta šiek tiek aukštesnėje temperatūroje (555 – 570 °C) nei priešingas procesas (514 – 538 °C). Nustatyta monoklininės fazės aktyvacijos energija buvo lygi 1,01 eV, o kubinės fazės – 1,09 eV. Tai rodo, jog žematemperatūrinė fazė yra stabilesnė.
9. Nustatyta, kad Ce–Gd–O oksalatinio gelio kaitinimo atmosfera turi įtakos galutinės $Ce_{0,9}Gd_{0,1}O_{1,95}$ keramikos struktūrinėms ir paviršiaus morfologinėms ypatybėms. Remiantis gautaisiais duomenimis, nustatyta, jog oras yra tinkamesnė kaitinimo aplinka GDC kristalizacijai ir dalelių augimui.
10. Iš Ramano spektroskopijos analizės rezultatų, pagal A_g virpesių smailės padėtį buvo apskaičiuota tiksli $Ca_{1-x}Sr_xMoO_4$ junginių molinė sudėtis. Šios smailės poslinkis link mažesnio bangos skaičiaus yra susijęs su kovalentinio ryšio silpnėjimu tarp MoO_4^{2-} tertraedro ir M^{2+} jono, kurį lemia didėjanti Sr^{2+} jonų koncentracija mėginyje. Apskaičiuotas nuokrypis nuo teorinės sudėties siekė ne daugiau nei 0,32 %. Remiantis FTIR analizės rezultatais nustatyta, jog zolių-gelių procesas ir kaitinimo temperatūra labiau veikia galutinių junginių morfologines ypatybes nei jų pradinė fazinė sudėtis. Tai tik patvirtina naudojamo vandeninio zolių-gelių metodo unikalumą ir tinkamumą daugiakomponenčių molibdatinių oksidinių sistemų sintezei.

GYVENIMO APRAŠYMAS

CURRICULUM VITAE

ASMENINĖ INFORMACIJA	
Vardas, pavardė	Giedrė Gaidamavičienė
Gimimo data	1991-02-09
Adresas	Architektų g. 91-49, Vilnius
Telefono numeris	+37065639452
El. pašto adresas	giedre.prievelyte@gmail.com

IŠSILAVINIMAS IR KVALIFIKACIJA	
2010 – 2014	Chemijos bakalauro kvalifikacinis laipsnis, Vilniaus universitetas
2014 – 2016	Chemijos magistro kvalifikacinis laipsnis, Vilniaus universitetas

DARBO PATIRTIS		
2017-09 – 2019-05	Vilniaus universiteto, bendrosios ir neorganinės chemijos laboratorija	Vyresnioji specialistė
2019-06 – iki dabar	Vilniaus universiteto, bendrosios ir neorganinės chemijos laboratorija	Laborantė

DALYVAVIMAS MOKYMUOSE IR TARPTAUTINĖSE MOKYKLOSE	
2016-10-17 – 2016-10-21	Jaunųjų mokslininkų bendrųjų kompetencijų gebėjimų mokymai
2017-08-27 – 2017-08-31	19th international school Advanced materials and technologies, Palanga, Lietuva
2018-08-27 – 2018-08-31	20th international school Advanced materials and technologies, Palanga, Lietuva
2019-08-19 – 2019-08-23	21st international school Advanced materials and technologies, Palanga, Lietuva

PAPILDOMA VEIKLA	
2019-09 – iki dabar	Vilniaus universiteto, chemijos ir geomokslų fakulteto, respublikinių mokyklų mokinių laboratorinių darbų praktikos veiklos koordinatorė.

ACKNOWLEDGEMENTS

I would like to express my deepest gratitude to my supervisor **Assoc. Prof. Dr. Artūras Žalga** for imparting his wisdom and great knowledge to me as well as motivating and supporting me throughout my studies and research. His unconditional encouragement and guidance were vital in keeping this work proceeding in the right direction, and without his assistance this project would not have been realized.

I am particularly grateful to Dr. Edvardas Kazakevičius from Faculty of Physics of Vilnius University for performing impedance spectroscopy measurements, and I greatly appreciate his patience in interpreting the results obtained. I would also like to pay my special regards to Dr. Brigita Abakevičienė from Faculty of Mathematics and Natural Sciences of Kaunas University of Technology for her valuable comments and help throughout the completion of this work.

I wish to extend my warmest thanks to all my colleagues from Faculty of Chemistry and Geoscience of Vilnius University for their support and assistance with the multitude of measurements and experiments undertaken during these years.

Finally, I would like to acknowledge the unwavering love, faith and care from my family and friends that has kept me going on even throughout the most difficult of times. This journey would not have been possible without them.

LIST OF PUBLICATIONS

Articles in journals included in the thesis

1. A. Žalga, **G. Gaidamavičienė**, Ž. Gricius, E. Užpurvytė, J. Gadeikis, A. Diktanaitė, M. Barré, T. Šalkus, A. Kežionis, E. Kazakevičius, Aqueous sol-gel synthesis, thermoanalytical study and electrical properties of $La_2Mo_2O_9$, *Journal of Thermal Analysis and Calorimetry* 132(3) (2018) 1499-1511.
2. **G. Gaidamavičienė**, B. Abakevičienė, A. Žalga, Oxalic acid assisted synthesis of the gadolinium-doped ceria oxide-ion conductor as electrolyte for the solid oxide fuel cells, *Chemical Papers* 73(4) (2019) 891-899.
3. **G. Gaidamavičienė**, A. Žalga, Synthesis, a structural and thermoanalytical study of $Ca_{1-x}Sr_xMoO_4$ ceramic, *Materials Chemistry and Physics* 241 (2020) 122339.
4. **G. Gaidamavičienė**, G. Janulevičius, E. Venslauskaitė, A. Žalga, Aqueous sol-gel synthesis, thermoanalytical study and luminescent properties of $M_{0.05}Eu_{0.05}Ca_{0.9}MoO_4$ (M=Li, Na, K, Rb, Cs) nanocrystallites, *Journal of Thermal Analysis and Calorimetry* 140 (2020) 2185-2201.

Articles in journals not included in the thesis

1. J. Gružauskaitė, J. Jasinskaitė, R. Meškys, G. Gaidamavičienė, A. Žalga, A. Laurynėnas, M. Dagys, Gold-coated magnetic nanocatalyst containing wired oxidoreductases for mediatorless catalysis of carbohydrate oxidation by oxygen, *Catalysis Communications* 135 (2020) 105848.
2. A. Diktanaitė, G. Gaidamavičienė, E. Kazakevičius, A. Kežionis, A. Žalga, Aqueous sol-gel synthesis, thermal analysis, characterization and electrical properties of V_2O_5 doped Bi_2O_3 system, *Thermochimica Acta* 685 (2020) 178511.

Published contributions to academic conferences

1. G. Gaidamavičienė, A. Žalga, E. Kazakevičius, Aqueous sol-gel synthesis and thermoanalytical study of $La_{1.9}Ca_{0.1}Mo_2O_{8.95}$, *60th International Conference for Students of Physics and Natural Sciences Open Readings 2017*, March 14 – 17, 2017, Vilnius, Lithuania.
2. G. Gaidamavičienė, A. Žalga, $Ca_{1-x}Sr_xMoO_4$ sintezė ir apibūdinimas, *Chemija ir cheminė technologija 2017*, April 27, 2017, Kaunas, Lithuania.

3. G. Gaidamavičienė, E. Kazakevičius, A. Žalga, Synthesis and X-Ray diffraction analysis of calcium and strontium doped lanthanum molybdate, *Chemistry and Chemical Technology 2017*, April 28, 2017, Kaunas, Lithuania.
4. G. Gaidamavičienė, E. Kazakevičius, A. Žalga, Aqueous sol-gel synthesis, characterization and electrical properties of $La_{2-x}Ca_xMo_2O_{9-\delta}$, *The International Conference Dedicated to the 215th Birth Anniversary of Ignacy Domeyko*, July 28 – 30, 2017, Vilnius, Lithuania.
5. G. Gaidamavičienė, A. Žalga, Thermoanalytical study of strontium substituted Ca–Mo–O nitrate-tartrate gel precursors prepared by sol-gel synthesis, *4th Central and Eastern European Conference on Thermal Analysis and Calorimetry*, August 28 – 31, 2017, Chisinau, Moldova.
6. G. Gaidamavičienė, E. Kazakevičius, A. Žalga, Synthesis, properties and thermoanalytical study of calcium substituted LAMOX oxide-ion conductor, *4th Central and Eastern European Conference on Thermal Analysis and Calorimetry*, August 28 – 31, 2017, Chisinau, Moldova.
7. G. Gaidamavičienė, A. Žalga, Sol-gel synthesis, crystal structure and surface morphology of $CaMoO_4$, $SrMoO_4$ and $Ca_{0.5}Sr_{0.5}MoO_4$ ceramics, *19th international school Advanced Materials and Technologies*, August 27 – 31, 2017, Palanga, Lithuania.
8. G. Gaidamavičienė, T. Murauskas, A. Žalga, Thermoanalytical and structural studies on alkaline earth metals substituted $La_2Mo_2O_9$ materials, *61st International Conference for Students of Physics and Natural Sciences Open Readings 2018*, April 20 – 23, 2018, Vilnius, Lithuania.
9. G. Gaidamavičienė, T. Murauskas, P. Normantas, V. Aleksa, A. Žalga, Spectroscopic study of La-RE-Mo-O tartrate precursors and $La_{2-x}RE_xMo_2O_9$ (RE=Nd, Sm, Eu, Dy) ceramics obtained by sol-gel method, *61st International Conference for Students of Physics and Natural Sciences Open Readings 2018*, April 20 – 23, 2018, Vilnius, Lithuania.
10. G. Gaidamavičienė, E. Užpurvytė, A. Žalga, Aqueous sol-gel synthesis and characterization of barium doped LAMOX materials, *61st International Conference for Students of Physics and Natural Sciences Open Readings 2018*, April 20 – 23, 2018, Vilnius, Lithuania.
11. G. Gaidamavičienė, Ž. Gricius, T. Murauskas, M. Smolianskis, V. Aleksa, A. Žalga, Raman and infrared study of $La_{2-x}Y_xMo_2O_9$, *61st International Conference for Students of Physics and Natural Sciences Open Readings 2018*, April 20 – 23, 2018, Vilnius, Lithuania.

12. G. Gaidamavičienė, J. Gadeikis, T. Murauskas, Ž. Tokarevas, V. Aleksa, A. Žalga, Raman spectroscopic study on the structure of $La_{2-x}Dy_xMo_2O_9$, *61st International Conference for Students of Physics and Natural Sciences Open Readings 2018*, April 20 – 23, 2018, Vilnius, Lithuania.
13. E. Venslauskaitė, G. Gaidamavičienė, Ž. Gricius, A. Žalga, Synthesis and characterization of samarium doped ceria ceramics, *61st International Conference for Students of Physics and Natural Sciences Open Readings 2018*, April 20 – 23, 2018, Vilnius, Lithuania.
14. G. Gaidamavičienė, A. Žalga, Preparation and analysis of $Ca_xSr_{1-x}MoO_4$ ceramics with scheelite-type structure, *20th international school Advanced Materials and Technologies*, August 27 – 31, 2018, Palanga, Lithuania.
15. G. Gaidamavičienė, E. Kazakevičius, A. Žalga, Synthesis and characterization of alkaline earth metals doped $La_2Mo_2O_9$ ceramics, *62nd International Conference for Students of Physics and Natural Sciences Open Readings 2019*, April 19 – 22, 2019, Vilnius, Lithuania.
16. G. Gaidamavičienė, A. Žalga, Characterization of $La_{1.9}Ca_{0.1}Mo_2O_{8.95}$ ceramics synthesized by the aqueous sol-gel synthesis, *Chemistry and Chemical Technology 2019*, May 16, 2019, Vilnius, Lithuania.
17. G. Gaidamavičienė, A. Žalga, Influence of Ba^{2+}-doping on the structural and thermal properties of $La_2Mo_2O_9$ ceramic, *21st international school Advanced Materials and Technologies*, August 19 – 23, 2019, Palanga, Lithuania.
18. G. Gaidamavičienė, A. Žalga, Synthesis, structural and thermoanalytical study of $Ca_{1-x}Sr_xMoO_4$ ceramic, *5th Central and Eastern European Conference on Thermal Analysis and Calorimetry & 14th Mediterranean Conference on Calorimetry and Thermal Analysis*, August 27 – 30, 2019, Roma, Italy.
19. G. Gaidamavičienė, A. Žalga, Aqueous sol-gel synthesis and thermoanalytical study of alkaline earth metals doped $La_2Mo_2O_9$ oxide-ion conductor, *5th Central and Eastern European Conference on Thermal Analysis and Calorimetry & 14th Mediterranean Conference on Calorimetry and Thermal Analysis*, August 27 – 30, 2019, Roma, Italy.
20. G. Gaidamavičienė, A. Žalga, Synthesis and characterization of gadolinium doped ceria oxide ceramic, *63rd International Conference for Students of Physics and Natural Sciences Open Readings 2020*, April 17 – 20, 2020, Vilnius, Lithuania.

Article I

Synthesis, a structural and thermoanalytical study of $Ca_{1-x}Sr_xMoO_4$ ceramic

G. Gaidamavičienė, A. Žalga

Materials Chemistry and Physics 241 (2020) 122339

Materials Chemistry and Physics 241 (2020) 122339

Contents lists available at ScienceDirect

Materials Chemistry and Physics

journal homepage: www.elsevier.com/locate/matchemphys

Synthesis, a structural and thermoanalytical study of $Ca_{1-x}Sr_xMoO_4$ ceramic

Giedrė Gaidamavičienė, Artūras Žalga *

Department of Applied Chemistry, Institute of Chemistry, Faculty of Chemistry and Geosciences, Vilnius University, Naugarduko Str. 24, 03225, Vilnius, Lithuania

HIGHLIGHTS

- Sol-gel synthesis of nano- and micro-sized $Ca_{1-x}Sr_xMoO_4$ ceramics in the sol-gel process using tartaric acid as a ligand.
- Thermal decomposition mechanism of Ca–Sr–Mo–O tartrate gel precursors.
- Rietveld refinement of the $Ca_{1-x}Sr_xMoO_4$ system.
- SEM analysis of surface morphology of the samples for the $Ca_{1-x}Sr_xMoO_4$ ceramic materials.
- FT-IR and Raman spectroscopical investigation of synthesized ceramics heat-treated at different temperatures.

GRAPHICAL ABSTRACT

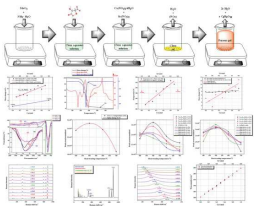

ARTICLE INFO

Keywords:
Sol–gel processes
Thermal properties
Rietveld refinement
Spectroscopy

ABSTRACT

For the first time, nano- and micro-sized double-mixed $Ca_{1-x}Sr_xMoO_4$ (x = 0.0, 0.1, 0.2, 0.3, 0.4, 0.5, 0.6, 0.7, 0.8, 0.9 and 1.0) ceramics have been successfully synthesized by an aqueous sol-gel synthesis method in the sol-gel process using tartaric acid as a ligand. An additional novelty of this work was to show the pathways of chemical reactions that occurred under the heat-treatment of the as-prepared Ca–Sr–Mo–O tartrate gel precursors. The structural, morphological, textural and chemical properties of both the tartrate gel precursors and alkaline earth metal molybdates were obtained by thermal analysis (TG/DSC), X-ray diffraction (XRD), scanning electron microscopy (SEM), infrared spectroscopy (FT-IR), and RAMAN spectroscopy (RS). The mechanism of thermal decomposition of both the tartaric acid and metal tartrates between all multicomponent $Ca_{1-x}Sr_xMoO_4$ samples was established and qualitatively compared. Moreover, in support of data from the TGA/DSC curves the quantitative distribution of intermediate products in the gel precursors during the heat-treatment was also estimated. In addition, theoretically determined data of the carbon residues were compared with the corresponding mass change from the TGA curve as a match by suggested reaction mechanism. By combining thermoanalytical investigation with the X-ray diffraction of samples heat-treated at a different temperature the relation of a final composition and its crystallite size with the thermal decomposition process of volatile components was estimated. Scanning electron microscopy was used for both the characterization of surface morphology and estimation of the particle size in the ceramic. FT-IR spectroscopy was applied in order to estimate the possible differences between multicomponent $Ca_{1-x}Sr_xMoO_4$ systems taking into account the size of crystallites and the nature of surface morphology. Finally, the Raman spectroscopic technique confirmed the initial composition of the elements in the synthesized ceramic and clearly showed that the distribution of both calcium and strontium atoms corresponds to the product, which is composed of a single-phase crystalline compound.

* Corresponding author.
E-mail address: arturas.zalga@chf.vu.lt (A. Žalga).

https://doi.org/10.1016/j.matchemphys.2019.122339
Received 13 August 2019; Received in revised form 8 October 2019; Accepted 17 October 2019
Available online 23 October 2019

1. Introduction

In the past decades, metal molybdates with scheelite type structure attracted many scientists attention due to their unique structural [1–3], electronic [3–6] and catalytic [7–9] properties. These specific characteristics could be modified incorporating other ions to produce binary solid solutions with better properties than individual compounds [10–15]. The influence on the characteristic properties of such either substituted or doped systems mainly depends on both the nature of elements and their relation into the functional group of molybdate [12, 13]. From this point of view, it is clear that the greater the difference in the nature of the metal, the more diverse the structure of the final compound usually forms [2,16]. Besides, a metallic radius, ionic properties, valence and acid-base characteristics are the most important factors that play an essential role in the association with oxygen atoms in the molybdate group [7]. Thus, comparing two similar atoms as calcium and strontium by the chemical properties there is clear that their molybdates ($MMoO_4$) crystallize into the scheelite structure, which has tetragonal crystal lattice with I41/a space group [2,3,17]. In such structure, oxygen atoms are located by cubic close-packed array where tetrahedral and octahedral units are formed. Each M^{2+} ion (M = Ca, Sr) is connected by eight oxygen atoms forming bisdisphenoid polyhedral while Mo ions are surrounded by four oxygen atoms forming a tetrahedral unit. These tetrahedrals are completely isolated against each other, but they are connected with MO_8 polyhedrals by sharing its corner. Every MO_8 polyhedra shares four of its edges with four other MO_8 polyhedra extending in the c-directions [2,3,6,17–19].

In despite the similar crystal structure of both calcium and strontium molybdates, the mix preparation of these double oxides is a great challenge for several reasons. From the concept of the first one, which is mainly focussed on the synthesis of separate metal molybdates, there is clear that after obtaining the pure components the critical stage remains a mixing procedure that significantly affects the final properties of obtained ceramic [3–5,13,20]. On the other hand, the synthesis of solid-state reaction [3,5,7,10,11,15,17–19,21] usually is the simplest and cheapest method for the preparation of most oxide-based ceramics. The critical factors remain as follows: the mixing stage of the initial powders and heat-treatment temperature, which should be higher than the melting point of starting compounds. Other techniques [22–31], which are based on the mixing stages at low temperatures between many scientists attract lots of attention and the competition in this area is always really high. Therefore, there is no surprise that the synthesis of double calcium-strontium molybdate was done and published in several articles [3–5,13,20], but detail studies on its formation and crystallization are still rare. It should be also mentioned that the synthesis of the final compound starts in a simple way, which is shown below in equation (Eq.) 1.

$$(1-x)Ca^{2+} + x\,Sr^{2+} + MoO_4^{2-} \rightarrow Ca_{1-x}Sr_xMoO_4 \quad (1)$$

The control of this Eq. depends on such factors as the nature of starting compounds, pressure, temperature, solvent, voltage, sonochemical and microwave radiation, flux additives, coordination agents and etc.

The choose of the desired controlling stage depends on the resultant phase and its properties. Therefore, the crystallite growth dynamic, surface morphology features, in addition, the purity and homogeneity of the obtained ceramic should be clearly predicted. In the case of sol-gel synthesis, the control of Eq. (1) is concentrating on the enhanced solubility of initial salts, which reveals the quality of final ceramics already after gel formation. The use of tartaric acid as a ligand in the sol-gel process [32–36] enhanced the solubility of all initial salts in the water and sustained it until the removal of all solvent molecules from the reaction mixture has occurred. Besides, the tartaric acid assisted synthesis technique is quite simple, cheap and environmentally friendly compared with other methods.

It is also well-known that an aqueous sol-gel synthesis method is mainly based on the dissolution of either metal oxide or its salt in water, which is used as a solvent. The drawback of this preparation way emerges when water molecules start to react with metal ions after their dissolution by composing corresponding hydroxides, which usually possesses low solubility. The removal of this hydrolysis process consists of replacing the hydroxy groups by other anions. Such competition effect of ligand reduces the level of hydrolysis with solvent and enhances the solubility of metal ions, which are strongly coordinated by ligand molecules. In this case, tartaric acid molecules coordinate similarly both the calcium and strontium ions, therefore, the synthesis process of $Ca_xSr_{1-x}MoO_4$ compound goes identically as occurred in separate double oxides.

In addition, it should be mentioned that this technology is quite rarely used and the synthesis of the $Ca_xSr_{1-x}MoO_4$ system using tartaric acid as a ligand is published for the first time in our knowledge. In order to verify the uniqueness and flexibility of this synthesis technique in the case of double mixed metal molybdates, the thermal decomposition process of as-prepared gel precursors was performed. From the obtained results the mechanism of the formation of final ceramic materials was proposed. Moreover, the structural, morphological and spectroscopical investigations revealed that all obtained compounds showed a single-phasic character and possessed a high level of homogeneity.

2. Material and methods

In the first stage of this synthesis, the calcium (II) nitrate tetrahydrate ($Ca(NO_3)_2{\cdot}4H_2O$ 99% Alfa Aesar) and strontium (II) nitrate ($Sr(NO_3)_2$ 99,0% Alfa Aesar) were dissolved in deionized water. Next, the powders of molybdenum (VI) (MoO_3, 99.95% Alfa Aesar) oxide were mixed with aqueous ammonia ($NH_3{\cdot}H_2O$ 25% Penta) solution. This dissolution process is shown in Eq. (2).

$$MoO_3(s) + 2NH_3 \cdot H_2O(aq) \rightarrow MoO_4^{2-}(aq) + 2\,NH_4^+ + H_2O(1) \quad (2)$$

In order to reduce the possibility of a precipitate of molybdates under the acidic conditions, an excess of the tartaric acid (L-(+)-Tartaric acid ($C_4H_6O_6$) (TA) ≥99.5% Sigma-Aldrich) into the reaction mixture was added, as follows in Eq. (3), respectively.

$$MoO_4^{2-}(aq) + 4C_4H_6O_6(aq) \rightarrow \left[MoO_4(C_4H_6O_6)_{4-q}\right]^{2-}(aq) + qC_4H_6O_6(aq) \quad (3)$$

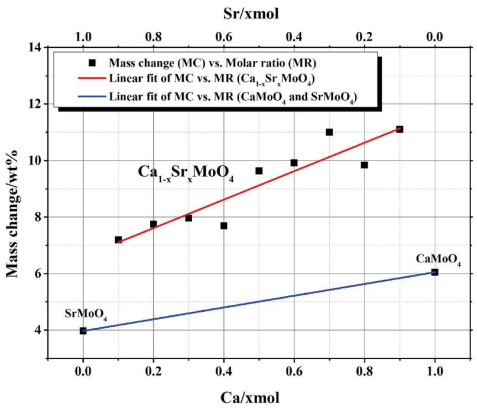

Fig. 1. Mass change vs. molar ratio graph of tartaric acid during the evaporation process for Ca–Sr–Mo–O tartrate gel precursors.

After that, under continuous stirring and heating, the obtained clear solution of the reaction mixture was mixed with the source of calcium and strontium ions. An obtained clear aqueous solution of ions-mixture was evaporated and this way as-formed gel precursor was dried in an oven at 120 °C for several hours until no solvent molecules remain in the obtained gel powders. The corresponding chemical processes are shown in the scheme of Eq. (4).

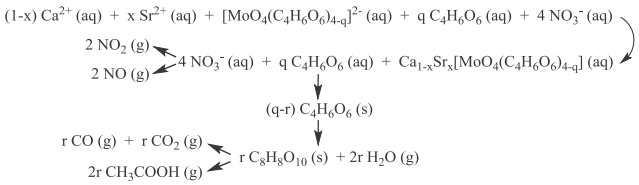

(4)

The gel precursor, with an initial composition as given in Eq. (5), was ground in an agate mortar and obtained powders were used for the thermal analysis, which performed with TG–DSC, STA 6000 PerkinElmer instrument using a sample weight of about 10 mg and a heating rate of 20° min^{-1} under the continuous airflow (20 $cm^3 min^{-1}$) at ambient pressure from room temperature to 950 °C.

$$Ca_{1-x}Sr_x\left[MoO_4(C_4H_6O_6)_{4-q}\right](s) + (q-r)C_4H_6O_6(s) \xrightarrow{\text{drying at } 120^\circ C} Gel\ precursor \quad (5)$$

The rest of gel powders was divided into equal pieces, additionally heat-treated in the range of temperature from 350 °C to 700 °C for 5 h in the air atmosphere and investigated by x-ray diffraction (XRD) analysis. The XRD patterns were recorded in the air at room temperature with a powder x-ray diffract meter Rigaku MiniFlex II using CuKα_1 radiation. The patterns were recorded at a standard rate of 1.5 $2\theta/min^{-1}$. In order to evaluate the trend of crystallization, the Rietveld refinement of the obtained XRD patterns was performed using X'Pert HighScore Plus software. Besides, the characteristic vibrations of functional groups in all heat-treated samples were estimated using a PerkinElmer Frontier FTIR spectrometer. Finally, Raman spectroscopy was successfully applied for the estimation of phase composition in the obtained ceramic materials. The Raman spectra at the room temperature were recorded with a combined Raman and scanning near-field optical microscope (SNOM) WiTec Alpha 300 R using a 532 nm excitation laser source.

3. Results and discussion

3.1. Thermal analysis

Thermal analysis is a powerful technique that enables the progress of such investigation fields as phase changes, reaction mechanism, decomposition of volatile components and chemical stability in both the starting materials and the final multicomponent compounds (See Appendix A). Moreover, this analysis explores the influence of temperature trough either heat consumption or its release from the sample, which is the main indicator that confirms possible changes in the material from its energetical and structural variations that usually takes place at higher temperatures.

According to Eq. (6), there is clearly the amount of tartaric acid removal during the evaporation process occurs in all cases in relatively small quantities.

$$q\ C_4H_6O_6(aq) \rightarrow (q-r)C_4H_6O_6(s) + r\ C_8H_8O_{10}(s) + 2r\ H_2O(g) \quad (6)$$

The value of a coefficient r slightly depends on the nature of alkaline earth metal, when the decomposition of tartaric acid generates the carbon monoxide, carbon dioxide and two molecules of acetic acid (Eq. (7)), the mass loss differs by 2% comparing Sr–Mo–O gel with the Ca–Mo–O tartrate precursor, respectively.

$$r\ C_8H_8O_{10}(s) \rightarrow r\ CO\ (g) + r\ CO(g) + r\ CO_2(g) + 2r\ CH_3COOH(g) \quad (7)$$

This relation is shown in Figure (Fig. 1), where the difference between strontium molybdate and calcium molybdate is well defined. Besides, it is worth to mention that despite the tendency of weight loss growth during the evaporation process, the influence of this effect is much higher in mixed $Ca_{1-x}Sr_xMoO_4$ system than in separate alkaline earth metal molybdates. This behaviour is explained by the common ion effect when two different cations create weaker coordination power than was observed in separate cases. By this reason, the loss of tartaric acid increases from 3 wt% to 5 wt%, respectively, and it is directly related with the first mass change in the range of temperature from 30 °C to 143 °C as is shown in Fig. 2.

In this case, the opposite process of mass loss is observed, when the case of Ca–Mo–O gel precursor losses less weight than corresponding Ca–Sr–Mo–O and Sr–Mo–O samples. However, it also should be mentioned that the differences between all samples are really negligible, and the thermal decomposition of gel precursors is more affected by the temperature than by the initial composition of elements. This range of temperature is explained by the evaporation of water molecules from the

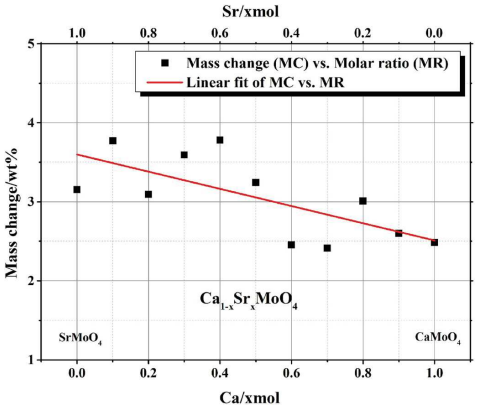

Fig. 2. Mass change vs. molar ratio graph for Ca–Sr–Mo–O tartrate gel precursors in the range of temperature from 30 °C to 143 °C.

sample according to Eq. (6).

The further increase of temperature from about 143 °C shows the decomposition process of tartaric acids dimer as is presented in Eq. (7), respectively. This heat-treatment stage and the whole decomposition of tartaric acid was well described by Chattaway in 1920 [37], besides, the proceeding of this process adjusted to the current synthesis conditions is presented in Fig. 3.

It is also important to note that the decomposition of tartaric acids dimer into the carbon oxides and acetic acids competes with another process, which shown in Eq. (8), especially at a higher temperature.

$$(r-k)C_8H_8O_{10}(s) \rightarrow k\ CO_2(g) + k\ C_7H_8O_8(s) \rightarrow 2k\ CH_3COCOOH \quad (8)$$

As a result, after both decomposition steps, two different heat effects were observed in the DSC curve respectively. The first one, which starts at about 185 °C of temperature, is attributed to the release of carbon dioxide as shown in Eq. (7). Slightly after that, the tendency of DSC curve changes into endothermic character, which indicates the evaporation of pyruvic acid from the tartaric acid residue. This endothermic process dominates until the temperature reaches the value of 220 °C, after that the emission of heat that produces after the release of CO_2 is observed again. The broad exothermic peak continues in the whole range of temperature from 220 °C to 293 °C with a small interruption at 285 °C. This is the main reason why the peak position of this process changes into 271 °C and it is slightly less compared with the cases for corresponding metal molybdate precursors as shown in Fig. 4. Such effect of competition for both CO_2 release and pyruvic acid evaporation processes reveals interesting features of the decomposition of intermediate products when at the same time two different kind of actions taking places. In the case of the decomposition of metal molybdate tartrate precursors, this exothermic effect is much more elongate pronounced and no changes of heat trend were observed at all. This means that an action of the presence of metals in the gel precursor weakens the heat consumption effect during the evaporation process of the pyruvic acid from the sample.

The broad exothermic band in the DSC curve proves this process and schematically this effect is shown in Eq. (9). Additionally, also should be noted that this burning of the residue of tartaric acid only really slightly depends on the heat-treatment atmosphere because of the decrease of mass change near to zero from the precursor itself according to Eq. (10). In such cases, the slightly different burning mechanism was observed, but the result remains the same.

$$(k-s)C_7H_8O_8(s) + O_2(g) \rightarrow 3s\ CO_2(g) + 4s\ H_2O(g) \quad (9)$$

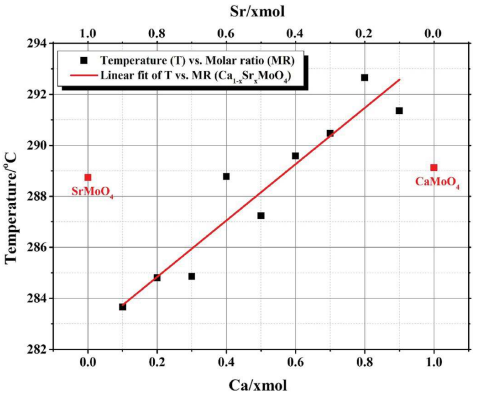

Fig. 4. Temperature vs. molar ratio graph in the point of complete decomposition of tartaric acid.

$$(k-s)C_7H_8O_8(s) + s\ CO_2(g) \rightarrow 2s\ CO(g) + 4s\ H_2O(g) \quad (10)$$

Such a conclusion shows that in this aqueous sol-gel synthesis method a tartaric acid plays not only the role of complexing agent but also acts as a self-oxidizing fuel during the decomposition of the gel precursor.

The almost identical situation is observed in the gel precursors when the decomposition of tartaric acid coincides with the previously examined case. Fig. 4 shows the temperature of the complete decomposition of tartaric acid for the Ca–Sr–Mo–O tartrate gel precursors. The similar values of the decomposition temperature of tartaric acid for $CaMoO_4$ and $SrMoO_4$ systems were registered because of unequal mass change during the evaporation procedure whereas the metal mixed tartrate gel precursors for $Ca_{1-x}Sr_xMoO_4$ composition clearly showed the tendency of growth by increased the degree of substitution.

This result only confirms the previously made conclusion about the different influence of separate metals and their mixture to the formation of gel precursor during the evaporation procedure. Besides, the connection between the amount of tartaric acid in the gel precursor and

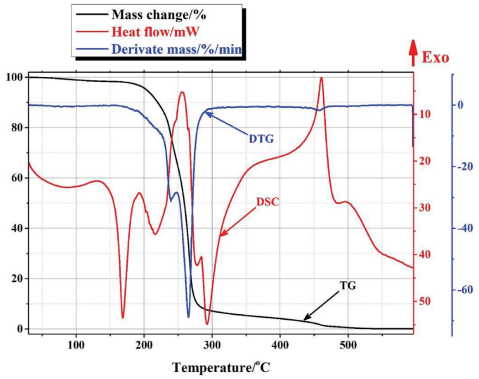

Fig. 3. Combined TG–DTG–DSC curves of the tartaric acid precipitated from the acidic water solution by the evaporation procedure.

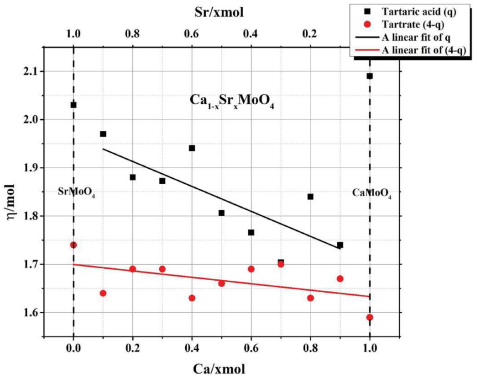

Fig. 5. Amount of substance vs. molar ratio graph of the tartaric acid and tartrates in the gel precursors.

it lost during the gelation process is also well seen in Fig. 5 when the amount of substance of tartaric acid for the separate metal molybdates well fits with the results placed in Fig. 1. However, the amount of tartrates in the coordination sphere of metals shows similar characteristics independently from both the nature of alkaline earth metal and the substitution degree in the corresponding molybdate.

Such a result indicates that the initial amount of tartaric acid, which was used during the synthesis procedure, does not significantly affect the complexation of metal cations in the gel precursor. In this case, it is only important to estimate the minimal amount of ligand in the reaction mixture in order to the dissolution of initial salts. On the other hand, an additional amount of complexing agent reduces the possibility of precipitation process during the gelation procedure, which makes a significant influence on the homogeneity of the as-prepared gel precursor.

Moreover, the end of the decomposition of tartaric acid creates favourable conditions for crystallization of the final ceramic. This process is confirmed by the endothermic character of the DSC curve in the range of temperature from about 295 °C to 395 °C. Further increase in temperature leads to the decomposition processes of the corresponding gel precursor, which determines the characteristic properties of obtained ceramic. These results of crystallization and decomposition are presented in Eq. (11).

$$Ca_{1-x}Sr_x\left[MoO_4(C_4H_6O_6)_{4-q}\right](s) \rightarrow Ca_{1-x}Sr_x\left[MoO_4(C_2H_2)_{4-q}\right](s) + (8-2q)CO_2(g) + (8-2q)H_2O(g) \quad (11)$$

The amount of volatile compounds that remain in the gel precursor depends on the number of tartrates, which coordinates the cations of metals. The last mass change corresponds to this residue that is shown as a fragment of $(C_2H_2)_{(4-q)}$ in Eq. (11). The corresponding q and r coefficients are given in Table 1, which directly related to the data of the substance amount according to Eqs. (3) and (11) and synthesis scheme 4.

The number of hydrogen, which remained in the ceramic sample, had an influence on the errors that appeared comparing both, the data obtained from the experimental results and the calculated values as shown in Fig. 6.

The tendency of mass changes remains the same in both cases and the intersection of the straight lines lies near the centre. Such a result proofs the logic of the suggested decomposition mechanism for investigated metal tartrate systems. Moreover, this residual composition of carbon and hydrogen in the ceramic sample (eq. (11)) explains the mass change of such multi-component system at somewhat higher temperatures in the nitrogen atmosphere. This way of possible mass changes is shown in Eqs. (12) and (13), respectively, realizing both oxidative and inert conditions.

Table 1
Substance amount for corresponding gel precursors.

Sample name	Amount of tartaric acid (TA)/ mol(q-r)	Amount of tartrates/ mol (4–q)	Amount of decomposed TA during the evaporation/mol (r)	Sum of TA and tartrates/ mol (4–r)
$CaMoO_4$	2.09	1.59	0.320	3.68
$Ca_{0.9}Sr_{0.1}MoO_4$	1.74	1.67	0.590	3.41
$Ca_{0.8}Sr_{0.2}MoO_4$	1.84	1.63	0.530	3.47
$Ca_{0.7}Sr_{0.3}MoO_4$	1.71	1.70	0.590	3.41
$Ca_{0.6}Sr_{0.4}MoO_4$	1.77	1.69	0.540	3.46
$Ca_{0.5}Sr_{0.5}MoO_4$	1.81	1.66	0.530	3.47
$Ca_{0.4}Sr_{0.6}MoO_4$	1.94	1.63	0.430	3.57
$Ca_{0.3}Sr_{0.7}MoO_4$	1.87	1.69	0.440	3.56
$Ca_{0.2}Sr_{0.8}MoO_4$	1.88	1.69	0.430	3.57
$Ca_{0.1}Sr_{0.9}MoO_4$	1.97	1.64	0.390	3.61
$SrMoO_4$	2.03	1.74	0.230	3.77

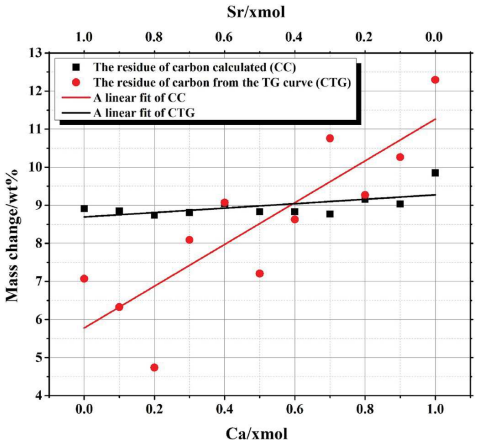

Fig. 6. Mass change vs. molar ratio graph for Ca–Sr–Mo–O tartrate gel precursors in the range of temperature from 520 °C to 760 °C.

$$Ca_{1-x}Sr_x\left[MoO_4(C_2H_2)_{4-q}\right](s) + (10-2.5q)(O_2)(g) \rightarrow Ca_{1-x}Sr_xMoO_4(s) + (8-2q)CO_2(g) + (4-q)H_2O(g) \quad (12)$$

$$Ca_{1-x}Sr_x\left[MoO_4(C_2H_2)_{4-q}\right](s) \rightarrow Ca_{1-x}Sr_xMoO_4(s) + (4-q)C_2H_2(g) \quad (13)$$

3.2. X-ray diffraction

The room temperature XRD patterns of Ca–Sr–Mo–O tartrate gel precursors annealed at 700 °C are shown in Fig. 7. As can be seen, in all cases single-phase crystal phase for the mixed $Ca_{1-x}Sr_xMoO_4$ ceramic was obtained. The well-expressed shift of the main peak was also identified. Corresponding Rietveld analysis of all investigated samples (See Appendix B) heat-treated in the range of temperature from 350 °C to 700 °C was done and presented in Table 2. The X-ray diffraction data of remaining ceramic materials are presented as supplementary material.

This analysis confirms the conclusion that was made from the TG–DTG–DSC curves about the beginning of the crystallization process. Moreover, it is also clear that the formation of the final compounds lies in the temperature of the start of decomposition of corresponding metal tartrates. Depending on the investigated case, the onset temperature of this process slightly varies according to the initial composition for final ceramic.

3.3. SEM micrographs

Scanning electron microscopy (SEM) is an important technique that, combined with thermal analysis and X-ray diffraction, enables the observation of growing tendencies of crystallites as well as particles. Fig. 8 shows the pictures of the surface morphology of the Ca–Sr–Mo–O tartrate gel precursor that was heat-treated at different temperatures. From there is well seen that the range of temperature from 400 °C to 600 °C (Fig. 8 (a), (b) and (c)) only slightly affects the particle size.

According to the data from Table 2, in this case, the size of crystallites increases from 12 nm to 35 nm. Similar growing tendencies of particles could be identified from corresponding SEM micrographs, presented in Fig. 8. The changes in surface morphology for analysed

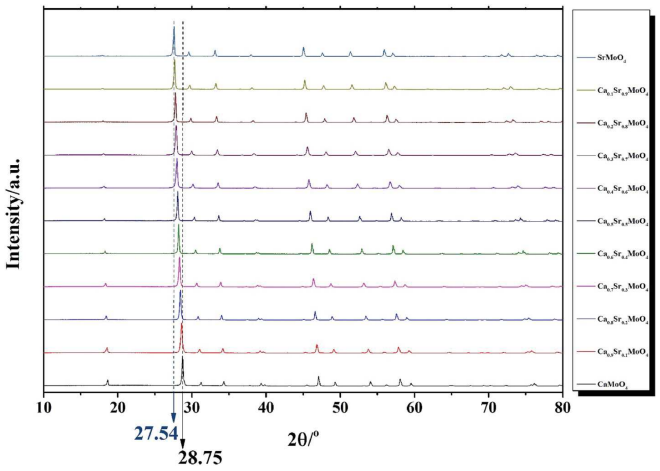

Fig. 7. XRD patterns of the Ca–Sr–Mo–O tartrate gel precursors heat-treated at the temperature of 700 °C for 5 h in the air.

samples are minimal and no significant structural rearrangements were observed. Such a result means that thermal decomposition of the corresponding metal tartrates follows the emission of carbon oxides, depending on the heat-treatment atmosphere as shown in Eqs. (12) and (13), which slightly slows down the crystallization process of the final multicomponent ceramic compounds. By further increase of heat-treatment temperature to 700 °C, the burning and decomposition effects lose them energy and this gives the possibility rather for both the growth of crystallites and particles. In the case of $Ca_{0,8}Sr_{0,2}MoO_4$ ceramic, the size of crystallites increases almost twice to 74 nm and the dimensions of particles change from nano-to micro-size.

A similar observation of the tendency for morphology according to the heat-treatment temperature was found in the Ca–Sr–Mo–O tartrate gel precursor for $Ca_{0,5}Sr_{0,5}MoO_4$ ceramic. As is seen from Fig. 9, the significant change in particle size also takes place above 600 °C of temperature. This is well seen in Fig. 9 (d) when the size of particles increases almost twice, compared with the previous case, and the individual fractions of particles were not identified.

This result suggests a conclusion that by increasing the strontium amount (Figs. 9 and 10) in the corresponding multicomponent oxide the homogeneity of the system also increases. Such an effect is directly related to the slightly different onset point of crystallization of strontium and calcium molybdates. Moreover, the thermal stability of corresponding metal molybdates also plays an important role in the frame of both the crystallization and the growth of particles.

Fig. 10 presents the surface morphology of the Ca–Sr–Mo–O tartrate gel precursor for the $Ca_{0,2}Sr_{0,8}MoO_4$ ceramic, which is really similar to that shown in Fig. 9. Nevertheless, from the SEM images of lower magnification (in the left bottom corner), it is clearly seen that the surface of less substituted systems (Fig. 8 (d) and 10 (d)) composed of the spherical particles, which fully cover the visible surface.

Meanwhile, the morphology of the Ca–Sr–Mo–O tartrate gel precursor for $Ca_{0,5}Sr_{0,5}MoO_4$ ceramic mainly consists of smooth surface with several islands of well-defined spherical particles. Such a result makes an important conclusion about the dominance of either $CaMoO_4$ or $SrMoO_4$ system, which means that the influence on the growth of the particles at the temperature of 700 °C is the biggest when the smallest degree of substitution by alkaline earth metal is realized.

3.4. FT-IR analysis

By continuing, further studies on the Ca–Sr–Mo–O tartrate gel precursors heat-treated at different temperatures the infrared spectroscopy (IR) was performed (See Appendix C) as an important investigation technique, which enables the fixation of the vibrational frequency of bonds for the crystalline ceramics with the initial composition of $Ca_{1-x}Sr_xMoO_4$. Generally, the infrared bands for inorganic materials are broader, fewer in number and appear at lower wavenumbers than those observed for organic materials [38]. The most interesting region of the characteristic vibrations that have the same vibrational frequency of bonds in the $Ca_{1-x}Sr_xMoO_4$ crystalline structure is in the range of wavenumber from 1000 cm^{-1} to 500 cm^{-1}. This range of wavenumber is not detailed studied, therefore, its qualitative relation according to the final composition of obtained ceramic materials is also rarely examined. Nevertheless, as seen in Fig. 11 (a) the Ca–Sr–Mo–O tartrate gel precursor heat-treated at 400 °C for $Ca_{0,5}Sr_{0,5}MoO_4$ ceramic possesses two broad bands in the FT-IR spectrum. The first one in the range of wavenumber from 1750 cm^{-1} to 1000 cm^{-1} is attributed to the vibrational frequency of bonds, which corresponds to the organic residue of metal tartrates. By increasing the heat treatment temperature, this band of characteristic vibration disappears (Fig. 11(b–d)). Taking into account the data obtained from the thermal analysis of the corresponding sample, such a result lets make a conclusion about the decomposition of organic kind products into the carbon oxide gases at temperatures above 400 °C.

Thereafter, the second band of the vibrational frequency of bonds corresponds to the metal-oxygen vibrations, which create a complex of atoms in the crystal structure of $Ca_{0,5}Sr_{0,5}MoO_4$ ceramic. The intensity, width and shape of this band depend on several factors such as the degree of crystallinity, surface area and crystal structure of the ceramic precursor. The number and size of crystallites usually are defined as the degree of crystallinity. By increasing the heat-treating temperature, the crystallinity of crystalline compounds also increases. Meanwhile, the opposite effect is observed when the crystallites and particles tend to grow and the surface area has a tendency to decrease. The influence of these factors determines the size of the area (Peak area) for the band of characteristic vibrations in the range of wavenumber from 1000 cm^{-1} to 500 cm^{-1}. Fig. 12 corresponds graphically to these effects and

Table 2
Agreement indices, crystallite sizes and lattice parameter for the $Ca_{1-x}Sr_xMoO_4$ ceramic heat-treated at different temperatures.

Sample composition	Heat-treating temperature/°C	Weighted R profile	Goodness of fit	Crystallite size/nm	Lattice parameter (a = b)/pm	Lattice parameter (c)/pm
$CaMoO_4$	350	9.03070	1.70161	2.79	519.1552	1136.8330
	400	8.00789	1.02980	19.62	522.4100	1144.2870
	500	8.70444	1.20424	34.45	522.5589	1144.5930
	600	11.36286	2.10192	54.59	522.6251	1144.5690
	700	11.34951	1.88364	76.55	522.7625	1144.3230
$Ca_{0.9}Sr_{0.1}MoO_4$	350	10.70766	2.52509	2.79	513.9407	1141.39407
	400	8.24800	1.45024	13.11	523.2491	1147.9940
	500	7.73238	1.23551	21.12	523.3171	1148.2050
	600	9.59967	2.01608	35.52	523.4093	1148.8310
	700	12.34855	3.29645	48.65	523.5107	1149.5380
$Ca_{0.8}Sr_{0.2}MoO_4$	350	–	–	–	–	–
	400	9.16016	1.86361	12.24	524.8412	1154.0160
	500	7.45806	1.16842	21.22	525.0697	1154.3440
	600	9.20278	1.91847	34.63	525.0998	1154.9500
	700	13.13632	3.83775	72.79	525.4389	1155.5160
$Ca_{0.7}Sr_{0.3}MoO_4$	350	–	–	–	–	–
	400	7.66417	1.22728	12.00	526.7002	11.60.1720
	500	7.62366	1.29860	20.83	526.7130	11.60.5480
	600	9.46512	2.02849	38.20	526.8537	11.61.2130
	700	11.38996	2.88429	62.39	527.0233	1161.6880
$Ca_{0.6}Sr_{0.4}MoO_4$	350	–	–	–	–	–
	400	8.27202	1.56947	12.22	528.1176	1166.2550
	500	8.15853	1.35968	22.80	528.5681	1167.0810
	600	9.29906	1.97344	35.72	528.5277	1167.5930
	700	13.21026	3.70580	102.71	529.0508	1167.6080
$Ca_{0.5}Sr_{0.5}MoO_4$	350	–	–	–	–	–
	400	7.25980	1.12391	10.44	530.5035	1172.9540
	500	8.00231	1.38954	20.45	530.4146	1173.6350
	600	9.46282	2.02884	36.06	530.2272	1173.7320
	700	13.03338	3.34058	76.00	530.6589	1173.1200
$Ca_{0.4}Sr_{0.6}MoO_4$	350	7.48980	2.59112	2.79	521.027	1167.428
	400	7.44161	1.24404	10.01	532.3578	1179.3040
	500	8.78488	1.64735	19.46	532.2154	1179.8150
	600	8.88975	1.80848	34.61	532.0759	1179.8670
	700	11.68023	3.01354	53.25	532.0723	1179.9390
$Ca_{0.3}Sr_{0.7}MoO_4$	350	6.30053	1.89928	3.38	531.967	1182.327
	400	7.53253	1.15408	11.53	533.912	1185.219
	500	6.97944	1.16852	17.68	533.7233	1185.2830
	600	9.18326	1.79048	35.11	533.7805	1185.9950
	700	10.52613	2.48622	49.40	533.6454	1186.4190
$Ca_{0.2}Sr_{0.8}MoO_4$	350	–	–	–	–	–
	400	7.47882	1.15896	11.16	535.651	1191.774
	500	8.03231	1.34033	20.07	535.4813	1191.7080
	600	10.27405	2.35936	47.71	535.4473	1192.2580
	700	12.06726	3.08418	80.50	535.6157	1191.7510
$Ca_{0.1}Sr_{0.9}MoO_4$	350	8.29466	1.75462	2.79	535.8577	1181.0230
	400	7.20916	1.10094	12.90	537.3528	1197.2000
	500	8.23016	1.63363	29.90	537.1782	1197.5820
	600	10.47861	2.69856	55.31	537.0697	1197.8300
	700	11.98377	3.34126	63.01	537.0390	1197.8890
$SrMoO_4$	350	7.30471	1.26084	6.63	539.3264	1200.4890
	400	7.90881	1.28802	12.02	538.7699	1202.6080
	500	9.00312	1.50032	29.94	538.4937	1202.6620
	600	10.52758	2.72813	53.64	538.6781	1203.2830
	700	12.72914	3.62930	75.62	538.9070	1202.4940

quantitatively describes the influence of heat-treatment temperature to the sum of these factors.

From the data points presented in Fig. 12, it is clear that the highest peak area worth was observed at the heat-treatment temperature of 500 °C. This result was mainly determined by the degree of crystallinity whereas the surface area and crystal structure of the ceramic material in the range from 400 °C to 500 °C of temperature did not change significantly. By further increasing the heat-treating temperature the size of the peak area decreases especially in the sample that was heat-treated at 700 °C of temperature. This effect is directly related to the surface morphology of the sample, while the rapid growth of crystallites and particles, seen from Table 2 and SEM micrographs, makes the tendency of decreasing of the peak area in the FT-IR spectrum. The influence of the crystal structure to the changes in the peak area is better seen in Fig. 13. In this case, it is well seen that strontium molybdate and the samples with a lower degree of substitution have a higher crystallinity and surface area at the temperature of 400 °C than those with the higher amount of calcium in the corresponding metal molybdates. The dominance of crystal structure effect continues and at 500 °C of temperature. In the FT-IR spectrum of $SrMoO_4$ sample, the peak area even decreases by the increasing the heat-treatment temperature to 500 °C. Such behaviour confirms the difference in the crystallization point of calcium and strontium molybdates at elevated temperatures. Meanwhile, the increase of heat-treating temperature from the 600 °C–700 °C shows similar peculiarities of the changes in the size of peak area, which were concluded in earlier cases.

It is also important to make attention to the fact that the crystal structure effect of strontium molybdate plays only until the degree of

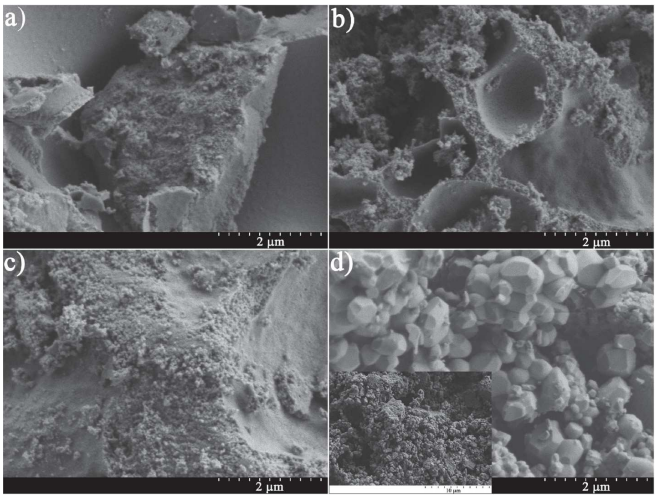

Fig. 8. SEM micrographs of Ca–Sr–Mo–O tartrate gel precursor for $Ca_{0.8}Sr_{0.2}MoO_4$ ceramic heat-treated at the temperatures of (a) 400 °C, (b) 500 °C, (c) 600 °C, and 700 °C in air for 5 h at ambient pressure.

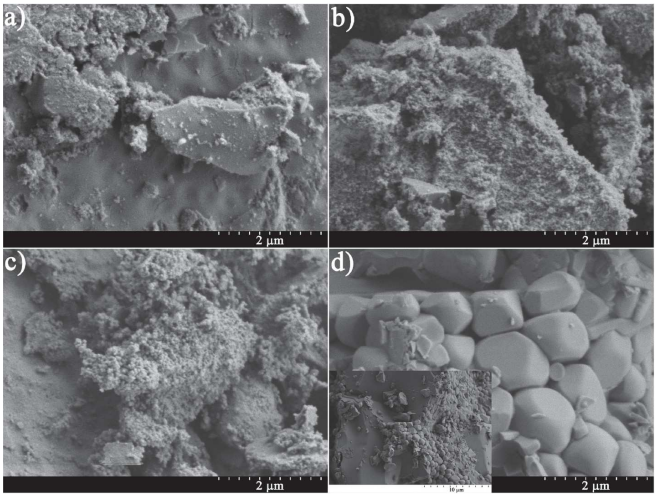

Fig. 9. SEM micrographs of Ca–Sr–Mo–O tartrate gel precursor for $Ca_{0.5}Sr_{0.5}MoO_4$ ceramic heat-treated at the temperatures of (a) 400 °C, (b) 500 °C, (c) 600 °C, and 700 °C in air for 5 h at ambient pressure.

substitution x = 0.7. Further increase of calcium amount in the $Ca_{1-x}Sr_xMoO_4$ system determines a similar curve shape comparing all later cases. Especially taking account into the curves of $Ca_{0.3}Sr_{0.7}MoO_4$ and $Ca_{0.4}Sr_{0.6}MoO_4$ ceramics, which completely differs from the strontium molybdate case and show behaviour that is characteristic to the tendencies of the peak area changes for pure calcium molybdate.

Fig. 14 shows the graph of peak area vs. heat-treating temperature for the $Ca_{1-x}Sr_xMoO_4$ ceramics (x = 0.0–0.4). Similar to the cases, which were studied in Fig. 13, the most distinguished curve belongs to the sample that is close to the $Ca_{0.5}Sr_{0.5}MoO_4$ compound (Fig. 12). Besides, the curve of pure calcium molybdate also shows exceptional behaviour, especially at the temperature of 400 °C, when the size of the peak area was the smallest comparing with all cases. By increasing the heat-treating temperature the size of peak area also increased and this change of growth was the biggest between all samples placed in this Fig. Moreover, a similar change of growth was observed from the XRD

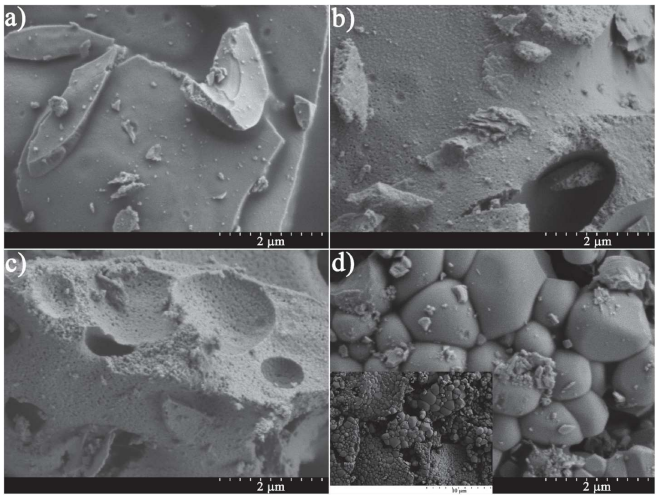

Fig. 10. SEM micrographs of Ca–Sr–Mo–O tartrate gel precursor for $Ca_{0.2}Sr_{0.8}MoO_4$ ceramic heat-treated at the temperatures of (a) 400 °C, (b) 500 °C, (c) 600 °C, and 700 °C in air for 5 h at ambient pressure.

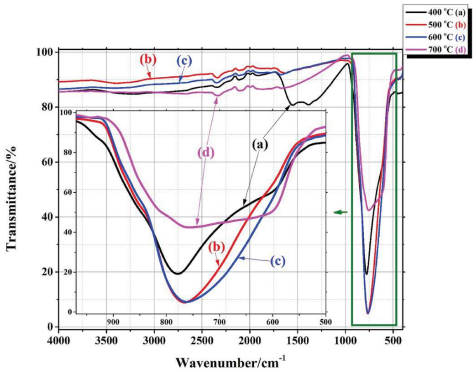

Fig. 11. FT–IR transmittance spectra of the Ca–Sr–Mo–O tartrate gel precursors for $Ca_{0.5}Sr_{0.5}MoO_4$ ceramic heat-treated at (a) 400 °C, (b) 500 °C, (c) 600 °C, and (d) 700 °C of temperature for 5 h in the air atmosphere.

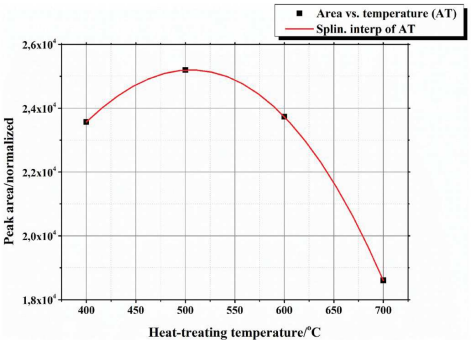

Fig. 12. Peak area vs. heat-treating temperature graph of Ca–Sr–Mo–O tartrate gel precursor for $Ca_{0.5}Sr_{0.5}MoO_4$ ceramic heat-treated at different temperatures.

data presented in Table 2, when the size of crystallites increased from 19.62 nm (at 400 °C) to 34.45 nm (at 500 °C). Comparing this case with the peak area changes of the $SrMoO_4$ curve it is clear that in despite the similar tendencies of crystallites growth the crystallization mechanism of both systems slightly differs. This difference could be explained by means of the different radius of alkaline earth metals, which creates an almost identical crystal structure of corresponding metal molybdates with well-pronounced different distances in all directions inside the crystal lattice.

In conclusion, it is obvious that, in despite similarity that came analysing results, the factors, which most affect the crystallization process act differently at the desired temperatures. The reduce of their action is the main task for further investigations, but one is clear that this tartaric acid assisted synthesis approach expands the possible control of production for such mixed crystalline systems.

3.5. Raman spectra

In this work, the Raman spectroscopy was also used in order to expand the obtained results from FT-IR analysis and XRD diffraction. As is clear from the previous sections the calcium molybdate, strontium molybdate and ternary $Ca_{1-x}Sr_xMoO_4$ oxides crystallize to the tetragonal scheelite crystal structure (space group $I4_1/a$, symmetry C_{4h}^6). In this kind of multi-component system, the molybdenum atom is surrounded by four oxygen atoms that form a tetrahedron. In the complexes, created from tetrahedrons, the metal ion is surrounded by eight oxygen atoms creating a pseudocubic configuration. As a result, the crystal structure is composed of the tetragonal lattices, which each contain only 12 atoms.

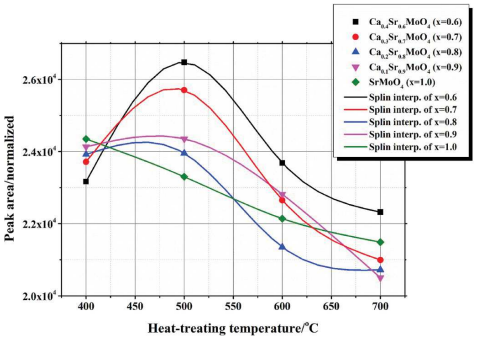

Fig. 13. Peak area vs. heat-treating temperature graph of Ca–Sr–Mo–O tartrate gel precursors for $Ca_{1-x}Sr_xMoO_4$ ceramics heat-treated at different temperatures.

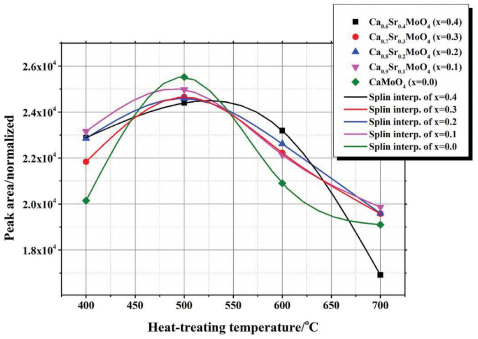

Fig. 14. Peak area vs. heat-treating temperature graph of Ca–Sr–Mo–O tartrate gel precursors for $Ca_{1-x}Sr_xMoO_4$ ceramics heat-treated at different temperatures.

According to group theory calculations in such crystal lattice exists 26 different vibrations [39,40].

$$\Gamma = 3\,A_g + 5\,B_g + 5\,E_g + 5\,A_u + 3\,B_u + 5\,E_u \quad (14)$$

In this case (Eq. (14)), the A_g, B_g and E_g vibrations are Raman active modes while $4A_u$ and $4E_u$ are IR active modes. The B_u vibrations are silent modes and the remaining modes ($1A_u$ and $1E_u$) are assigned to the acoustic vibrations. The crystal structure of alkaline earth metal molybdates mainly composed of MoO_4^{2-} groups in which the strong covalent bonds between molybdenum and oxygen atoms are realized. Meanwhile, the cations of either calcium or strontium interact with these groups by a weak covalent bonding. This is the reason why all vibrations in the Raman spectrum could be divided into two main groups. The first set is directly related to the internal vibrations that occur inside MoO_4^{2-} molecular units with a stationary mass centre. The second one corresponds to the motion of M^{2+} cations in the rigid molecular units [41]. In order to apply the rules of group theory for the $Ca_{1-x}Sr_xMoO_4$ system, the Raman spectroscopy was performed for the Ca–Sr–Mo–O tartrate gel precursors. The corresponding Raman spectra are presented in Fig. 15, respectively.

According to the group theory, the Raman spectra consists of 13 modes, but in this case, only 11 modes were identified. Besides, in some

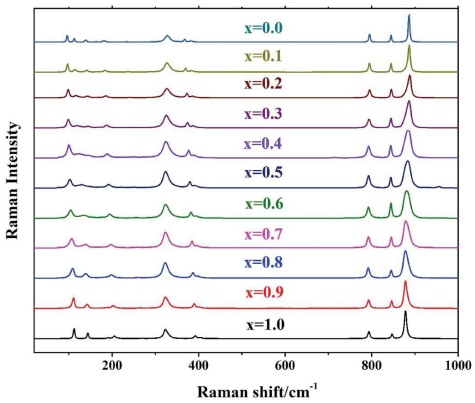

Fig. 15. Raman spectra of the Ca–Sr–Mo–O tartrate gel precursors for $Ca_{1-x}Sr_xMoO_4$ ceramics heat-treated at 700 °C of temperature for 5 h in the air atmosphere.

cases, even 12 vibration modes were found. The main reason for such results could be caused by both the low vibration intensity or overlapping of modes. In the Raman spectra, a dominant intense mode is observed at 877 cm^{-1} for x = 1.0 compound and at 887 cm^{-1} for x = 0.0 system. This mode is assigned to the symmetric vibrations of Mo–O stretching mode A_g of ν_S(Mo–O) and antisymmetric stretching mode of ν_{as}(Mo–O) at 847 cm^{-1} for $CaMoO_4$ oxide and at 845 cm^{-1} for $SrMoO_4$ compound [3].

The corresponding modes that were identified from the Raman spectrum of $SrMoO_4$ oxide, which are common and for the rest ceramic samples are presented in Fig. 16. In addition, Table 3 shows the values of lattice parameters and unit cell volume for the $CaMoO_4$ and $SrMoO_4$ powders obtained in this work and compared with those reported in the literature [42–45]. According to the obtained results, the negligible differences that occurred between the Raman active modes could be related to the nature of used synthesis technique that slightly affects the crystallite sizes and the degree of structural order in the crystal lattice

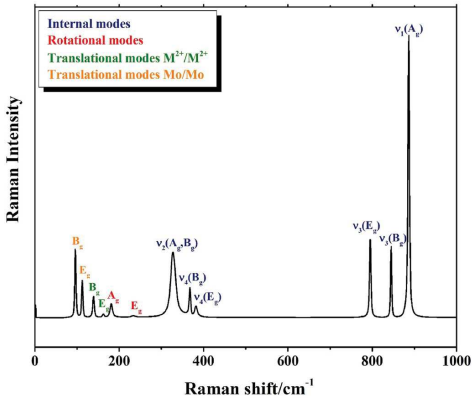

Fig. 16. Indexes of the vibrations modes for the Raman spectrum of Sr–Mo–O tartrate gel precursors for $SrMoO_4$ ceramic.

Table 3
Values of lattice parameters and unit cell volume for the $CaMoO_4$ and $SrMoO_4$ systems.

Active Raman modes for $CaMoO_4$		Wavenumber/cm^{-1} (this work)	Ref.			Active Raman modes for $CaMoO_4$		Wavenumber/cm^{-1} (this work)	Ref.	
			[42]	[43]	[44]				[44]	[45]
ν_1 (A_g)		877	878	878	879	ν_1 (A_g)		887	887	886
ν_3 (B_g)		847	844	847	848	ν_3 (B_g)		845	845	845
ν_3 (E_g)		793	797	793	794	ν_3 (E_g)		795	796	795
ν_4 (E_g)		402	401	402	403	ν_4 (E_g)		383	382	381
ν_4 (B_g)		392	393	391	392	ν_4 (B_g)		368	367	367
ν_2 (A_g, B_g)		323	333	323	323	ν_2 (A_g, B_g)		327	327	327
E_g		267	263	267	269	E_g		234	234	234
A_g		204	205	205	205	A_g		180	182	180
M^{2+}/M^{2+}	B_g	-	219	-	219	M^{2+}/M^{2+}	B_g	163	163	163
	E_g	190	189	189	191		E_g	139	139	138
Mo/Mo	E_g	143	145	145	145	Mo/Mo	E_g	112	112	112
	B_g	112	110	111	112		B_g	96	96	95

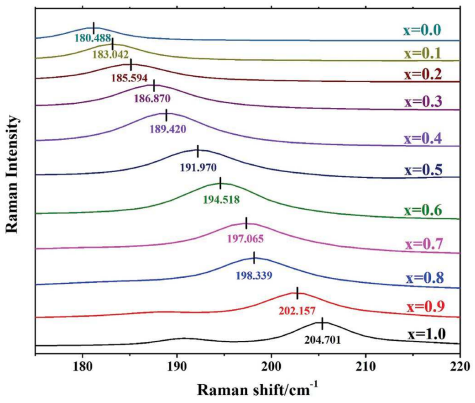

Fig. 17. The shift of A_g mode in Raman spectra for $Ca_{1-x}Sr_xMoO_4$ system in the range of interval from 175 cm^{-1} to 220 cm^{-1}.

[40].

In order to define the decrease of calcium amount in the multicomponent oxide, the Raman spectra of A_g mode for the $Ca_{1-x}Sr_xMoO_4$ system in Fig. 17 is presented. From the spectra, it is clear that by the substitution of calcium by strontium ions in $CaMoO_4$ oxide the small shift of the A_g mode is observed in the range of wavenumber from 205 cm^{-1} to 180 cm^{-1}. This shift into the values of lower wavenumber is determined according to the changes of the ionic radius in the alkaline earth metals. The A_g mode corresponds to the interatomic distances in the MoO_4^{2-} tetrahedra, which are strongly affected by the decrease of the covalent bonding between the molybdate and M^{2+} ions. As a result, after the replacement of Ca^{2+} by Sr^{2+} ion the volume of crystal lattice for the $Ca_{1-x}Sr_xMoO_4$ oxides tends to increase [3]. A set of these effects determines A_g shift, which values define the distribution of calcium ions in the $Ca_{1-x}Sr_xMoO_4$ system.

In an ideal case, the dependency for the $Ca_{1-x}Sr_xMoO_4$ system from $x = 0.0$ to $x = 1.0$ measuring the peak position of A_g mode is a linear. The interval of this line is divided into ten equal sections of $\Delta\nu$ according to Eq. (15).

$$\Delta\nu = \frac{\nu_{CaMoO_4} - \nu_{SrMoO_4}}{number\ of\ intervals} \tag{15}$$

The points at the ends of each section correspond to the A_g mode, which characterizes the relevant multicomponent oxide. For example, the theoretical value of $Ca_{0.9}Sm_{0.1}MoO_4$ compound is defined as is shown in Eq. (16).

$$\underset{for\ Ca_{0.9}Sr_{0.1}MoO_4}{\nu_{calculated}} = \nu_{CaMoO_4} - \Delta\nu \tag{16}$$

For the $Ca_{0.8}Sr_{0.2}MoO_4$ sample, the calculations follow further in the same way as shown in Eq. (17), respectively.

$$\underset{for\ Ca_{0.8}Sr_{0.2}MoO_4}{\nu_{calculated}} = \underset{for\ Ca_{0.9}Sr_{0.1}MoO_4}{\nu_{CaMoO_4}} - \Delta\nu \tag{17}$$

This operation of calculations is following further until the value ν for strontium molybdate is reached. Meanwhile, the calculated molar composition for the corresponding compound is related to Eq. (18) as follows.

$$\eta_{calculated} = \frac{\eta_{measured} \times \eta_{initial}}{\nu_{calculated}} \tag{18}$$

The rest values obtained from Raman spectra and recalculated according to the $\Delta\nu$ intervals are placed in Table 4, respectively. The graphical view of the data placed in Table 4 is illustrated in Fig. 18.

In conclusion, it should be noted that the Raman spectroscopy significantly supplements the determination of elemental composition in the multicomponent $Ca_{1-x}Sr_xMoO_4$ system. The dependencies of the values for A_g mode vs. molar part of alkaline earth metals, shown in Fig. 18, clearly reveal that the deviation from the ideal case is small and it is caused mainly by the unexpected measurement errors, which could be eliminated by estimating the whole range of the analysed samples.

4. Conclusions

Thermal analysis of the Ca–Sr–Mo–O tartrate gel precursors for the $Ca_{1-x}Sr_xMoO_4$ ceramic allowed the estimation of the decomposition process course that enabled the creation of a possible reaction mechanism on the formation of final multicomponent crystalline compounds.

Table 4
Values of the Raman mode A_g and molar composition for $Ca_{1-x}Sr_xMoO_4$ system measured and calculated.

Initial sample composition	$\eta_{initial}$/mol	Raman mode A_g ($\nu_{measured}$)/cm^{-1}	$\eta_{calculated}$/mol	Raman mode A_g ($\nu_{calculated}$)/cm^{-1}
$CaMoO_4$	1	204.701	1	204.7010
$Ca_{0.9}Sr_{0.1}MoO_4$	0.9	202.157	0.89945	202.2797
$Ca_{0.8}Sr_{0.2}MoO_4$	0.8	198.339	0.79392	199.8584
$Ca_{0.7}Sr_{0.3}MoO_4$	0.7	197.065	0.69868	197.4371
$Ca_{0.6}Sr_{0.4}MoO_4$	0.6	194.518	0.59487	195.0158
$Ca_{0.5}Sr_{0.5}MoO_4$	0.5	191.970	0.49838	192.5945
$Ca_{0.4}Sr_{0.6}MoO_4$	0.4	189.420	0.39842	190.1732
$Ca_{0.3}Sr_{0.7}MoO_4$	0.3	186.870	0.29859	187.7519
$Ca_{0.2}Sr_{0.8}MoO_4$	0.2	185.594	0.20028	185.3306
$Ca_{0.1}Sr_{0.9}MoO_4$	0.1	183.042	0.10007	182.9093
$SrMoO_4$	0	180.488	0	180.4880

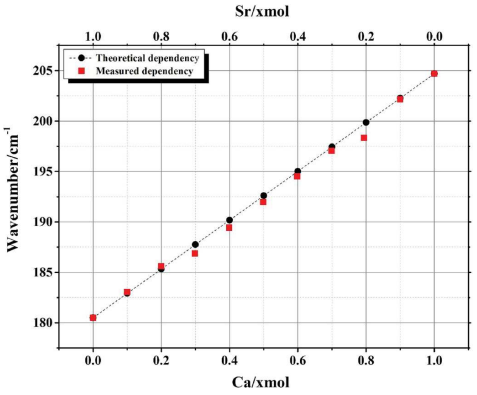

Fig. 18. Theoretical and measured dependencies of A_g mode (ν) vs. molar part of alkaline earth metals in the $Ca_{1-x}Sr_xMoO_4$ system.

This case revealed two important stages of decomposition, such as dimer formation then degradation of the tartaric acid and straight after that the combustion of corresponding metal tartrates. The DSC measurement clearly showed that the thermal degradation of tartaric acid differs from corresponding metal tartrates and takes place below 300 °C of temperature. According to the enhanced thermal stability of metal molybdates, their decomposition into the ceramic and volatile carbon-hydrogen-oxygen based materials takes place at much higher temperatures than the fission of corresponding tartaric acid residues. Besides, this process characterizes almost identical behaviour of either substituted $Ca_{1-x}Sr_xMoO_4$ system or separate metal molybdates under the condition of heat-treatment. Therefore, the difference of thermal decomposition between both calcium and strontium tartrates are not well pronounced because of their similar influence to the stability of corresponding molybdates. The realization of such a chemical environment on the point of the stage of formation of the final ceramic materials indicates that the tartaric acid assisted synthesis technique is suitable for the preparation of this multicomponent system in the range of heat-treatment temperature from 350 °C to 700 °C. Moreover, according to both the Raman and infrared spectroscopic results, there is clear that the sol-gel processing and heat-treatment temperature much more affects the morphological features than the initial composition of final ceramics. Such a conclusion only enhance the uniqueness and suitability of this preparation technique for the synthesis of this multicomponent system for the metal molybdate based compounds.

5. Supplementary material

The TGA/DSC/DTG curves of corresponding gel precursors as a source for the data analysed in section 2.1. are given in Appendix A. The X-ray diffraction patterns of the remaining samples are shown in Appendix B. Finally, the FT-IR spectra of gel precursors heat-treated at different temperatures for $Ca_{1-x}Sr_xMoO_4$ ceramic are presented in Appendix C.

Declaration of competing interest

The authors declare that they have no known competing financial interests or personal relationships that could have appeared to influence the work reported in this paper.

Appendix A. Supplementary data

Supplementary data to this article can be found online at https://doi.org/10.1016/j.matchemphys.2019.122339.

References

[1] A. Bayat, A.R. Mahjoub, M.M. Amini, Synthesis of high crystalline hierarchical self-assembled MMoO4 (M=Ca, Sr and Ba) super structures: having hydrophilic surfaces and obvious red-shifted photoluminescence behavior, Mater. Chem. Phys. 223 (2019) 583–590, https://doi.org/10.1016/j.matchemphys.2018.11.031.
[2] F.A. Rabuffetti, S.P. Culver, L. Suescun, R.L. Brutchey, Structural disorder in AMoO4 (A = Ca, Sr, Ba) scheelite nanocrystals, Inorg. Chem. 53 (2) (2014) 1056–1061, https://doi.org/10.1021/ic4025348.
[3] S.D. Ramarao, S.R. Kiran, V.R.K. Murthy, Structural, lattice vibrational, optical and microwave dielectric studies on Ca1−xSrxMoO4 ceramics with scheelite structure, Mater. Res. Bull. 56 (2014) 71–79, https://doi.org/10.1016/j.materresbull.2014.04.064.
[4] F. Li, H. Xie, H. Xi, F. Dang, X. Wang, Luminescent properties of sol-gel processed red-emitting phosphor Ca0.6 Sr0.4-1.5x-0.5y Mo0.4 W0.6 O4:Eux Liy. Luminescence, the journal of biological and chemical luminescence 30 (5) (2015) 600–604, https://doi.org/10.1002/bio.2792.
[5] Z. Yang, C. Hou, G. Duan, F. Yang, P. Liu, C. Wang, et al., The photoluminescent property and optical transition analysis of host sensitized Ca0.5Sr0.5MoO4:Dy3+ phosphor, J. Alloy. Comp. 604 (2014) 346–351, https://doi.org/10.1016/j.jallcom.2014.03.121.
[6] H.N. Im, M.B. Choi, S.Y. Jeon, S.J. Song, Structure, thermal stability and electrical conductivity of CaMoO4+δ, Ceram. Int. 37 (1) (2011) 49–53, https://doi.org/10.1016/j.ceramint.2010.08.004.
[7] A.M. Huerta-Flores, I. Juárez-Ramírez, L.M. Torres-Martínez, J.E. Carrera-Crespo, T. Gómez-Bustamante, O. Sarabia-Ramos, Synthesis of AMoO4 (A = Ca, Sr, Ba) photocatalysts and their potential application for hydrogen evolution and the degradation of tetracycline in water, J. Photochem. Photobiol. A Chem. 356 (2018) 29–37, https://doi.org/10.1016/j.jphotochem.2017.12.029.
[8] J.H. Bi, L. Wu, Y.F. Zhang, Z.H. Li, J.Q. Li, X.Z. Fu, Solvothermal preparation, electronic structure and photocatalytic properties of PbMoO4 and SrMoO4, Appl. Catal. B Environ. 91 (1–2) (2009) 135–143, https://doi.org/10.1016/j.apcatb.2009.05.016.
[9] Y. Wu, T. Yu, B.-S. Dou, C.-X. Wang, X-f Xie, Z.-L. Yu, et al., A comparative study on perovskite-type mixed oxide catalysts A′ xA1− xBO3− λ (A′= Ca, Sr, A= La, B= Mn, Fe, Co) for NH3 oxidation, J. Catal. 120 (1) (1989) 88–107, https://doi.org/10.1016/0021-9517(89)90253-4.
[10] Y. Hu, W. Zhuang, H. Ye, D. Wang, S. Zhang, X. Huang, A novel red phosphor for white light emitting diodes, J. Alloy. Comp. 390 (1–2) (2005) 226–229, https://doi.org/10.1016/j.jallcom.2004.07.063.
[11] W.Q. Yang, H.G. Liu, G.K. Liu, Y. Lin, M. Gao, X.Y. Zhao, et al., Trivalent europium-doped strontium molybdate red phosphors in white light-emitting diodes: synthesis, photophysical properties and theoretical calculations, Acta Mater. 60 (15) (2012) 5399–5407, https://doi.org/10.1016/j.actamat.2012.06.052.
[12] X. Ma, Z. Zhu, J. Li, Z. You, Y. Wang, C. Tu, Optical properties of Ho3+:SrMoO4 single crystal, Mater. Res. Bull. 44 (3) (2009) 571–575, https://doi.org/10.1016/j.materresbull.2008.07.005.
[13] L. Wan, S. Lü, L. Sun, X. Qu, Bi3+ enhanced red emission in Sr0.5Ca0.4MoO4:Eu3+ phosphor, Opt. Mater. 36 (3) (2014) 628–632, https://doi.org/10.1016/j.optmat.2013.10.044.
[14] Q. Wei, D. Chen, Luminescent properties and the morphology of SrMoO4:Eu3+ powders synthesized via combining sol-gel and solid-state route, Open Phys. 8 (5) (2010), https://doi.org/10.2478/s11534-009-0098-5.
[15] S. Wei, L. Yu, F. Li, J. Sun, S. Li, Photoluminescent properties of Eu3+-doped alkaline earth metal molybdates red phosphors with high quenching concentration, Ceram. Int. 41 (1) (2015) 1093–1100, https://doi.org/10.1016/j.ceramint.2014.09.034.
[16] L.Y. Li, Y.S. Huang, L.Z. Zhang, Z.B. Lin, G.F. Wang, Growth, mechanical, thermal and spectral properties of Cr3+:MgMoO4 crystal, PLoS One 7 (1) (2012), https://doi.org/10.1371/journal.pone.0030327.
[17] A. Sleight, Accurate cell dimensions for ABO4 molybdates and tungstates, Acta Crystallogr. Sect. B Struct. Crystallogr. Cryst. Chem. 28 (10) (1972) 2899–2902, https://doi.org/10.1107/S0567740872007186.
[18] S.N. Achary, S.J. Patwe, M.D. Mathews, A.K. Tyagi, High temperature crystal chemistry and thermal expansion of synthetic powellite (CaMoO4): a high temperature X-ray diffraction (HT-XRD) study, J. Phys. Chem. Solids 67 (4) (2006) 774–781, https://doi.org/10.1016/j.jpcs.2005.11.009.
[19] G. Wandahl, A.N. Christensen, Neutron powder diffraction profile refinement studies on CaMoO4. A comparison with single-crystal data, Acta chemica scandinavica Series A Physical and inorganic chemistry 41 (6) (1987) 358–360.
[20] W. Shi, J. Chen, S. Gao, Preparation and characterization of red-luminescence phosphors Ca 0.5 Sr 0.5 MoO 4: EU 3+ for white-light-emitting diodes, J. Chin. Ceram. Soc. 39 (2) (2011) 219–222.
[21] Z.A. Mikhaylovskaya, E.S. Buyanova, S.A. Petrova, Sheelite-related strontium molybdates: synthesis and characterization, Chimica Techno Acta 5 (4) (2018) 189–195, https://doi.org/10.15826/chimtech.2018.5.4.03.
[22] G. Ahmad, M.B. Dickerson, B.C. Church, Y. Cai, S.E. Jones, R.R. Naik, et al., Rapid, room-temperature formation of crystalline calcium molybdate phosphor

microparticles via peptide-induced precipitation, Adv. Mater. 18 (13) (2006) 1759–1763, https://doi.org/10.1002/adma.200600243.
[23] A. Cameirão, R. David, F. Espitalier, F. Gruy, Effect of precipitation conditions on the morphology of strontium molybdate agglomerates, J. Cryst. Growth 310 (18) (2008) 4152–4162, https://doi.org/10.1016/j.jcrysgro.2008.06.024.
[24] G. Braziulis, G. Janulevicius, R. Stankeviciute, A. Zalga, Aqueous sol–gel synthesis and thermoanalytical study of the alkaline earth molybdate precursors, J. Therm. Anal. Calorim. 118 (2) (2013) 613–621, https://doi.org/10.1007/s10973-013-3579-0.
[25] H. Gocmez, O. Özcan, Low temperature synthesis of nanocrystalline α-Al2O3 by a tartaric acid gel method, Mater. Sci. Eng. A 475 (1–2) (2008) 20–22, https://doi.org/10.1016/j.msea.2006.12.147.
[26] Y. Yin, Y. Gao, Y. Sun, B. Zhou, L. Ma, X. Wu, et al., Synthesis and photoluminescent properties of CaMoO4 nanostructures at room temperature, Mater. Lett. 64 (5) (2010) 602–604, https://doi.org/10.1016/j.matlet.2009.12.014.
[27] P. Parhi, S.S. Singh, A.R. Ray, A. Ramanan, Mechanochemically assisted room temperature solid state metathesis reaction for the synthesis of MMoO4 (M =Ca, Sr and Ba), Bull. Mater. Sci. 29 (2) (2006) 115–118, https://doi.org/10.1007/BF02704602.
[28] J.H. Ryu, J.-W. Yoon, C.S. Lim, W.-C. Oh, K.B. Shim, Microwave-assisted synthesis of CaMoO4 nano-powders by a citrate complex method and its photoluminescence property, J. Alloy. Comp. 390 (1–2) (2005) 245–249, https://doi.org/10.1016/j.jallcom.2004.07.064.
[29] N. Sharma, K.M. Shaju, G.V. Subba Rao, B.V.R. Chowdari, Z.L. Dong, T.J. White, Carbon-coated nanophase CaMoO4as anode material for Li ion batteries, Chem. Mater. 16 (3) (2004) 504–512, https://doi.org/10.1021/cm0348287.
[30] Y. Wang, S. Gai, C. Li, X. Zhang, N. Niu, F. He, et al., Controlled synthesis and luminescent properties of uniform SrMoO4 hollow microstructures and application as drug carrier, RSC Adv. 3 (17) (2013) 5945, https://doi.org/10.1039/C3RA22615H.
[31] V.D. Zhuravlev, O.G. Reznitskikh, Velikodnyi YA, T.A. Patrusheva, O.V. Sivtsova, Analysis of solid solutions stability in scheelite-type molybdates and tungstates, J. Solid State Chem. 184 (10) (2011) 2785–2789, https://doi.org/10.1016/j.jssc.2011.08.003.
[32] G. Gaidamaviciene, B. Abakeviciene, A. Zalga, Oxalic acid assisted synthesis of the gadolinium-doped ceria oxide-ion conductor as electrolyte for the solid oxide fuel cells, Chem. Pap. 73 (4) (2019) 891–899, https://doi.org/10.1007/s11696-018-0648-7.
[33] A. Zalga, G.E. Gaidamaviciene, Z. Gricius, E. Uzpurvyte, J. Gadeikis, A. Diktanaite, et al., Aqueous sol-gel synthesis, thermoanalytical study and electrical properties of La2Mo2O9, J. Therm. Anal. Calorim. 132 (3) (2018) 1499–1511, https://doi.org/10.1007/s10973-018-7120-3.
[34] R. Stankeviciute, A. Zalga, Sol-gel synthesis, crystal structure, surface morphology, and optical properties of Eu2O3-doped La2Mo3O12 ceramic, J. Therm. Anal. Calorim. 118 (2) (2014) 925–935, https://doi.org/10.1007/s10973-014-3882-4.
[35] G. Braziulis, R. Stankeviciute, A. Zalga, Sol-gel derived europium doped CaMoO4: Eu3+ with complex microstructural and optical properties, Mater Sci-Medzg. 20 (1) (2014) 90–96, https://doi.org/10.5755/j01.ms.20.1.4797.
[36] A. Zalga, Z. Moravec, J. Pinkas, A. Kareiva, On the sol-gel preparation of different tungstates and molybdates, J. Therm. Anal. Calorim. 105 (1) (2011) 3–11, https://doi.org/10.1007/s10973-011-1367-2.
[37] F.D. Chattaway, F.E. Ray, II.—the decomposition of tartaric acid by heat, J. Chem. Soc. Trans. 119 (0) (1921) 34–37, https://doi.org/10.1039/CT9211900034.
[38] B. Stuart, Infrared Spectroscopy: Fundamentals and Applications, John Wiley and Sons, Ltd, West Sussex, England, 2004, 0470011149. DOI. 10.
[39] A. Phuruangrat, T. Thongtem, S. Thongtem, Preparation, characterization and photoluminescence of nanocrystalline calcium molybdate, J. Alloy. Comp. 481 (1–2) (2009) 568–572, https://doi.org/10.1016/j.jallcom.2009.03.037.
[40] L. Cavalcante, J. Sczancoski, J. Espinosa, J.A. Varela, P. Pizani, E. Longo, Photoluminescent behavior of BaWO4 powders processed in microwave-hydrothermal, J. Alloy. Comp. 474 (1–2) (2009) 195–200, https://doi.org/10.1016/j.jallcom.2008.06.049.
[41] J. Sczancoski, L. Cavalcante, M. Joya, J.A. Varela, P. Pizani, E. Longo, SrMoO4 powders processed in microwave-hydrothermal: synthesis, characterization and optical properties, Chem. Eng. J. 140 (1–3) (2008) 632–637, https://doi.org/10.1016/j.cej.2008.01.015.
[42] M. Nicol, J.F. Durana, Vibrational Raman spectra of CaMoO4 and CaWO4 at high pressures, J. Chem. Phys. 54 (4) (1971) 1436–1440, https://doi.org/10.1063/1.1675034.
[43] V.M. Longo, ATd Figueiredo, A.B. Campos, J.W. Espinosa, A.C. Hernandes, C. Taft, et al., Different origins of green-light photoluminescence emission in structurally ordered and disordered powders of calcium molybdate, J. Phys. Chem. A 112 (38) (2008) 8920–8928, https://doi.org/10.1021/jp801587w.
[44] M. Liegeois-Duyckaerts, P. Tarte, Vibrational studies of molybdates, tungstates and related compounds—II: new Raman data and assignments for the scheelite-type compounds, Spectrochim. Acta A Mol. Spectrosc 28 (11) (1972) 2037–2051, https://doi.org/10.1016/0584-8539(72)80178-8.
[45] A.P.A. Marques, M.T.S. Tanaka, E. Longo, E.R. Leite, I.L.V. Rosa, The role of the Eu 3+ concentration on the SrMoO 4: Eu phosphor properties: synthesis, characterization and photophysical studies, J. Fluoresc. 21 (3) (2011) 893–899, https://doi.org/10.1007/s10895-010-0604-6.

Article II

Aqueous sol-gel synthesis, thermoanalytical study and luminescent properties of $M_{0.05}Eu_{0.05}Ca_{0.9}MoO_4$ (M=Li, Na, K, Rb, Cs) nanocrystallites

G. Gaidamavičienė, G. Janulevičius, E. Venslauskaitė, A. Žalga

Journal of Thermal Analysis and Calorimetry 140 (2020) 2185-2201

Journal of Thermal Analysis and Calorimetry
https://doi.org/10.1007/s10973-019-08962-7

Aqueous sol–gel synthesis, thermoanalytical study and luminescent properties of $M_{0.05}Eu_{0.05}Ca_{0.9}MoO_4$ (M=Li, Na, K, Rb, Cs) nanocrystallites

Giedrė Gaidamavičienė[1] · Gytautas Janulevičius[1] · Eglė Venslauskaitė[1] · Artūras Žalga[1]

Received: 18 June 2019 / Accepted: 25 October 2019

Abstract
Nano-sized $M_{0.05}Eu_{0.05}Ca_{0.9}MoO_4$ (M=Li, Na, K, Rb, Cs) ceramics have been successfully synthesized by an aqueous sol–gel synthesis method using a tartaric acid as a ligand. In order to reveal the influence of the peculiarities of the nature of dopants effect into the crystallization of $CaMoO_4$ double oxide, the thermal analysis of the as-prepared gels was performed. In addition, infrared spectroscopy was used in order to identify the functional groups from the characteristic stretching vibrations in the M–Eu–Ca–Mo–O tartrate gel precursors. Besides, to confirm the dynamics of growing crystallites in the final ceramics and to reveal the morphological changes on the surface, the x-ray diffraction and scanning electron microscopy were applied. Finally, photoluminescence measurements were used to estimate the optical properties of europium oxide as a dopant in the samples according to the nature of alkali metal. Therefore, according to the obtained results, it was estimated that luminescence intensity of Eu^{3+} ions is mainly affected by the chemical reaction, which takes place at about 973 K of temperature. This effect was partly confirmed from the results of the thermal decomposition of M–Eu–Ca–Mo–O tartrate gel precursors with an endothermic behaviour in the DSC curve, which indicates the crystallization mechanism of the $CaMoO_4$ double oxide.

Keywords Sol–gel synthesis · Thermal analysis · X-ray diffraction · Rietveld refinement · Optical properties

Introduction

$CaMoO_4$ is a well-known and important material. For its unique chemical and optoelectrical properties, it has been used in various fields as a luminescent [1], optical fibre [2], magnetic [3] and solid-state laser [4] material. Additionally, it can be used in humidity sensors [5], photocatalysts [6], scintillators [7] and cryogenic detectors [8]. Predominantly, $CaMoO_4$ has scheelite crystal structure [9] responsible for luminescence in blue and green parts of the spectrum [10], when excited with UV rays in 250–310 nm wavelength interval [11]. Calcium molybdate is also characterized by its strong physical and chemical resistances, which make it the preferred over its predecessors like $Y_2O_2S:Eu^{3+}$, $YVO_4:Eu^{3+}$, $Y_2SiO_5:Tb^{3+}$ or $Gd_2O_2S:Tb^{3+}$ [12]. In this structure, the Mo atoms are bonded to four oxygen, forming the [13] clusters [14], which can absorb ultraviolet region with high absorption cross section [15]. Charge transfer between can be observed between [13] cluster and dopant ion [16], thus making it possible to achieve luminescence in different parts of the spectrum by doping $CaMoO_4$ with rare-earth elements (RE). This peculiarity allows this material to be used as a matrix incorporated or saturated with dopant elements. By doping calcium molybdate with europium (III) ions (Eu^{3+}), strong red luminescence is achieved [17], while doping with terbium (III) ions (Tb^{3+})—strong green luminescence [18, 19]. It was observed that doping $CaMoO_4$ with two or more ions: rare-earth element (RE^{3+}) and charge-compensating element, for example Bi^{3+} [20] or alkali metal (Li^+, Na^+, K^+), luminescence intensity, is significantly improved without increasing RE^{3+} ion amount [21]. However, previously reported studies utilize inefficient or complex methods of synthesis, such as solid state or hydrothermal. Additionally, those methods require high annealing temperatures above or at 1173 K.

In recent years, microstructure and surface morphology have been proven to be essential part for achieving

✉ Artūras Žalga
arturas.zalga@chf.vu.lt

[1] Department of Applied Chemistry, Institute of Chemistry, Faculty of Chemistry and Geosciences, Vilnius University, Naugarduko Str. 24, 03225 Vilnius, Lithuania

Published online: 06 November 2019

characterizing desired material properties [22]. Therefore, it is crucial to adequately choose a method and conditions for the synthesis of the desired material. There are several published methods, among which are: pulse laser ablation (PLA) [23], mixed oxide [24], molten salt [25], solid state [26], hydrothermal and its variations [13, 27, 28], Czochralski [29] and precipitation [30], but generally, scheelite-type phosphors are synthesized by conventional solid-state reaction method [31]. This approach usually requires annealing at high temperatures for several hours and subsequent grinding. This crushing process changes the phosphor surfaces, resulting in the loss of emission intensity. Therefore, demand for alternative synthesis methods such as hydrothermal method or sol–gel process arise, as it was also shown that phosphors prepared via an wet chemical routes have higher uniformity in particle-size distribution with high crystallinity and exhibit higher photoluminescence intensity than those prepared by the solid-state reaction [32]. Therefore, sol–gel is an important method for its simplicity, repeatability, mild synthesis conditions, potential industrial application and desirable achieved product morphology.

Moreover, we provide a simple aqueous route for synthesizing high-purity scheelite $CaMoO_4$ phase substituted with RE element and a charge-compensating alkali ion. To our knowledge, such scale research was not published yet, as most of the published material presents solid-state or hydrothermal synthesis, and none of it compares the effect of all the substituted alkali ions (Li, Na, K, Rb, Cs). Additionally, thermal characterization of these materials is very scarce. While previous materials used Eu(III) ion hosts have been reported to have poor thermal stability [33], similar structures, such as $Ho^{3+}/Tm^{3+}/Yb^{3+}$-codoped $CaWO_4$, have been reported to have very high thermal stability, with only phase transition/organic impurity decomposition below 773 K after which the mass remained constant [34]. On the other hand, it gives this work an extra novelty and relevance, because of this synthesis technique that is based on the use of tartaric acid as a ligand during the sol–gel processing, which is powerful enough to prepare pure calcium molybdate with stabile crystal structure, uniform surface morphology and identical properties [35, 36]. Besides, our proposed synthesis procedure does not have any side effects to the final ceramic product and there are no typical undesirable consequences for the environment because of uses of tartaric acid that is found in food industry. According to that, it is obvious that this research enables to estimate the influence of the nature of alkali metal to the luminescent properties of Eu^{3+} ion in the host of $CaMoO_4$.

Materials and methods

The samples of $M_{0.05}Eu_{0.05}$ $Ca_{0.9}MoO_4$ (M=Li, Na, K, Rb, Cs) were prepared by the tartaric acid-assisted synthesis (TAS) approach during the mixing stage of the initial salts employing an tartaric acid as a chelating agent that interacts as a ligand at the molecular level with the reaction mixture during the both dissolution in water and sol–gel formation.

Lithium (I) nitrate ($LiNO_3$, 99% Alfa Aesar), sodium (I) nitrate ($NaNO_3$ 99,5% Alfa Aesar), potassium (I) nitrate (KNO_3, 99,5% Alfa Aesar), rubidium (I) nitrate ($RbNO_3$ 99.9% Alfa Aesar), caesium (I) nitrate ($CsNO_3$, 99,8% Alfa Aesar), europium (III) oxide (Eu_2O_3, 99.99% Alfa Aesar), calcium (II) nitrate tetrahydrate ($Ca(NO_3)_2{\cdot}4H_2O$ 99% Alfa Aesar) and molybdenum (VI) oxide (MoO_3, 99.95% Alfa Aesar) were used as starting materials and weighed according to the desired stoichiometric ratio (Table 1).

Nitric acid (HNO_3 66% Reachem), distilled water and concentrated ammonia solution ($NH_3{\cdot}H_2O$ 25% Penta) were used as solvents and reagents to regulate the pH of the solutions. Tartaric acid (L–(+)–Tartaric acid ($C_4H_6O_6$) (TA) ≥ 99.5% Sigma-Aldrich) was applied for escalation

Table 1 Stoichiometric amount, molecular weight, melting and boiling points for the corresponding salts, which were used during the sol–gel synthesis procedure

Chemical formula	Amount/mol	Molecular weight[a]/g mol^{-1}	Melting point[a]/K	Solubility[a] in water/g L^{-1}
$LiNO_3$	0.05	68.946	528	522 at 293 K
$NaNO_3$	0.05	84.995	581	912 at 298 K
KNO_3	0.05	101.103	607	242 at 293 K
$RbNO_3$	0.05	147.473	581	650 at 298 K
$CsNO_3$	0.05	194.91	687	270 at 298 K
Eu_2O_3	0.05	351.926	2623	Negligible
$Ca(NO_3)_2{\cdot}4H_2O$	0.9	236.15	320	1290 at 293 K
MoO_3	1	143.95	1075	0.490 at 301 K
HNO_3	0.4431	63.0129	231	Miscible
$NH_3{\cdot}H_2O$	0.01336	17.031	195.4	310 at 298 K
$C_4H_6O_6$	4	150.087	446	575 at 293 K

[a]Information about the physical properties of reagents was gathered from the supplier

of solubility via coordination of starting compounds in the reaction mixture, especially, during the pH changes and evaporation before sol–gel formation. The synthesis scheme for the preparation of M–Eu–Ca–Mo–O tartrate gel precursors is shown in Fig. 1.

At first, MoO_3 was dissolved in a solution that consisted of 25 mL of distilled water and 1 mL of concentrated ammonia by stirring at 355–360 K of temperature. Then, after continuous stirring at approximately 355–360 K as long as the excess of ammonia had been evaporated, the tartaric acid was added to the reaction mixture. The amount of tartaric acid is directly related to the concentration of molybdenum oxide according to their molar ratio of Mo/TA = 0.25. After the dissolution of tartaric acid in the reaction mixture, the required amount of alkali metal nitrate was added. Then, under the continuous stirring and heating, the europium (III) oxide and concentrated nitric acid were poured to the beaker. A clear yellowish solution was obtained and subsequently concentrated by slowly vaporizing the reaction mixture at 360 K.

In the following stage, a yellow transparent sol was formed after nearly 95% of the water had been evaporated. After drying the sol precursor in an oven at 393 K, the fine-grained light brown gel powders were obtained. The well-dried gel powders were used for the thermal analysis in order to estimate their decomposition mechanism. Meanwhile, the residue of gel precursors was additionally heat-treated at the temperatures of 623 K, 673 K, 773 K, 873 K, 973 K, 1073 K, 1223 K and 1273 K for 5 h in the air.

Thermal measurements were taken with TG−DSC, STA 6000 PerkinElmer instrument using a sample weight of about 10 mg and a heating rate of 20° min^{-1} under the continuous air flow (20 cm^3 min^{-1}) at ambient pressure from room temperature to 1223 K. The Fourier transform infrared (FT-IR) spectra for the M–Eu–Ca–Mo–O tartrate gel precursors were recorded with a PerkinElmer Frontier FT-IR spectrometer. The corresponding gel precursors heat-treated at different temperatures, and the residual powders that were left after the thermal treatment were additionally investigated by x-ray diffraction (XRD) analysis. The XRD patterns were recorded in air at room temperature with a powder x-ray diffract meter Rigaku MiniFlex II using CuKα_1 radiation. The patterns were recorded at the standard rate of 1.5 2θ/min^{-1}. In addition, the Rietveld refinement of the obtained XRD patterns was performed using X'Pert High-Score Plus software. The scanning electron microscope (SEM) Hitachi SU-70 was used to study the surface morphology and microstructure of the obtained ceramic samples. Finally, the measurements of photoluminescence (PL) and photoluminescence excitation (PLE) spectra were taken by using a PerkinElmer LS-55 spectrometer.

Results and discussion

Thermal analysis

The TG/DTG/DSC measurements of the M–Eu–Ca−Mo–O tartrate (M=Li, Na, K, Rb, and Cs) gel precursors, which were taken up to 1223 K at a heating rate of 20° min^{-1} in flowing air (20 cm^3 min^{-1}) at ambient pressure with a sample mass of about 10 mg are shown in Fig. 2, respectively.

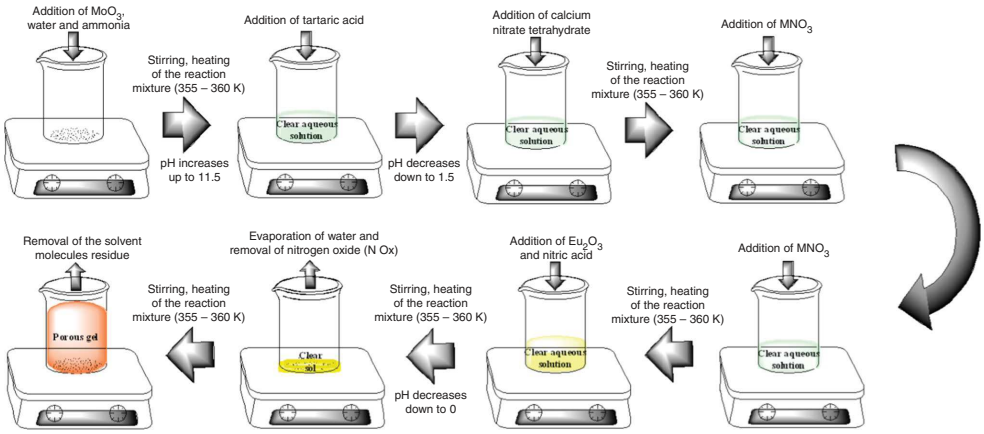

Fig. 1 Synthesis scheme of the sol–gel preparation for the M–Eu–Ca–Mo–O tartrate gel precursors and $M_{0.05}Eu_{0.05}Ca_{0.9}MoO_4$ (M=Li, Na, K, Rb, Cs) ceramics

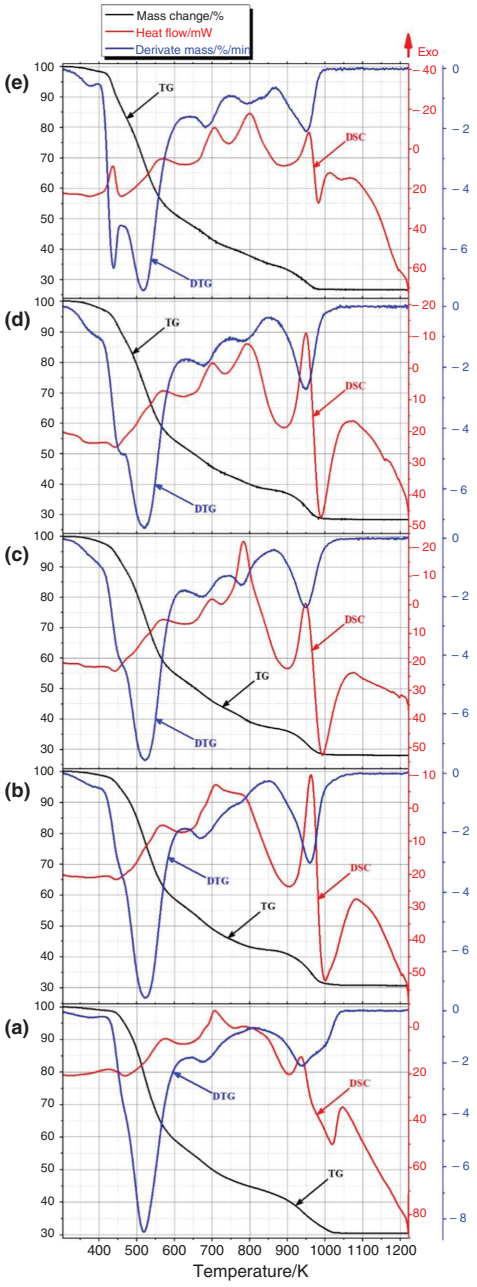

Fig. 2 Combined TG–DTG–DSC curves of the Li–Eu–Ca–Mo–O tartrate gel precursor for $Li_{0.05}Eu_{0.05}Ca_{0.9}MoO_4$ (**a**), $Na_{0.05}Eu_{0.05}Ca_{0.9}MoO_4$ (**b**), $K_{0.05}Eu_{0.05}Ca_{0.9}MoO_4$ (**c**), $Rb_{0.05}Eu_{0.05}Ca_{0.9}MoO_4$ (**d**) and $Cs_{0.05}Eu_{0.05}Ca_{0.9}MoO_4$ (**e**) ceramics

Tables 2–6 show data, which were deducted from Fig. 2 and supplements quantitatively the general view of thermal decomposition processes in M–Eu–Ca–Mo–O tartrate gel precursors.

In addition, it is also important to note that in the frame of this study a new investigation approach to the analysis of the thermal processes was applied during which it is possible to reveal and to calculate the overlapping chemical and physical changes. In this case, the nature of alkali metal plays a very important role, taking into account that all synthesis procedures were made in similar manner, and the way of the thermal decomposition of initial gels was not identical. These discrepancies allow us to estimate the influence of both the initial composition to the crystallization for the final ceramic materials and thermal decomposition of intermediate organic parts from the gel precursors. Especially, an important role goes to the exothermic effect in the DSC curve between 400 and 450 K of temperature, which thermal behaviour tends to increase by changing the nature of alkali metal in the sample. This exothermic effect was identified from the slope of DTG curves, which gradually converts into the peak by changing the nature of alkali metal in the initial composition. In our previous report, [37] we suggested a stage between the temperature of 421 K and 493 K assign to the thermal decomposition of tartaric-acids dimer ($C_8H_8O_{10}$) into carbon monoxide (CO), carbon dioxide (CO_2) and two acetic acid (CH_3COOH) molecules. Meanwhile, by investigating this case, it is clear that the decomposition effect of tartaric-acids dimer is not very well pronounced and this process is closely related to the evaporation and removal of volatile components from the M–Eu–Ca–Mo–O tartrate gel. Besides, an enhanced ionic character of the alkali metal reduces the coordination of unreacted tartaric acid molecules, for that reason their decomposition into the carbon oxides occurs at much lower temperature than was expected. Nevertheless, the decomposition of unreacted tartaric acid occurs up to 568 K in all cases with the mass loss of about 36–43%. The mass of the gel precursors during this decomposition stage, in the range of temperature from 300 K to 568 K, decreases by 36–37%, and this is typical for $Li_{0.05}Eu_{0.05}$ $Ca_{0.9}MoO_4$ and $Na_{0.05}Eu_{0.05}$ $Ca_{0.9}MoO_4$ initial composition compounds. Meanwhile, the mass change for K–Eu–Ca–Mo–O and Rb–Eu–Ca–Mo–O tartrate gel precursors increases to 40.261% and 41.176%, respectively, indicating enhanced ionic character of corresponding alkali metals. Moreover, the thermal behaviour of DSC curve clearly shows several heat

Table 2 Thermoanalytical data of the Li–Eu–Ca–Mo–O tartrate gel precursor for $Li_{0.05}Eu_{0.05}Ca_{0.9}MoO_4$ ceramic

Stage No.	Range of temperature/K	Mass			Heat			
		Change/%	Onset/K	Residual/%	Flow/mJ	Onset/K	End/K	Enthalpy/J g^{-1}
I	**299.15–567.71**	**36.340**	–	**63.660**	**|3417.3295|**	–	–	**|338.6415|**
	299.15–423.68	1.179	300.20	98.821	365.822	301.55	404.32	36.2513
	335.15–472.24	5.800	447.99	94.068	–524.763	383.35	464.31	–52.0016
	423.68–**567.71**	34.997	545.60	**63.660**	1757.492	435.12	555.62	174.1593
	476.16–651.87	38.937	553.25	54.645	–1538.505	516.39	619.13	–152.4586
II	**567.71–837.64**	**20.243**	–	**43.417**	**|5595.698|**	–	–	**|554.50745|**
	567.71–706.09	14.506	569.37	49.554	1987.493	578.00	702.20	196.9512
	651.87–745.76	7.222	690.09	47.226	–1263.800	680.80	739.16	–125.2367
	706.09–**837.68**	6.021	757.92	**43.417**	512.477	715.29	826.02	50.7841
	752.76–899.13	6.165	872.98	40.680	–2125.351	–	884.56	–210.6123
III–IV	**837.64–1047.87**	**12.858**	–	**30.559**	**|11,965.847|**			**|1185.75945|**
	837.64–938.93	6.281	901.72	37.235	1630.386	853.23	933.35	161.5636
	899.13–1016.58	9.677	964.84	30.940	–2001.290	909.78	966.97	–198.3185
	938.93–**1047.87**	6.673	975.40	**30.559**	4262.548	943.70	1039.35	422.3986
	1016.58–1214.46	0.408	1016.65	30.559	–6017.895	1023.88	1209.91	–596.3452
V	**1047.87–1219.40**	**0**	–	**30.559**	**|3008.9475|**	–	–	**|298.1726|**

Bold values denote important points which summarize and relate obtained results in each stage of the thermal decomposition of the gel precursors

Table 3 Thermoanalytical data of the Na–Eu–Ca–Mo–O tartrate gel precursor for $Na_{0.05}Eu_{0.05}Ca_{0.9}MoO_4$ ceramic

Stage No.	Range of temperature/K	Mass			Heat			
		Change/%	Onset/K	Residual/%	Flow/mJ	Onset/K	End/K	Enthalpy/J g^{-1}
I	**298.54–566.54**	**36.662**	–	**63.338**	**|1262.226|**	–	–	**|123.58265|**
	298.54–419.54	1.719	300.50	98.281	226.062	302.31	406.41	22.1304
	366.02–447.46	3.612	433.19	95.978	–93.623	388.65	439.89	–9.1653
	422.23–519.29	19.718	487.93	78.200	684.940	–	517.40	67.0524
	457.87–538.74	22.913	492.14	71.294	–28.362	505.18	537.85	–2.7765
	519.29–**566.54**	14.981	532.95	**63.338**	16.569	–	549.07	1.6220
	538.74–634.95	15.954	541.68	55.573	–425.340	539.29	604.06	–41.6387
II	**566.54–791.67**	**19.756**	–	**43.582**	**|2340.106|**	–	–	**|229.0853|**
	566.54–671.01	11.361	676.73	51.753	854.829	572.39	669.81	83.6837
	634.95–685.80	4.960	668.36	50.284	–26.063	662.24	672.43	–2.5515
	671.01–705.97	3.620	671.92	48.668	32.084	–	694.64	3.1409
	685.80–733.87	3.863	697.88	46.464	–286.833	686.37	726.13	–28.0796
	705.97–**791.67**	4.947	733.62	**43.582**	71.851	720.17	774.70	7.0338
	733.87–909.17	6.279	734.87	40.293	–1711.552	741.97	849.23	–167.5529
III–IV	**791.67–1081.89**	**12.944**	–	**30.638**	**|29,800.0545|**	–	–	**|2917.27405|**
	791.67–964.67	8.895	960.52	34.637	9905.070	795.43	958.53	969.6593
	909.17–997.02	8.959	961.69	31.491	–5755.782	927.70	988.22	–563.4637
	964.67–**1081.89**	3.878	971.69	**30.638**	9153.367	970.79	1067.04	896.0614
	997.02–1.204.68	0.769	1004.57	30.670	–8260.119	1020.85	808.74	–808.6264
V	**1081.89–1223**	**0.047**		**30.591**	**|4130.0595|**	–	–	**|404.3132|**

Bold values denote important points which summarize and relate obtained results in each stage of the thermal decomposition of the gel precursors

Table 4 Thermoanalytical data of the K−Eu–Ca−Mo–O tartrate gel precursor for $K_{0.05}Eu_{0.05}Ca_{0.9}MoO_4$ ceramic

Stage No.	Range of temperature/K	Mass			Heat			
		Change/%	Onset/K	Residual/%	Flow/mJ	Onset/K	End/K	Enthalpy/J g^{-1}
I	**300–566.72**	**40.268**	–	**59.732**	**|833.988|**	–	–	**|82.66305|**
	300–363.15	0.257	300.45	99.743	41.258	302.29	–	4.0894
	320–363	0.412	358.34	99.588	–37.501	–	357.54	–3.7170
	363.15–417	2.357	407.07	97.485	75.906	349.83	–	7.5237
	363.14–443.15	4.557	426.84	94.967	–115.882	386.74	437.04	–11.4859
	417.15–470.15	7.755	442.80	89.448	192.597	423.94	467.02	19.0898
	443.15–496.15	11.268	448.49	83.068	–18.070	455.73	–	–1.7911
	470.15–520.15	14.713	491.53	74.26	54.380	–	514.74	5.3900
	496.15–**566.72**	13.003	508.91	**59.732**	–29.444	–	498.42	–2.9184
	566.72–643.15	17.560	563.50	51.746	–537.900	537.38	615.67	–53.3155
II	**566.72–784.73**	**19.452**	–	**40.28**	**|6133.3665|**	–	–	**|607.926|**
	566.72–695.34	13.529	651.38	46.22	1175.772	–	687.73	116.5399
	643.15–729	6.807	655.42	44.018	–475.431	661.97	720.51	–47.1237
	695.34–**784.73**	6.153	760.87	**40.28**	1574.903	–	777.32	156.1010
	729.15–883.15	7.088	799.64	36.795	–5276.621	750.70	829.90	–523.0073
III–IV	**784.73–1058.52**	**12.079**	**800.83**	**28.201**	**|28,301.855|**	–	–	**|2805.219|**
	784.73–950.46	7.425	800.83	32.848	9286.744	789.37	944.07	920.4821
	883.15–991.64	7.889	906.92	28.683	–5329.557	913.90	983.01	–528.2542
	950.46–**1058.52**	3.780	973.53	**28.201**	7400.922	958.42	1044.15	733.5635
	991.64–1196	0.514	1100.94	28.092	–7292.643	1001.77	1157.00	–722.8311
V	**1058.52–1223**	**0.142**	–	**28.059**	**|3646.3215|**	–	–	**|361.41555|**

Bold values denote important points which summarize and relate obtained results in each stage of the thermal decomposition of the gel precursors

changes, which are less defined in the range from about 450 K to 550 K of temperature. Finally, the last, fifth case is characterized by the biggest mass change, which is equal to 43.323%; however, the DSC curve has similar behaviour to those cases, which are shown in Fig. 2a, b.

As shown in Tables 2–6, stage II corresponds to the decomposition of metal tartrates. The mass of the gel precursors during this decomposition stage, in the range of temperature from 563 K to 803 K, decreases by 18.8–22.7%, except $Li_{0.05}Eu_{0.05}Ca_{0.9}MoO_4$ case, when the mass loss of about 20.2% ends at 837.5 K. The heat-treatment temperature of about 573 K is important because of the beginning of crystallization for the final $CaMoO_4$ double oxide. Furthermore, this endothermic process is competing with gradual decomposition of metal tartrates, which takes place until the partial stabilization of TG curve at about 873 K of temperature. By further increasing the heating temperature from 823 to 973 K, the mass change of the samples varies from 11.1 to 12.9% and is directly related to the burning of carbon-based residue, which is formed from the tartaric acid and metal tartrates at lower temperatures. Finally, the last mass change of the M−Eu–Ca−Mo–O tartrate gel precursors in the range of temperature from 1047 to 1223 K does not exceed 0.1%, and, except endothermic behaviour because of further growth of crystalline phases, no significant changes in the DSC curve were identified. Besides, it is important to note that in all cases, except for $Li_{0.05}Eu_{0.05}Ca_{0.9}MoO_4$ ceramic, the tendency of slight mass changes above 973 K was observed. The main reason of these changes is directly related to the partial releasing and evaporation of molybdenum oxide from the multicomponent oxide.

In order to show both the decomposition process of tartaric acid in the gel precursors and the overall mass change peculiarities of volatile components in the gels according to the gas atmosphere, the thermal analysis of as-prepared samples was also performed under inert flow. In this case, the TG/DTG/DSC measurements of the M–Eu–Ca−Mo–O tartrate (M=Li, Na, K, Rb, and Cs) gel precursors, which were carried out up to 1200 K at a heating rate of 20° min^{-1} in flowing nitrogen (20 cm^3 min^{-1}) at ambient pressure with a sample mass of about 5 mg, are shown in Fig. 3, respectively.

From these results, one is clear that the decomposition stages of tartaric acid only slightly depend according to the

Table 5 Thermoanalytical data of the Rb–Eu–Ca–Mo–O tartrate gel precursor for $Rb_{0.05}Eu_{0.05}Ca_{0.9}MoO_4$ ceramic

Stage No.	Range of temperature/K	Mass			Heat			
		Change/%	Onset/K	Residual/%	Flow/mJ	Onset/K	End/K	Enthalpy/J g^{-1}
I	**299.65–566.19**	**41.176**	–	**58.824**	**|968.5145|**	–	–	**|96.70655|**
	299.65–341.30	0.191	332.47	99.809	21.426	301.89	309.68	2.1394
	311.49–362.61	0.658	359.52	99.342	–76.810	318.40	356.71	–7.6695
	341.30–419.11	3.123	411.80	96.78	184.814	346.82	403.29	18.4537
	362.61–443.88	5.967	412.08	93.451	–89.368	392.30	437.43	–8.9234
	419.11–467.32	8.872	449.18	87.89	182.701	423.33	466.79	18.2428
	443.28–462.24	4.444	447.68	89.078	14.545	443.31	462.11	1.4524
	452.06–488.34	8.733	469.46	82.715	–14.978	455.42	–	–1.4955
	467.32–513.95	13.153	507.30	74.796	58.483	473.33	513.86	5.8396
	488.34–540.30	17.470	512.51	65.47	–44.617	507.34	–	–4.4550
	513.95–**566.19**	15.676	514.07	**58.824**	23.612	521.77	551.35	2.3577
	538.58–636	16.082	534.84	51.387	–514.321	537.12	602.70	–51.3551
II	**566.19–800.49**	**18.842**	–	**39.982**	**|4880.842|**	–	–	**|487.35315|**
	566.19–697.16	12.879	694.33	45.884	1415.820	573.47	693.07	141.3699
	648.68–737.53	6.915	691.67	43.312	–678.975	668.83	729.14	–67.7958
	697.16–**800.49**	5.841	701.52	**39.982**	847.161	708.83	779.09	84.5892
	708.83–883	7.419	722.70	37.712	–3363.451	751.14	847.33	–335.8414
III–IV	**800.49–1066.81**	**11.314**	–	**28.668**	**|29,664.8425|**	–	–	**|2962.04135|**
	800.49–949.68	7.338	943.04	32.567	7739.260	814.75	944.69	772.7669
	883–988.42	8.647	940.99	29.120	–6127.124	913.50	980.54	–611.7948
	949.68–**1066.81**	3.998	981.70	**28.668**	7613.912	957.72	1041.22	760.2508
	988.42–1219	0.524	1045.41	28.596	–13,005.642	995.33	1115.96	–1298.6163
V	**1066.81–1223**	**0.072**	–	**28.596**	**|6502.821|**	–	–	**|649.30815|**

Bold values denote important points which summarize and relate obtained results in each stage of the thermal decomposition of the gel precursors

heating atmosphere. The heating range in case of inert gas flow from 303 to 770 K (Fig. 3 left side) is almost identical compared with the cases presented in Fig. 2. Moreover, the behaviour of TG curves remains the same up to 873 K of temperature, and this concludes about similar heat-treatment effects, which are confirmed by DSC curves. Finally, the last mass change of the M–Eu–Ca–Mo–O tartrate gel precursors in the range of temperature from 873 to 950 K is attributed to the decomposition of a mixture from carbon and oxygen atoms, which are composed from the gel residue. This effect is confirmed by the results obtained from the K–Eu–Ca–Mo–O sample, where the behaviour of TG and DSC curves reiterates only in a more stretched range of temperature compared with the measurement in air flow.

In conclusion, it is also important to note that the total mass loss of all gel precursors well matches with the results obtained in an air atmosphere, while a prior mass change for the K–Eu–Ca–Mo–O sample above 873 K of temperature has no sufficient influence on the results, which were obtained in other heating conditions. Therefore, such an action is important only in the inert atmosphere and it is determined by the stability of final ceramics in a reducing environment. In this case, the combustion process in the air at temperatures above 873 K eliminates any specific conditions created by elemental carbon present in the sample.

FT-IR analysis

In order to show the characteristic group frequencies for the gel precursors in the mid-infrared region, the infrared spectroscopy (FT-IR) was performed. Corresponding FT-IR spectra are shown in Fig. 4, respectively.

According to the initial composition of the obtained M–Eu–Ca–Mo–O tartrate gel precursors, it is obvious that the stretching bands, which belong to the functional group frequencies of tartaric acid, in the infrared spectra are expected. It is well known that carboxylic acids (RCOOH) exist as dimers due to strong intermolecular hydrogen bonding. These compounds show a strong broad O–H stretching band in the 3300–2500 cm^{-1} range. The C=O stretching

band of the dimer is observed near 1700 cm^{-1}, while the free acid band is observed at higher wavenumbers (1760 cm^{-1}). In addition, carboxylic acids show characteristic C–O stretching and in-plane and out-of-plane O–H bending bands at 1240, 1430 and 930 cm^{-1}, respectively [38].

The range from 1660 to 1620 cm^{-1} is characteristic to the nitrate NO_2 asymmetric stretching. This band overlaps with the intensive stretching of the C=O group at 1700 cm^{-1} in the carboxylic acids. Moreover, the weak band of nitrate NO_2 symmetric stretching in the range from 1300 to 1270 am^{-1} is also observed. In addition, barely visible characteristic peak of nitrate N–O stretching in the range from 870 to 840 cm^{-1} was detected. Meanwhile, the characteristic stretching for the nitrate NO_2 bending (710–690 cm^{-1}) was not found [38]. Such a result explains the emergence of a peak in the DSC curve at 413.37 K, which tends to increase from the Li–Eu–Ca–Mo–O to Cs–Eu–Ca–Mo–O sample. This exothermal effect is closely related to the decomposition processes of the nitrate residue that left in the gel precursors after the evaporation procedure. The amount of corresponding nitrates in the gel precursors increases negligible and slightly influences the decomposition of the tartaric-acids dimer in the range of temperature from 416.55 to 455.48 K.

Fig. 3 Combined TG−DTG−DSC curves of the Li–Eu–Ca–Mo–O tartrate gel precursor for $Li_{0.05}Eu_{0.05}Ca_{0.9}MoO_4$ (**a**), $Na_{0.05}Eu_{0.05}Ca_{0.9}MoO_4$ (**b**), $K_{0.05}Eu_{0.05}Ca_{0.9}MoO_4$ (**c**), $Rb_{0.05}Eu_{0.05}Ca_{0.9}MoO_4$ (**d**) and $Cs_{0.05}Eu_{0.05}Ca_{0.9}MoO_4$ (**e**) ceramics. The overall view of the curves is shown on the right, and the highlighted temperature range from 303 to 770 K is presented on the left

The characteristic infrared bands of five-atom inorganic molecules, as well as for CrO_4^{2-} group, commonly are at the 890 cm^{-1} and 378 cm^{-1} of wavenumber. In all cases, the band at about 890 cm^{-1} observed in the FT-IR spectra, which is attributed to the vibrations of MoO_4^{2-} functional group [38]. Moreover, the vibrational frequencies of tetrahedral MoO_4^{2-}-type compound for their M–O vibrations are observed at 897 cm^{-1} (ν_1) and 837 cm^{-1} (ν_3), respectively [39]. Finally, the metal–oxygen characteristic vibrations similar to those observed in the crystalline Powellite structure of $CaMoO_4$ are attributed to the range from 800 to 500 cm^{-1} [40].

Table 6 Thermoanalytical data of the Cs−Eu–Ca−Mo–O tartrate gel precursor for $Cs_{0.05}Eu_{0.05}Ca_{0.9}MoO_4$ ceramic

Stage No.	Range of temperature/K	Mass			Heat			
		Change/%	Onset/K	Residual/%	Flow/mJ	Onset/K	End/K	Enthalpy/J g^{-1}
I	**299.79–561.54**	**43.323**	–	**56.677**	**|4359.4235|**	–	–	**|428.23425|**
	299.79–343.22	0.223	311.10	99.777	75.404	300.10	342.06	7.4071
	307.22–380.70	1.122	366.67	98.878	–47.110	333.49	361.68	–4.6277
	343.22–416.55	1.795	366.93	97.945	284.770	348.44	408.20	27.9735
	380.70–437.25	5.754	428.13	93.151	598.481	380.91	432.13	58.7899
	416.55–455.48	10.374	448.27	87.592	–720.661	420.79	449.57	–70.7919
	437.25–501.66	18.169	484.88	74.974	1301.827	440.10	501.07	127.8809
	455.48–**561.54**	30.676	486.13	**56.677**	326.086	455.71	533.85	32.0320
	487.08– 655.99	32.384	487.97	47.016	–2010.169	513.30	654.22	–197.4625
II	**561.54–800.77**	**18.833**	–	**37.844**	**|8610.0095|**	–	–	**|584.026|**
	561.54–704.83	13.810	688.15	42.964	2799.474	–	513.86	274.9975
	655.99–747.23	6.571	691.16	40.471	–1469.809	668.70	735.49	–144.3820
	704.83–**800.77**	5.409	710.50	**37.844**	1676.101	710.10	786.61	164.6465
	747.23–879.37	6.480	842.71	34.237	–3319.082	760.05	844.12	–326.0395
III–IV	**800.77–1007.27**	**11.152**	–	**26.692**	**|14,321.867|**	–	–	**|1406.86315|**
	800.77–958.45	9.360	936.22	28.315	6359.627	808.79	954.96	624.7178
	879.37–981.29	7.226	937.04	27.068	–3761.429	919.90	978.40	–369.4920
	985.45–**1007.27**	1.528	969.50	**26.692**	2027.409	963.81	1002.90	199.1561
	981.29–1042.75	0.185	983.51	26.721	–1027.722	986.96	1039.12	–100.9550
V	**1007.27–1220.77**	**0.169**	–	**26.523**	**|5297.426|**	–	–	**|520.376|**
	1007.27–1121.24	0.085	–	26.683	220.355	1028.07	1050.37	21.6459
	1042.75–1188.61	0.094	–	26.635	–4061.851	1045.16	1179.22	–399.0031
	1121.24–**1220.77**	0.090	–	**26.523**	501.359	1151.11	–	49.2495

Bold values denote important points which summarize and relate obtained results in each stage of the thermal decomposition of the gel precursors

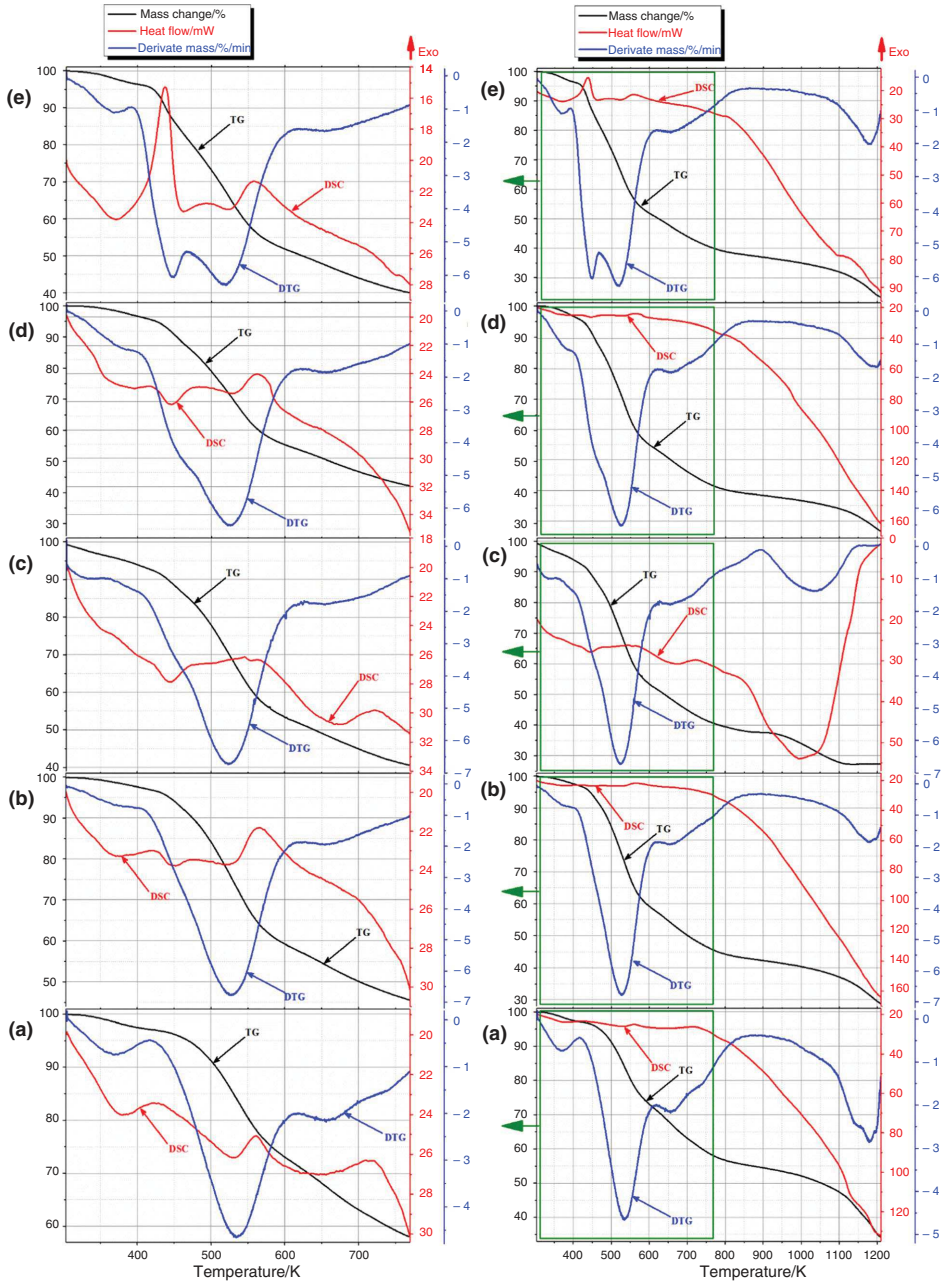
Mass change/%
Heat flow/mW
Derivate mass/%/min
Exo
(e)
(d)
(c)
(b)
(a)
TG
DSC
DTG
Temperature/K

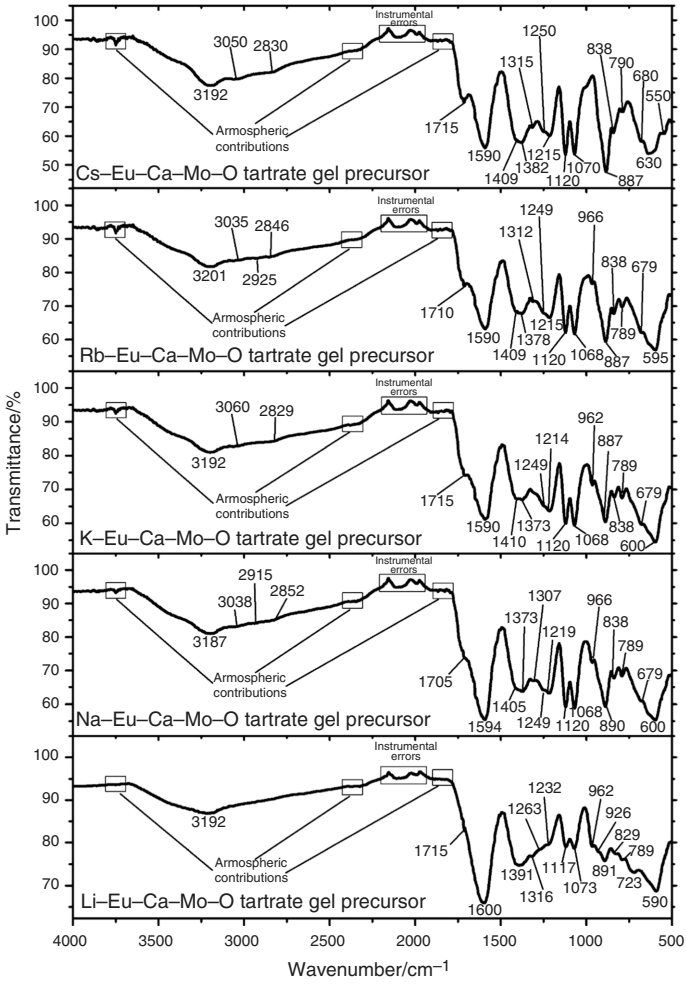

Fig. 4 FT-IR transmittance spectra of the M–Eu–Ca–Mo–O tartrate gel precursors dried at 393 K of temperature

X-ray diffraction

The powder x-ray diffraction (XRD) patterns of the Li–Eu–Ca−Mo–O tartrate gel precursor heat-treated at different temperatures shown in the top nine panels of Fig. 5 are well matched with the standard ICSD card of $CaMoO_4$ that is presented in the bottom panel.

No characteristic peaks attributable to the impurities by increasing heat-treatment temperature from 623 to 1273 K were identified. In addition, it is important to mention that drying of Li–Eu–Ca−Mo–O tartrate gel precursor for $Li_{0.05}Eu_{0.05}Ca_{0.9}MoO_4$ ceramic at 393 K showed fully amorphous character and no characteristic peaks to any crystalline compound from the XRD pattern were found. Besides, these results are in a good agreement with the TG−DTG−DSC data, when the crystallization of the final tetragonal phase below 623 K of temperature was estimated. Moreover, an important conclusion was made, by comparing these analysis

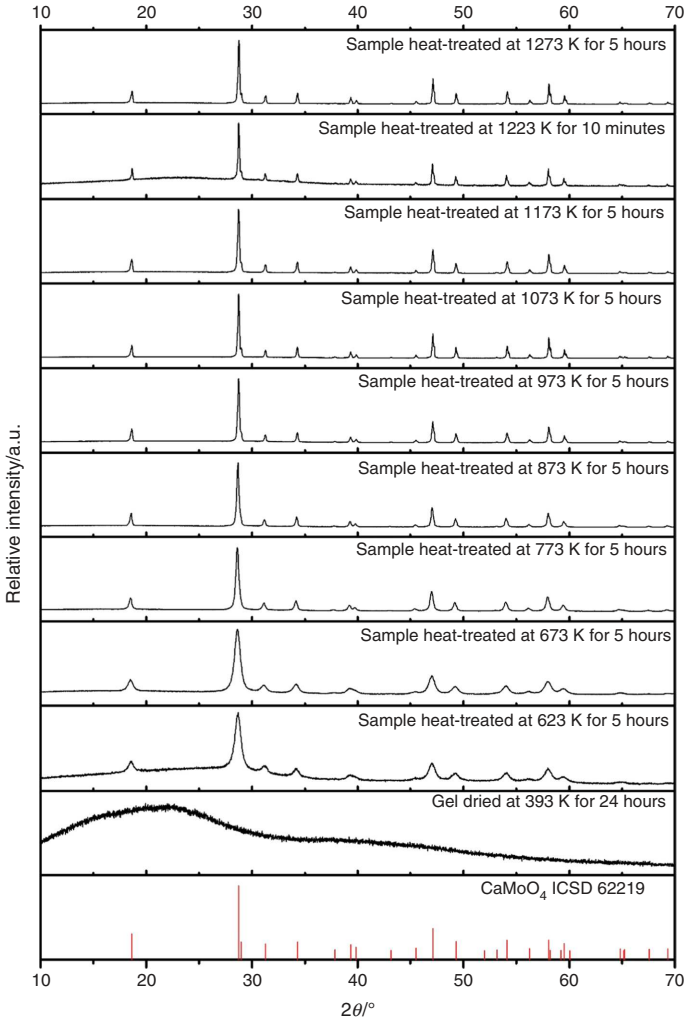

Fig. 5 Standard ICSD card of $CaMoO_4$ and XRD patterns of the Li–Eu–Ca−Mo–O tartrate gel precursor dried at 393 K for 24 h and heat-treated at temperatures of 623 K, 673 K, 773 K, 873 K, 973 K, 1073 K, 1173 K and 1273 K for 5 h in air

techniques that the crystallization of the final ceramic starts from about 568 K immediately after the initial decomposition of unreacted tartaric acid molecules into the elemental carbon and carbon oxides. According to above subject, the experimental and analysis results of other samples showed almost identical peculiarities. The end of the initial decomposition of tartaric acid for $Li_{0.05}Eu_{0.05}Ca_{0.9}MoO_4$, $Na_{0.05}Eu_{0.05}Ca_{0.9}MoO_4$, $K_{0.05}Eu_{0.05}Ca_{0.9}MoO_4$, $Rb_{0.05}Eu_{0.05}Ca_{0.9}MoO_4$ ceramics was similar and equal to 566 K of temperature, respectively. Meanwhile, the start of crystallization for $Cs_{0.05}Eu_{0.05}Ca_{0.9}MoO_4$ compound began at slightly lower 561 K of temperature. This effect was assigned to the increased ionic character of caesium, which plays a much more important role during the sol–gel formation stage, comparing it with other cases.

In order to prove that the crystallization of the final ceramics plays crucial role not only for the thermal decomposition of metal tartrates, but also strongly affects the

Table 7 Crystallite sizes, lattice parameter and density for the $M_{0.05}Eu_{0.05}Ca_{0.9}MoO_4$ (M=Li, Na, K, Rb, Cs) ceramics heat-treated at different temperatures for 5 and 0.15 h in air

Sample	Heat-treating temperature/K	Duration/h	Crystallite size/nm	Lattice parameter/pm		Density/g cm^{-3}
				a	c	
$Li_{0.05}Eu_{0.05}Ca_{0.9}MoO_4$	623	5	10.49	522.373	1143.005	4.26
$Na_{0.05}Eu_{0.05}Ca_{0.9}MoO_4$	623	5	10.83	522.397	1143.158	4.26
$K_{0.05}Eu_{0.05}Ca_{0.9}MoO_4$	623	5	8.20	522.358	1143.056	4.26
$Rb_{0.05}Eu_{0.05}Ca_{0.9}MoO_4$	623	5	8.30	522.270	1142.526	4.26
$Cs_{0.05}Eu_{0.05}Ca_{0.9}MoO_4$	623	5	8.98	522.427	1142.807	4.26
$Li_{0.05}Eu_{0.05}Ca_{0.9}MoO_4$	673	5	13.54	522.102	1142.770	4.26
$Na_{0.05}Eu_{0.05}Ca_{0.9}MoO_4$	673	5	13.17	522.202	1142.855	4.26
$K_{0.05}Eu_{0.05}Ca_{0.9}MoO_4$	673	5	11.29	522.307	1143.094	4.26
$Rb_{0.05}Eu_{0.05}Ca_{0.9}MoO_4$	673	5	11.37	522.298	1143.269	4.26
$Cs_{0.05}Eu_{0.05}Ca_{0.9}MoO_4$	673	5	13.89	522.285	1143.098	4.26
$Li_{0.05}Eu_{0.05}Ca_{0.9}MoO_4$	773	5	30.77	522.301	1142.666	4.26
$Na_{0.05}Eu_{0.05}Ca_{0.9}MoO_4$	773	5	26.78	522.471	1142.881	4.26
$Rb_{0.05}Eu_{0.05}Ca_{0.9}MoO_4$	773	5	25.61	522.429	1142.851	4.26
$Ca_{0.9}Rb_{0.05}Eu_{0.05}MoO_4$	773	5	22.61	522.540	1143.104	4.26
$Cs_{0.05}Eu_{0.05}Ca_{0.9}MoO_4$	773	5	20.48	522.509	1143.229	4.26
$Li_{0.05}Eu_{0.05}Ca_{0.9}MoO_4$	873	5	49.35	522.060	1142.922	4.26
$Na_{0.05}Eu_{0.05}Ca_{0.9}MoO_4$	873	5	42.79	522.101	1142.953	4.26
$K_{0.05}Eu_{0.05}Ca_{0.9}MoO_4$	873	5	39.58	522.462	1144.031	4.25
$Rb_{0.05}Eu_{0.05}Ca_{0.9}MoO_4$	873	5	41.06	522.452	1143.169	4.26
$Cs_{0.05}Eu_{0.05}Ca_{0.9}MoO_4$	873	5	47.10	522.227	1142.464	4.26
$Li_{0.05}Eu_{0.05}Ca_{0.9}MoO_4$	973	5	69.49	522.193	1142.434	4.26
$Na_{0.05}Eu_{0.05}Ca_{0.9}MoO_4$	973	5	62.38	522.292	1142.858	4.26
$K_{0.05}Eu_{0.05}Ca_{0.9}MoO_4$	973	5	69.92	522.776	1144.652	4.25
$Rb_{0.05}Eu_{0.05}Ca_{0.9}MoO_4$	973	5	72.52	522.545	1143.326	4.25
$Cs_{0.05}Eu_{0.05}Ca_{0.9}MoO_4$	973	5	53.48	522.464	1142.756	4.26
$Li_{0.05}Eu_{0.05}Ca_{0.9}MoO_4$	1073	5	96.87	522.215	1142.095	4.26
$Na_{0.05}Eu_{0.05}Ca_{0.9}MoO_4$	1073	5	78.51	522.498	1143.205	4.26
$K_{0.05}Eu_{0.05}Ca_{0.9}MoO_4$	1073	5	52.55	523.019	1145.099	4.24
$Rb_{0.05}Eu_{0.05}Ca_{0.9}MoO_4$	1073	5	54.78	522.707	1143.638	4.25
$Cs_{0.05}Eu_{0.05}Ca_{0.9}MoO_4$	1073	5	90.49	522.514	1142.921	4.26
$Li_{0.05}Eu_{0.05}Ca_{0.9}MoO_4$	1173	5	71.10	522.246	1142.217	4.26
$Na_{0.05}Eu_{0.05}Ca_{0.9}MoO_4$	1173	5	81.91	522.492	1143.019	4.26
$K_{0.05}Eu_{0.05}Ca_{0.9}MoO_4$	1173	5	78.28	522.749	1143.999	4.25
$Rb_{0.05}Eu_{0.05}Ca_{0.9}MoO_4$	1173	5	135.13	522.668	1143.655	4.25
$Cs_{0.05}Eu_{0.05}Ca_{0.9}MoO_4$	1173	5	84.42	522.481	1142.981	4.26
$Li_{0.05}Eu_{0.05}Ca_{0.9}MoO_4$	1223	0.15	110.36	522.939	1144.544	4.24
$Na_{0.05}Eu_{0.05}Ca_{0.9}MoO_4$	1223	0.15	336.88	523.020	1144.328	4.24
$K_{0.05}Eu_{0.05}Ca_{0.9}MoO_4$	1223	0.15	141.21	523.385	1145.669	4.23
$Rb_{0.05}Eu_{0.05}Ca_{0.9}MoO_4$	1223	0.15	190.14	523.227	1145.105	4.24
$Cs_{0.05}Eu_{0.05}Ca_{0.9}MoO_4$	1223	0.15	105.76	523.113	1144.228	4.24
$Li_{0.05}Eu_{0.05}Ca_{0.9}MoO_4$	1273	5	85.81	522.351	1142.570	4.26
$Na_{0.05}Eu_{0.05}Ca_{0.9}MoO_4$	1273	5	146.74	522.586	1143.192	4.25
$K_{0.05}Eu_{0.05}Ca_{0.9}MoO_4$	1273	5	57.37	522.564	1143.153	4.26
$Rb_{0.05}Eu_{0.05}Ca_{0.9}MoO_4$	1273	5	53.45	522.482	1142.924	4.26
$Cs_{0.05}Eu_{0.05}Ca_{0.9}MoO_4$	1273	5	76.37	522.497	1142.939	4.26

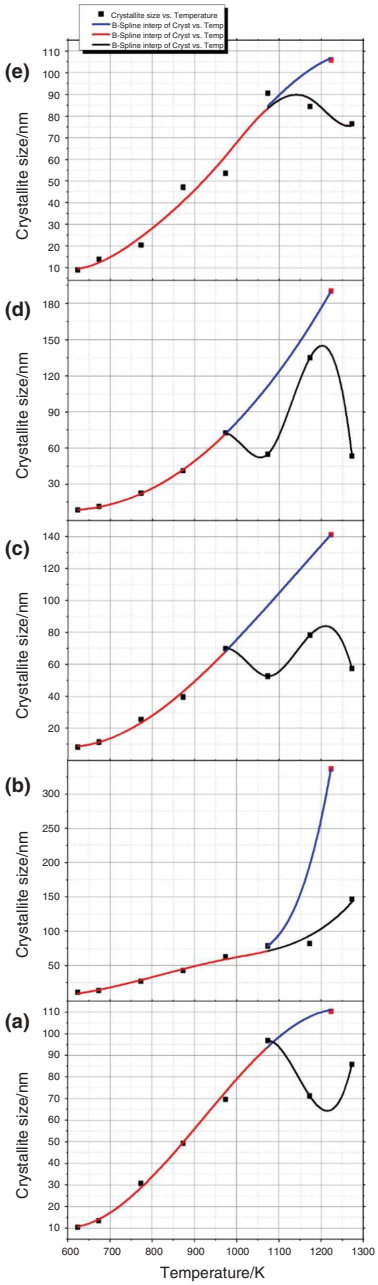

Fig. 6 Plot of crystallite size versus heat-treatment temperature for $Li_{0.05}Eu_{0.05}Ca_{0.9}MoO_4$ (**a**), $Na_{0.05}Eu_{0.05}Ca_{0.9}MoO_4$ (**b**), $K_{0.05}Eu_{0.05}Ca_{0.9}MoO_4$ (**c**), $Rb_{0.05}Eu_{0.05}Ca_{0.9}MoO_4$ (**d**) and $Cs_{0.05}Eu_{0.05}Ca_{0.9}MoO_4$ (**e**) ceramics

physical properties, the Rietveld refinement analysis of XRD patterns for the synthesized multicomponent oxides was applied. The crystallite sizes and lattice parameter for the $Li_{0.05}Eu_{0.05}Ca_{0.9}MoO_4$, $Na_{0.05}Eu_{0.05}Ca_{0.9}MoO_4$, $K_{0.05}Eu_{0.05}Ca_{0.9}MoO_4$, $Rb_{0.05}Eu_{0.05}Ca_{0.9}MoO_4$, and $Cs_{0.05}Eu_{0.05}Ca_{0.9}MoO_4$ compounds heat-treated at different temperatures are shown in Table 7.

The dependency of the crystallite size versus temperature, collected from the Table 7, is shown in Fig. 6, respectively.

From these curve graphs, it is clear that by increasing the sintering for $M_{0.05}Eu_{0.05}Ca_{0.9}MoO_4$ ceramics from 623 to 973 K, the values of crystallite size tend to increase; however, at somewhat higher temperatures their decreasing trends were observed. It is important to take attention to the fact that for $Li_{0.05}Eu_{0.05}Ca_{0.9}MoO_4$, $Na_{0.05}Eu_{0.05}Ca_{0.9}MoO_4$ and $Cs_{0.05}Eu_{0.05}Ca_{0.9}MoO_4$ ceramics, the decrease in the size for crystallites starts only above 1073 K of temperature. Meanwhile, the crystallites for $K_{0.05}Eu_{0.05}Ca_{0.9}MoO_4$ and $Rb_{0.05}Eu_{0.05}Ca_{0.9}MoO_4$ ceramics start to decrease already above 973 K. This effect is directly related to the crystallization of europium oxide [41], besides, depending on the nature of alkali metal in the ceramic, the growth of crystallites takes place at a different temperature.

SEM micrographs

According to such quite unexpected results obtained from the Rietveld refinement of XRD patterns, the surface morphology of $K_{0.05}Eu_{0.05}Ca_{0.9}MoO_4$ and $Rb_{0.05}Eu_{0.05}Ca_{0.9}MoO_4$ samples sintered at 1073 K for 5 h in air was also investigated. Corresponding SEM micrographs of these ceramics are shown in Fig. 7.

As shown in Fig. 7a, the surface of the K–Eu–Ca−Mo–O tartrate gel precursor for $K_{0.05}Eu_{0.05}Ca_{0.9}MoO_4$ ceramic heat-treated at 1073 K consists of spherical-like aggregated particles, which size varies from 200 nm to 1.2 µm. Meanwhile, the surface morphology of the Rb–Eu–Ca−Mo–O tartrate gel precursor for $Rb_{0.05}Eu_{0.05}Ca_{0.9}MoO_4$ ceramic (Fig. 7b) consists of similar particles to those observed from the case shown in Fig. 7a, which sizes varies from 200 nm to 1.8 µm, respectively. In conclusion, it is clear that surface of both samples is almost identical and the difference that comes into existence is only related to the degree of either agglomeration or aggregation of individual particles.

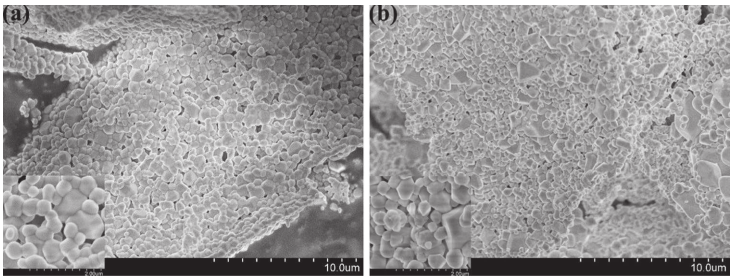

Fig. 7 SEM micrographs of M–Eu–Ca−Mo–O tartrate gel precursors for $K_{0.05}Eu_{0.05}Ca_{0.9}MoO_4$ (**a**) and $Rb_{0.05}Eu_{0.05}Ca_{0.9}MoO_4$ (**b**) ceramics heat-treated at 1073 K temperatures

PL analysis

In order to show the relation between the growth mechanism of the crystallites and luminescence properties of the ceramics prepared at 773 K of temperature, the photoluminescence (PL) measurement were applied. Corresponding PL excitation spectra of the $M_{0.05}Eu_{0.05}Ca_{0.9}MoO_4$ (where M=Li, Na, K, Rb, Cs) ceramics are shown in Fig. 8. The characteristic bands were registered with a fixed excitation at 395 nm of wavelength with emerged transitions from $^7F_0 \rightarrow {}^5L_6$ to $^7F_0 \rightarrow {}^5D_2$. This result matches well with UVLED and blue LED, respectively [42].

The PLE spectra (Fig. 9) show characteristic $^5D_0 \rightarrow {}^7F_J$ (J = 0, 1, 2, 3, 4) Eu^{3+} emission lines, which are summed up in Table 8 [43].

From the data displayed in the Table 8, it is clear that $^5D_0 \rightarrow {}^7F_3$ transition is forbidden, which is observed only in $Na_{0.05}Eu_{0.05}Ca_{0.9}MoO_4$, $Cs_{0.05}Eu_{0.05}Ca_{0.9}MoO_4$, $Rb_{0.05}Eu_{0.05}Ca_{0.9}MoO_4$ samples, and such phenomena are explained only as J—mixing [43]. The characteristic emissions of Eu^{3+} from $^5D_1$ are less common case; however, the peaks of $^5D_1 \rightarrow {}^7F_2$ and $^5D_1 \rightarrow {}^7F_1$ transitions were observed, which intensities are comparable with $^5D_0 \rightarrow {}^7F_1$ characteristic emission. Meanwhile, the $^5D_0 \rightarrow {}^7F_0$ transition is strictly forbidden according to the standard Judd–Ofelt theory; however, as was mentioned before, it could be explained by assuming that this transition is due to J—mixing [43]. Moreover, this transition is also an indicator of C_{nv}, C_n or C_s symmetries, because other symmetries do not produce observable spectral line. According to the results obtained in this work, a comparative study of the substitution effect on the intensity of luminescence by comparing intensity of $^5D_0 \rightarrow {}^7F_2$ transition was also performed. Despite the fact that this transition of 4f configuration is hypersensitive to the symmetry and crystal field of Eu^{3+} ion, the ratio R of intensities for $^5D_0 \rightarrow {}^7F_2$ and $^5D_0 \rightarrow {}^7F_1$ characteristic emissions was used instead and expressed as $I(^5D_0 \rightarrow {}^7F_2)/I(^5D_4 \rightarrow {}^7F_1)$, respectively. Figure 10 shows the before-mentioned ratio R distribution and its dependency from the crystallite size for $M_{0.05}Eu_{0.05}Ca_{0.9}MoO_4$ ceramics.

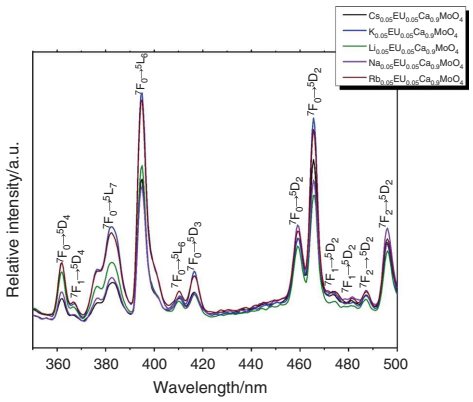

Fig. 8 PL (λ_{ex} = 395 nm) spectra of M–Eu–Ca−Mo–O tartrate (M=Li, Na, K, Rb and Cs) gel precursors for $M_{0.05}Eu_{0.05}Ca_{0.9}MoO_4$ ceramics heat-treated at 773 K

From Fig. 10, it is clear that either growing or decreasing correlation cannot be observed. However, these results showed an interesting trend, which is directly related to both the sizes of crystallite that grew up at 773 K and the formation mechanism of obtained crystals at higher heat-treating temperatures. It is well known that smaller crystallites produce higher luminescence intensity. This is due to the fact that smaller crystallites would have less surface imperfections quenching luminescence and less energy would be wasted in bulk material as heat dissipation. On the other hand, this study also proved that further growth of crystallites at much higher temperatures completely differs according to the nature of alkali metal. This effect mainly depends from the distribution of metal salts in the gel, which formation, during the sol–gel processing, was influenced by interaction of individual ion. By the way, such conclusion shows that the optical properties of prepared ceramics are strongly affected by several factors, and the correlation is not always expected. Moreover, the tendencies of differences of

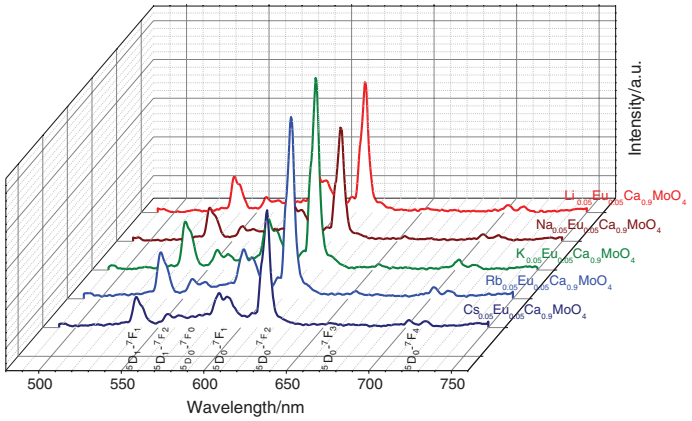

Fig. 9 PLE (λ_{em} = 616 nm) spectra of M–Eu–Ca–Mo–O tartrate (M=Li, Na, K, Rb and Cs) gel precursors for $M_{0.05}Eu_{0.05}Ca_{0.9}MoO_4$ ceramics heat-treated at 773 K

Table 8 Overview of the transitions observed in luminescence spectra of europium (III) compounds [43]

Transition	Dipole character	Wavelength	Remarks
$^5D_0 \rightarrow {}^7F_0$	ED	570–585	Only observed in C_n, C_{nv} and C_s symmetry
$^5D_0 \rightarrow {}^7F_1$	MD	585–600	Intensity largely independent of environment
$^5D_0 \rightarrow {}^7F_2$	ED	610–630	Hypersensitive transition; intensity very strongly dependent on environment
$^5D_0 \rightarrow {}^7F_3$	ED	640–660	Forbidden transition
$^5D_0 \rightarrow {}^7F_4$	ED	680–710	Intensity dependent on environment, but no hypersensitivity

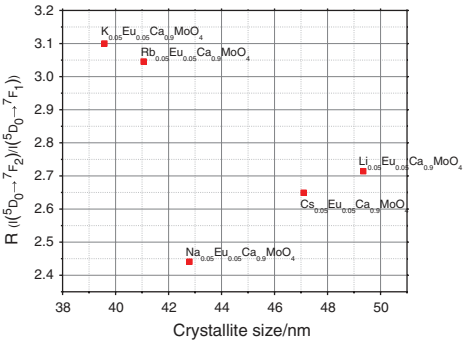

Fig. 10 Plot of R versus crystallite size for $M_{0.05}Eu_{0.05}Ca_{0.9}MoO_4$ ceramics

both the physical properties and structural features for each ceramic sample remain even by increasing the heat-treating temperature.

Conclusions

Summarizing the results obtained from the TG/DTG/DSC, XRD, SEM and PL measurements, it can be concluded that the tartaric acid-assisted synthesis of M–Eu–Ca–Mo–O tartrate (M=Li, Na, K, Rb, and Cs) gel precursors for nano-sized $M_{0.05}Eu_{0.05}Ca_{0.9}MoO_4$ ceramics is suitable preparation technique, which enables the detail investigation of multicomponent metal oxides in the frame of their chemical and physical properties. According to the thermal analysis, the decomposition of metal–tartrate gel precursors occurs in similar manner. Meanwhile, the emerging differences that mainly focus on the thermal decomposition of unreacted tartaric acid molecules, which mechanism depends on the coordination ability of the corresponding alkali metal. Besides, in all cases, except for $Li_{0.05}Eu_{0.05}Ca_{0.9}MoO_4$ ceramic, the tendency of slight mass changes above 973 K was observed. The FT-IR spectra of the M–Eu–Ca–Mo–O tartrate gels revealed that a small number of nitrates were left in the precursors. The XRD patterns correlated with the results of thermal analysis perfectly do not indicate any

characteristic peaks attributable to the impurities by increasing the heat-treatment temperature from 623 to 1273 K. The dependency of the crystallite size versus temperature clearly showed that by increasing the heat-treating temperature from 623 to 973 K for $M_{0.05}Eu_{0.05}Ca_{0.9}MoO_4$ ceramics, the values of crystallite size tend to increase; however, at higher temperatures the decreasing trends of crystallites were observed. The reason of this behaviour directly depends from the start of the crystallization of europium (III) oxide. The study of surface morphology indicated the almost identical trends of morphological properties for the analyzed samples with the spherical particles, which size varies from 200 nm to 1.5 μm. The results of the PL studies revealed that the crystallite size and the mechanism of their growing tendencies for the $M_{0.05}Eu_{0.05}Ca_{0.9}MoO_4$ compounds are closely related to the ratio R of intensities for $^5D_0 \rightarrow {}^7F_2$ and $^5D_0 \rightarrow {}^7F_1$ characteristic emissions. Finally, it was concluded that the nature of alkali metal strongly affects the distribution of Eu_2O_3 in the $CaMoO_4$ host and the reasons of such behaviour are basically determined by the different chemical activity of alkali metals in the range of temperature from 623 to 1073 K.

Acknowledgements This research was funded by the European Social Fund under the No 09.3.3-LMTK-712 "Development of Competences of Scientists, other Researchers and Students through Practical Research Activities" measure.

References

1. Hou ZY, Chai RT, Zhang ML, Zhang CM, Chong P, Xu ZH, et al. Fabrication and luminescence properties of one-dimensional CaMoO4:Ln^{3+} (Ln=Eu, Tb, Dy) Nanofibers via Electrospinning Process. Langmuir. 2009;25(20):12340–8.
2. Gao DJ, Lai X, Cui CH, Cheng P, Bi J, Lin DM. Oxidant-assisted preparation of $CaMoO_4$ thin film using an irreversible galvanic cell method. Thin Solid Films. 2010;518(12):3151–5.
3. Lei F, Yan B. Hydrothermal synthesis and luminescence of CaMO4:RE^{3+} (M=W, Mo; RE=Eu, Tb) submicro-phosphors. J Solid State Chem. 2008;181(4):855–62.
4. Thongtem T, Kungwankunakorn S, Kuntalue B, Phuruangrat A, Thongtem S. Luminescence and absorbance of highly crystalline $CaMoO_4$, $SrMoO_4$, $CaWO_4$ and $SrWO_4$ nanoparticles synthesized by co-precipitation method at room temperature. J Alloy Compd. 2010;506(1):475–81.
5. Hosseinpour-Mashkani SS, Hosseinpour-Mashkani SS, Sobhani-Nasab A. Synthesis and characterization of rod-like CaMoO4 nanostructure via free surfactant sonochemical route and its photocatalytic application. J Mater Sci Mater Electron. 2016;27(5):4351–5.
6. Silva MMS, Sena MS, Lopes-Moriyama AL, Souza CP, Santos AG. Experimental planning of the synthesis of strontium molybdate by EDTA-citrate and its structural influence, morphology and optical bandgap. Ceram Int. 2018;44(14):16606–14.
7. Sun Y, Ma JF, Jiang XH, Fang JR, Song ZW, Gao C, et al. Ethylene glycol-assisted electrochemical synthesis of $CaMoO_4$ crystallites with different morphology and their luminescent properties. Solid State Sci. 2010;12(7):1283–6.
8. Parchur AK, Ningthoujam RS, Rai SB, Okram GS, Singh RA, Tyagi M, et al. Luminescence properties of Eu^{3+} doped $CaMoO_4$ nanoparticles. Dalton Trans. 2011;40(29):7595–601.
9. Wang YG, Ma JF, Tao JT, Zhu XY, Zhou J, Zhao ZQ, et al. Low temperature synthesis of $CaMoO_4$ nanoparticles. Ceram Int. 2007;33(4):693–5.
10. Raju GSR, Pavitra E, Ko YH, Yu JS. A facile and efficient strategy for the preparation of stable $CaMoO_4$ spherulites using ammonium molybdate as a molybdenum source and their excitation induced tunable luminescent properties for optical applications. J Mater Chem. 2012;22(31):15562–9.
11. Li X, Yang ZP, Guan L, Guo JX, Wang Y, Guo QL. Synthesis and luminescent properties of $CaMoO_4$:Tb^{3+}, R + (Li +, Na +, K +). J Alloy Compd. 2009;478(1–2):684–6.
12. Zhang ZJ, Chen HH, Yang XX, Zhao JT. Preparation and luminescent properties of Eu^{3+} and Tb^{3+} ions in the host of $CaMoO_4$. Mater Sci Eng B Solid State Mater Adv Technol. 2007;145(1–3):34–40.
13. Luo YS, Dai XJ, Zhang WD, Yang Y, Sun CQ, Fu SY. Controllable synthesis and luminescent properties of novel erythrocyte-like $CaMoO_4$ hierarchical nanostructures via a simple surfactant-free hydrothermal route. Dalton Trans. 2010;39(9):2226–31.
14. Marques VS, Cavalcante LS, Sczancoski JC, Alcantara AFP, Orlandi MO, Moraes E, et al. Effect of different solvent ratios (water/ethylene glycol) on the growth process of $CaMoO_4$ crystals and their optical properties. Cryst Growth Des. 2010;10(11):4752–68.
15. Parchur AK, Ningthoujam RS. Preparation and structure refinement of Eu^{3+} doped $CaMoO_4$ nanoparticles. Dalton Trans. 2011;40(29):7590–4.
16. Dutta S, Som S, Sharma SK. Luminescence and photometric characterization of $^{K+}$ compensated $CaMoO_4$:Dy^{3+} nanophosphors. Dalton Trans. 2013;42(26):9654–61.
17. Haque MM, Kim DK. Luminescent properties of Eu^{3+} activated MLa2(MoO4)(4) based (M=Ba, Sr and Ca) novel red-emitting phosphors. Mater Lett. 2009;63(9–10):793–6.
18. Cavalli E, Boutinaud P, Mahiou R, Bettinelli M, Dorenbos P. Luminescence dynamics in Tb^{3+}-doped $CaWO_4$ and $CaMoO_4$ crystals. Inorg Chem. 2010;49(11):4916–21.
19. Parchur AK, Prasad AI, Ansari AA, Rai SB, Ningthoujam RS. Luminescence properties of Tb^{3+}-doped $CaMoO_4$ nanoparticles: annealing effect, polar medium dispersible, polymer film and core-shell formation. Dalton Trans. 2012;41(36):11032–45.
20. Zhang JH, Wang L, Jin Y, Zhang X, Hao ZD, Wang XJ. Energy transfer in $Y_3Al_5O_{12}$:Ce^{3+}, Pr^{3+} and $CaMoO_4$:Sm^{3+}, Eu^{3+} phosphors. J Lumin. 2011;131(3):429–32.
21. Liu XG, Li L, Noh HM, Jeong JH, Jang K, Shin DS. Controllable synthesis of uniform $CaMoO_4$:Eu^{3+}, M^+(M=Li, Na, K) microspheres and optimum luminescence properties. RSC Adv. 2015;5(13):9441–54.
22. Laguna M, Nunez NO, Becerro AI, Ocana M. Morphology control of uniform $CaMoO_4$ microarchitectures and development of white light emitting phosphors by Ln doping (Ln=Dy^{3+}, Eu^{3+}). CrystEngComm. 2017;19(12):1590–600.
23. Cho K, Choi J, Kim KM, Kim TW, Lee JI, Ryu JH. Pulsed laser synthesis of Er^{3+}/Yb^{3+}Co-doped $CaMoO_4$ colloidal nanocrystal and its upconversion luminescence. J Nanosci Nanotechnol. 2016;16(6):6344–9.
24. Choi GK, Kim JR, Yoon SH, Hong KS. Microwave dielectric properties of scheelite (A=Ca, Sr, Ba) and wolframite (A=Mg, Zn, Mn) AMoO(4) compounds. J Eur Ceram Soc. 2007;27(8–9):3063–7.
25. Yan SX, Zhang JH, Zhang X, Lu SZ, Ren XG, Nie ZG, et al. Enhanced red emission in $CaMoO_4$:Bi^{3+}, Eu^{3+}. J Phys Chem C. 2007;111(35):13256–60.

26. Parhi P, Singh SS, Ray AR, Ramanan A. Mechanochemically assisted room temperature solid state metathesis reaction for the synthesis of $MMoO_4$ (M=Ca, Sr and Ba). Bull Mat Sci. 2006;29(2):115–8.
27. Yu S, Lin ZB, Zhang LZ, Wang GF. Preparation of monodispersed Eu^{3+}:$CaMoO_4$ nanocrystals with single quasihexagon. Cryst Growth Des. 2007;7(12):2397–9.
28. Yoon JW, Ryu JH, Shim KB. Photoluminescence in nanocrystalline MMoO4 (M=Ca, Ba) synthesized by a polymerized complex method. Mater Sci Eng B Solid State Mater Adv Technol. 2006;127(2–3):154–8.
29. Wangkhem R, Yaba T, Singh NS, Ningthoujam RS. Red emission enhancement from $CaMoO_4$:Eu^{3+} by co-doping of Bi^{3+} for near UV/blue LED pumped white pcLEDs: energy transfer studies near. J Appl Phys. 2018;123(12):10.
30. Yin YK, Gao Y, Sun YZ, Zhou BB, Ma L, Wu X, et al. Synthesis and photoluminescent properties of $CaMoO_4$ nanostructures at room temperature. Mater Lett. 2010;64(5):602–4.
31. Shi S, Gao J, Zhou J. Effects of charge compensation on the luminescence behavior of Eu^{3+} activated $CaWO_4$ phosphor. Opt Mater. 2008;30(10):1616–20.
32. Kim KM, Ryu JH, Mhin SW, Park GS, Shim KB. Luminescence of nanocrystalline Tb(3)Al(5)O(12): Ce(3+) phosphors synthesized by nitrate-citrate gel combustion method. J Electrochem Soc. 2008;155(10):J293–6.
33. Lian JB, Qin H, Liang P, Liu F. Co-precipitation synthesis of $Y_2O_2SO_4$:Eu^{3+} nanophosphor and comparison of photoluminescence properties with Y_2O_2:Eu^{3+} and Y_2O_2S:Eu^{3+} nanophosphors. Solid State Sci. 2015;48:147–54.
34. Cho H, Hwang SM, Bin Lee J, Ka DH, Kim TW, Lee BS, et al. White luminescence of Ho^{3+}/Tm^{3+}/Yb^{3+}-codoped $CaWO_4$ synthesized via citrate complex route assisted by microwave irradiation. Trans Nonferrous Met Soc China. 2014;24:S134–40.
35. Braziulis G, Janulevicius G, Stankeviciute R, Zalga A. Aqueous sol-gel synthesis and thermoanalytical study of the alkaline earth molybdate precursors. J Therm Anal Calorim. 2014;118(2):613–21.
36. Braziulis G, Stankeviciute R, Zalga A. Sol–gel derived europium doped $CaMoO_4$:Eu^{3+} with complex microstructural and optical properties. Mater Sci Medzg. 2014;20(1):90–6.
37. Zalga A, Gaidamaviciene GE, Gricius Z, Uzpurvyte E, Gadeikis J, Diktanaite A, et al. Aqueous sol-gel synthesis, thermoanalytical study and electrical properties of $La_2Mo_2O_9$. J Therm Anal Calorim. 2018;132(3):1499–511.
38. Stuart B. Infrared spectroscopy: fundamentals and applications. West Sussex: Wiley; 2004.
39. Nakamoto K. Infrared and Raman Spectra of Inorganic and Coordination Compounds. Handbook of Vibrational Spectroscopy. 2006.
40. Braziulis G, Stankeviciute R, Zalga A. Sol-gel derived europium doped $CaMoO_4$:Eu^{3+} with complex microstructural and optical properties. Mater Sci. 2014;20(1):90–6.
41. Curtis C, Tharp A. Ceramic properties of europium oxide. J Am Ceram Soc. 1959;42(3):151–6.
42. Liu J, Lian HZ, Shi CS. Improved optical photoluminescence by charge compensation in the phosphor system $CaMoO_4$:Eu^{3+}. Opt Mater. 2007;29(12):1591–4.
43. Binnemans K. Interpretation of europium(III) spectra. Coord Chem Rev. 2015;295:1–45.

Article III

Aqueous sol-gel synthesis, thermoanalytical study and electrical properties of $La_2Mo_2O_9$

A. Žalga, G. Gaidamavičienė, Ž. Gricius, E. Užpurvytė, J. Gadeikis, A. Diktanaitė, M. Barré, T. Šalkus, A. Kežionis, E. Kazakevičius

Journal of Thermal Analysis and Calorimetry 132(3) (2018) 1499-1511

Journal of Thermal Analysis and Calorimetry
https://doi.org/10.1007/s10973-018-7120-3

Aqueous sol–gel synthesis, thermoanalytical study and electrical properties of $La_2Mo_2O_9$

Artūras Žalga[1] · Giedrė Gaidamavičienė[1] · Žygimantas Gricius[1] · Emilija Užpurvytė[1] · Jonas Gadeikis[1] · Austėja Diktanaitė[1] · Maud Barré[2] · Tomas Šalkus[3] · Algimantas Kežionis[3] · Edvardas Kazakevičius[3]

Received: 20 October 2017 / Accepted: 24 February 2018

Abstract
Nano- and micro-sized $La_2Mo_2O_9$ ceramics have been successfully synthesized by an aqueous sol–gel synthesis method using a tartaric acid as a ligand. Thermal analysis of both as-prepared La–Mo–O tartrate gel precursor and $La_2Mo_2O_9$ double oxide heat-treated at different temperatures was performed. The high-temperature phase transition from α to β-phases was additionally investigated by broadband high-temperature impedance spectroscopy techniques. The α ↔ β phase transition was characterized by monitoring the conductivity and a transfer of heat with respect to temperature. The crystalline phase stability of monoclinic $La_2Mo_2O_9$ compound was confirmed by x-ray diffraction measurements, while the dense nanoscale surface composed of the particles, ranging from 50 to 100 μm, was confirmed by scanning electron microscopy.

Keywords LAMOX · Sol–gel processing · Thermal analysis · Electrical properties · Phase transition

Introduction

Multicomponent crystalline oxide materials that exhibit a high electrical conductivity associated with the phase transitions and an anomalous mobility of oxide anions attract both a fundamental and practical interest, in particular, owing to the prospects of their use in many solid-state ionic devices, i.e., as a solid-state electrolyte in solid oxide fuel cells, oxygen pumps and membranes for oxygen separation, oxygen sensors, etc. [1, 2]. From this point of view, yttria-stabilized zirconia (YSZ) is an excellent solid electrolyte and commonly employed as an oxide ion conductor in technological applications [3]. Besides, several authors reported an ionic conductivity enhancement of the yttria-stabilized zirconia films and bulk materials when decreasing crystallite size to the nano- or sub-micrometer range [4–9]. Nevertheless, the contemporary enhancements to improve the ionic conductivity are not sufficient; therefore, there is a need for new oxide ion conductors that have higher ionic conductivity compared with YSZ at intermediate temperature. In recent years, the $La_2Mo_2O_9$-type compounds, known as the LAMOX family, which was originally reported by Lacorre et al. [10], have attracted great interest due to their high oxygen-ion conductivity at medium temperatures [11]. $La_2Mo_2O_9$ undergoes a reversible transition from monoclinic α to cubic β structure at ~ 853 K, leading to an increase in the ionic conductivity up to two orders of magnitude and reaching values higher than those corresponding to YSZ [12]. Depending on the rate of cooling of the sample after its preparation, $La_2Mo_2O_9$ can exist at room temperature as a stable monoclinic α phase, metastable cubic β_{ms} phase, or a mixture of these phases [1]. Besides, the reasons how the temperature affects the transition from cubic β to monoclinic α phases are not fully clear. It is obvious that this phase transition of non-substituted $La_2Mo_2O_9$ into the pseudo-monoclinic α-phase is detrimental for practical applications due to a

✉ Artūras Žalga
arturas.zalga@chf.vu.lt

[1] Department of Applied Chemistry, Institute of Chemistry, Faculty of Chemistry and Geosciences, Vilnius University, Naugarduko str. 24, 03225 Vilnius, Lithuania

[2] Département des Oxydes et Fluorures, Institut des Molécules et Matériaux du Mans (IMMM, UMR 6283), Le Mans, France

[3] Faculty of Physics, Vilnius University, Saulėtekio av. 3, 10222 Vilnius, Lithuania

Published online: 06 March 2018

drastic drop in the conductivity below 833 K and mechanical failure caused by the high thermal expansion between the high- and low-temperature polymorphs [13]. The possibilities of reducing the structure changes in $La_2Mo_2O_9$ by the influence of temperature remain a great challenge in today's science. In addition, the applicability of $La_2Mo_2O_9$ is also limited due to its lower stability under reducing atmosphere, because of the presence of Mo^{6+}, which is likely to join electrons by causing structure changes that strongly affects the conductivity as well as performance of used device [2]. Despite the above-mentioned drawbacks, $La_2Mo_2O_9$ remains interesting because of its unique crystal structure and elemental composition, which allows the possibility of the substituting and doping that leads to the stabilization of high-temperature cubic phase and low decrease in conductivity at room temperature. For example, the substitution of molybdenum by tungsten significantly increases the resistance against the reduction environment impact, while replacing lanthanum side by Sr^{2+}, Y^{3+}, Zr^{4+} and Nb^{5+} ions stabilizes the β-phase and in some cases even increases the conductivity, which has an excellent characteristics only for high-temperature metastable cubic β_{ms} phase. Nevertheless, in order to explain in detail the possible influence of nonessential structural changes according to the substitution or addition, the further investigation and comparative study of non-substituted $La_2Mo_2O_9$ ceramic by different techniques are required. It is also well known that the preparation technique has significant effect on the chemical and physical characteristics of final material; therefore, the relation of phase transition in the range of temperature between 783 and 853 K during the initial formation from starting compounds and reversible changes of annealed ceramic has additional motivation and is highly desirable.

Currently, there are various ways to synthesize LAMOX compounds. One of the most common is a solid-state route, where the initial ingredients are mixed and heated up to high temperatures [14]. However, this method does not allow to obtain directly dense ceramic samples, since a milling step is necessary before sintering. Indeed, even if this step leads to the decrease in the grain size and thus to a higher sinterability, it also leads to the apparition of impurities, especially when the milling balls/jar are made of zirconia. For instance, in 2011 a study was published claiming that $La_2Mo_2O_9$ ceramic samples were obtained by solid-state synthesis in the temperature range of 1233–1373 K [15]. Other, more classical ways have been used, such as the citrate method [16], a Pechini or modified Pechini route [6, 17–19], the microwave-assisted method [20] and the EDTA complexation method [21]. Another popular way obtaining the sample of interest is a polyol process. The polyol process concerns the preparation of metallic powders by reduction of inorganic compounds in liquid polyols. A general reaction on model has been established with a reaction via the solution: dissolution of the solid precursor; reduction in solution; homogeneous nucleation and growth of the metallic phase from the solution [22].

From this point of view, in this work we have successfully synthesized $La_2Mo_2O_9$ ceramic via rather rarely used aqueous tartaric acid-assisted sol–gel synthesis technique, which allowed to obtain monophasic crystalline compound at relatively low temperature of 823 K. In addition, it is important to note that the crystallization of high-temperature metastable cubic β_{ms} phase started from 783 K. Moreover, it was also showed that the increase in annealing temperature to 1473 K does not change the position of characteristic peaks for $La_2Mo_2O_9$ ceramic as presented in the XRD patterns. These obtained results are very important for showing the highest capabilities of this synthesis technique, which was used in this work. The reason of selecting tartaric acid as a chelating agent lies within a couple of essential features that overcome some of the problems arising during the synthesis with citric acid. One of the improvements is the potential reduction of toxicity. This effect is justified regarding the study of thermal decomposition of a citric acid, which reveals that at 448 K, citric acid is converted into aconitic acid. Further heating results in formation of methyl maleic anhydride (III). Aconitic acid may also decompose to acetone [23], while the decomposition of tartaric acid mainly produces carbon dioxide and monoxide [24]. Also, citric acid has a higher molecular mass which causes a higher expansion of the gel precursor when it is being heat-treated to obtain a gel. During the sudden expansion, a part of the sample might be dropped out of the crucible. Finally, tartaric acid has been found to be a more effective chelating agent for LAMOX ceramics when the calcination is carried out at temperatures above 1323 K [25].

Experimental

The synthesis of La–Mo–O tartrate gel precursor for $La_2Mo_2O_9$ ceramic was prepared by an aqueous sol–gel synthesis by using tartaric acid as a chelating agent that interacts as a ligand at the molecular level with the reaction mixture during the both dissolution in water and sol–gel formation. Lanthanum (III) oxide (La_2O_3, 99.99% Alfa Aesar) and molybdenum (VI) oxide (MoO_3, 99.95% Alfa Aesar) were used as starting materials and weighed according to the desired stoichiometric ratio. Nitric acid (HNO_3 66% Reachem), distilled water and concentrated ammonia solution ($NH_3 \cdot H_2O$ 25% Penta) were used as solvents and reagents to regulate the pH of the solutions. Tartaric acid (L–(+)–tartaric acid ($C_4H_6O_6$) (TA) ≥ 99.5%

Sigma-Aldrich) was applied for escalation of solubility via coordination of starting compounds in the reaction mixture, especially, during the pH changes and evaporation before sol–gel formation. At first, MoO_3 was dissolved in a solution that consisted of 25 mL of distilled water and 0.5 mL of concentrated ammonia by stirring at 353–363 K temperature.

Then, after continuous stirring at approximately 353–363 K as long as the excess of ammonia had been evaporated, the tartaric acid with a molar ratio of Mo/TA = 0.25 was added during the continuous stirring to the reaction mixture at the same temperature.

Secondly, the lanthanum (III) oxide and concentrated nitric acid were added to the beaker. A clear solution was obtained and subsequently concentrated by slowly vaporizing the reaction mixture at 333 K.

In the following stage, a yellow transparent sol was formed after nearly 95% of the water had been evaporated under continuous stirring. After drying in an oven at 393 K, fine-grained dark blue gel powders were obtained.

Next to that, the La–Mo–O tartrate gel precursor for $La_2Mo_2O_9$ ceramics were heat-treated for 5 h at 823, 873, 1073, and 1273 K. Finally, the powders were pelletized and ceramic sintered at 1473 K for 5 h in air. In addition, it is also important to note that all values related to the selection of heat treatment temperatures, duration time, and pressing conditions had been developed empirically by performing numerous tests to ensure the formation of a dense ceramics with no cracks or cavities.

The thermal analysis was performed with TG–DSC, STA 6000 Perkin-Elmer instrument using a sample mass of about 5 mg and a heating rate of either 20° min^{-1} for a gel precursor or 40° min^{-1} for sintered ceramics under airstream (20 cm^3 min^{-1}) at ambient pressure by raising the temperature up to 1223 K. The sample mass, heating rate, atmosphere and its flow rate were selected empirically during numerous tests to ensure the best signal peak efficiency and to minimize the noises and background signals, which occur because of the influence of corundum crucible and equipment limits. X-ray diffraction (XRD) patterns were recorded in air at room temperature by employing a powder x-ray diffractometer Rigaku MiniFlex II using Cu $K_{\alpha 1}$ radiation. The spectra were recorded at the standard rate of 1.5 2θ min^{-1}. The sample was spread on the glass-holder in order to obtain maximum intensity of the characteristic peaks in the XRD pattern. The Rietveld refinement of the obtained XRD patterns was performed using X'Pert HighScore Plus software. The scanning electron microscopes (SEM) Hitachi TM3000 and Hitachi SU-70 were used to study the surface morphology and microstructure of the obtained ceramic samples. The measurements of electrical properties were performed using two different impedance spectroscopy techniques by newly developed impedance spectrometer [26, 27]. Sintered ceramics were processed, obtaining cylindrical samples of around 1.5 mm height and up to 3 mm diameter with Pt paste electrodes.

Results and discussion

Synthesis

The dissolution process of molybdenum (VI) oxide in water and ammonia solution is given in Eq. 1:

$$MoO_3\ (s) + 2NH_3 \cdot 2H_2O\ (aq) \rightarrow (NH_4)_2MoO_4 \cdot 2H_2O\ (aq) \quad (1)$$

According to Ref. [28], the formation of $[(MoO_4)_p(C_4H_4O_6)_qH_r]^{(2p+2q-r)-}$ coordination compound is most likely, in this synthesis stage. Generally, the chemical reaction that occurred after this procedure can be written as shown in Eq. 2:

$$p(NH_4)_2MoO(aq) + qC_4H_6O_6(aq) \rightarrow [(MoO_4)_p(C_4H_4O_6)_qH_r]^{(2p+2q-r)-}(aq) + 2pNH_4^+(aq) \quad (2)$$

By slowly vaporizing the final reaction mixture, the chemical reactions that took place in this synthesis step are listed in Eqs. 3 and 4:

$$La_2O_3(s) + 6HNO_3(aq)_{excess} \rightarrow 2La(NO_3)_3(aq) + 3H_2O(l) \quad (3)$$

$$[(MoO_4)_p(C_4H_4O_6)_qH_r]^{(2p+2q-r)-}(aq) + pLa^{3+}(aq) \rightarrow La_p[(MoO_4)_p(C_4H_4O_6)_qH_r]^{3p-(2p+2q-r)}(aq) \quad (4)$$

After drying in an oven, the dark blue gel powders were obtained, as illustrated in Eq. 5:

$$La_p[(MoO_4)_p(C_4H_4O_6)_qH_r]^{3p-(2p+2q-r)}(aq) + 3pC_4H_4O_6(aq) \xrightarrow{\text{drying at } 120^\circ C} \text{dark blue gel} \quad (5)$$

Thermal analysis

In this work, the thermal analysis as a powerful tool was properly used for both the detailed investigation of thermal decomposition of La–Mo–O tartrate gel precursor and the crystal phase transition from monoclinic α-phase to cubic β-phase for $La_2Mo_2O_9$ ceramic. As can be seen in Fig. 1, the analysis of TG–DTG–DTA curves, which reveal the thermal decomposition of as-prepared La–Mo–O tartrate gel precursor, is rather complicated as expected, but one fact is clear, due to the relatively high amount of tartaric acid in the reaction mixture, the final mass loss of about 61% occurs up to 953 K. Further increase in heating temperature does not change the sample mass significantly,

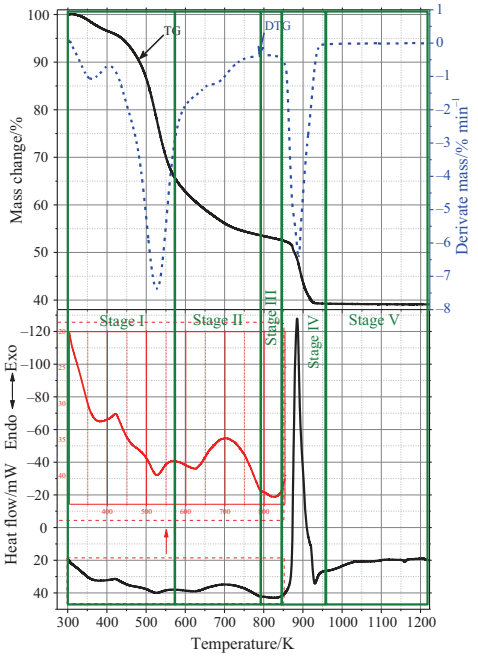

Fig. 1 Combined TG–DTA curves of the La–Mo–O tartrate gel precursor for $La_2Mo_2O_9$ ceramic

which gives the conclusion that the decomposition of all volatile organic parts in the gel precursor occurred below 953 K. Besides, it is also important to note that the sublimation of MoO_3 does not start above 1073 K of temperature, which concludes about high stability of final crystalline compound. This result also confirms that above 1173 K the melting point of the final double oxide shifts to the higher temperatures, while in the case of $La_2Mo_3O_{12}$ ceramic, as reported in our previous work, such behavior was not observed [29]. In addition, the mass of the sample powder tablet, sintered at 1473 K for 5 h in air atmosphere, has not changed and this fully satisfies the conclusion about the formation of really high stability of the final $La_2Mo_2O_9$ ceramic. Table 1 shows the data, which were deducted from Fig. 1, and supplements quantitatively the general view of thermal decomposition processes in La–Mo–O tartrate gel precursor.

Therefore, the decomposition processes of the La–Mo–O tartrate system could be roughly divided into at least five stages that clearly indicate all mass losses and heat flow transformations occurring during the sample heating in the appropriate range of temperature. The first stage of the sample mass loss is closely related to the complete decomposition of residue tartaric acid, the excess of which has been added to reaction mixture in order to avoid precipitation during the gelation process. It is well known that the decomposition of tartaric acid usually occurs in three steps [24]. At first, tartaric acid loses one molecule of water and this dehydration of water molecules starts during the both final aqueous sol solution evaporating procedure on the hot plate and drying process in the oven at 393 K for 24 h in air atmosphere. It is also important to mention the fact that complete decomposition of nitric acid during the evaporating process allowed to improve the initial tartaric acid decomposition and also accelerated the dehydration of water molecules from the gel precursor. Besides, the temperature of hot plate was increased to 523 K, which enabled the tartaric acid removal process, before gel formation, in which the mass loss was of about 18.9%. This amount of tartaric acid loss was calculated taking in account the additives of starting compounds and residue of the sample mass from the reaction mixture before and after gelation process. According to the data presented in Table 1 and Eq. 6, the first mass loss of the as-prepared La–Mo–O gel precursor in stage I consists of 4.3% and this step may be formulated, as follows:

$$2C_4H_6O_6(s) \rightarrow C_8H_8O_{10}(s) + 2H_2O\ (g) \qquad (6)$$

In the range of temperature from 303 to 420 K, a broad endothermic band with heat flow of 1078.1 mJ and $\Delta H = 106.7\ J\ g^{-1}$ on the DSC curve corresponds to the first interval of the mass loss in the stage I. In addition, this combination of tartaric acids (TA) in the beginning of stage I, as presented in Eq. (6), is in a good agreement with the total amount (34.57%) of unreacted TA with molybdate ions (MoO_4^{2-}), which mass loss contains of 34.5% (Table 1, Stage No. I, row 2).

By further increasing the temperature from 421 to 493 K, the decomposition of tartaric-acids dimer ($C_8H_8O_{10}$) into carbon monoxide (CO), carbon dioxide (CO_2) and two acetic acid (CH_3COOH) molecules starts. The removal of these molecules from the gel is carried out simultaneously, and it is characterized by a broad endothermic band (110.6 mJ; $\Delta H = 11.0\ J\ g^{-1}$), which attributed to the evaporation of the acetic acid from the sample. The exothermic behavior of the DSC curve at about 423 K of temperature is related to the removal of CO and CO_2 molecules. Next to that, at somewhat higher temperatures, the dimer of tartaric acids already breaks down into two molecules of pyruvic acid ($CH_3COCOOH$) and one molecule of carbon dioxide. Quantitatively, this decomposition process is characterized from 494 to 573 K of temperature and presented in Table 1 stage I row fourth. The last third endothermic band of stage I is attributed to the thermal evaporation of pyruvic acid; meanwhile, the exothermic behavior in the DSC curve is directly related to

Table 1 Thermoanalytical data for the La–Mo–O tartrate gel precursor

Stage no.	Range of temperature/K	Mass			Heat			
		Change/ %	Onset/ K	Residual/ %	Flow/mJ	Onset/ K	End/ K	Enthalpy/ J g^{-1}
I	**303–573**	**34.5**	**–**	**65.5**	**2702.6**	**–**	**–**	**267.4**
	303–420	4.3	321.2	95.7	1078.1	320.3	419.4	106.7
	421–493	7.9	463.3	87.8	110.6	428.1	488.4	11.0
	494–573	22.3	499.5	65.5	260.2	499.5	553.9	25.8
II	**574–793**	**12.0**	**–**	**53.5**	**1215.3**	**–**	**–**	**120.2**
	574–658	7.2	617.7	58.3	250.8	609.2	649.4	24.8
	659–793	4.8	681.6	53.5	–964.5	668.4	785.6	–95.4
III	**794–843**	**0.8**	**823.2**	**52.7**	**52.9**	**812.1**	**842.7**	**5.2**
IV	**844–953**	**13.3**	**866.7**	**39.4**	**15,473.4**	**–**	**–**	**1530.8**
	844–953	–	–	–	–13,531.7	872.3	931.0	–1338.7
	891–938	–	–	–	1941.7	891.6	939.9	192.1
V	**954–1223**	**0.1**	**–**	**39.3**	**–**	**–**	**–**	**–**

Bold values indicate the begining and the end processes of the first stage, which summarize below listed the decomposition and the transformation processes

the releasing of carbon dioxide from the gel precursor. After the thermal decomposition of the free-tartaric acid in the La-Mo–O tartrate gel precursor with the mass change of 34.5%, the second stage of the partial breakdown of corresponding metal tartrates, as shown in Eq. 7, takes place:

$$16\ La_{10}[(MoO_4)_{10}(C_4H_4O_6)_{14}]H_{18} \rightarrow \underbrace{160\ La^{3+} + 160\ MoO_4^{2-} + C_{747}O_{454}}_{\text{Homogeneous solid mixture}} + 149\ CO_2 + 592\ H_2O \quad (7)$$

attributed to the releasing of carbon dioxide molecules from the residue of the gel precursor. In addition, it is also important to mention that after this range of temperature all hydrogen atoms were escaped in the form of water molecules. This is the main reason why after the second decomposition stage the changes of sample mass almost

As shown in Table 1 stage II row one, the initial decomposition of metal tartrates $La_{10}[(MoO_4)_{10}(C_4H_4O_6)_{14}]H_{18}$ begins with the removing of oxygen excess from the gel precursor. These oxygen ions are eliminated with the carbon and hydrogen atoms according to the amount ratios of carbon dioxide and water molecules, as seen from Eq. 7, respectively. The mass of the gel precursor during this decomposition stage, in the range of temperature from 574 to 793 K, decreases by 12%, and the transformation changes of this process could be divided into two different thermal effects. The first one, with endothermic character, starts at 574 K of temperature and is attributed to the evaporation of water molecules from the sample residue. Meanwhile, the other change of mass, from the 659 to 793 K of temperature, is related to well-expressed exothermic behavior in the DSC curve and is stopped and the crystallization of β-$La_2Mo_2O_9$ cubic phase has started. This endothermic effect in the DSC curve is taking place from the 794 to 843 K, as shown in Fig. 1 and Table 1 stage III, respectively. This crystallization process is presented in Eq. 8:

$$\underbrace{160\ La^{3+} + 160\ MoO_4^{2-} + C_{747}O_{454}}_{\text{Homogeneous solid mixture}} \rightarrow \underbrace{80\ La_2Mo_2O_9 + C_{747}O_{374}}_{\text{Homogeneous solid mixture (black powders)}} \quad (8)$$

It is also important to note that the heat consumption (569.5 mJ, $\Delta H = 5.2$ J g^{-1}) during the crystallization of

metastable ceramic is similar to those values that were obtained and calculated according to the follow-up investigations of $\alpha \leftrightarrow \beta$ phase transition in the $La_2Mo_2O_9$ powders.

Finally, the last mass change (13.3%) of the La–Mo–O tartrate gel precursor in the range of temperature from 844 to 953 K is attributed to burning of inorganic carbon, which is formed from the tartrates at lower temperatures. This combustion process is presented in Eq. 9 as follows:

$$80\ La_2Mo_2O_9 + C_{747}O_{374} + 560\ O_2 \rightarrow 80\ La_2Mo_2O_9 + 747\ CO_2 \quad (9)$$

Homogeneous solid mixture **white powders**

This exothermic process is overlapped with both the growing of crystallites and the size of individual particles, which are characterized by the heat absorption. This is the reason why the symmetry of the exothermic peak in this range of temperature is not regular, and after abrupt increase is being observed the decrease with tendency into endothermic behavior. Before calculating the total release of the heat during the burning of organic residues in the sample, it is important to estimate the endothermic effects into the overall process. As seen in Table 1 stage IV row 1, the total heat is equal to the sum of exothermic and endothermic processes, which have occurred in the same time.

By further increasing the heating temperature from 954 to 1223 K, the mass change of the sample is extremely low, does not exceed 0.1%, and no significant changes in the DSC curve were identified. It means that after the sintering of the La–Mo–O tartrate gel precursor, the homogenous substance was formed with the thermal properties similar to those of $La_2Mo_2O_9$ ceramic.

In order to confirm the phase transition at elevated temperatures in sintered La–Mo–O tartrate samples, their DSC measurements were performed. Table 2 shows the thermoanalytical data of the $\alpha \rightarrow \beta$ phase transition for the $La_2Mo_2O_9$ ceramics, which compare the influence of the sample mass and initial annealing temperature into the onset of this action.

The corresponding DSC curves of the La–Mo–O tartrate gel precursor, which was heat-treated at 873, 1273 and 1473 K temperatures, are shown in Fig. 2. From these results, it is clear that different surface morphology, which much depends on the heat treatment temperature, significantly affects both the onset temperature and the end temperature of the phase transition. Besides, it also influences the peak position, heat flow and enthalpy similarly as end temperature, which illustrate the state of monoclinic phase at room temperature and its relation to the surface properties.

Figure 3 displays the onset temperature of the phase transition of $La_2Mo_2O_9$ ceramics as a function from sintering temperature. In this case, it is well seen that the initial mass, which was used for the measurement, slightly influenced the beginning of the phase transition from the monoclinic crystalline phase into metastable high-temperature cubic phase shown in the plot as the black curve and blue curve, respectively. The red dashed curve shows the linear dependency of the initial mass of LAMOX ceramic from the onset temperature, which is somewhere in the middle of analyzed samples. On the other hand, it is obvious that the onset temperature depends on the surface structure of the analyzed sample and this dependency is nonlinear.

The dependency of the end temperature, peak position, heat flow and enthalpy from the sintering temperature of the LAMOX ceramic is shown in Figs. 4 and 5. From these curve graphs, it is clear that by increasing the sintering temperature of LAMOX ceramic from 873 to 1473 K the values of end temperature, peak position, heat flow and

Table 2 Thermoanalytical data of the $\alpha \rightarrow \beta$ phase transition for the $La_2Mo_2O_9$ ceramics under the influence of the sample mass and sintering temperature

Measurement conditions	Sintering temperature/K	Sample mass/mg	$\alpha \rightarrow \beta$ phase transition peak properties				
			Temperature			Heat	
			Onset/K	End/K	Peak position/K	Flow/mJ	Enthalpy/J g^{-1}
Heating from 573 to 1073 K at 40°/min	873	5.448	826.02	843.55	834.23	28.894	5.3034
	1273	5.023	827.38	850.06	839.53	40.291	8.0213
	1273	20.627	827.86	845.28	837.70	107.909	5.214
	1473	5.460	828.45	843.64	836.87	21.172	3.8776

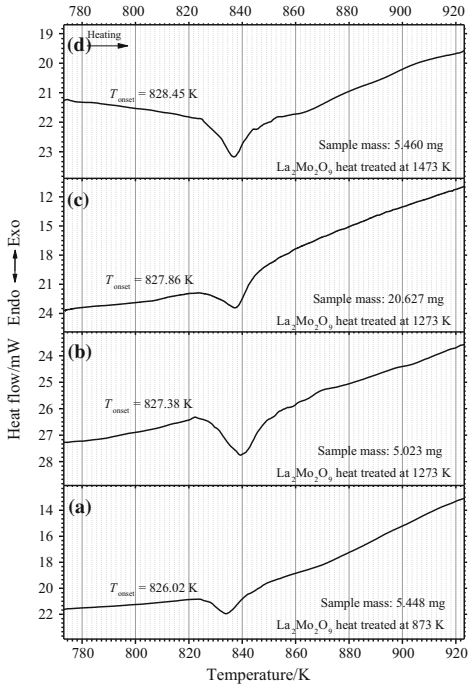

Fig. 2 DTA curves of the $La_2Mo_2O_9$ ceramic heat-treated at 873, 1273, and 1473 K with different mass of the samples

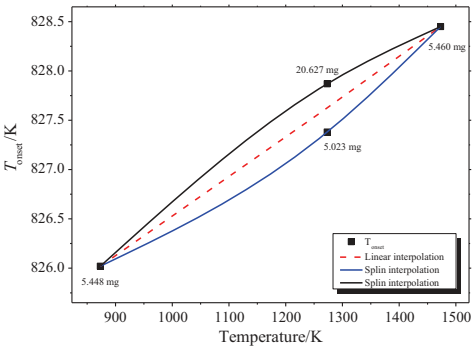

Fig. 3 The onset temperature of the phase transition of $La_2Mo_2O_9$ ceramic as a function from sintering temperature

enthalpy tend to increase and at the higher temperatures start to decrease again. This phenomenon is explained by the two competing effects, like the surface area and degree of crystallinity. The LAMOX sample heat-treated at 873 K

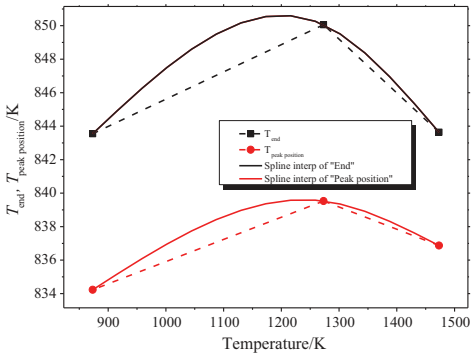

Fig. 4 The end temperature and peak position of the phase transition of $La_2Mo_2O_9$ ceramic as a function from sintering temperature

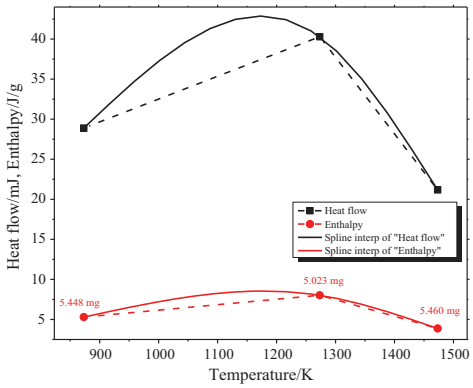

Fig. 5 The heat flow and enthalpy of the phase transition of $La_2Mo_2O_9$ ceramic as a function from sintering temperature

of temperature usually composed of particles with size from 100 to 200 nm, which is characterized by a large surface area. It means that in such conditions the area of grain boundary is either larger or similar to the surface, which is created by the particles itself. By increasing the thermal treatment, the surface area tends to decrease, but the degree of crystallinity increases. In other words, the surface area of grain boundary decreases, but the area of particles surface increases and this leads to the increase in energy of phase transition. From the temperature of 1273 K, the surface area decreases further, but the crystallinity increases much slower and this leads to the decreasing of energy of phase transition, as is shown in Figs. 4 and 5.

In order to show how this behavior of the onset temperature, end temperature, peak position, heat flow and

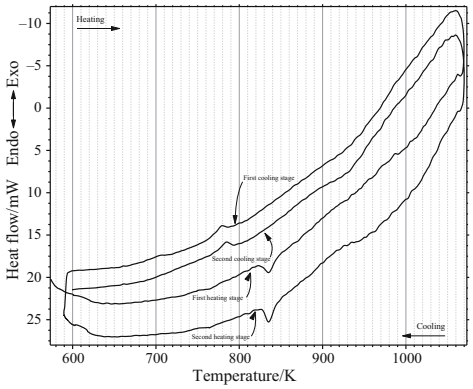

Fig. 6 DTA curve of the $La_2Mo_2O_9$ ceramic heat-treated at 873 K

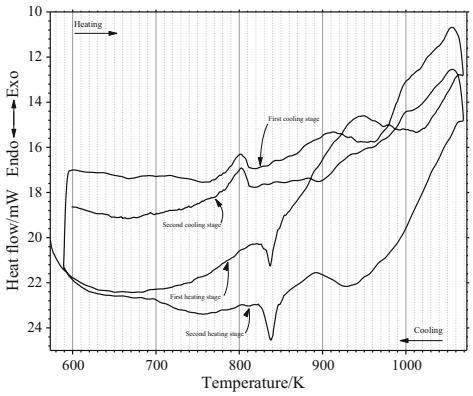

Fig. 7 DTA curve of the $La_2Mo_2O_9$ ceramic heat-treated at 1473 K

enthalpy depends on the amount of monoclinic phase, which have formed after several heating and cooling procedures, the LAMOX ceramic was additionally investigated by DSC analysis, as shown in Figs. 6 and 7, respectively.

From the first view, it is clear that the tendency of $\alpha \rightarrow \beta$ phase transition for the $La_2Mo_2O_9$ ceramic is similar to both samples heat-treated at 873 and 1273 K, respectively. The formation of cubic phase starts from about 843 K and ends at about 845 K. This stage was more or less similar in both cases during the additional thermal treatment, as seen from DSC results (Figs. 6 and 7). Meanwhile, the reversible phase transition from cubic to monoclinic phase started at lower temperature and its range was slightly different comparing the two cases mentioned above. In other words, the transformation of cubic phase starts from about 789 K and ends at 773 K for the case of LAMOX sample initially heat-treated at 873 K. Meanwhile, the initial formation of monoclinic phase in the range of temperature from 812 to 783 K was identified in the case of LAMOX sample initially heat-treated at 1473 K. This difference of reversible phase transition shows that the stability and surface structure of the ceramic heat-treated at 1473 K is better, because the heating range from 573 to 1073 K during the measurement slightly affects both the morphology and crystallinity of LAMOX sample that was heat-treated at 873 K.

Table 3 shows the thermoanalytical data of the $\alpha \rightarrow \beta$ phase transition for the $La_2Mo_2O_9$ ceramic under the influence of the sintering temperature and the amount of measurement. The graphical view of the data collected in Table 3 is presented in Figs. 8–12. From these results, one is clear that onset temperature of differently heat-treated samples after the first heating procedure tends to increase slightly from 826.84 to 830.32 K and during the second heating stage the opposite change direction of onset temperature from 829.39 to 828.22 K was observed. Such change in onset temperature is directly related to the transformations of surface morphology and the size of crystallites in the sample heat-treated at 873 K because of measurement that was performed in the range of temperature from 573 to 1073 K. This elevation of temperature made a lot of changes to the size of crystallites, which influenced the increase in T_{onset} from 826.84 to 829.39 K. In this case, almost identical effect was observed comparing the samples which were heat-treated at 873 and 1273 K (Fig. 3). Besides, after the second heating stage of the same sample the onset temperature only slightly decreased, this suggests only minimal changes in surface morphology and crystal structure, which were caused by phase transition during the cooling procedure.

After the analysis of phase transition during the cooling the sample (Fig. 8), it is clear that the onset temperature tends to increase regardless of the amount of measurements. Nevertheless, the values of T_{onset} remain almost identical of both samples.

Similar behavior was observed analyzing the results from the values of end temperature and peak position during the cooling procedure, as shown in Figs. 9 and 10. It confirms that the phase transition from metastable cubic phase to monoclinic room temperature phase during the cooling of the sample is only little affected by the surface morphology. In this case, the values of onset temperature, end temperature and peak position increased only because of the change of crystallites, which tend to decrease during the cooling. On the other hand, though the values of end temperature and peak position during the heating procedure show both declining nature and increasing character,

Table 3 Thermoanalytical data of the α → β phase transition for the $La_2Mo_2O_9$ ceramic under the influence of the sintering temperature and the amount of measurements

Measurement conditions	Sample	Sample mass/mg	Heating/cooling stages	α ↔ β phase transition peak properties				
				Temperature			Heat	
				Onset/K	End/K	Peak position/K	Flow/mJ	Enthalpy/J g^{-1}
Heating from 573 to 1073 K at 40°/min	LAMOX-873	5.282	First stage	826.84	845.08	835.65	28.301	5.3580
			Second stage	829.39	844.22	835.53	27.529	5.2119
	LAMOX-1473	5.581	First stage	830.32	843.20	837.10	32.011	5.7357
			Second stage	828.22	843.81	838.09	30.504	5.4656
Cooling from 1.073 to 573 K at 40°/min	LAMOX-873	5.282	First stage	788.69	769.06	778.82	− 15.546	− 2.9431
			Second stage	792.42	774.34	784.56	− 15.163	− 2.8706
	LAMOX-1473	5.581	First stage	811.64	787.59	802.16	− 17.827	− 3.1943
			Second stage	811.91	783.55	802.71	− 25.745	− 4.6130

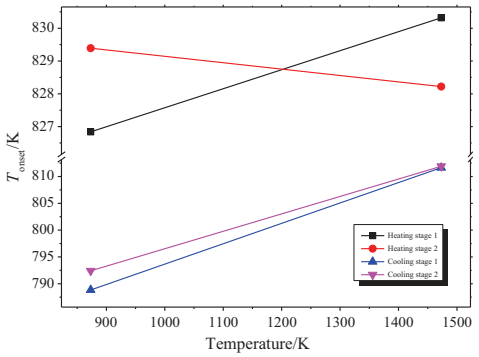

Fig. 8 The onset temperature change trend of the phase transition of $La_2Mo_2O_9$ ceramic depending on the temperature of sintering

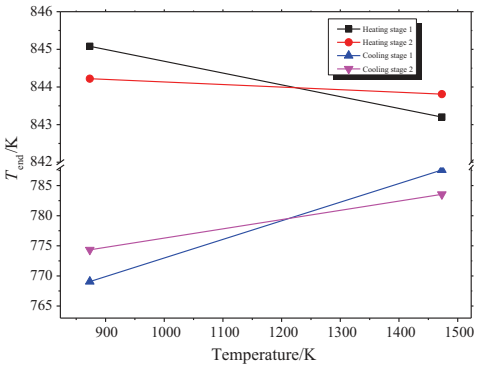

Fig. 9 The end temperature change trend of the phase transition of $La_2Mo_2O_9$ ceramic depending on the temperature of sintering

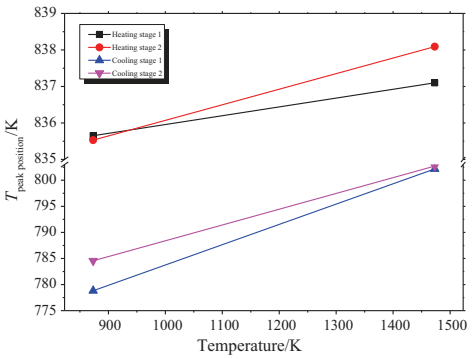

Fig. 10 The peak position temperature change trend of the phase transition of $La_2Mo_2O_9$ ceramic depending on the temperature of sintering

however, their numeric values are more or less similar comparing with the changes in onset temperature.

Figures 11 and 12 show the identical character of heat flow and enthalpy of both samples, which is expressed by Eq. 10.

$$Q = \Delta H * m \tag{10}$$

where Q—heat flow [mJ], ΔH—enthalpy [J g^{-1}]; and m—sample mass [mg].

As shown in Fig. 3, the sample mass slightly influences the onset temperature and especially the heat that is released during the phase transition. The recalculation of heat into the enthalpy lets to avoid sample mass influence to the value of energy that is released or absorbed during the transformation of the explored crystal structure.

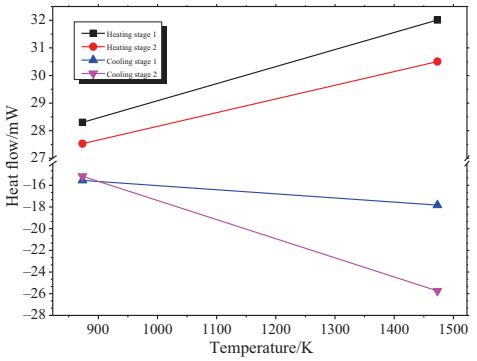

Fig. 11 The values of the heat flow change trend of the phase transition of $La_2Mo_2O_9$ ceramic depending on the temperature of sintering

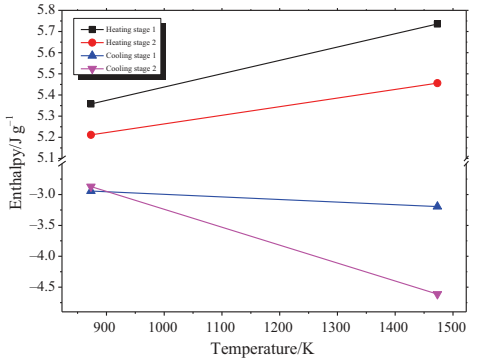

Fig. 12 The values of the enthalpy change trend of the phase transition of $La_2Mo_2O_9$ ceramic depending on the temperature of sintering

Figures 11 and 12 show almost identical dependency, because of really similar mass of the samples, which were used during the measurement. The heat and enthalpy values in the case of ceramic which was heat-treated at 873 K are similar independently from the amount of measurement. This result can be explained by the crystallization and structure rearrangement during the heating, because specific conditions were created when achieved relatively high 1073 K of temperature. In such case, the crystallization and morphological changes in the ceramic compensated each other and either heat or enthalpy remains similar. From this point of view, a completely different dependency was estimated in the sample that was heat-treated at 1473 K. Comparing with the ceramic that was prepared at 873 K, in this sample the heat as well as

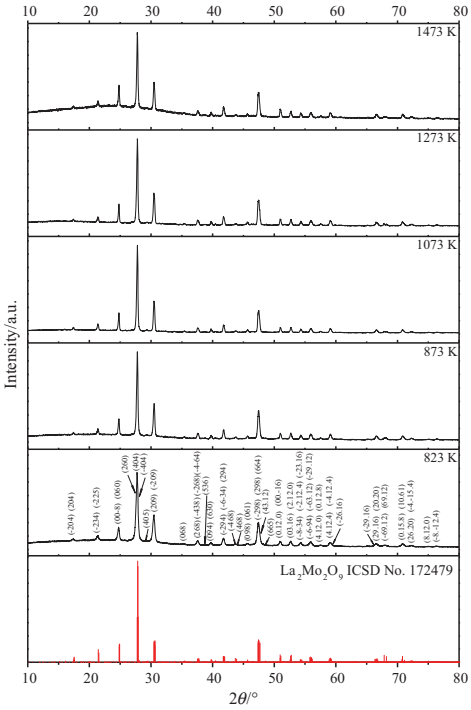

Fig. 13 Standard ICSD card of $La_2Mo_2O_9$ and XRD patterns of the La–Mo–O tartrate gel precursor heat-treated at 823, 873, 1073, 1273, and 1473 K temperatures

enthalpy tends to grow depending on the amount of measurements. This tendency is directly related only to the recrystallization processes during the phase transition in the final ceramic. The minimal surface changes, caused by its increased density, affect only really slightly on energy transformation in this case.

In conclusion, it is clear that the additional heating of obtained ceramic influences significantly the phase transition processes and could potentially affect the final physical properties expressed by ionic conductivity in this material. This is the main reason why further investigations of ionic conductivity of this system related to the crystallization and changes of surface morphology under elevated temperature must be explored.

X-ray diffraction

The powder x-ray diffraction (XRD) patterns of La–Mo–O tartrate gel precursor heat-treated at different temperatures

shown in the top five panels of Fig. 13 are well matched with the standard ICSD card of $La_2Mo_2O_9$ that is presented in the bottom panel. No characteristic peaks attributable to the impurities by increasing of sintering temperature from 823 to 1473 K were identified. These results led us to conclude about the high stability of obtained ceramic material, because no crystallization of the side crystal phases in whole sintering range was estimated. Besides, in contrast to our previous work with $La_2Mo_3O_{12}$ [29], no melting of the LAMOX sample has not started above 1273 K. In addition, it is also interesting to mention that sintering of La–Mo–O tartrate gel precursor for $La_2Mo_2O_9$ ceramic at 773 K showed fully amorphous character and no characteristic peaks of any crystalline compound from the XRD pattern were found. Besides, this result is in a good agreement with the TG–DSC data, when the crystallization of the final cubic phase from about 813 K of temperature was estimated.

In order to prove that the crystallization plays crucial role in phase transition for $La_2Mo_2O_9$ ceramic, the Rietveld refinement analysis of all samples was also performed. The agreement indices and crystallite sizes for the $La_2Mo_2O_9$ ceramic annealed at different temperatures are shown in Table 4.

From the data placed in Table 4, it is clear that by the increasing the sintering temperature the size of crystallites also increases. The crystallites size in the room temperature monoclinic phase is about 70 nm independently from the final sintering temperature above 1073 K of the final ceramic. It means that the investigations of phase transition of the samples heat-treated below 1073 K should be done with great care, because of growing of crystallites can dramatically affect the heat of phase transition. In addition, one may identify a formation of a pseudo-amorphic state in a sample, heat-treated at 1473 K. This kind of behavior could be clarified given the rather small surface area of the powder resulting from an insufficient amount of the sample being measured with x-ray diffractometer.

In conclusion, it is clear that the formation and crystallization of the final ceramics mainly depend on several factors like aqueous sol–gel processing conditions, sintering time and temperature.

SEM micrographs

In order to show both the crystal growth and densification of obtained ceramics by increasing sintering temperature, the surface morphology was investigated. Corresponding SEM micrographs of the La–Mo–O sample heat-treated at 823, 873, and 1473 K are shown in Fig. 14. From the x-ray diffraction studies, it is clear that the crystallization of the $La_2Mo_2O_9$ ceramic starts at 823 K by the formation of well-agglomerated spherical particles in size of about 82–85 nm, as seen from both the above right micrograph (Fig. 14b) and the enlarge picture in Fig. 14a. In addition, there is well seen at least several layers of differently arranged spherical particles, which differs mostly by its density. In the less dense layer, the surface mainly composed of both well-agglomerated particles and the pores between them, diameter of which reaches more than 100 nm. Unlike porous layers, the surface of dense sheets mainly consists of well-aggregated spherical particles, size of which varies from 82 to 85.5 nm. As shown in the lower left part picture of Fig. 14c, by increasing the sintering temperature to 873 K the surface morphology of the analyzed sample has changed completely. In this case, due to thermal decomposition and melting of the aggregates and agglomerates the growing of both the particles and pores was observed. It is also important to note that the surface, in this case, is mainly composed of spherical and elliptical particles, size of which varies from 100 to 200 nm. Besides, the size of pores also increases and varies from 100 to 400 nm. The formation of porous surface morphology of the synthesized LAMOX sample is the critical stage due to the thermal treatment and can be a serious problem in order to obtain final dense-structured materials. This is the reason why additional measures like careful and meticulous powder grinding and pressing are needed. Therefore, the LAMOX powders heat-treated at the required temperature, well-grinded and properly pressed were additionally sintered at 1473 K. The results of obtained surface morphology and internal structure are shown in Fig. 14d, respectively. In this case, the formation of really dense structure with the circular shape crystals of size varying from 100 to 200 μm was achieved. Such surface morphology and single-crystal structure, confirmed

Table 4 Agreement indices and crystallite sizes for the $La_2Mo_2O_9$ ceramic heat-treated at different temperatures

Annealing temperature/K	Weighted R profile	Goodness of fit	Crystallite size/nm
823	9.37840	1.45016	31.76
873	10.47023	1.65312	53.98
1073	10.30845	1.63767	72.49
1273	12.23407	1.99644	74.49
1473	11.61758	2.15370	71.56

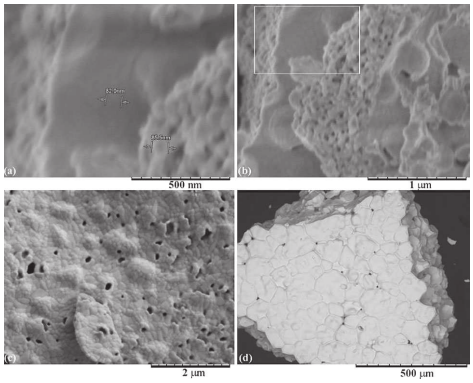

Fig. 14 SEM micrographs of La–Mo–O tartrate gel precursor for $La_2Mo_2O_9$ ceramic heat-treated at **a** 823 K, **b** 823 K, **c** 873 K and **d** 1473 K temperatures

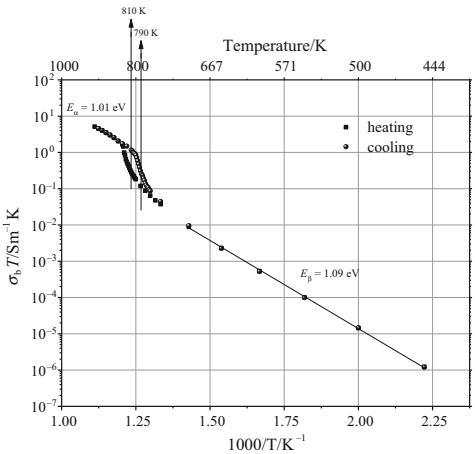

Fig. 15 Arrhenius plots of temperature dependencies of standard deviation for α and β crystal phase transition processes in $La_2Mo_2O_9$ ceramic

by XRD, of the obtained LAMOX-type material is very important because of the interpretations of its electrical properties, which are done with great care. Moreover, the relatively large crystals with dense structure allow to eliminate all factors that usually significantly affect the physical properties of the sample.

Impedance analysis

The typical Arrhenius plots of temperature dependencies of standard deviation for α and β crystal phase transition processes in $La_2Mo_2O_9$ ceramic are shown in Fig. 15. According to these results, the ionic conductivity starts to increase by two orders from about 790 K and ends at about 831 K of temperature. These onset and end temperatures slightly differ compared to the values (T_{onset} = 829.27 K, T_{end} = 811.78 K), which were estimated using DSC analysis and are presented in Table 3. The resulting initial and final temperature differences can be explained by the different heating rate of the sample during measurement. In this case, the heating and cooling rates of the analyzed ceramic were chosen with great care and equal to 3 degree per minute. Despite this assumption, when the difference between onset temperatures reaches 40 degrees and the difference between end temperatures is equal to 20 degrees, only one conclusion is suggested that the formation of cubic beta-phase needs more energy and this process is less favourable than corresponding crystallization of monoclinic phase. Besides, the slightly higher activation energy of 1.09 eV of beta-$La_2Mo_2O_9$ phase formation also confirms that cubic crystal structure is less stable comparing with monoclinic one and its stabilization at room temperature is rather complicated as expected. Moreover, the nature of fixed signal, like heat changes and values of electrical current, also plays an important role in identifying the onset and end temperatures of phase transition in $La_2Mo_2O_9$ crystal system. The combination of this broadband high-temperature impedance spectroscopy and differential scanning calorimetry techniques led us to find both the explanation and the relationship between electrical properties and structural changes in investigated material, especially, in the case of large particles with size of about 100–200 μm and small crystallites whose sizes do not exceed 72 nm.

Conclusions

For the first time, to our knowledge the aqueous tartaric acid-assisted sol–gel synthesis technique was successfully proposed for the preparation of La–Mo–O tartrate gel and $La_2Mo_2O_9$ ceramic materials. The detailed TG–DSC analysis of La–Mo–O tartrate precursor clearly revealed that its thermal decomposition mainly consists of three stages during which the fully inter-oxidation of tartaric acid, partial decomposition of metal tartrates and the final burning of residue of inorganic carbon were occurred. The formation of the final ceramic with the initial composition of $La_2Mo_2O_9$ cubic phase was established from the 793 to

844 K of temperature. The further DSC investigation of $La_2Mo_2O_9$ ceramic revealed that heating and cooling rates play an important role in both onset and end temperatures. Besides, comparing the results obtained from the detailed investigation of La–Mo–O tartrate gel precursor and $La_2Mo_2O_9$ ceramics, it is clear that by increasing the heating rate the onset temperature also increases. With the help of DSC and IS analyses, it was concluded that the phase transition from cubic to monoclinic crystal system occurs under more favorable conditions and its activation energy is slightly smaller.

Acknowledgements This research was funded by a Grant (S-LZ-17-7) from the Research Council of Lithuania.

References

1. Alekseeva OA, Antipin AM, Gagor A, Pietraszko A, Novikova NE, Sorokina NI, et al. Single-crystal structure of vanadium-doped $La_2Mo_2O_9$. Crystallogr Rep. 2013;58(6):829–34.
2. Borah L, Paik B, Hashmi SA, Pandey A. Conductivity and electrical modulus studies of La2-x Nd (x) Mo1.7W0.3O9-delta oxygen ion conductor. Ionics. 2012;18(8):747–57.
3. Xia T, Li JY, Li Q, Liu XD, Meng J, Cao XQ. Synthesis, structural characterization and electrical property of new oxide ion conductors: La3MMo2O12 (M = In, Ga and Al). Solid State Ionics. 2006;177(37–38):3267–73.
4. Zhang YW, Yang Y, Jin S, Tian SJ, Li GB, Jia JT, et al. Sol-gel fabrication and electrical property of nanocrystalline (RE2O3)(0.08)(ZrO2)(0.92) (RE = Sc, Y) thin films. Chem Mater. 2001;13(2):372–8.
5. Kosacki I, Suzuki T, Petrovsky V, Anderson HU. Electrical conductivity of nanocrystalline ceria and zirconia thin films. Solid State Ionics. 2000;136:1225–33.
6. Zhuang Z, Wang XP, Li D, Zhang T, Fang QF. Ionic conductivity enhancement of $La_2Mo_{2-x}W_xO_9$ nanocrystalline films deposited on alumina substrates by the sol–gel method. J Am Ceram Soc. 2009;92(4):839–44.
7. Wang JX, Wang Q, Wang XP, Li C, Fang QF. Synthesis and characterization of fine grained high density $La_2Mo_2O_9$-based oxide-ion conductors. J Mater Sci Technol. 2008;24(5):761–5.
8. Abdala PM, Custo GS, Lamas DG. Enhanced ionic transport in fine-grained scandia-stabilized zirconia ceramics. J Power Sources. 2010;195(11):3402–6.
9. Bellino MG, Lamas DG, de Reca NEW. Enhanced ionic conductivity in nanostructured, heavily doped ceria ceramics. Adv Funct Mater. 2006;16(1):107–13.
10. Lacorre P, Goutenoire F, Bohnke O, Retoux R, Laligant Y. Designing fast oxide-ion conductors based on $La_2Mo_2O_9$. Nature. 2000;404(6780):856–8.
11. Liu X, Fan HQ, Li Q, Shi J. Monoclinic distortion shrinkage and enhanced properties of $La_2Mo_2O_9$ oxide ion conductors synthesized by an isobaric-microwave assisted method. Ecs Solid State Lett. 2013;2(9):N27–30.
12. Baque L, Vega-Castillo J, Georges S, Caneiro A, Djurado E. Microstructural and electrical characterizations of tungsten-doped $La_2Mo_2O_9$ prepared by spray pyrolysis. Ionics. 2013;19(12):1761–74.
13. Marrero-Lopez D, Pena-Martinez J, Ruiz-Morales JC, Perez-Coll D, Martin-Sedeno MC, Nunez P. Structural and electrical characterization of Nb^{5+} and Cr^{6+} substituted $La_2Mo_2O_9$. Bol Soc Esp Ceram. 2008;47(4):213–8.
14. Georges S, Goutenoire F, Bohnke O, Steil MC, Skinner SJ, Wiemhofer HD, et al. The LAMOX family of fast oxide-ion conductors: overview and recent results. J New Mat Electr Syst. 2004;7(1):51–7.
15. Kolesnikova DS, Kharitonova EP, Voronkova VI. Synthesis and phase transitions of oxide-ion conducting compound $La_2Mo_2O_9$ doped with alkaline metals. Crystallogr Rep. 2011;56(2):315–20.
16. Marrero-Lopez D, Pena-Martinez J, Perez-Coll D, Nunez P. Effects of preparation method on the microstructure and transport properties of $La_2Mo_2O_9$ based materials. J Alloys Compd. 2006;422(1–2):249–57.
17. Zhuang Z, Wang XP, Sun AH, Li Y, Fang QF. Sol-gel synthesis and transport property of nanocrystalline $La_2Mo_2O_9$ thin films. J Sol-Gel Sci Technol. 2008;48(3):315–21.
18. Subasri R, Matusch D, Nafe H, Aldinger F. Synthesis and characterization of $(La_{1-x}M_x)_{(2)}Mo_2O_9$-delta; M = Ca^{2+}, Sr^{2+} or Ba^{2+}. J Eur Ceram Soc. 2004;24(1):129–37.
19. Wang JX, Wang XP, Liang FJ, Cheng ZJ, Fang QF. Enhancement of conductivity in $La_2Mo_2O_9$ ceramics fabricated by a novel three-stage thermal processing method. Solid State Ionics. 2006;177(17–18):1437–42.
20. Saradha T, Muzhumathi S, Subramania A. Microwave-assisted combustion synthesis of nanocrystalline $La_2Mo_2O_9$ oxide-ion conductor and its characterization. J Solid State Electr. 2008;12(2):143–8.
21. Cheng H, Wang HE, Li L, Lu ZG, Qian D. Facile synthesis of $La_2Mo_2O_9$ nanoparticles via an EDTA complexing approach. Rare Met. 2008;27(4):340–4.
22. Fievet F, Lagier J, Blin B, Beaudoin B, Figlarz M. Homogeneous and heterogeneous nucleations in the polyol process for the preparation of micron and submicron size metal particles. Solid State Ionics. 1989;32–33:198–205.
23. Barbooti MM, Al-Sammerrai DA. Thermal decomposition of citric acid. Thermochim Acta. 1986;98:119–26.
24. Chattaway FD, Ray FE. II—The decomposition of tartaric acid by heat. J Chem Soc Trans. 1921;119:34–7.
25. Arumugam Manithiram PNK, Sundaram SK, Chan S-W. Front Matter. Developments in Solid Oxide Fuel Cells and Lithium Ion Batteries: Wiley, 2006; p. i–viii.
26. Kezionis A, Kazlauskas S, Petrulionis D, Orliukas AF. Broadband method for the determination of small sample's electrical and dielectric properties at high temperatures. IEEE Trans Microw Theory. 2014;62(10):2456–61.
27. Kazlauskas S, Kezionis A, Kazakevicius E, Orliukas AF. Charge carrier relaxation and phase transition in scandium stabilized zirconia ceramics. Electrochim Acta. 2014;134:176–81.
28. Cruywagen JJ, Heyns JBB, Rohwer EA. Molybdenum(Vi) complex-formation. 4. Equilibria and thermodynamic quantities for the reactions with tartrate in 1.0-Mol Dm-3 sodium-chloride. J Chem Soc Dalton. 1990;6:1951–6.
29. Stankeviciute R, Zalga A. Sol-gel synthesis, crystal structure, surface morphology, and optical properties of Eu2O3-doped La2Mo3O12 ceramic. J Therm Anal Calorim. 2014;118(2):925–35.

Article IV

Oxalic acid assisted synthesis of the gadolinium-doped ceria oxide-ion conductor as electrolyte for the solid oxide fuel cells

G. Gaidamavičienė, B. Abakevičienė, A. Žalga

Chemical Papers 73(4) (2019) 891-899

Chemical Papers
https://doi.org/10.1007/s11696-018-0648-7

ORIGINAL PAPER

Oxalic acid assisted synthesis of the gadolinium-doped ceria oxide-ion conductor as electrolyte for the solid oxide fuel cells

Giedrė Gaidamavičienė[1] · Brigita Abakevičienė[2] · Artūras Žalga[1]

Received: 26 June 2018 / Accepted: 20 November 2018

Abstract
The aim of this paper is to investigate the thermal behavior of as-prepared Gd–Ce–O acetate–oxalate (GCO–AO) precursors and their affinity to the decomposition processes of the starting materials by means of thermogravimetric and differential scanning calorimetric analyses (TG/DTG/DTA). Moreover, the influence of the temperature, heating atmosphere, and heat treatment time on both the morphology and crystal structure of the Ce–Gd–O gel precursor were additionally investigated in detail using a scanning electron microscopy (SEM), X-ray diffraction (XRD) and Fourier transform infrared spectroscopy (FT–IR). The obtained TG/DTG/DTA results revealed that the formation of the gadolinium-doped ceria (GDC) ceramic was closely related to the thermal decomposition processes of the initial compounds: gadolinium (III) acetate and cerium (IV) acetate. The powder XRD patterns of the heat-treated GCO–AO sample revealed that the crystallization process for the GDC ceramic starts at 1173 K, whereas the temperature and heat treatment time significantly affected on the surface morphology and the size of the obtained particles. Besides, the spectra of FT–IR analysis showed that the vibration modes of the oxygen–metal–oxygen (O–M–O) in GDC ceramic heat-treated at different temperatures were equivalent, although the sample heat-treated at 1273 K demonstrated a completely different optical behavior. In that case a strong absorption outspread in the region from 1000 to 500 cm^{-1} was observed, which could be attributed to the initial formation of the nano-sized spherical particles in size of about 50–100 nm.

Keywords Co-precipitation synthesis · Sol–gel processing · Thermal analysis · X-ray diffraction

Introduction

During the last decade the solid oxide fuel cells (SOFC's) have been intensely investigated as a next generation green energy system as they exhibit high ionic conductivity, chemical and thermal stability and also have a high efficiency as well as generate low pollution emissions (Arabaci and Oksuzomer 2012; Firmino et al. 2017; Myung et al. 2012; Priya et al. 2018; Zalga et al. 2018; Zhou et al. 2006). To develop a commercially attractive SOFC, it must be able to operate at a relatively low temperature range of 573–1073 K, also to demonstrate a long-term performance stability, high conversion efficiency and low assisting material cost (Hong et al. 2011; Liang et al. 2011; Milcarek et al. 2016; Pumiglia et al. 2017; Su et al. 2017; Zhu et al. 2011).

Nowadays, a high performance SOFC is limited to work only under a relatively high temperatures. The most basic SOFC design consists of three components: an electrolyte, an anode and a cathode (Escudero and Fuerte 2017; Molero-Sanchez et al. 2017). The electrochemical reaction uses oxygen gas, which is reduced to oxide ions at the cathode, and a fuel that is oxidized at the anode. The cathode is typically a perovskite-like material (Kivi et al. 2017), while the anode is a cermet (i.e., a composite material consisting of a ceramic constituent and a metal) (Le et al. 2018; Nurk et al. 2016). In addition, an electrolyte used in this process is generally a doped solid ceramic oxide that eases the generation of oxygen vacancies and carries the charge between the cathode and the anode. SOFC electrolytes must possess mechanical properties that are sufficient to survive the rigorous environment (Accardo et al. 2018; Daza et al. 2018). The most widely used ceramic in SOFC is an yttrium stabilized

✉ Artūras Žalga
arturas.zalga@chf.vu.lt

[1] Department of Applied Chemistry, Institute of Chemistry, Faculty of Chemistry and Geosciences, Vilnius University, Naugarduko Str. 24, 03225 Vilnius, Lithuania

[2] Institute of Materials Science, Kaunas University of Technology, Barsausko 59, 51423 Kaunas, Lithuania

Published online: 22 November 2018

zirconium (YSZ) ceramic (De Marco et al. 2017; Gerstl et al. 2016). It is a traditional fuel cell electrolyte which exhibits a necessary ionic conductivity and low electrical resistance at high temperatures, but lacks all these properties at relatively low temperatures. Also this ceramic exhibits a metastable tetragonal phase which is essential for the structural hardening during cooling (Diaz-Parralejo et al. 2011; Fenech et al. 2011; Morales et al. 2010). As a potential low operating temperature replacement for YSZ electrolyte a gadolinium-doped ceria (GDC, $Ce_{0.9}Gd_{0.1}O_{1.95}$) is considered (Accardo et al. 2016; Batista and Muccillo 2016, 2018). Ceria-based electrolytes have a relatively large unit cells compared to systems based on zirconia and, as a consequence, ceria-based systems have larger channels through which oxygen ions can pass during the conduction (Chourashiya and Jadhav 2011; Zalga et al. 2011). Moreover, decreasing the temperature of operation for Gd doped ceria to 873 K appears to minimize the reduction of the electrolyte; however, lower temperatures result in the greater loss of power density due to the decrease in the ionic conductivity. To address the significant problem with ceria based materials a number of approaches have been taken, such as looking for the ideal doping ratio and an appropriate ion to balance stability with adequate oxide ion conductivity to decrease the operating temperature, improve materials processing, etc. (Chourashiya and Jadhav 2011).

A great success overcoming the challenges could be achieved using so-called solution-based synthetic methods, which play a crucial role in the design and production of fine ceramics and have been successful in overcoming many of the limitation of the traditional solid-state, high-temperature methods. For example, the metal complexes with organic ligands have been used for the preparation of ceramics and metal oxide thin films by both co-precipitation synthesis and sol–gel process, using metal nitrates, chlorides, acetates, and oxalates as starting materials. Besides, metal salts are very useful, inexpensive, and very easy to handle compared to metal alkoxides, hence they are good alternatives for the conversion to oxides by thermal decomposition. They can be also dissolved in many kinds of organic solvents in which metal complexes are formed. This is the main reason why these wet synthesis routes are attractive compared to other techniques as they possess the advantages such as a good control of the starting materials and the processing parameters, a high purity of the raw materials, and a low temperature of the process. A good homogeneity of the product could be achieved by controlling the stoichiometry of the starting solution (Braziulis et al. 2014; Zalga et al. 2011).

In this study, we report the aqueous oxalic acid assisted syntheses of Ce–Gd–O acetate–oxalate gel precursor for $Ce_{0.9}Gd_{0.1}O_{1.95}$ ceramic, which was additionally heat-treated at 1173 K, 1273 K, 1373 K and 1473 K of temperatures. Besides, Ce–Gd–O acetate–oxalate precursor powder was also sintered at 1223 K in air and nitrogen atmospheres for 10 min at ambient pressure to proof the possible differences according to synthesis condition and heat treatment time on both the surface morphology and the crystallite sizes of the final ceramic.

The main novelty of this work was to obtain stabile $Ce_{0.9}Gd_{0.1}O_{1.95}$ ceramic in the range of temperature from 1173 to 1473 K and to investigate its effects of morphological changes to the characteristic vibrations of functional M–O (M=Ce and Gd) groups using scanning electron microscopy (SEM) and FT–IR spectroscopy.

Materials and methods

The sample of $Ce_{0.9}Gd_{0.1}O_{1.95}$ was prepared by the oxalic acid assisted synthesis (OAS) approach during the mixing stage of the initial salts employing an oxalic acid as a precipitating agent at higher pH values. Gadolinium (III) acetate tetrahydrate ($Gd(CH_3COO)_3{\cdot}4H_2O$, 99.9% AlfaAesar), cerium (VI) acetate hydrate ($Ce(CH_3COO)_4{\cdot}H_2O$, 99.9% AlfaAesar) were used as starting materials and weighed according to the desired stoichiometric ratio. Acetic acid (CH_3COOH, 99.8% PENTA), distilled water and ammonium hydroxide solution (NH_4OH 25% PENTA) were used as solvents and reagents to adjust the pH of the solutions. Oxalic acid ($C_2H_2O_4{\cdot}2\ H_2O$ (OA), 99.5% Sigma), was applied as an agent both to increase of the solubility via coordination of starting compounds in the reaction mixture and to form the precipitates of initial salts at higher pH values. At first, gadolinium (III) acetate tetrahydrate and cerium (VI) acetate hydrate (OAS) were dissolved in a mixture of acetic acid and distilled water at 323 K. Then oxalic acid was dissolved in a small amount of distilled water separately and added to the reaction mixture by continuous stirring at the same temperature. Moreover, after several hours of mixing in a closed beaker with a watch glass the pH of the reaction mixture was increased to 9.0 by adding ammonia. The obtained white precipitate was separated from the solution by filtration and dried at 373 K for 24 h in air. Moreover, the oxalate precursor powder was additionally sintered at 1173 K, 1273 K, 1373 K and 1473 K of temperatures for 5 h under air atmosphere. Furthermore, the as-prepared Gd–Ce–O oxalate precursor sample was also heat-treated at 1223 K for 10 min at an ambient pressure in air.

Thermal measurements were performed with TG−DTA, STA 6000 Perkin-Elemer instrument using a sample weight of about 10 mg and a heating rate of 20° min^{-1} under the continuous air flow (20 $cm^3\ min^{-1}$) at ambient pressure from room temperature to 1273 K. The residual powders that were left after thermal treatment were additionally investigated by XRD analysis. X-ray diffraction (XRD) patterns were recorded in air at room temperature with a powder X-ray diffract meter Rigaku MiniFlex II using Cu Kα_1 radiation.

The Rietveld refinement of the obtained XRD patterns were performed using X'Pert HighScore Plus software. The spectra were recorded at the standard rate of 1.5 $2\theta/\text{min}^{-1}$. The scanning electron microscope (SEM) Hitachi SU-70 was used to study the surface morphology and microstructure of the obtained ceramic samples. Finally, the Fourier transform infrared (FT–IR) spectra were recorded with a Perkin-Elmer Frontier FT–IR spectrometer.

Results and discussion

Thermal analysis

The TG/DTG/DTA measurements of the initial salts and Gd–Ce–O oxalate precursor, which were carried out up to 1273 K at a heating rate of 20° min^{-1} in flowing air (20 cm^3 min^{-1}) at ambient pressure with a sample mass of about 10 mg in Fig. 1 are shown, respectively. At the initial stage of explanation of the results, presented in Fig. 1, it is important to note that the thermal decomposition of both cerium and gadolinium acetates slightly differs from the corresponding oxalates, which formed after addition of oxalic acid into reaction mixture. Nevertheless, the final mass change of about 40% in the TG curve (Fig. 1b) has a closely linked manner in terms of quantitative change of mass with the thermal decomposition of the initial acetates, residue quantity in the sample and the onset temperature of the final decomposition stage. In general, the decomposition processes of the starting compounds and GDC oxalate precursor could be roughly divided into three periods that clearly indicate all mass changes and heat flow transformations occurring during the sample heating in the appropriate range of temperature. The first mass change of about 2.6% in the TG curve (Fig. 1b enlarged picture at the right top corner) is identified from 303 to 413 K temperatures and is related to the removal of surface absorbed water from the precursor powder as confirmed by both a small peak in DTG curve and an endothermic effect of about 344.3 mJ ($\Delta H = 34.2$ J/g) in DTA curve.

The further increase of temperature from 414 to 593 K followed by the mass change of about 7.0% leads to the broad exothermic process and to the second well-defined endothermic effect simultaneously. In this case, the emission of heat is attributed to the partial decomposition of ammonium oxalate that formed in a small amount as an impurity during the precipitation of GDC precursor powder by ammonia solution. Meanwhile, the sharp endothermic peak of about 187.8 mJ ($\Delta H = 18.7$ J/g) at 507 K of temperature is related to the evaporation of water molecules from the coordination sphere of corresponding metals in the precursor powders. The further increase of temperature from 594 to 668 K indicated by the mass change of 38.0%, as presented

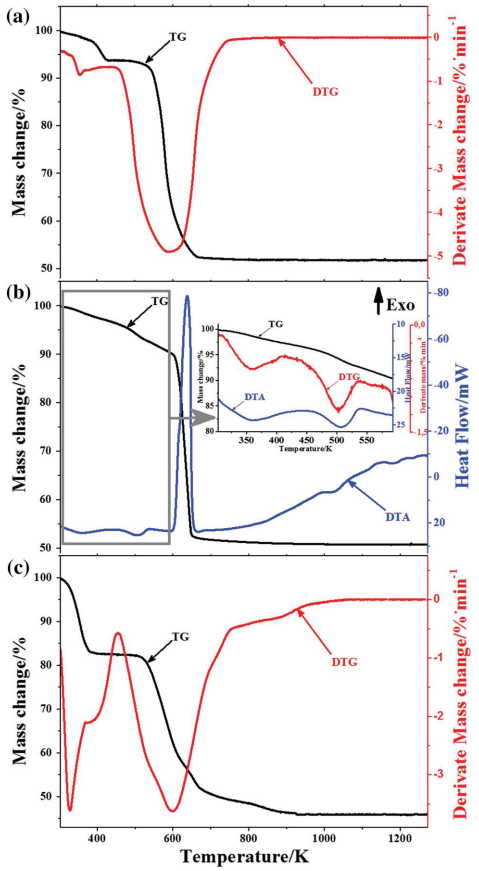

Fig. 1 Combined TG/DTG/DTA curves of the cerium acetate hydrate (**a**), gadolinium-doped ceria oxalate precursor (**b**), and gadolinium acetate tetrahydrate (**c**) in flowing air

in Table 1, corresponds to the thermal decomposition of cerium and gadolinium oxalates, which formed after precipitation by ammonia solution in the last synthesis stage.

The sharp exothermic peak of about − 7515.4 mJ ($\Delta H = -746.5$ J/g) well matched the formation of carbon dioxide from the corresponding oxalate with a relatively high heat flow compared to other decomposition processes in the sample. By further increasing the temperature from 669 to 923 K, the mass of the residue decreases slightly up to 1.2%. In this stage, the mass change is closely related to the final burning of elemental carbon that formed during the partial decomposition of the initial salts in the precursor powder. This conclusion was confirmed by the exothermic

Table 1 Thermoanalytical data for the Ce–Gd–O oxalate gel precursor

Range of temperature/K	Weight			Heat			
	Loss/%	Onset/K	Residual/%	Flow/mJ	Onset/K	End/K	Enthalpy/J g^{-1}
303–413	2.6	309.55	97.4	344.3	322.25	395.75	34.2
414–593	7.0	506.15	93.3	−264.5	415.55	582.65	−26.3
			90.4	187.8	474.75	528.55	18.7
594–668	38.0	615.55	52.4	−7515.4	610.95	650.15	−746.5
669–923	1.2	683.15	51.2	–	–	–	–

behavior of the DTA curve in this range of temperature. Moreover, the thermal decomposition of gadolinium acetate tetrahydrate also shows a similar character in the TG–DTG curves after the greatest mass change up to 673 K, as shown in Fig. 1c. This is the reason why the final mass change in the TG curve is attributed to the decomposition of residue that came from the gadolinium oxalate in the sample powder. Finally, from 973 K the mass of the sintered ceramic remains constant while the exothermic nature of the DTA curve makes a suggestion about crystallization process of the final material at the temperature higher than 1173 K. Besides, the consolidation and stabilization of the GDC crystal phase occurs above 1273 K, therefore, as-precipitated Gd–Ce–O oxalate powder were additionally heat-treated at 1173 K, 1273 K, 1373 K and 1473 K for 5 h in air at ambient pressure.

X-ray diffraction

The XRD patterns of the gadolinium-doped ceria oxalate precursor and GDC ceramic powders heat-treated at 1173 K, 1273 K, 1373 K and 1473 K are presented in Fig. 2, respectively. As seen in the XRD panel (a) of Fig. 2, the drying of the as prepared gadolinium-doped ceria oxalate precursor at 373 K of temperature causes no characteristic peaks to appear. This result gives the conclusion about the low crystallization of the initial salts during the precipitation process.

Meanwhile, the characteristic peaks in the XRD patterns of all GDC powders heat-treated at 1173 K, 1273 K, 1373 K and 1473 K are well matched for the standard ICSD card of $Ce_{0.9}Gd_{0.1}O_{1.95}$.

To show the tendency of the crystallization for $Ce_{0.9}Gd_{0.1}O_{1.95}$ ceramic, the Rietveld refinement analysis of all samples was also performed. The agreement indices, crystallite sizes and lattice parameter for the $Ce_{0.9}Gd_{0.1}O_{1.95}$ compound heat treated at different temperatures are shown in Table 2.

This result let us conclude that the crystallization of gadolinium-doped ceria above 1173 K has occurred. It is also noticed, that there were no significant changes between all the estimated samples. This compliance between the characteristic peaks of four separate GDC samples is confirmed

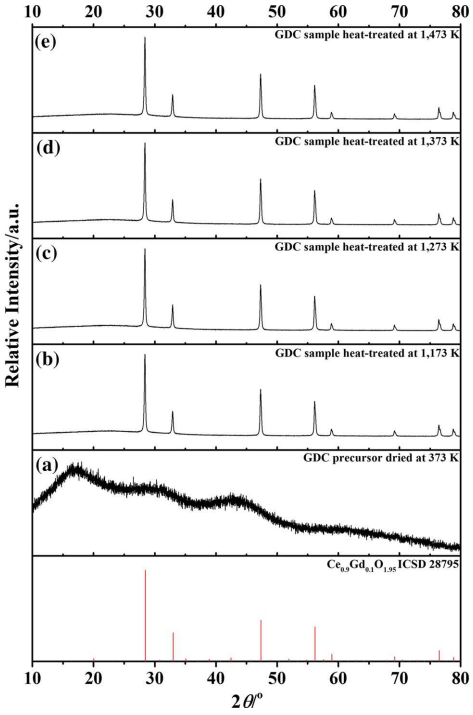

Fig. 2 Standard ICSD card of $Ce_{0.9}Gd_{0.1}O_{1.95}$ and XRD patterns of gadolinium-doped ceria oxalate precursor dried at 373 K and heat-treated at 1173 K, 1273 K, 1373 K and 1473 K temperatures for 5 h in air at ambient pressure

by both high stability of the final crystal structure and a lack of impurity phases in the final ceramic powders.

To show a single-phase formation of the gadolinium-doped ceria under the synthesis conditions the XRD measurements and the Rietveld refinement analysis of the final ceramic heat-treated at different atmospheres were performed. The corresponding results are presented in the Table 3 and the Fig. 3.

Table 2 Agreement indices, crystallite sizes and lattice parameter for the $Ce_{0.9}Gd_{0.1}O_{1.95}$ ceramic heat-treated at different temperatures

Heat-treating temperature/K	Weighted *R* profile	Goodness of fit	Crystallite size/nm	Lattice parameter/pm
1173	9.50443	1.57092	55.01	541.883
1273	9.66036	1.62627	55.44	541.893
1373	9.55569	1.59464	55.34	541.891
1473	9.70284	1.63989	55.03	541.898

Table 3 Agreement indices, crystallite sizes and lattice parameter for the $Ce_{0.9}Gd_{0.1}O_{1.95}$ ceramic heat-treated at 1223 K in different atmospheres

Heat-treating temperature/K	Heating atmosphere	Duration/min	Weighted *R* profile	Goodness of fit	Crystallite size/nm	Lattice parameter/pm
1223	Air	10	9.10234	1.44141	40.78	541.666
1223	Nitrogen	10	7.45141	1.01236	26.98	542.314

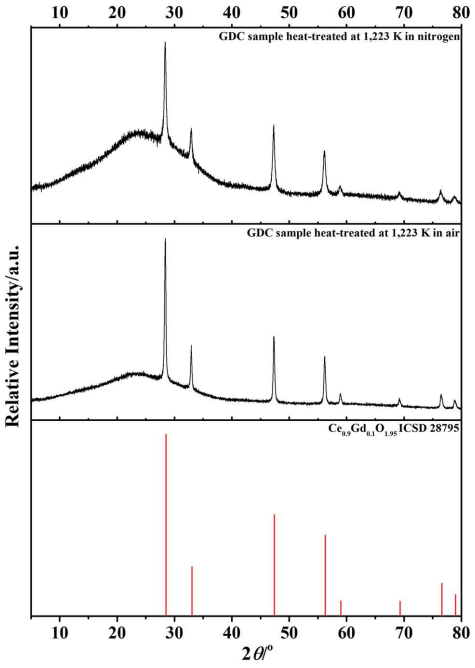

Fig. 3 Standard ICSD card of $Ce_{0.9}Gd_{0.1}O_{1.95}$ and XRD patterns of gadolinia-doped ceria oxalate precursor heat-treated at 1223 K in air and nitrogen atmosphere for 10 min at ambient pressure

As seen from Fig. 3 top two panels, no characteristic peaks of the potential impurity phases could be identified. Besides, it can be clearly seen that the intensities of the characteristic peaks are quite low as well as their width, which implies the formation of nano-sized crystals. It is also important to note that the synthesis conditions have no effect on the crystal phase composition of the investigated samples. However, despite the fact that the obtained results suggest identical crystal phase formation in both cases, the view of XRD patterns though slightly differs. It must be noted that the peak width of the sample heat-treated in nitrogen atmosphere is broader compared to the ceramic heat-treated in air.

As can be seen from Table 3, the heat-treatment of the Ce–Gd–O oxalate precursor in nitrogen atmosphere slightly more affects both the lattice parameter and crystallite size of the final cubic $Ce_{0.9}Gd_{0.1}O_{1.95}$ crystal structure comparing with the sample, which was prepared in air. This result let us to conclude that an air atmosphere is a more favorable condition for the crystallization of the final GDC ceramic. Such conclusion confirms the fact that in air the sintering of Gd–Ce–O oxalate precursor leads to the better oxidation of the intermediate products, which is the critical stage creating more favorable conditions of the crystallization of the final ceramic.

SEM microscopy

To understand the crystal growth of the final products, we investigated the influence of the temperature, heating atmosphere, and the heat treatment time on the morphology of the Ce–Gd–O gel precursor. The SEM micrographs of the GDC sample heat-treated at 1173 K, 1273 K, 1373 K and 1473 K for 5 h are shown in Fig. 4, respectively.

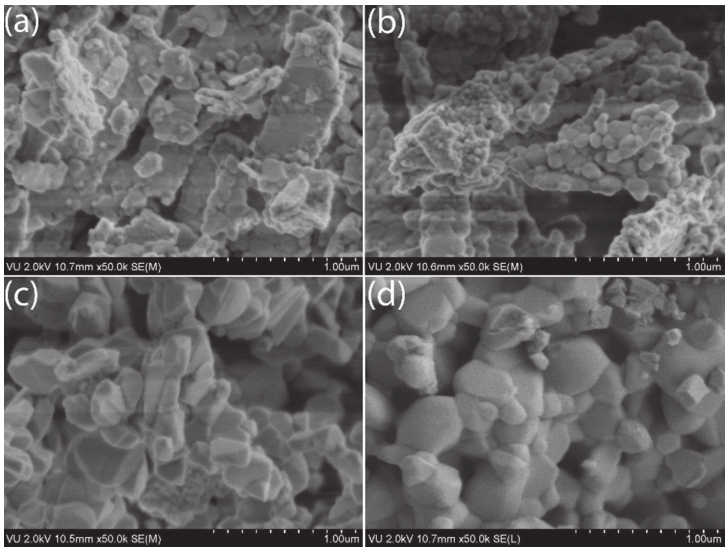

Fig. 4 SEM micrographs of GDC acetate–oxalate precursor gel heat-treated at (**a**) 1173 K, (**b**) 1273 K, (**c**) 1373 K, and 1473 K temperatures at ambient pressure in air for 5 h

As seen from Fig. 4a, the surface of the gadolinium-doped ceria oxalate precursor heat-treated at 1173 K consists of plate-like particles that vary in size from 100 nm to 1 μm. By increasing the sintering temperature to 1273 K, as displayed in Fig. 4b, the formation of spherical particles less than 100 nm was observed. Besides, it is interesting to note that in this case the conglomeration of the aggregates tends to increase from 1–2 to 3–4 μm in comparison with the previous case, but the size and shape of the individual particles can be better defined. The size of spherical particles varies from 50 to 100 nm. Meanwhile, a completely different surface morphology of the sample heat-treated at 1373 K is shown in Fig. 4c. Further increase of heat treatment temperature up to 1273 K leads to the agglomeration of close-packed crystals with well-defined edges and shapes, varying from 200 to 800 nm. Finally, by increasing the heat treatment temperature up to 1473 K the tendency of crystal growing remains (Fig. 4d) and the size of crystalline structures increases by both the individual particles up to about 1 μm and its close-packed agglomerates up to 4–5 μm.

The SEM micrographs of the GDC sample heat-treated at 1223 K for 10 min in air and nitrogen atmosphere are shown in Fig. 5 in this case, it could be clearly distinguished that the heating atmosphere has no significant influence on the crystal size and surface morphology of as-prepared ceramic samples at 1223 K.

In both cases the formation of irregularly shaped plate-like crystals in size of about 1–5 μm were observed and no changes in the surface morphology were identified.

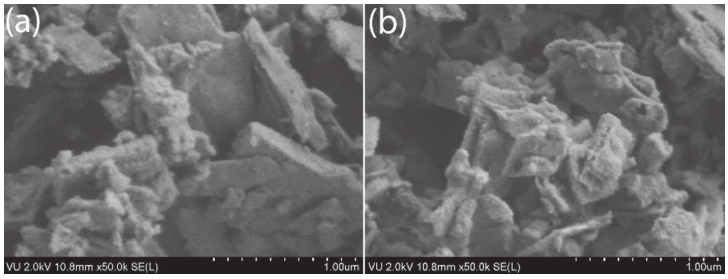

Fig. 5 SEM micrographs of GDC acetate–oxalate precursor gel heat-treated at 1223 K in air (**a**) and nitrogen (**b**) for 10 min

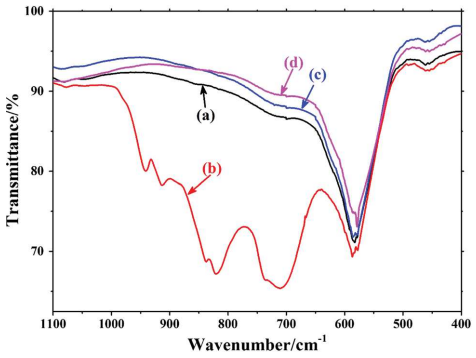

Fig. 6 FT−IR transmittance spectra of GDC sample heat-treated at (**a**) 1173 K, (**b**) 1273 K, (**c**) 1373 K, and (**d**) 1473 K of temperatures

FT−IR analysis

In despite of several articles (Arabaci 2015; Arabaci and Oksuzomer 2012; Chavan et al. 2012; Choolaei et al. 2018; Pezeshkpour et al. 2017; Tao et al. 2009; Zarkov et al. 2016, 2018) published in recent years about investigation of the characteristic vibrations of functional groups using FT–IR spectroscopy for GDC ceramic, there is a clear lack of data, especially in the region of 1000–400 cm^{-1}. To investigate the characteristic vibrations of functional groups of the as-prepared ceramic at different temperatures and relate the similarities and differences between the obtained XRD and SEM results the FT–IR spectroscopy was applied. The infrared spectra of the synthesized GDC sample heat-treated at 1173 K, 1273 K, 1373 K and 1473 K for 5 h are shown in Fig. 6. FT–IR curves of the GDC specimens heat-treated at 1173 K, 1373 K and 1473 K qualitatively are very similar as they exhibit a well-defined absorption bands centered at around 580 cm^{-1} and 458 cm^{-1} in the region of 650–400 cm^{-1}, whereas the absorption bands of the sample heat-treated at 1273 K take place from the 1000 to 500 cm^{-1} with a well-defined dispersion at 942 cm^{-1}, 914 cm^{-1}, 838 cm^{-1}, 820 cm^{-1}, 736 cm^{-1}, 712 cm^{-1}, 586 cm^{-1}, 577 cm^{-1} and 458 cm^{-1}.

The reason of these differences could be defined as an interconversion and agglomeration of plate-like particles into a close-packed spherical particles that are less than 100 nm in diameter, because of crystallites size that remains constant irrespective of the heating temperature.

Conclusions

Summarizing results obtained from the TG/DTG/DTA, XRD, SEM and FT−IR measurements it can be concluded that an oxalic acid assisted synthesis of gadolinium-doped ceria produced a relatively pure amorphous powder, initially enriched by the oxalate salts as an impurities formed of both the salts of metal precursors and the precipitating agent. According to the thermal analysis, the reaction product reaches a thermodynamic equilibrium under the conditions of 1273 K, when the final consolidation and stabilization of the crystal phase occurs, therefore, the compound heat-treated at the temperatures above 1273 K exhibits a great thermal and chemical stability. The XRD crystallography correlated with the results of thermal analysis perfectly, indicating no essential differences in crystal structure of the sample from the point of thermal equilibrium. Moreover, to account for the structural interconversions at relatively low temperatures, the study of surface morphology indicates the crucial transition of irregularly shaped plate-like crystals to the spherical nano-sized particles, which subsequently conglomerated into a close-packed agglomerates, hence uniformity was obtained necessary to reduce the ohmic voltage loss and increase the potential efficiency of a ceramic electrolyte. Finally, it must be noted that the dramatic increase of surface area of the spherical nano particles at 1273 K causes the higher concentration of different characteristic vibrations of oxygen–metal–oxygen bonds at the surface of specimen, however, at different sintering temperatures the deviation of optical properties is lost indicating nano-sized particles being a metastable phase in the process of crystal growth.

Acknowledgements The research leading to these results has received funding from Lithuanian–French Programme "Gilibert" under project agreement no S-LZ-17-7.

References

Accardo G, Ferone C, Cioffi R, Frattini D, Spiridigliozzi L, Dell'Agli G (2016) Electrical and microstructural characterization of ceramic gadolinium-doped ceria electrolytes for ITSOFCs by sol–gel route. J Appl Biomater Funct Mater 14:E35–E41. https://doi.org/10.5301/jabfm.5000265

Accardo G, Frattini D, Ham HC, Han JH, Yoon SP (2018) Improved microstructure and sintering temperature of bismuth nano-doped GDC powders synthesized by direct sol–gel combustion (vol 44, pg 3800). Ceram Int 44:10020. https://doi.org/10.1016/j.ceramint.2018.02.0221

Arabaci A (2015) Effect of Sm and Gd dopants on structural characteristics and ionic conductivity of ceria. Ceram Int 41:5836–5842. https://doi.org/10.1016/j.ceramint.2015.01.013

Arabaci A, Oksuzomer MF (2012) Preparation and characterization of 10 mol% Gd doped CeO_2 (GDC) electrolyte for

SOFC applications. Ceram Int 38:6509–6515. https://doi.org/10.1016/j.ceramint.2012.05.030
Batista RM, Muccillo ENS (2016) Dilatometry analysis of the sintering process of nanostructured gadolinia-doped ceria. J Therm Anal Calorim 126:1007–1013. https://doi.org/10.1007/s10973-016-5674-5
Batista RM, Muccillo ENS (2018) Analysis of the sintering process in gadolinia-doped ceria by thermodilatometry and correlation with microstructure evolution. J Therm Anal Calorim 132:851–857. https://doi.org/10.1007/s10973-018-6969-5
Braziulis G, Janulevicius G, Stankeviciute R, Zalga A (2014) Aqueous sol–gel synthesis and thermoanalytical study of the alkaline earth molybdate precursors. J Therm Anal Calorim 118:613–621. https://doi.org/10.1007/s10973-013-3579-0
Chavan AU, Jadhav LD, Jamale AP, Patil SP, Bhosale CH, Bharadwaj SR, Patil PS (2012) Effect of variation of NiO on properties of NiO/GDC (gadolinium doped ceria) nano-composites. Ceram Int 38:3191–3196. https://doi.org/10.1016/j.ceramint.2011.12.023
Choolaei M, Cai Q, Slade RCT, Horri BA (2018) Nanocrystalline gadolinium-doped ceria (GDC) for SOFCs by an environmentally-friendly single step method. Ceram Int 44:13286–13292. https://doi.org/10.1016/j.ceramint.2018.04.159
Chourashiya MG, Jadhav LD (2011) Synthesis and characterization of 10%Gd doped ceria (GDC) deposited on NiO-GDC anode-grade-ceramic substrate as half cell for IT-SOFC. Int J Hydrog Energy 36:14984–14995. https://doi.org/10.1016/j.ijhydene.2010.12.083
Daza PCC, Meneses RAM, Rodrigues ACM, da Silva CRM (2018) Ionic conductivities and high resolution microscopic evaluation of grain and grain boundaries of cerium-based codoped solid electrolytes. Ceram Int 44:13699–13705. https://doi.org/10.1016/j.ceramint.2018.04.210
De Marco V, Iannaci A, Lo Faro M, Sglavo VM (2017) Influence of copper-based anode composition on intermediate temperature solid oxide fuel cells performance. Fuel Cells 17:708–715. https://doi.org/10.1002/fuce.201700020
Diaz-Parralejo A, Cuerda-Correa EM, Macias-Garcia A, Diaz-Diez MA, Sanchez-Gonzalez J (2011) Tailoring the properties of Yttria-stabilized zirconia powders prepared by the sol–gel method for potential use in solid oxide fuel cells. Fuel Process Technol 92:183–189. https://doi.org/10.1016/j.fuproc.2010.05.033
Escudero M, Fuerte A (2017) Performance of ceria-electrolyte solid oxide fuel cell using simulated biogas mixtures as fuel. Adv Energy Power 5:20–26. https://doi.org/10.13189/aep.2017.050202
Fenech J, Dalbin M, Barnabe A, Bonino JP, Ansart F (2011) Sol–gel processing and characterization of (RE-Y)-zirconia powders for thermal barrier coatings. Powder Technol 208:480–487. https://doi.org/10.1016/j.powtec.2010.08.046
Firmino H, Araújo A, Dutra R, Nascimento R, Rajesh S, Macedo D (2017) One-step synthesis and microstructure of CuO-SDC composites. Cerâmica 63:52–57. https://doi.org/10.1590/0366-69132017633652088
Gerstl M, Nenning A, Iskandar R, Rojek-Wockner V, Bram M, Hutter H, Opitz AK (2016) The sulphur poisoning behaviour of gadolinia doped ceria model systems in reducing atmospheres. Materials 9:649. https://doi.org/10.3390/ma9080649
Hong YS, Kim SH, Kim WJ, Yoon HH (2011) Fabrication and characterization GDC electrolyte thin films by e-beam technique for IT-SOFC. Curr Appl Phys 11:S163–S168. https://doi.org/10.1016/j.cap.2011.03.071
Kivi I, Aruväli J, Kirsimäe K, Möller P, Heinsaar A, Nurk G, Lust E (2017) Influence of humidified synthetic air feeding conditions on the stoichiometry of $(La_{1-x}\ Sr_x)_yCoO_{3-\delta}$ and $La_{0.6}Sr_{0.4}Co_{0.2}Fe_{0.8}O_{3-\delta}$ cathodes under applied potential measured by electrochemical in situ high-temperature XRD method. J Solid State Electrochem 21:361–369. https://doi.org/10.1007/s10008-016-3379-0
Le MV, Tsai DS, Nguyen TA (2018) BSCF/GDC as a refined cathode to the single-chamber solid oxide fuel cell based on a LAMOX electrolyte. Ceram Int 44:1726–1730. https://doi.org/10.1016/j.ceramint.2017.10.103
Liang B et al (2011) Effect of the adding ferrum in nickel/GDC anode-supported solid-oxide fuel cell in the intermediate temperature. Int J Hydrog Energy 36:10975–10980. https://doi.org/10.1016/j.ijhydene.2011.05.142
Milcarek RJ, Wang K, Garrett MJ, Ahn J (2016) Performance investigation of dual layer Yttria-stabilized Zirconia–Samaria-doped ceria electrolyte for intermediate temperature solid oxide fuel cells. J Electrochem Energy Convers Storage 13:011002. https://doi.org/10.1115/1.4032708
Molero-Sanchez B, Moran E, Birss V (2017) Rapid and low-energy fabrication of symmetrical solid oxide cells by microwave methods Acs. Omega 2:3716–3723. https://doi.org/10.1021/acsomega.7b00275
Morales M, Roa JJ, Capdevila XG, Segarra M, Pinol S (2010) Mechanical properties at the nanometer scale of GDC and YSZ used as electrolytes for solid oxide fuel cells. Acta Mater 58:2504–2509. https://doi.org/10.1016/j.actamat.2009.12.036
Myung JH, Ko HJ, Lee JJ, Lee JH, Hyun SH (2012) Synthesis and characterization of NiO/GDC-GDC dual nano-composite powders for high-performance methane fueled solid oxide fuel cells. Int J Hydrog Energy 37:11351–11359. https://doi.org/10.1016/j.ijhydene.2012.04.140
Nurk G et al (2016) Mobility of Sr in gadolinia doped ceria barrier layers prepared using spray pyrolysis, pulsed laser deposition and magnetron sputtering methods. J Electrochem Soc 163:F88–F96. https://doi.org/10.1149/2.0531602jes
Pezeshkpour S, Abdullah AZ, Salamatinia B, Horri BA (2017) Ionic-gelation synthesis of gadolinium doped ceria ($Ce_{0.8}Gd_{0.2}O_{1.90}$) nanocomposite powder using sodium-alginate. Ceram Int 43:7123–7135. https://doi.org/10.1016/j.ceramint.2017.02.145
Priya NSC, Sandhya K, Rajendran DN (2018) Study on electrical conductivity and activation energy of doped ceria nanostructures. Electrochem Energy Technol 3:49–53. https://doi.org/10.1515/eetech-2017-0004
Pumiglia D et al (2017) Aggravated test of intermediate temperature solid oxide fuel cells fed with tar-contaminated syngas. J Power Sources 340:150–159. https://doi.org/10.1016/j.jpowsour.2016.11.065
Su SC, Zhang WX, Wu J, Zhou CC (2017) Effect of component thickness and anode composition on the residual stress of micro-tubular solid oxide fuel cell. Int J Electrochem Sci 12:9121–9130. https://doi.org/10.20964/2017.10.50
Tao YK, Shao J, Wang JX, Wang WG (2009) Morphology control of $Ce_{0.9}Gd_{0.1}O_{1.95}$ nanopowder synthesized by sol–gel method using PVP as a surfactant. J Alloy Compd 484:729–733. https://doi.org/10.1016/j.jallcom.2009.05.027
Zalga A, Moravec Z, Pinkas J, Kareiva A (2011) On the sol–gel preparation of different tungstates and molybdates. J Therm Anal Calorim 105:3–11. https://doi.org/10.1007/s10973-011-1367-2
Zalga A et al (2018) Aqueous sol–gel synthesis, thermoanalytical study and electrical properties of $La_2Mo_2O_9$. J Therm Anal Calorim 132:1499–1511. https://doi.org/10.1007/s10973-018-7120-3
Zarkov A et al (2016) Synthesis of nanocrystalline gadolinium doped ceria via sol–gel combustion and sol–gel synthesis routes. Ceram Int 42:3972–3988. https://doi.org/10.1016/j.ceramint.2015.11.066

Zarkov A, Mikoliunaite L, Katelnikovas A, Tautkus S, Kareiva A (2018) Preparation by different methods and analytical characterization of gadolinium-doped ceria. Chem Pap 72:129–138. https://doi.org/10.1007/s11696-017-0264-y

Zhou XL, Ma JJ, Deng FJ, Meng GY, Liu XQ (2006) Preparation and properties of ceramic interconnecting materials, $La_{0.7}Ca_{0.3}CrO_3$-delta doped with GDC for IT-SOFCs. J Power Sources 162:279–285. https://doi.org/10.1016/j.jpowsour.2006.06.091

Zhu B, Ma Y, Wang XD, Raza R, Qin HY, Fan LD (2011) A fuel cell with a single component functioning simultaneously as the electrodes and electrolyte. Electrochem Commun 13:225–227. https://doi.org/10.1016/j.elecom.2010.12.019

NOTES

Vilniaus universiteto leidykla
Saulėtekio al. 9, III rūmai, LT-10222 Vilnius
El. p. info@leidykla.vu.lt, www.leidykla.vu.lt
Tiražas 20 egz.